

Imaging of mixing processes in spark-ignition engines via quantitative laser-induced fluorescence

Von der Fakultät für Ingenieurwissenschaften, Abteilung Maschinenbau und Verfahrenstechnik
der

Universität Duisburg-Essen

zur Erlangung des akademischen Grades

eines

Doktors der Ingenieurwissenschaften

Dr.-Ing.

genehmigte Dissertation

von

Patrick Kranz
aus
Leverkusen

Gutachter: Univ.-Prof. Dr.-Ing. Sebastian A. Kaiser
PD Dr.-Ing. habil. Lars Zigan

Tag der mündlichen Prüfung: 17.08.2020

*The important thing is to not stop questioning.
Curiosity has its own reason for existing.*

– Albert Einstein

Acknowledgments

This thesis was created during my time at the Institute for Combustion and Gas Dynamic – Reactive fluids at the University of Duisburg-Essen. At this point I would like to express my greatest appreciation to my supervisor Sebastian A. Kaiser. With his expertise, patience, and understanding I got the best supervision one can imagine, and he made my graduation even more successful. I would also like to emphasize his continuous support in the work on our publications and my dissertation as well as his always existing confidence in me in the handling of projects and measurement campaigns in the industry.

I also want to thank Christof Schulz and Sebastian A. Kaiser for giving me the possibility to work on many different exciting projects together with many different international institutions and companies. The research work in this thesis was funded by the Federal Ministry of Education and Research (BMBF, Germany) within the project “OMeGa-E” (project 13N13034) and by the “Research Association for Combustion Engines e.V.” (FVV, Germany – Frankfurt a. Main) within the project “Bioptic-3” (project 1203). I would also thank the colleagues from the departments Advance Development of SI Engines and Optical Measurements at Volkswagen AG for their technical support during the measurement campaigns at Volkswagen and LaVision GmbH for their support on measurement equipment.

Moreover, I definitely want to thank all my colleagues and fellow students at the engine group who I used to work with over the last 4 years during my time at the IVG. In particular I would like to thank Kai Banke, Philipp Barth, Daniel Fuhrmann, Martin Goschütz, Niklas Jüngst, Ali Shahbaz, Syahar Shawal, Sebastian Wiemann, and Ming Zhao for the good time spend and for their helpful discussions on optical diagnostics and other related topics. I am happy for the good friendships I made, and the valuable time spend in the engine group.

In any case I would like to thank Natascha Schlösser, Beate Endres, Birgit Nelius, Jörg “Aldi” Albrecht, and Erdal Akyildiz for their anytime support at the test bench, in lab, and everywhere else where it was needed. Without your help I would have not been able to finish all the work that was done. Additionally, I would like to express all my gratitude for the help I got from student workers and graduate students I supervised and worked with.

Definitely, I would like to acknowledge my parents, Agnes and Peter, and my sister Kristina for their fundamental support, help, and love brought to me throughout my whole life. Without you, I would not be what I am. Also, I would like to express thanks to my closest friends for being understandable and for the fruitful discussions about every day’s life. Last but not least, my acknowledgments definitely belong to my future wife Nina, who was always there for me, and constantly brought comprehensive understanding for the work I do.

Wermelskirchen, August, 2020



(Patrick Kranz)

Abstract

In this work, laser-induced fluorescence (LIF) imaging of tracers is used to quantitatively study mixture formation in two optically accessible spark-ignited engines. Two strategies for mixture formation are examined, late direct injection of a multicomponent gasoline-type fuel in a motored engine, and port-fuel injection of methane in a fired engine. In both experiments, the influence of temperature on the quantification is accounted for.

In direct-injection engines, fuel components of different volatility can segregate in the transient evaporating spray. The resulting spatial mixture inhomogeneities may influence ignition and combustion. The optical diagnostic presented here images the effect of preferential evaporation of a multi-component gasoline surrogate fuel. It is based on LIF of two aromatic “tracers” added in small quantities to the non-fluorescing surrogate fuel. The latter consists of a mixture of light to medium volatiles *n*-pentane and *iso*-octane, represented by the tracer 1,4-difluorobenzene, and heavy component *n*-undecane, represented by 1-methylnaphthalene. In experiments in an optically accessible engine motored on nitrogen, LIF from the two tracers is spectrally separated and detected on two cameras, with channel crosstalk corrected during the post-processing. Consistent with previous measurements in a pressure vessel, the light components are preferentially found downstream, towards the front of the evaporated fuel jet. Throughout large regions of the field of view, about 20% surplus of 1-methylnaphthalene is found, and throughout smaller ones about 40% of 1,4-difluorobenzene. An increase in in-cylinder tumble and retarded injection both are found to reduce segregation of fuel components. To better assess the influence of the (unknown) local temperature on measurement accuracy, the temperature is calculated via an adiabatic-mixing model and in separate experiments measured via two-color thermometry based on LIF of anisole (methoxybenzene). In the relevant range of crank angles, the local temperature is found to be 25 K lower in regions of high fuel concentration than in the rest of the charge, implying a systematic temperature-induced error of about 0.11 in the fuel-tracer ratio.

Port-fuel injection can also cause mixture inhomogeneity late in the cycle. This is particularly so for natural gas as the fuel. To obtain spatio-temporally resolved information on air-fuel mixing in the cylinder of a gas-fueled engine, an LIF technique was developed and combined with infrared absorption measurements and a CFD simulation. LIF of anisole, vaporized into the gaseous fuel, is captured by a two-camera system, providing one instantaneous image of the air/fuel ratio per cycle. In advances over previous implementations, the technique simultaneously measures temperature to improve the accuracy in the measured air/fuel ratio. In some experiments, structured laser illumination planar imaging (SLIPI) is used, extending the detection limit but reducing spatial resolution compared to conventional LIF imaging. In general, the mixture formation after closed-valve injection is found to consist of tumble convection with gradual mixing. Variations in engine speed and intake pressure significantly influence the initial penetration of the fuel-rich fresh charge into the combustion chamber and thus the overall mixture formation.

Kurzfassung

In dieser Arbeit wird laserinduzierte Fluoreszenz (LIF) an Marker-Substanzen (Tracer) zur quantitativen bildgebenden Untersuchung der Gemischbildung in optisch zugänglichen Ottomotoren eingesetzt. Zwei Gemischbildungsstrategien werden untersucht: späte Direkteinspritzung eines Mehrkomponenten-Benzin-Modellkraftstoffs im geschleppten Motor und Saugrohrenblasung von Methan im gefeuerten Betrieb. In beiden Experimenten wird der Einfluss der Temperatur auf die Quantifizierung berücksichtigt.

Bei der Direkteinspritzung von Flüssigkraftstoff können sich Komponenten unterschiedlicher Flüchtigkeit im verdampfenden Kraftstoffstrahl voneinander trennen. Die resultierende Gemischinhomogenität kann Zündung und Verbrennung beeinträchtigen. Die hier vorgestellte optische Messmethode bildet den Effekt der präferentiellen Verdampfung eines Mehrkomponenten-Ersatzkraftstoffs ab. Die Methode basiert auf LIF von zwei aromatischen „Tracern“, die in geringen Konzentrationen dem nicht-fluoreszierenden Ersatzkraftstoff zugesetzt werden. Eine Mischung aus leicht- bis mittelflüchtigen *n*-Pentan und *iso*-Oktan, repräsentiert durch den Tracer 1,4-Difluorbenzol, und dem schwerflüchtigen *n*-Undecan, repräsentiert durch 1-Methylnaphthalin, bildet den Basiskraftstoff. In Experimenten im geschleppten optischen Motor werden die LIF-Signale beider Tracer spektral getrennt von zwei Kameras detektiert, wobei das Kanalübersprechen in der Nachbearbeitung korrigiert wird. In Übereinstimmung mit früheren Messungen in einer Hochdruckkammer finden sich die leichten Komponenten vorzugsweise stromabwärts, an der Vorderseite des verdampften Kraftstoffstrahls. Großflächig ist etwa 20 % Überschuss an 1-Methylnaphthalin und in kleineren Bereich etwa 40 % an 1,4-Difluorbenzol zu sehen. Zunehmende Tumbleströmung oder verspätete Einspritzung reduzieren die Entmischung. Um den Einfluss der (unbekannten) lokalen Temperatur auf die Messgenauigkeit besser beurteilen zu können, wird diese durch adiabate Mischung berechnet und in einem separaten Experiment durch Zweifarben-LIF-Thermometrie an Anisol (Methoxybenzol) gemessen. Im relevanten Kurbelwinkelbereich ist die lokale Temperatur in Bereichen hoher Kraftstoffkonzentration um 25 K niedriger als im Rest der Ladung, was einen systematischen temperaturinduzierten Fehler im gemessenen Kraftstoffverhältnis von ca. 0.11 führt.

Auch Saugrohrenblasung, insbesondere von Erdgas, kann zu einer inhomogenen Kraftstoff-Luft-Verteilung gegen Ende des Zyklus führen. Um die Entwicklung des Luft-Kraftstoffverhältnisses im gefeuerten Betrieb zu untersuchen, wurde eine bildgebende LIF-basierte Messtechnik entwickelt. Die LIF-Messung wurde mit einer punktförmigen Infrarot-Absorptionsmesstechnik und einer CFD-Simulation verglichen, um zusätzliche Informationen in Zeit und Raum zu erhalten. LIF von Anisol, das in den gasförmigen Kraftstoff verdampft wird, wird von einem Zwei-Kamera-System erfasst, das ein Bild des Luft-Kraftstoff-Verhältnisses pro Zyklus liefert. Im Gegensatz zu früheren Implementierungen wird gleichzeitig die Temperatur gemessen und genutzt, um die Genauigkeit des gemessenen Luft-Kraftstoff-Verhältnisses zu verbessern. Zur Erweiterung der Nachweisgrenze unter Verringerung der räumlichen Auflösung wird „Structured laser illumination planar imaging“ (SLIPI) erprobt. Insgesamt besteht die Gemischbildung nach Eindüsung bei geschlossenen Ventilen aus konvektivem „Tumble“-Transport mit gradueller Durchmischung. Eine Änderung in Einlassdruck oder Motordrehzahl beeinflusst signifikant die Ausbreitung des kraftstoffreichen Frischgases nach Einlass öffnet und damit die weitere Durchmischung.

Table of contents

Acknowledgments	III
Abstract	V
Kurzfassung	VII
Nomenclature	XII
a) Table of symbols and indices.....	XII
b) List of abbreviations.....	XIV
c) Definitions and conventions.....	XVI
Chapter 1 - Introduction	1
Chapter 2 - Fundamentals	5
2.1 Four-stroke engine cycle	5
2.2 Pressure analysis	8
2.2.1 Pressure indication	8
2.2.2 Compression	8
2.3 Combustion stoichiometry	9
2.4 Natural gas port-fuel injection	10
2.5 Mixture formation with gasoline direct injection.....	10
2.5.2 Liquid jet and droplet break-up.....	13
2.5.3 Droplet evaporation	16
2.6 Light sources	17
2.6.1 Nd:YAG lasers.....	17
2.6.2 LEDs	19
2.7 Detectors and amplifiers	20
2.7.1 Camera sensors	20
2.7.2 Image intensifier and relay optics.....	22
2.8 Laser-induced fluorescence of organic molecules	23
2.8.1 Photophysical principle.....	24
2.8.2 Fuel/air ratio LIF.....	27
2.8.3 Temperature dependence of LIF	28
2.9 Structured laser illumination planar imaging.....	29
2.10 Particle image velocimetry.....	31
2.10.1 Seeding particles	32
2.10.2 Vector-field computation.....	32
Chapter 3 - Imaging of mixing processes in SI engines	34
3.1 Imaging in optically accessible engines.....	34
3.2 Liquid-fuel visualization	36
3.2.1 Engine Combustion Network.....	36
3.2.2 Liquid-fuel penetration	37
3.3 Gas-phase LIF imaging.....	39
3.3.1 Imaging of fuel-components.....	39
3.3.2 Imaging of in-cylinder air-fuel mixing	41

3.3.3	Imaging of temperature.....	44
Chapter 4	- Preferential evaporation of a multi-component gasoline surrogate in a direct-injection engine	50
4.1	Imaging strategy.....	50
4.2	Test bench	51
4.2.1	Engine, injector, and periphery.....	51
4.2.2	Surrogate fuel.....	52
4.3	In-cylinder velocity and spray morphology	53
4.3.1	Gas-velocity imaging.....	53
4.3.2	Spray visualization via diffuse back-illumination and Mie scattering .	55
4.3.3	In-cylinder bulk flow	63
4.3.4	Thermodynamic condition of the bulk gas	67
4.3.5	Spray-flow interaction	68
4.4	LIF experiments	77
4.4.1	Tracer-fluorescence characteristics	77
4.4.2	Optical arrangement.....	79
4.4.3	Measurements	80
4.5	LIF data post-processing and quantification.....	81
4.5.1	Tracer-concentration ratio	81
4.5.2	Fuel-mass composition	84
4.5.3	Temperature via two-color LIF thermometry.....	85
4.5.4	Temperature and fuel concentration via adiabatic mixing	86
4.6	Results and discussion	93
4.6.1	Preferential evaporation.....	93
4.6.2	Temperature imaging.....	96
4.6.3	Measurement uncertainty.....	98
4.6.4	Fuel composition and concentration.....	100
4.7	Section conclusions.....	107
Chapter 5	- Mixture formation in a port-fueled natural gas engine.....	110
5.1	Imaging strategy.....	110
5.2	Test bench	110
5.2.1	Engine and periphery	110
5.2.2	Fuel supply.....	111
5.2.3	Operating conditions.....	112
5.3	LIF experiment.....	113
5.3.1	Tracer seeding.....	113
5.3.2	Anisole-fluorescence characteristics	113
5.3.3	Optical arrangement.....	114
5.3.4	Measurements	115
5.4	Data post-processing and quantification.....	116
5.4.1	Dynamic-background elimination via SLIPI.....	117
5.4.2	Temperature calibration.....	119
5.4.3	Beam-splitter correction	120
5.4.4	Temperature correction.....	120
5.5	Results and discussion	122
5.5.1	Linearity between fuel/air ratio and LIF signal	122
5.5.2	Temperature and air/fuel ratio	127

5.5.3	Comparison with IR-absorption measurements and CFD simulation	128
5.5.4	Variation of engine operating parameters.....	134
5.5.5	Effect of SLIPI and Gaussian filtering.....	135
5.5.6	Cyclic variability.....	138
5.5.7	Single-shot precision and accuracy.....	140
5.6	Section conclusions.....	143
Chapter 6 - Overall conclusions and future work		145
6.1	Overall conclusions.....	145
6.2	Future work.....	148
Chapter 7 - Bibliography.....		150
7.1	Author's contributions to publications.....	160
7.1.1	Journal articles.....	160
7.1.2	Conference papers.....	162
7.1.3	Conferences poster.....	162
7.2	Supervised student projects and theses.....	162
Chapter 8 - Appendices.....		163

Nomenclature

a) Table of symbols and indices

Symbol	Unit	Description
$C_{\text{ext},i}^*$	mm ²	Effective extinction cross-section
c_0	km/s	Speed of light (299 792 km/s in vacuum)
c_i	mass-%	Fuel-component fraction
c_f	mass-%	Fuel-component fraction in homogeneous mixture
c_p	kJ/(kg K)	Specific constant pressure heat capacity
c_v	kJ/(kg K)	Specific constant volume heat capacity
d, D	mm	Diameter
dQ	J/K	Change in heat
dS	J/K	Change in entropy
E_e	mJ/(cm ² ns)	Laser irradiance
f	mm	Focal length
$FF_i^{(j)}$	-	Fluorescence signal in flatfield from tracer i in channel (j)
$FNR^{(k)}$	-	Component-nitrogen ratio of fuel component (k)
$h_{v,Tini}^{(k)}$	kJ/kg	Latent heat of vaporization of fuel component (k)
H/C	-	Molar hydrogen-to-carbon ratio
I	count/pixel	Intensity (generic)
\tilde{I}_i	-	Density corrected intensity
I_0	count/pixel	Baseline intensity
k_{fl}	1/s	Rate of spontaneous emission
k_{tot}	1/s	Rate of all deexcitation processes
$\tilde{k}_q^{O_2}$	m ³ /s	Rate coefficient of quenching by oxygen
k_{SV}	bar ⁻¹	Stern-Volmer coefficient
l	m	Length (generic)
l_{st}	-	Stoichiometric ratio
LVF	-	Liquid volume fraction
m	various	Slope in a linear function
m_i	kg	Mass of fluid i
\dot{m}_i	kg/h	Mass flow of fluid i
n_i	1/cm ³	Number density of fluid i
σ	N/m	Surface tension
p	bar	Pressure (generic)
p_{cyl}	bar	In-cylinder pressure
p_{ind}	bar	Indicated mean effective pressure
p_s	mm	Period of SLIPI modulation
q_i	kJ/kg	Specific heat
R^2	-	Coefficient of determination
r_b	-	Signal ratio DFB/1MN “blue/red”

r_c	-	Signal ratio anisole “blue/red”
Re	-	Reynolds number
R_s	kJ/(kg K)	Specific gas constant
$S_1, S_2 \dots$	eV	Electronic states
$S_i^{(j)}$	count	Fluorescence signal from tracer i in channel (j)
$S_{FF}^{(j)}$	count	Fluorescence signal during calibration (flatfield) channel (j)
t	μ s	Time after some event (generic)
T	K	Temperature (generic)
T_{2C}	K	Temperature from two-color LIF thermometry
T_{AM}	K	Adiabatic mixing temperature
T_{core}	K	Adiabatic core temperature
u, v	m/s	Components of a velocity vector
$\langle v \rangle$	m/s	Spatially averaged velocity
v	m/s	Local velocity (generic)
V	m^3	Volume (generic)
W_v	J	Performed work
We	-	Weber number
x	mm	Axial fuel penetration
$x^{(j)}$	-	Signal leakage
$x_f^{(j)}$	-	Fuel mole-fraction of component (j)
x_{O_2}	-	Oxygen mole-fraction
Z	-	Ohnesorge number
Δt	μ s	Temporal difference (e.g. delay)
ΔT	K	Temperature difference (generic)
Δx	mm	Spatial difference
Φ	mJ/cm ²	Laser fluence
Ω	°	Angle of incidence
α	°	Spray angle
ε	-	Relative error
ϕ	-	Fuel/air equivalence ratio
ϕ_{fl}	-	Fluorescence quantum yield
κ	-	Isentropic coefficient
λ	-	Air/fuel ratio (generic)
λ_{FF}	-	Overall air/fuel ratio in homogenous operation (flatfield, calibration, MFC)
λ_{PFI}	-	Overall air/fuel ratio measured by the exhaust-gas analyzer with PFI (measurement, PFI)
η	-	Quantum efficiency
μ_l	kg/(s m)	Dynamic viscosity of a liquid
ρ	kg/m ³	Fluid density (generic)
Π	-	Collection efficiency
σ	-	Standard deviation

σ_{abs}	mm ²	Absorption cross-section
τ	mm	Optical thickness
ω	mass-%	Overall fuel-mass fraction
ω_{h}	mass-%	Overall fuel-mass fraction in homogeneous mixture

b) List of abbreviations

Abbreviation	Full description
1MN	1-methylenaphthalene
2CT	Two-color (LIF) thermometry
AM	Adiabatic mixing
ANI	Anisole (methoxybenzene)
AOI	Angle of incidence
APS	Active-pixel sensor
BDC	Bottom-dead center (piston position)
BG	Background
BMBF	Federal ministry of education and research
BP	Band pass (filter)
BPt	Boiling point
BS	Beam splitter
CA	Crank angle
CCD	Charge-coupled device
CCV	Cycle-to-cycle variation (variability)
CFD	Computational fluid dynamics
CMOS	Complementary metal-oxide semiconductor
CNG	Compressed natural gas
COV	Coefficient of variation (one-standard deviation by mean)
CVC	Constant-volume chamber
DBI	Diffuse back-illumination
DFB	1,4-difluorobenzene
DI	Direct injection
DSLR	Digital single-lens reflex
ECN	Engine combustion network
EOI	End of injection
FARLIF	Fuel/air ratio laser-induced fluorescence
FF	Flatfield
FFT	Fast-Fourier transform
FOV	Field of view
FT	Fourier transformation
FQY	Fluorescence quantum yield
FVV	Research Association for Combustion engines (<i>Ger.</i> : Forschungsvereinigung Verbrennungskraftmaschinen)
FWHM	Full width at half-maximum

GDI	Gasoline direct injection
HC	Hydrocarbon
HCCI	Homogeneous-charge compression ignition
ICCD	Intensified CCD
IR	Infrared
IRO	Intensified relay optics
ITV	Institute for Combustion Technology
IVG	Institute for Combustion and Gas dynamic
IVL	Intake-valve lift
LED	Light-emitting diode
LES	Large-eddy simulation
LIF	Laser-induced fluorescence
LLG	Laser Laboratorium Göttingen e.V.
LP	Long pass (filter)
LVF	Liquid-volume fraction
MCP	Micro-channel plate
MFC	Mass-flow controller
MOS-FET	Metal-oxide-semiconductor field-effect transistor
Nd:YAG	Neodymium-doped yttrium aluminum garnet
Nd:YLF	Neodymium-doped yttrium lithium fluoride
NG	Natural gas
PD	Pulse duration
PFI	Port-fuel injection
PIV	Particle image velocimetry
PTU	Programmable timing unit
px	Pixel
Q-switch	Quality switch
RANS	Reynolds-averaged Navier-Stokes (e.g. CFD simulation)
RCM	Rapid-compression machine
RGB	Red, green, blue (in terms of light transmission or emission)
SIDI	Spark-ignition direct-injection
SLIPI	Structured laser illumination planar imaging
aSOI	(after) Start of injection
TC	Thermo couple
TDC	Top-dead center (piston position)
TEA	Triethylamine
TUD	Technische Universität Darmstadt
UDE	University of Duisburg-Essen
UV	Ultraviolet
WG	White glass (filter)

c) Definitions and conventions

- This work assigns 0°CA to compression top-dead center, i.e., crank angles during intake and compression are negative, during power and exhaust are positive.
 - If not explicitly stated, start of injection is always the hydraulic start, when fuel first exits the nozzle outlet.
 - Bold, italic variables, e.g. $\mathcal{S}^{(b)}$, are matrices representing images.
 - Image acquired with fuel supply far upstream of the intake valves are mostly referred as “flatfields”. Fuel injection takes place by injection for liquid fuel and via mass-flow controller for gaseous fuel.
 - Note the ambiguity of the fuel/air ratio ϕ with air/fuel ratio λ , and standard deviation σ with their meaning in spectroscopy, for example ϕ with the fluorescence-quantum yield ϕ_{fl} in Eq. (2-14). Both are the symbols traditionally used in this context.
-

Chapter 1 - Introduction

Internal combustion engines have been developed since the end of the 19th century, and since then hardly any other large mass product has influenced the everyday life of mankind like the passenger car. Therefore, the combustion engine has become indispensable for mobility, but has gotten subject to enormous limitations in pollutant emissions to prevent nowadays climate change. Greenhouse gases like CO₂, CH₄, and NO_x as well as particulate matter emissions (e.g. soot) are main pollutants from internal combustion engines, which, along with other sources and applications, cause severe damage to the global ecosystem, food crops, and human health. The *Umweltbundesamt* – Germany [1] report that in the year of 1990 12% of all greenhouse emissions in Germany were caused by road transportation, which increased to almost 18% by the year 2017. Moreover, the *Health Effects Institute* – USA [2] classified total air pollution to be the fifth leading risk factor for mortality worldwide in the year 2017. In addition, the global pollution caused by passenger-car engines is expected to further increase throughout the next years due to a steadily rising demand in private mobility in emerging countries and stronger interconnected world trade. To reduce pollutant emissions new power-train technologies are required. Electrification of private mobility is a recent approach to reduce pollution in urban regions. However, electricity is still mainly produced by fossil power plants with vast amount of pollutant emissions, the production of batteries is resource intensive, and the required infrastructure for electric mobility will not be given in the near future. Therefore, internal combustion engines will still be the main power train for private mobility. But legal requirements as the Euro 6d emission standard starting in 2020 will further tighten the restrictions on pollutant emission of internal combustion engines. Because of the restrictions on emissions it is even more important to improve the resource efficiency of internal combustion engines and to develop more efficient exhaust-gas after-treatment systems. Recent approaches for reducing engine-out emissions are either the use of alternative or renewable fuels, (natural gas, biofuel), which have the potential to significantly reduce CO₂ emissions and/or by improving the fuel efficiency using advanced injection and combustion strategies (e.g. direct injection of gasoline, natural gas, or hydrogen).

The development of new injection and combustion strategies requires a comprehensive investigation of in-cylinder phenomena in the formation of the combustible mixture. Also, CFD simulations may require new models that may be created from experimental results from the combustion chamber of engines. Measurements of the in-cylinder pressure from single engine cycles can provide temporally resolved insights on overall thermodynamic quantities like heat-release rate or cyclic fluctuation of the mean-effective pressure. To extend data to other quantities such as species concentration or temperature, point-like measurements via single-port probes have been employed in internal combustion engines in the past. These techniques usually provide high temporal resolution but suffer from missing spatial information on the measured quantity. To overcome this drawback, laser-based imaging in single-cylinder research engines with large windows has proven to be suitable. Even though these “optical” engines are significantly modified from production engines, cannot operate over the full load-speed range, and are resource-intensive facilities, the large optical access to the combustion chamber provides convenient application of imaging diagnostics to acquire spatially resolved data. To

study in-cylinder mixing phenomena, laser-induced fluorescence (LIF) imaging of a fluorescent additive – a tracer – doped to the fuel is a widely-used diagnostic for such of “optical” engines [3]. After suitable calibration versus the quantity of interest and interpretation of the fluorescence signal, quantitative insights on the fuel distribution, air/fuel ratio, temperature, fuel composition and residual gas concentration can be gathered.

To address recent engine development activities, the content of this thesis focusses on the quantitative investigation of the mixing process in spark-ignited engines via LIF imaging. Two injection strategies will be investigated via novel LIF-imaging techniques. On the one hand, the effect of preferential evaporation of a gasoline type multi-component fuel after direct injection (DI) and, on the other, the air-fuel mixing with closed-valve port-fuel injection (PFI) of natural gas will be studied. Both injections strategies provide the opportunity to reduce engine-out emissions, and to increase the overall efficiency of engines compared to the widely used PFI of gasoline.

DI of a multi-component fuel is subject to complex mechanisms of mass- and heat transport during the transition from liquid spray to fuel vapor. Diverse volatility classes of the fuel may evaporate differently in the spatio-temporal evolution of the injection jet, which again may cause mixture inhomogeneity, delayed evaporation, and wall wetting. The light components evaporate first, while heavier components evaporate later. Due to simultaneous convection, the low- and high-volatility components are thus spatially separated after evaporation. Since there is not a suitable optical diagnostic to quantitatively image the effect of preferential evaporation in internal combustion engines, experimental data are not available to check corresponding simulation models. Exactly here the first part of this work fills the gap.

The study was carried out in the scope of the project “Bioptic 3” (FVV, Frankfurt/Main, project No. 1203 [4]). The main goal was to transfer and optimize the LIF technique for imaging the effect of preferential evaporation from its previous application in “Bioptic 2” [5], a static high-pressure vessel, to the more complex environment of an optically accessible direct-injection engine. Cross-influences of parameters other than fuel concentration, which may lead to miss-interpretation of preferential evaporation, will be addressed, correction procedures introduced, and typical experimental results discussed. Moreover, this work contributes to the Engine Combustion Network (ECN) by using the “Spray G” injector for gasoline fuel at standardized conditions. The facility for this experiment is the optically accessible single-cylinder engine with spark-ignition and direct injection at the *Institute for Combustion and Gas Dynamics* (IVG) of the University of Duisburg-Essen. The engine has optical access through the piston window and the top part of the combustion chamber through a transparent cylinder liner. In order to describe the engine operating conditions as precisely as possible, the flow velocity was measured by particle-image velocimetry (PIV), and the penetration depth of the liquid fuel was characterized via diffuse back-illumination and Mie scatter imaging prior to the LIF experiment. Flow fields and liquid-penetration depths could provide valuable comparison with subsequent CFD simulations of that engine.

For LIF imaging, two fluorescent tracers of volatilities matching those of the light and heavy components of fuel are added to the multi-component surrogate. The surrogate consists of the light and medium components *n*-pentane and *iso*-octane, represented by the aromatic

tracer 1,4-difluorobenzene, and the heavy component *n*-undecane, represented by 1-methylnaphthalene. Both tracers fluoresce in distinct spectral regions, which makes it possible to detect their LIF separately on two cameras by appropriate filter combinations. LIF imaging is then applied to the gas phase after full evaporation. Measurement uncertainties, in particular the influence of temperature inhomogeneity, are addressed and corrected for. Temperature was measured in a separate experiment by means of two-color LIF thermometry by replacing the 1-methylnaphthalene and 1,4-difluorobenzene by anisole (methoxybenzene). The resulting temperature fields are compared to spatially resolved mixing temperature modeled by conservation of energy for an adiabatic system and photophysical relations of the tracer's LIF signal. Afterwards, the actual fuel-component fractions are calculated via a thermodynamic model relating the tracer-concentration ratio to the fuel composition. Finally, the effects of a change in intake-valve lift and injection timing on the spatio-temporal development of the fuel-component segregation is discussed.

Not only for DI engines, but also for engines with PFI, the injection parameters influence the mixture formation in the cylinder and the mixture may not be homogeneous at ignition. PFI of liquid fuel is the most common strategy for fuel supply to car engines, but the use of natural gas is less common. Tracer LIF imaging with gaseous fuels in optical engines is more challenging because most fluorescence tracers are liquid at room temperature and need to be evaporated into the gas. At increased pressure upstream of the injector the maximum tracer concentration is low which causes low signal intensities and poor precision. Therefore, LIF has less frequently been used with gaseous fuels. However, after calibration the signal can be interpreted as the local fuel/air ratio (FAR), the quantity of interest.

The second part of the thesis reports on the mixture formation after PFI of natural gas. The work was carried out in the scope of the project "OMeGa-E" (BMBF, Germany, project No. 13N13034). The main goal was to develop a quantitative LIF imaging technique to determine the local air/fuel (or fuel/air) ratio in a PFI methane engine with combustion. Since temperature is expected to affect the LIF signal and hence the quantification of the air/fuel ratio, it was additionally estimated by means of two-color anisole LIF thermometry. A procedure to correct the influence of temperature on the signal and the accuracy in the quantification of the air/fuel ratio for engine relevant temperature and pressure combinations are presented.

The engine experiments were carried out in an optically accessible single-cylinder engine at the research and development facility of the Volkswagen AG. Together with the Laser Laboratorium Göttingen e.V., infrared absorption was simultaneously applied to derive the air/fuel ratio over a short path located near the spark electrodes. In the first part of this study, typical LIF results are discussed and then compared to results from the infrared absorption technique. Additionally, the experimental results are compared to a Reynolds-average Navier-Stokes-CFD simulation (RANS-CFD), which in particular gives insight into experimental artifacts associated with heat transfer and extends the spatial domain beyond what can be examined via the spark-plug probe and imaging through the cylinder window. Then, the application of structured laser illumination planar imaging, to increase the detection limit in the air/fuel ratio, is reported, and the effect of engine speed, intake pressure, and overall air/fuel ratio on mixture formation is discussed. Especially the field-wide air-fuel mixing, cyclic

variations, the temporal evolution of the mixture near the spark plug, and mixture stratification near ignition are content of the study.

Chapter 2 - Fundamentals

2.1 Four-stroke engine cycle

Figure 2-1 shows sketches of a sectional view through a combustion chamber of an internal combustion engine. This kind of engine is also known as *Otto-engine*. Its cycle consists of four strokes, and each stroke consists of a piston movement from top-dead center (TDC) to bottom-dead center (BDC) or vice versa. Therefore, every stroke is equivalent to 180° rotation of the crank shaft, and a cycle is finished after the crank shaft has rotated by 720° . The reciprocating movement of the piston is a function of the rotation of the crank, while the valves open and close only once per cycle.

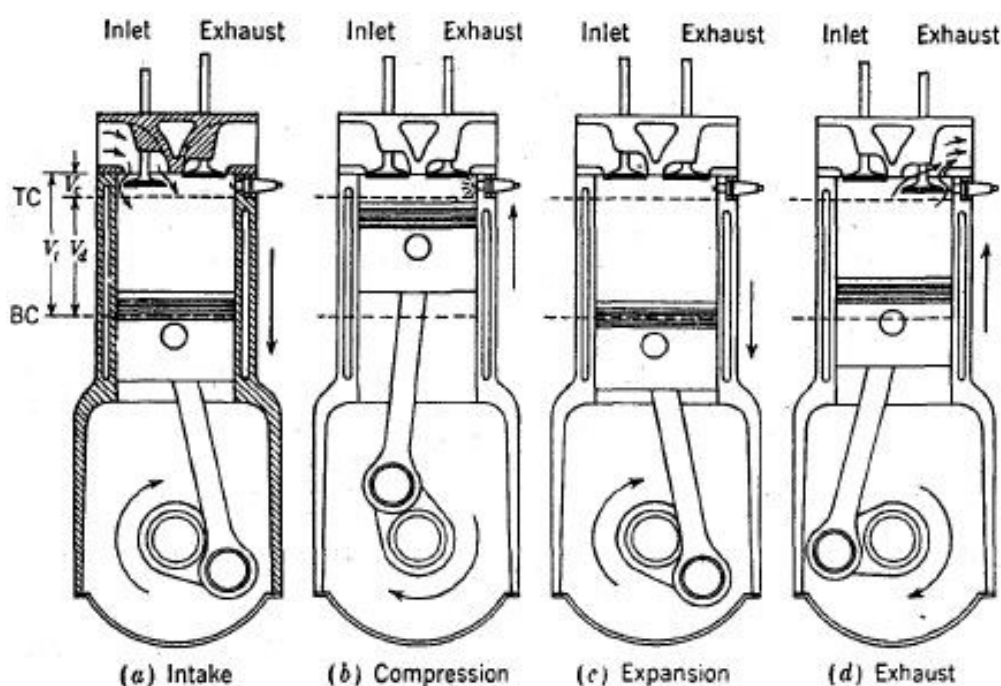


Figure 2-1: Schematic of each stroke in a four-stroke engine. Taken from [6].

In addition to the illustrations in Figure 2-1, Figure 2-2 shows a comparison of the real engine cycle with the idealized cycle. Figure 2-2a displays the p-V diagram of a real engine cycle, (b) the p-V diagram of the ideal cycle, and (c) a T-s diagram of the ideal cycle.

Intake stroke (Figure 2-1a):

During the intake stroke the piston moves from TDC down to BDC. The intake valves start to open just before the piston reaches TDC and close before or shortly after BDC. Modern engines are operated with a slight overlap in the opening of the intake and closing of the exhaust valves, which can increase the gas mass induced into the cylinder. By adjusting the valve

overlap it is possible to adjust the amount of the recirculated residual gases in the cycle. If the engine is operated with fuel supplied to the intake air, air-fuel mixing starts already in the intake system. After the intake stroke, the compression stroke starts.

Compression stroke (Figure 2-1b):

During the compression stroke the initial volume is compressed by the piston by the movement from BDC to TDC, which increases the in-cylinder pressure and temperature. The increase in pressure is to first order defined by the stroke and outer diameter of the piston as well as the clearance volume at TDC. However, in reality, thermal losses through the walls and mass losses through the piston rings influence the cylinder pressure. Engines with late direct injection (DI) supply the fuel to the combustion chamber during the compression stroke, such that air-fuel mixing takes place inside the cylinder of the engine. The compression stroke ends with ignition of the air-fuel mixture via a spark plug, with the exact ignition timing optimized in a complex trade-off between thermodynamics, heat losses, and emissions.

Power / expansion stroke (Figure 2-1c):

The expansion stroke starts at TDC. Heat is released due to the combustion of the air-fuel mixture. The mixture expands and pushes the piston down towards BDC. The work that is released in the expansion stroke needs to be higher than all losses to provide a positive impulse on the crank. Towards the end of the expansion stroke the exhaust valves open, which initiates the exhaust stroke.

Exhaust stroke (Figure 2-1d):

In the exhaust stroke the burned gas is pushed out of the cylinder. Ideally the pressure during this stroke would be equal to the pressure during the intake stroke to minimize gas exchange losses, as shown in Figure 2-2b. But in reality, the pressure in the exhaust stroke is slightly greater than ambient as shown by the p-V diagram in Figure 2-2a. Just before TDC, the intake valves open and from TDC the engine cycle starts again.

For four-stroke SI engines, the “dual combustion” or “mixed” cycle (Seiliger cycle) as shown in Figure 2-2 (b) and (c), with both, constant volume and constant pressure heat addition, is a widely adopted zero-dimensional and idealized model. In contrast to the real engine process in Figure 2-2a, the Seiliger cycle in Figure 2-2b is an ideal closed cycle without the exchange of gas that is often used for theoretical calculations.

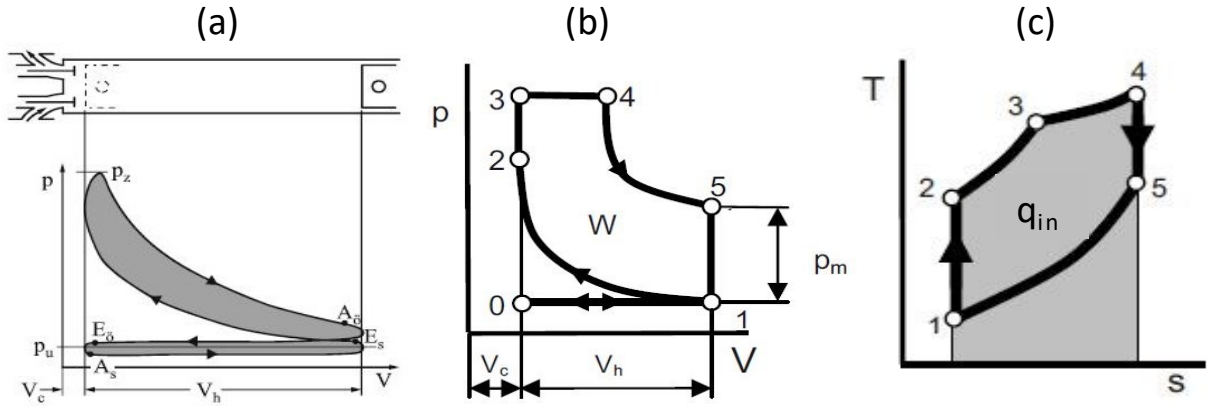


Figure 2-2: (a) Real p-V diagram of the four-stroke combustion cycle [7]; (b) p-V diagram of the theoretical dual combustion cycle; (c) T-s diagram of the theoretical dual combustion cycle. [8]

The process shown in Figure 2-2 (b) and (c) consists of six states where the transitions between states represent ideal (theoretical) changes. In the idealized process losses during gas exchange (states 0 and 1 in Figure 2-2b) are neglected. The process of compression from state 1 to 2 is assumed to be isentropic followed by transitions representing isochoric ($2 \rightarrow 3$) and isobaric ($3 \rightarrow 4$) heat addition. The isochoric q_v and isobaric q_p heat addition can be calculated by the first law of thermodynamics considering a reversible process

$$q_v = c_v \cdot (T_3 - T_2) \quad (2-1)$$

and

$$q_p = c_p \cdot (T_4 - T_3), \quad (2-2)$$

respectively. Temperatures T_i are the temperatures in Eq. (2-1) and (2-2) in each state, c_p is the isobaric and c_v the isochoric heat capacity. Overall, the indicated work W_t performed per cycle and cylinder is obtained by the integral over the enclosed area of the p-V diagram as defined in equation (2-3)

$$W_t = \oint p \, dV. \quad (2-3)$$

The indicated mean effective pressure (IMEP) p_{ind} is then defined as

$$p_{ind} = \frac{W_t}{V_h}, \quad (2-4)$$

where V_h is the displacement volume as denoted in Figure 2-2 (a) and (b).

2.2 Pressure analysis

2.2.1 Pressure indication

In engine experiments, most commonly the gas pressure in intake, exhaust, and cylinder are measured at kHz-rates synchronized with the position of the crank shaft. Since engines are reciprocating machines, not time, but the crank shaft position is related to the indicated pressure. Piezoresistive or piezoelectric pressure sensors are used for this purpose. These sensors provide high repetition rates at the desired dynamic range. In order to measure pressure in the combustion chamber a high dynamic range is required, which can be provided by piezoelectric sensors. However, the absolute pressure cannot be measured with piezoelectric sensors, therefore the in-cylinder pressure must be related to the absolute pressure in the intake port measured by piezoresistive sensors. In addition, calibrated amplifiers compensate for the influence of variations in temperature on the measured values.

2.2.2 Compression

Assuming an adiabatic and reversible system, isentropic changes are described by the ideal gas law

$$p \cdot V = m \cdot R_s \cdot T \quad (2-5)$$

and the isentropic relation

$$\frac{T_i}{T_0} = \left(\frac{p_i}{p_0}\right)^{\frac{\kappa-1}{\kappa}}. \quad (2-6)$$

In Eq. (2-5) p is the gas pressure, V the volume, m the mass, R_s the specific gas constant, and T the temperature. From the pressure ratio p_i/p_0 and the start temperature T_0 , the isentropic temperature T_i at state i can be calculated via equation (2-6). T_0 is usually unknown, and often approximated with the arithmetic average of the coolant and intake temperature just before the intake valves close. The isentropic exponent κ is the ratio of the constant volume heat capacity c_v to the constant pressure heat capacity c_p of the fluid

$$\kappa = \frac{c_p}{c_v} = f(T). \quad (2-7)$$

As the heat capacities c_p and c_v are temperature-dependent, the isentropic coefficient κ is also a function of temperature. Functional parametrizations of thermal properties for a large number of different fluids are i.e. given in [9].

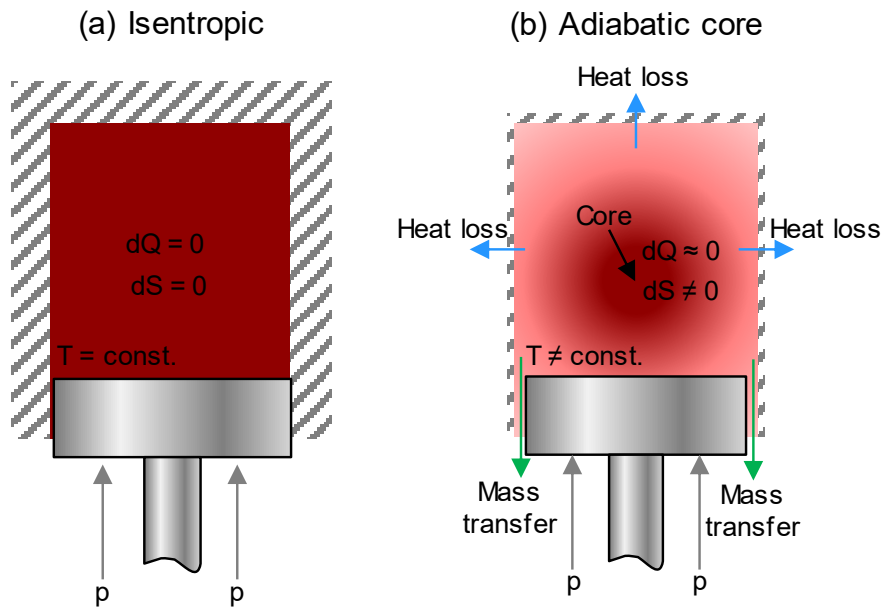


Figure 2-3: Schematics of heat and mass transfer in an isentropic process in (a) and a process with an adiabatic core in (b). The color in the background represents the temperature distribution.

In contrast to isentropic processes, which are adiabatic (no heat losses, $dQ = 0$) and reversible (constant entropy, $dS = 0$) as shown in Figure 2-3a, adiabatic processes are not necessarily reversible. During the compression stroke, the center of the volume in the combustion chamber shown in Figure 2-3b, to first order, is a reasonable example for an irreversible adiabatic process. If it is assumed that fast compression from volume V_1 at pressure p_1 to a smaller volume V_2 and higher pressure p_2 takes place, heat transfer in the core of the volume, far from surfaces, is negligible. The core is adiabatic $dQ \approx 0$ but may still be irreversible because entropy gets lost. However, this “adiabatic assumption” is only applicable far away from boundaries in the core (center) of the volume as compression takes place in a certain amount of time.

2.3 Combustion stoichiometry

For a certain engine operating condition, the global combustion stoichiometry is described by the mass of the chemical elements of the reactants (fuel and air) in the initial mixture and the composition of the products in the exhaust gas. The relative air/fuel ratio λ (or its inverse, the relative fuel/air equivalence ratio ϕ) in Eq. (2-8) is defined as the ratio of the actual air/fuel ratio to the stoichiometric ratio. Theoretically there is just enough oxygen available at stoichiometric ratio such that fuel in the mixture is completely converted to oxidized products. The air/fuel ratio λ is thus defined as

$$\lambda = \phi^{-1} = \frac{\dot{m}_{\text{air}}}{l_{\text{st}} \cdot \dot{m}_{\text{f}}} \quad (2-8)$$

with the stoichiometric ratio l_{st} for hydrocarbon (HC) fuels being

$$l_{st} = \frac{34.56 (4 + H/C)}{12.011 + 1.008 H/C}. \quad (2-9)$$

In Eq. (2-9) H/C is the molar hydrogen-to-carbon ratio of the fuel. The equation in (2-9) is derived from the chemical equation for complete combustion of a HC molecule as discussed in more detail in [10]. E.g., for methane (CH_4) the H/C ratio is 4, which, by Eq. (2-9), yields a stoichiometric ratio l_{st} of 17.23 (g O_2)/(g CH_4). Note that if the fuel contains oxygen or sulfur, that also needs to be included to the chemical reaction. If λ is equal to 1.0, then the mixture is stoichiometric, below 1.0 the mixture is fuel-rich, and above 1.0 the mixture is fuel-lean. [10]

2.4 Natural gas port-fuel injection

Port-fuel injection (PFI) with pulsed-operated injectors is used to supply fuel to each intake port or manifold separately. Moreover, the low cost of natural gas (NG) compared to gasoline and Diesel, and the limitations in pollutant emissions by the governments made NG a reasonable fuel in order to meet the desired requirements. Therefore, NG has recently become an alternative to liquid gasoline in passenger vehicles, buses, and combined heat-power units. It is usually stored as compressed gas at up to 700 bar on a passenger car. NG's main component is methane at concentrations from 80% to 100% depending on the place of origin. The most common injection strategy for NG is PFI into the intake manifold. NG has both, advantages and disadvantages compared to gasoline. On the one hand, compared to PFI of gasoline with naturally aspiration, the power output with NG is about 10% to 15% lower because it displaces more air in the air-fuel mixture. On the other hand, NG has the advantage to increase the knock resistance, allowing the use of high compression ratios up to 13:1, which eventually brings higher thermal efficiency. Wall wetting is also prevented since the already gaseous fuel does not residue on surfaces. In return, at given torque, the use of a higher compression ratio with NG leads to an increase in NO_x engine out emission, which must be considered in compromise to the increase in engine efficiency. Additionally, the emission of CO_2 is lower than with gasoline since CH_4 has a lower C/H ratio, but CH_4 , one of the main component of the pollutant emissions from NG, is one of the greenhouse gases. [11]

2.5 Mixture formation with gasoline direct injection

For SI engines gasoline direct injection (GDI) is an injection strategy where fuel is supplied directly to the combustion chamber and other than for Diesel DI, the air-fuel mixture is ignited by a spark plug. Gasoline engines were first operated with GDI in 1955, but not until 1995 implemented in engines in large-scale production. GDI brings following advantages compared to fuel supply to the intake system [11]:

- GDI provides a more controllable internal mixture formation (compared to fuel supply to the intake manifold) to better match the changes in engine operating requirements. The delayed fuel arrival due to transport from the intake port is removed, and the fuel delivery ratio is increased with GDI.

- Overall fuel-lean operation is possible – at least in part-load operation – by maintaining a combustible, close-to-stoichiometric air-fuel mixture in the vicinity of the spark plug at ignition. This improves the engine's specific fuel consumption since heat and reduces throttle losses compared to PFI.
- The cold fuel injected into the hot combustion chamber lowers the temperature of the charge which allows higher compression ratios since the cooling delays the onset of knock. This increases the possible power density (*downsizing*).
- A second late injection provides the opportunity to increase the exhaust-gas temperature. This reduces emissions especially during cold start by quickly providing the required heat to the catalyst.

Overall, the more controllable fuel supply and the overall fuel-lean strategy offer the opportunity to improve the overall engine performance. However, improvements in fuel consumption, power output, and pollutant emissions are opposed by increased costs for the GDI fuel delivery and exhaust-gas after treatment systems, especially in the case of the fuel-lean operation [11].

Depending on the required trade-off between engine emission and performance, different GDI strategies were developed. The overall fuel-lean operation with stratified air-fuel mixture requires *late injection* during the compression stroke, such that an ignitable mixture will be created in the region of the spark. The latter competes with homogeneous and overall stoichiometric operation via *early injection* typically once or multiple times during or just after the intake stroke to achieve the required air-fuel mixing. Both strategies have individual features in mixture preparation, combustion, and pollutant emissions. Injection late in the compression stroke usually causes fuel stratification and is restricted to part-load at low- to mid-speed engine operation, while homogeneous operation can cover the full load and speed range. Late fuel injection, however, needs precise mixture preparation controlled by the aerodynamic interaction of the spray with the surrounding gas and fast fuel evaporation to create a locally confined mixture ignitable by the spark plug. Additionally, the end-gas composition (unburned region after early flame development) needs to be such that the flame can propagate through the whole combustion chamber. Therefore, depending on the operating requirements, different fuel injector locations and combustion chamber designs may be beneficial. [11]

Table 2-1: Characteristics of GDI concepts. Table from [12]. Labels (+ good, 0 neutral, - bad) are classifications of the authors in [12].

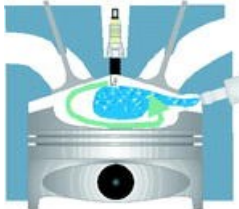
	Wall-guided	Air-guided	Spray-guided
Fuel economy	0	+	++
HC emission	0	+	++
Smoke emission	0	+	++
Power	0	-	0 to +
Robustness	0	-	-
Mixture preparation			

Table 2-1 summarizes three GDI concepts for mixture preparation. In the *wall-guided* injection strategy the piston bowl or other geometrical features of the combustion chamber are designed in such a way that an ignitable mixture is created near the spark electrode at ignition. In the *air-guided* injection strategy the bulk flow (tumble or swirl) should prevent wall wetting and mix fuel and air such that it is ignitable by the spark. Wall-wetting, however, can only be partially prevented. Additionally, the bulk flow in the combustion chamber is mainly affected by the geometrical features, such that wall and air guiding of the fuel takes place simultaneously. In the *spray-guided* injection strategy air-fuel mixing is controlled by the spatio-temporal evolution of the fuel spray and vapor jet. In the latter, the spark plug electrodes are placed in the region of the spray plumes where spray evaporation is sufficient to create a combustible mixture quickly after start of injection. Spray guided systems are therefore usually operated with stratified air-fuel mixture with an overall lean but locally stoichiometric air/fuel ratio. In part load operation at given torque, fuel-lean operation with late injection requires less throttling, which significantly reduces the pumping work compared to throttled stoichiometric operation. This is the primary advantage that makes stratified lean operation in part-load operation more efficient than stoichiometric operation. [11]

Exhaust-gas after treatment of GDI engines with stratified fuel-lean strategy, however, is more challenging. The conventional three-way catalyst for conversion of HC, CO, and NO_x to CO₂, H₂O, and N₂ does work at stoichiometric (or close to) and high exhaust gas temperatures. In the case of fuel-lean operation a so-called lean-NO_x storage catalyst is used, which stores the NO_x in lean operation and releases and reduces NO_x with engine operation switched to stoichiometric for a short period of time. However, this brings additional complexity and costs. [13]

2.5.2 Liquid jet and droplet break-up

Liquid jets are subject to different break-up mechanisms depending on the relative velocity of the liquid to the surrounding gas. The break-up mechanisms are classified into Rayleigh, first and second wind-induced, and atomization regime as shown in Figure 2-4.

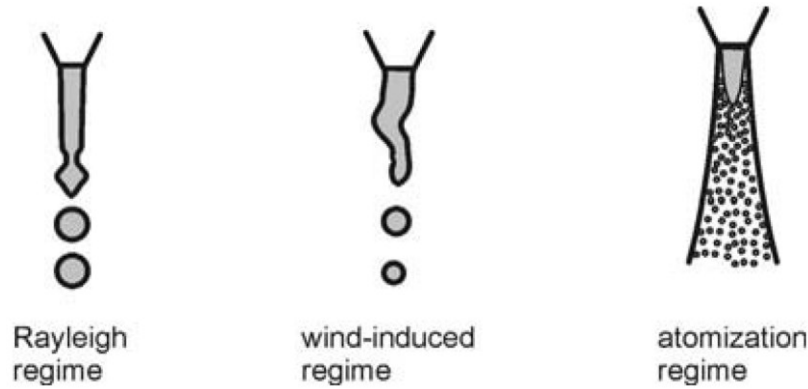


Figure 2-4: Schematics of the different break-up regimes in liquid jets. From [14].

Dimensionless numbers are used to characterize the break-up mechanisms into regimes. An important number is the liquid Weber number We_l

$$We_l = \frac{u^2 D \rho_l}{\sigma} \quad (2-10)$$

In Eq. (2-10) u is the velocity, D the characteristic length (e.g. the nozzle hole diameter), ρ_l is the density of the liquid fluid, and σ the surface tension. It describes the formation of droplets in multiphase flows by putting the fluids inertia in proportion to its surface tension. Another important indicator is the Reynolds number Re

$$Re = \frac{u D \rho_l}{\mu_l}, \quad (2-11)$$

which compares the inertial forces with the viscous forces within a fluid. μ_l is the dynamic viscosity of the liquid fluid. Ohnesorge [15] described the break-up mechanisms by the Weber and Reynolds number via

$$Z = \frac{\sqrt{We_l}}{Re} = \frac{\mu_l}{\sqrt{\sigma D \rho_l}} \quad (2-12)$$

The Ohnesorge number Z relates the influence of the viscous forces to the inertia and surface tension of the liquid droplet, hence the deformation of a droplet. Figure 2-5 shows the Ohnesorge diagram where Re versus Z is plotted. The jet break-up length at static condition and constant Z is solely a function of the velocity.

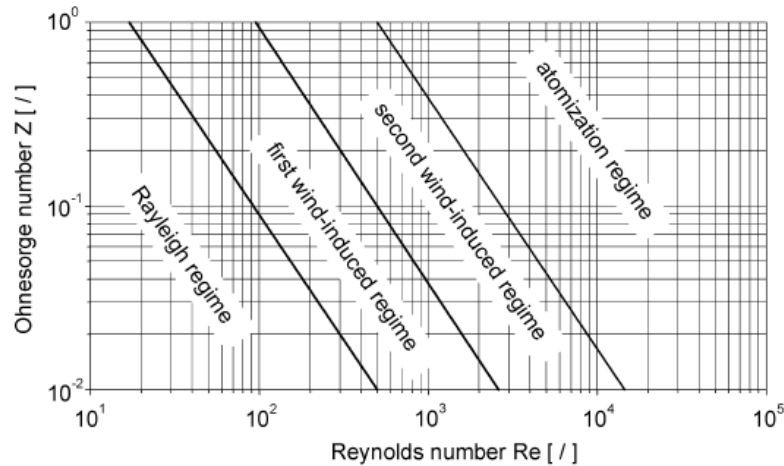


Figure 2-5: Classifications of the jet break-up regimes by the Ohnesorge number Z and the Reynolds number Re . From [14].

To explain the break-up regimes in more detail, Figure 2-6 shows a theoretical diagram of the liquid break-up length depending on the jet velocity. At low jet velocity, in region AB-C no proper jet is formed since the liquid is dripping from the nozzle. Between C-D the relation between jet break-up length and velocity is linear with droplets larger than the nozzle diameter, beyond D the relation becomes non-linear. In the first wind-induced region E-F, the mean droplet diameter is on the order of that of the nozzle. The break-up-relevant forces are amplified by the aerodynamic forces due to the increasing deviation in velocity between the liquid jet and the surrounding gas. The liquid break-up length decreases significantly. In the second wind-induced regime F-G and F-H the flow in the nozzle becomes turbulent, which induces short surface oscillations along the jet. The atomization regime is beyond H and G, where, due to turbulence (high Reynolds number), the surface length approaches zero. In that case, the spray cone is diverging directly after the jet leaves the nozzle. Some large droplets can still exist in the core of the spray multiple nozzle diameters downstream. Atomization is the relevant regime for engine sprays, where droplets several orders of magnitude smaller than the nozzle diameter are formed, which increases surface area and, thus, accelerates evaporation. [14]

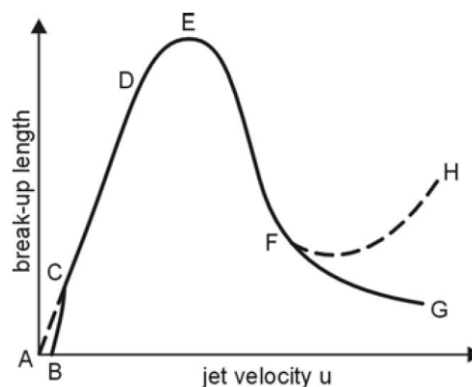


Figure 2-6: Schematic diagram relating the jet velocity u with the jet break-up length. See text for the meaning of the letters. Figure from [14].

However, since the ambient gas density also influences the jet atomization process, it must be accounted for, too. A visualization of all break-up and evaporation process is shown in Figure 2-7. Droplet break-up into smaller droplets might be caused by unstable surface waves which are induced by aerodynamic forces on the liquid/gas interface. Surface tension, however, prevents droplet break-up such that the behavior is described by the gas-phase Weber number via

$$We_g = \frac{u_{\text{rel}}^2 d \rho_g}{\sigma} \quad (2-13)$$

In Eq. (2-13) d is the characteristic length, e.g. droplet diameter, u_{rel} the droplet velocity relative to the gas, and ρ_g the gas density. The gas-phase Weber number is the ratio of the aerodynamic forces to the surface tension which gives a dimensionless approximate of tendency for droplet break-up. In high-pressure engine sprays, the Weber number is high in the vicinity of the injector nozzle where the primary droplet break-up occurs. Downstream in the spray the velocity is lower and the droplets are smaller due to evaporation as well as previous break-up which means a reduced tendency for droplet break-up in that region. [14]

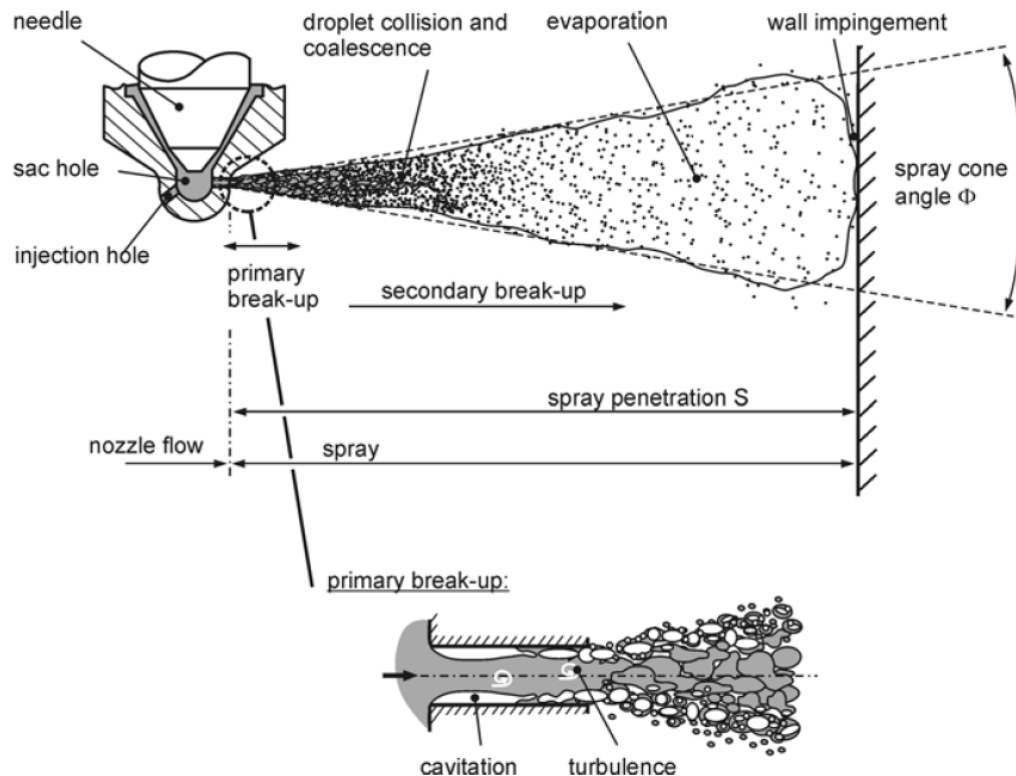


Figure 2-7: Schematic of jet and droplet break-up phenomena of a typical fuel spray. Figure from [14].

2.5.3 Droplet evaporation

For liquid fuel injection, droplet evaporation is crucial for spray propagation and mixing with the surrounding gas. Therefore, evaporation has significant influence on mixture formation and the subsequent chemical reactions in an engine.

Figure 2-8 shows a schematic of the temperature T and fuel mass fraction ω along the radial coordinate of a fuel droplet. The system consists of the liquid core, boundary layer, and the surrounding. The process of droplet evaporation is subject to strong interconnection of heat and mass transfer. Energy, necessary for evaporation, is transferred from the hot gas inside the combustion chamber into the cold fuel droplets via conductivity, convection, and radiation. Radiation is usually low compared to convection and diffusion, and often neglected in models. Mass is transferred diffusively and convectively from the liquid droplet to the boundary layer into the ambient gas. This process influences temperature, velocity, and vapor concentration as well as the overall physical properties of the mixture. [16]

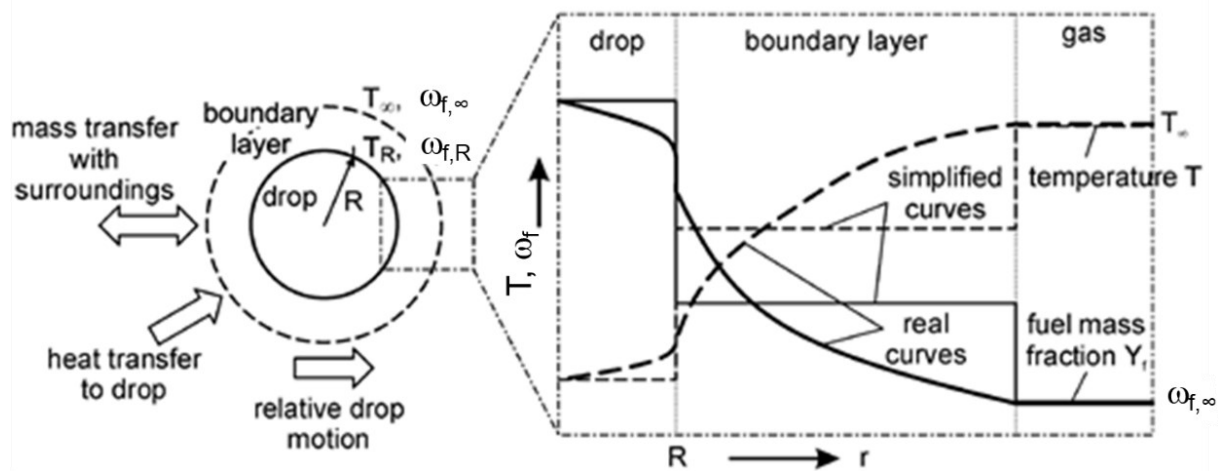


Figure 2-8: Schematic of the radial profile of temperature T and fuel-mass fraction ω_r during droplet evaporation. Schematic from [16].

Multi-component evaporation

Real engine fuels consist of a mixture of several components with different physical-chemical properties. Besides density, especially the volatility of each of the fuel components is significantly different. The effect of the droplet composition on the evaporation is shown in Figure 2-9. Many different components of different molecular weights form the liquid multi-component fuel shown in Figure 2-9a. Over the course of evaporation, the molecular weight of the liquid increases as shown in Figure 2-9b, since the more volatile components (light components) vaporize earlier and faster than the components with higher molecular weight (heavy components). Thus, the evolution of the gas-phase composition is the inverse of the evolution of the liquid composition. Due to convection the lighter components of the fuel vapor

segregate from the heavy fuel components during the spatio-temporal process of evaporation and transport. [16]

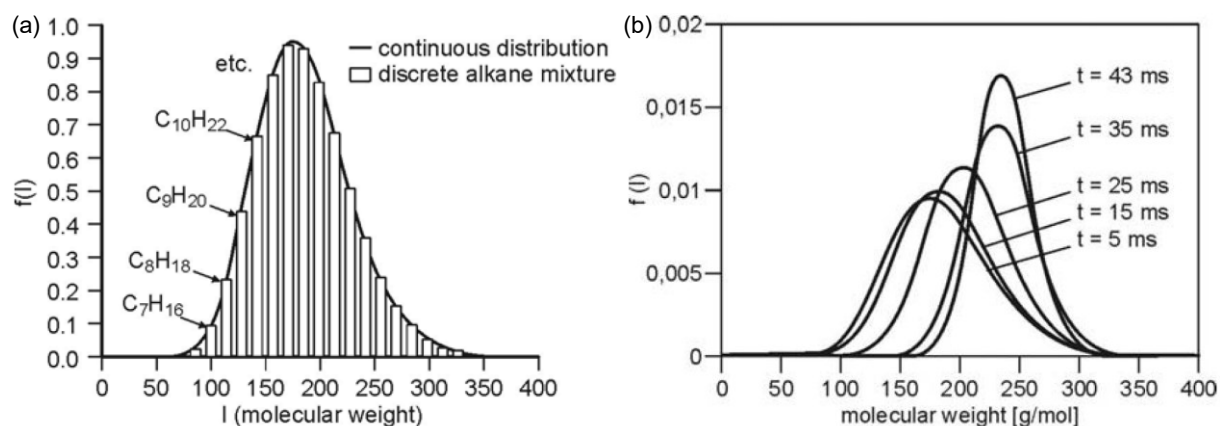


Figure 2-9: (a) distribution of the molar weight of a liquid multi-component fuel [16]. Evolution of the distribution of the liquid composition during evaporation of a multi-component Diesel fuel [17].

2.6 Light sources

2.6.1 *Nd:YAG lasers*

Neodymium-doped yttrium aluminum garnet (Nd:YAG) is a crystal used as an active medium in solid-state lasers. The Nd:YAG laser became popular in industry for the machining of parts and surfaces, and in science for laser-based diagnostics, i.e., at 532 nm for particle image velocimetry or 266 nm for laser-induced fluorescence. The active medium is pumped by flash lamps which are made from Xe or Kr. In Nd:YAG lasers operated at kHz-rates, however, diodes at 808 nm are commonly used. Nd:YAG has a maximum in the absorption of light at 808 nm where the highest input-to-output efficiency (by photon energy) can be achieved. The excitation and relaxation processes follow a so called “four-level system”, where excitation from the ground state to an electronically excited state by light absorption causes population inversion (more electrons in the excited than in the ground state) crucial for lasing. The excited electrons relax to a meta-stable state without light emission, from where they may relax to the higher vibrational levels of the ground state by emitting photons. An oscillator cavity with two highly reflective mirrors then creates resonator modes at distinct frequencies. During the transition from the meta-stable state to ground state the electrons of the Nd:YAG act like dipoles resonating at characteristic frequencies. The dipole oscillation is stimulated by the photons oscillating in the cavity. This stimulation greatly increases the probability of one certain transition between two material-characteristic states in the Nd:YAG. This stimulated transition differs from the transition for spontaneous emission. The electronical transition with the greatest probability in a Nd:YAG active medium is at 1064.1 nm. Other transitions with lower probabilities are at 1061.5 nm, 1073.8 nm, and 1318.8 nm. [18]

Opto-electronic quality switches (Q-switch, e.g. Pockels cell + polarizers) are used inside the cavity to decrease the pulse duration by blocking the resonator until maximum population inversion has reached. Q-switching increases the pulse energy because of the relatively long residence time of the Nd:YAG in the excited state ($\sim 230 \mu\text{s}$) compared to the pulse duration of the flash lamp ($\sim 100 \mu\text{s}$). With Q-switching laser pulses of less than 1 ns duration are possible [19].

Crystals from e.g. barium borate are used as non-linear optics to double, triple or quadruple the fundamental frequency from initially at 1064 nm to desired harmonics at 532 nm, 355 nm, or 266 nm outside of the resonator. Due to thermal losses, the pulse energy after frequency conversion is less than the initial energy, and photons at both, the initial and the converted frequencies are leaving the crystals. The desired wavelength may then be filtered from other wavelengths by spectrally selective mirrors and optics (e.g. Pellin-Broca prism). The output power is dependent on laser configuration, desired wavelength, and repetition rate [20].

External pulse stretcher

Q-switched Nd:YAG lasers emit short laser pulses of high power. To decrease the instantaneous power of a laser pulse, an external pulse stretcher utilizing a partly reflective cavity loop can extend the pulse duration. The pulse stretcher utilizes the time of propagation of the light. Figure 2-10 shows a schematic of the optical arrangement of a single cavity pulse-stretcher loop [21]. This loop consists of a beam splitter and two mirrors designed for the laser wavelength. Some portion of the incident laser light is reflected by the beam splitter while some portion is transmitted. The transmitted part is reflected by mirror M_1 onto M_2 that then again deflects the light towards the backside of the beam splitter as shown in Figure 2-10a. Arriving at the beam splitter again some portion of the light is transmitted and reflected. The reflected part of the light can propagate several round trips in the cavity loop. The optics of the arrangement are adjusted such that the initially reflected part of the laser pulse is spatially mapped onto the reflected beam. The divergency of the laser beam may need to be compensated by appropriate lenses inside the cavity loop.

The temporal delay Δt between the arrival at the beam splitter of the initial pulse with respect to the first reflected part of the beam can be adjusted by the length l of the cavity. Considering the speed of light c_0 of about 299 792 km/s in vacuum, the temporal delay can be calculated via $\Delta t = l/c_0$. I.e., if $l = 3.6 \text{ m}$, then $\Delta t = 12 \text{ ns}$. Combined with the initial pulse duration of i.e. 8 ns, the pulse duration after stretching with one round trip in the cavity is about 20 ns which can be seen by comparing the normalized intensity with and without pulse stretcher in Figure 2-10b. Kojima et al. [22] found that approximately 60% of the initial pulse needs to be guided through the ring cavity to achieve the best trade-off between lowest peak power and shortest pulse width.

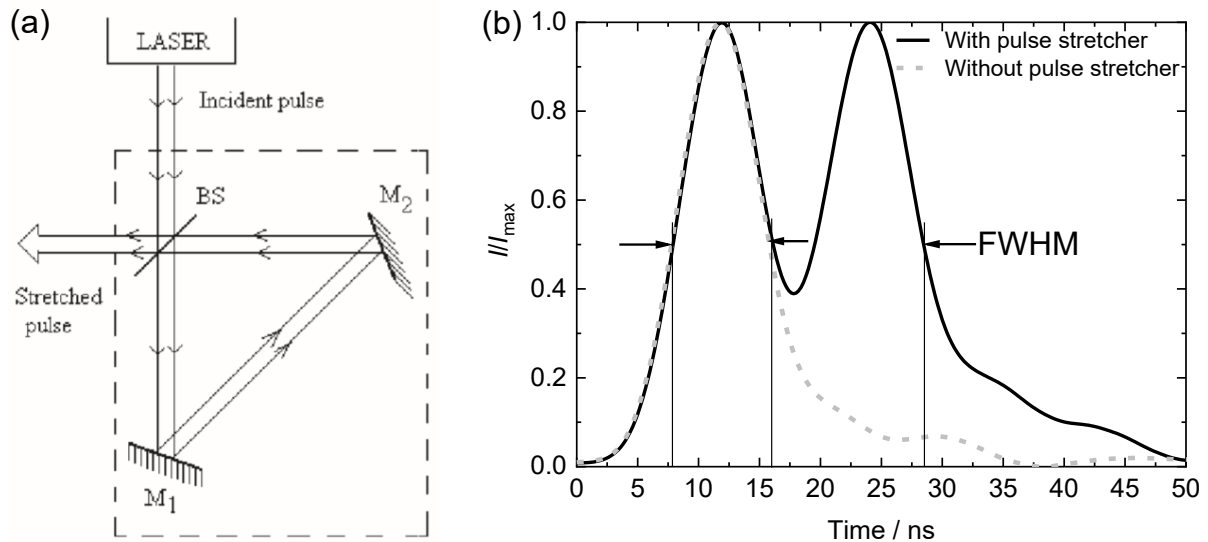


Figure 2-10: (a) schematic of a single cavity passive pulse stretcher loop. Mirrors M_1 and M_2 are 100% reflective, beam splitter (BS) is partly reflective, partly transmissive. Schematic from [21]. (b) peak-normalized pulse intensities measured with a photodiode with and without pulse stretcher at 266 nm (the laser used in Chapter 4). FWHM: Full width at half-maximum.

2.6.2 LEDs

A light-emitting diode (LED) is a non-coherent light source consisting of a two-lead semiconductor made from a strongly bonded material (p-type material, e.g. AlGaAs). Impurities (n-type material) are added to disturb the balance of the base material such that free electrons are created. The n-type material provides free electrons, or it takes electrons from the p-type material creating atom “holes”. The conductivity of the material increases. This p-n junction forms a certain bandgap where electrons can travel from the anode (n-type material) to cathode (p-type material) if a voltage is supplied. When filling the holes in the p-type material, the remaining energy is partly released by emission of photons. The emitted spectrum, usually broadband, depends on the bandgap energy of the active region of the LED. In this way it is possible to create different colors, i.e. red-green-blue (RGB) LEDs. [23]

In continuous operation the damage threshold of LEDs is low but operation at pulses of very short duration with currents exceeding the manufacturer specification can increase the instantaneous light intensity by a few order of magnitudes without damage [24]. For operation with short pulse duration, high frequencies of current supplied from electrical power circuits including MOS-FET gate drivers and specialized high-power transistors are required, as described by Willert et al. [25, 26].

2.7 Detectors and amplifiers

2.7.1 Camera sensors

CCD sensor

The charge-coupled device (CCD) sensor is an optoelectronic device that converts photons to electrons. It consists of a semiconducting substrate with metal conductors, an insulating oxide layer, and anode-cathode layers. Photons interact with the semiconductor material (photoelectric effect) and create a proportional number of free electrons temporarily stored in a MOS-capacitor. The whole sensor consists of an array of CCD elements called “pixels” represented by the green squares in Figure 2-11. The pixels are most commonly arranged in rectangular or quadratic form. [27]

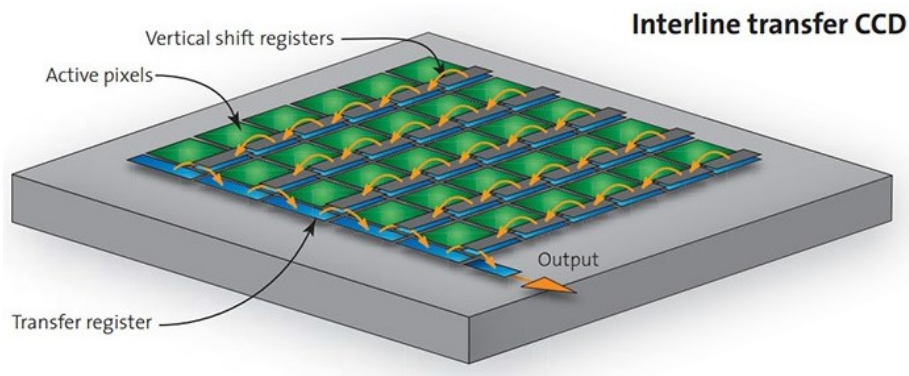


Figure 2-11: Schematic of the interline transfer CCD architecture. The green squares represent the pixels of the CCD sensor. Figure from [28]

Read-out may take place differently depending on the layout. Common layouts are the full-frame, frame-transfer, and interline-transfer CCD sensors. But all layouts basically include a similar read-out characteristic. It consists of simultaneous illumination of all active pixels followed by sequential read-out on a row-by-row basis. The charge stored in each pixel is moved simultaneously to a shift register near the pixels, and each row is then moved to a horizontal transfer register (see Figure 2-11). From the transfer register, the charge is clocked to the output amplifier. The charge is then converted to voltage by an electrometer resulting in individual voltages for each pixel. Cooling and a slow read-out speed can achieve a very low level of noise combined with a high dynamic range. However, the slow read-out speed also leads to low repetition rates. [28]

CMOS sensor

The general read-out architecture of each pixel of a complementary metal-oxide semiconductor (CMOS) sensor differs in functionality from the one of CCD sensors. Alike a CCD, CMOS sensors also detect photons by creating free electrons in the semiconductor

material. In contrast to CCD pixels, each pixel of a CMOS sensor has a build-in electronic circuit as shown in the schematic of Figure 2-12. Each pixel can be controlled and read out separately via MOS-FET transistors. This architecture brings individual access via line and row selectors to every pixel of the sensor. [27]

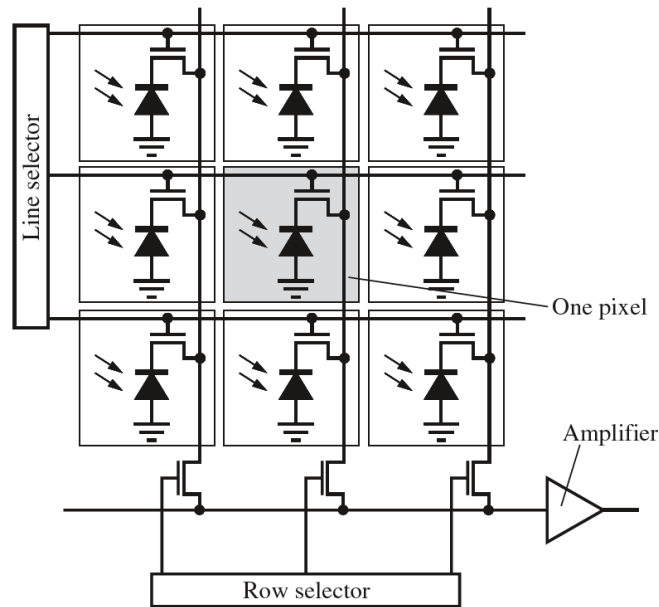


Figure 2-12: Schematic of a CMOS-sensor architecture taken from [27].

The advantages of CMOS sensors in comparison to CCD sensors are higher repetition rates due to amplification, and AD-conversion on chip as well as the possibility to read out only the desired region of the sensor. Since relatively high capacities of the long electrical lines the CMOS sensor architecture is subject to stronger electrical noise than the CCD sensor architecture. Due to the additional on-pixel electronics that complicate production, also a stronger fixed-pattern noise may be present on CMOS sensors in comparison to CCD sensors. [27]

Bayer array

The Bayer array is an arrangement of four sensor pixels with sensitivities in the red-green-green-blue (RGGB) spectral regions, respectively. This makes it possible to combine the signal from these individual spectral regions to a color image. The Bayer array is commonly used on sensors in digital single-lens reflex (DSLR) cameras. The Bayer array consists of a mosaic of color filters made from various substrates on a grid of photosensors (CCD or CMOS). Exemplarily, the sensitivity of a commercial *Canon 60D* DSLR camera is shown in Figure 2-13.

Half of the area of the sensor detects green light, while 25% of the area detects red and another 25% detects blue light. Since each pixel detects a distinct spectral region of the light,

color information outside the pixel's sensitivity is unknown at that certain location. Therefore, a demosaicing routine is usually applied to the raw sensor output. For example, in a "blue pixel" the exact intensity of the blue component is known. The intensity of green and red is then interpolated from the intensities in neighboring pixels. [29]

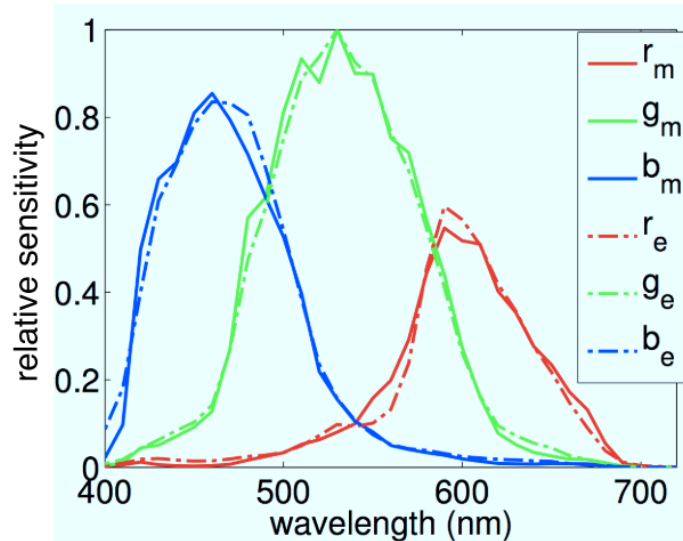


Figure 2-13: Measured (subscript m) and calculated (subscript e) sensitivities of each color channel of the Bayer sensor in the Canon 60D DSLR. Figure from [30].

2.7.2 Image intensifier and relay optics

An image intensifier with relay optic (IRO) is an opto-electronical device that converts and amplifies weak light to visible light that is finally detected by camera sensors designed for visible light. Figure 2-14 shows a schematic of the components of an IRO + CCD camera (ICCD) system.

An IRO consists of a gateable image intensifier which includes a photocathode, a micro-channel plate, and a phosphor screen and a lens-coupling system. The intensifier is a cathode-anode system with an electronical shutter. The incoming light is focused on the photocathode where, because of light-matter interactions, free electrons are being created when the photocathode's voltage is electronically gated. The electrons are then accelerated between the photocathode and the phosphor screen (anode). Between photocathode and phosphor screen a micro-channel plate (MCP) amplifies the number of electrons depending on the voltage applied to it.

MCPs consist of a plate made from highly resistive material of less than 2 mm thickness. The MCP has small channels of diameters of about $\sim 10 \mu\text{m}$ inclined by 10° with respect to the plate's surface. A strong electric field is applied to the plate such that the incoming electrons are accelerated and the channel's inclination with respect to the plate's top surface guarantees that the electrons hit the channel walls. Depending on the electric field applied to the MCP, the impact of the electrons on the channel walls releases several new electrons. After the MCP, the

electrons are further accelerated to the phosphor screen. Because of the impact of the electrons on the phosphor screen it starts to emit photons. Then, relay optics focus the emitted light onto the camera sensor. The phosphorescence lifetime depends on the type of phosphor, so the exposure time of the camera sensor should be chosen accordingly. The exposure time of the whole system is defined by the gating time that is applied to the photocathode.

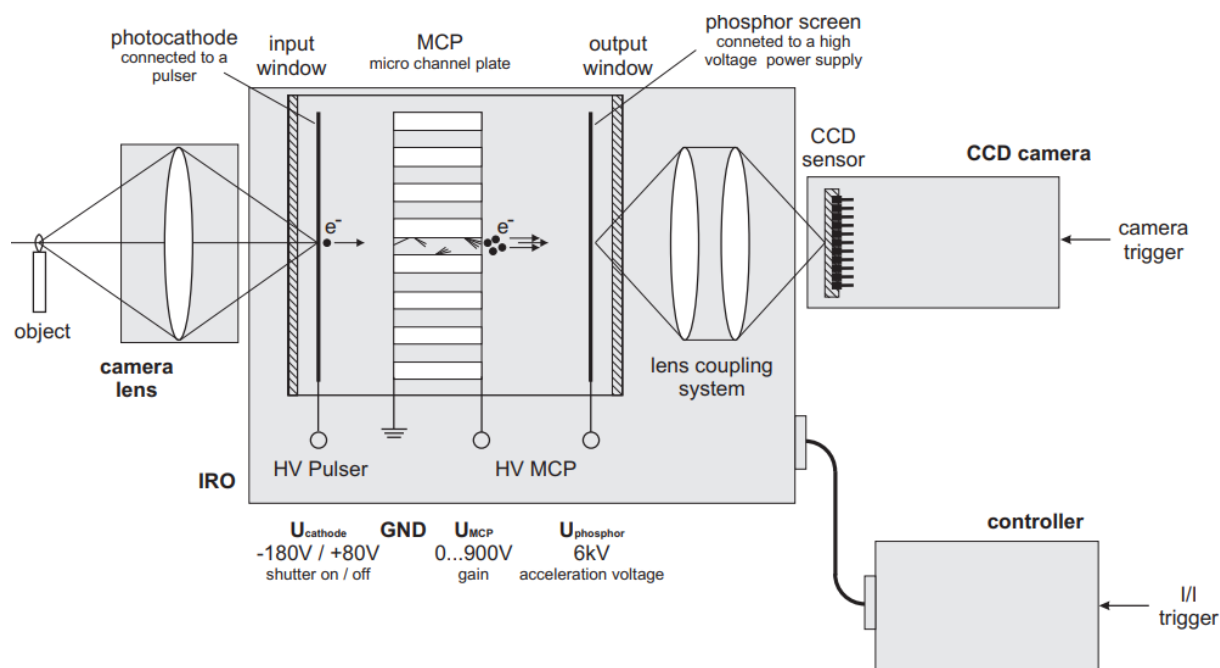


Figure 2-14: Schematic of an LaVision image intensified CCD system. Figure taken from [31].

The advantages of an ICCD system compared to a CCD camera are threefold: The spectral sensitivity of the system is extended into the UV and a weak signal can be intensified to increase the detected signal with respect to the read-out noise. Moreover, very short exposure times (~ 5 ns) in comparison to a non-intensified CCD ($\sim 30 \mu\text{s}$) are possible due to the fast-gated photocathode of the IRO. However, the spatial resolution is decreased significantly compared to a non-intensified CCD.

2.8 Laser-induced fluorescence of organic molecules

Laser-induced fluorescence (LIF) of organic molecules is a non-intrusive imaging technique, which can be used to measure diverse quantities. Schulz and Sick [3] summarize the applicability of LIF to obtain quantified information on fuel concentration, air/fuel ratio, temperature, fuel composition, and residual gas concentration in internal combustion engines. This section explains the fundamental principles of LIF from organic molecules and the related photophysical dependencies.

2.8.1 Photophysical principle

Fluorescence is an “in-elastic” photophysical process in which molecules are excited to a higher state of energy through absorption of photons (e.g. from a laser). The excess in energy in the excited state is partly reduced by spontaneous emission of photons. Detailed descriptions of the photophysical processes are given in [3, 32].

Molecules only exist in discrete energy states transitioned by e.g. an excess in energy via light absorption. Light absorption is only possible for *exact* wavelengths (mostly in the UV or near UV) depending on the electronic configuration of the molecule. The strength of absorption is given by the temperature and wavelength-dependent absorption cross-section $\sigma_{\text{abs}}(\lambda_{\text{ex}}, T)$. The energy of the exciting photons ΔE_{01} of wavelength λ is described by the Planck relationship $\Delta E_{01} = h c_0 / \lambda$ with h being the Planck’s constant and c_0 the speed of light in the medium. Since fluorophores, in this work called “tracers”, of different chemical groups can have fundamentally different fluorescence characteristics, and organic molecules will be used as fluorophores in the experiments, this section focuses on organic molecules only. For large organic molecules, commonly used for fluorescence imaging [3, 32], various vibrations of different frequencies and magnitudes contribute to electronic transitions. Each electronic state of the molecule consists of characteristic vibrational sub-levels with, in turn, finer rotational sub-levels superimposed on it. Oscillation and rotation in excited state is suppressed by collisions with other molecules. This creates a quasi-continuum of energetical sub-states. The quantum-mechanical idea of a harmonic oscillator with vibrational and rotational levels is shown in Figure 2-15a. The idealized potential in Figure 2-15a consists of harmonic oscillators and rigid rotors with vibrational levels v and superimposed finer rotational levels. The electronic population of each state is described by the Boltzmann distribution (not shown). More realistic is an anharmonic potential shown in Figure 2-15b. It includes the vibrational states and the Morse potentials of a molecule that is a more realistic representation of the process. [32]

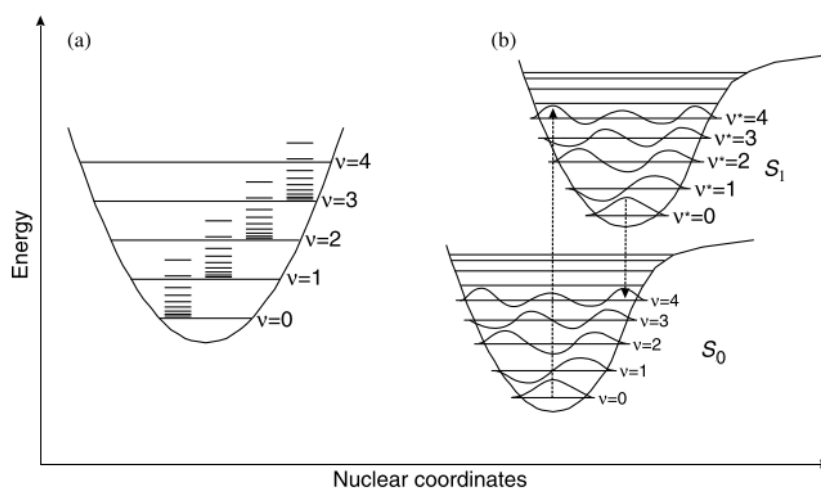


Figure 2-15: (a) Idealized potential (harmonic oscillator) with vibrational modes v and rotational energy ladders. (b) Morse potentials of the singlet ground state S_0 and first excited state S_1 . Figure (slightly modified) from [32].

Transitions between the ground state S_0 and an excited state S_1 occur due to excitation of the molecule by absorption of photons. Transitions most likely occur vertically, which was explained by the Born-Oppenheimer approximation and the Franck-Condon principle for light absorption. Born and Oppenheimer found that during transition between states the nuclei of the molecule is fixed in comparison to the electrons, since the mass of a neutron or proton is approximately 1870-times that of an electron. This means that light absorption is much faster than the movement of the nuclei of the molecule. Based on that, Franck and Condon explained that vertical transitions must have the highest probability. This also means that the higher vibrational level must be instantaneously compatible with the nuclear position and vibrational momentum of the initial electronic state. After transition, the nuclei must move to fit to the new electronic configuration and the instantaneously starting vibrations. The probability of a transition is described by perturbation calculations using the wave functions of the ground and excited state. The excited state is at non-equilibrium meaning that the molecule quickly relaxes to the vibrational level at lowest energy in that state. Kasha's rule states that return to the ground state always takes place from the lowest vibrational level. To return to the electronic ground state, the molecule either emits a photon or relaxes via vibrations without light emission. The Franck-Condon principle also applies for the return to ground state. [32]

The emitted photons have lower energy because of energy losses during the process of absorption and relaxation. This means that the emitted light is most likely (red-)shifted towards longer wavelengths. A "blue" shift is theoretically also possible, although with low probability, if an electron from a high vibrational level in the ground state relaxes from the excited state to a lower vibrational level than the initial one.

The Jabłoński's energy diagram in Figure 2-16 schematizes the photophysical population and deactivation processes that may occur during light absorption and emission of an organic molecule. According to [3] and [32] three deactivation processes of excited molecules can occur:

- *Radiative*: Excess energy is partly lost by spontaneous emission of photons, i.e. fluorescence, phosphorescence.
- *Non-radiative*: Energy is lost by relaxation via vibrational and rotational transfer.
- *Collisional*: Energy is transferred to a colliding species by electronic excitation.

Now the pathways of each deactivation process in relation to light absorption are explained in more detail. Most large organic molecules have a total electronic spin of $S = 0$ in the ground state with a multiplicity of $2S + 1 = 1$ meaning that all electrons are spin paired. This configuration is called "singlet". However, it is also possible, although not very likely, that $S = 1$ meaning that two unpaired electron spins in the ground state exist. The latter configuration is called "triplet". In the Jabłoński diagram in Figure 2-16 the ground state of a singlet molecule is denoted as S_0 , the first excited state of singlets as S_1 and of triplets as T_1 . Radiative transitions (fluorescence or phosphorescence) and non-radiative transitions are shown as straight or curved lines in the energy diagram. The population of the vibrational levels in the ground state are described by the Boltzmann distribution and, in general, more vibrational levels are populated with increasing temperature. After absorption of the exciting photon the electrons of the molecule reside in one of the vibrational and rotational levels of the first excited state $S_0 \rightarrow S_1$

or, if excitation energy is high enough, in the second excited state $S_0 \rightarrow S_2$. The probability to find electrons in one of the excited singlet states depends on the probability of transition (Boltzmann) and the energy of the exciting photon. The excitation process can be considered as an instantaneous process (time scale shorter than 10^{-6} ns). After some time in the excited state, energy decreases by vibrational and rotational relaxation, in which energy is transferred to other molecules until the lowest vibration level of the excited state is reached. [32]

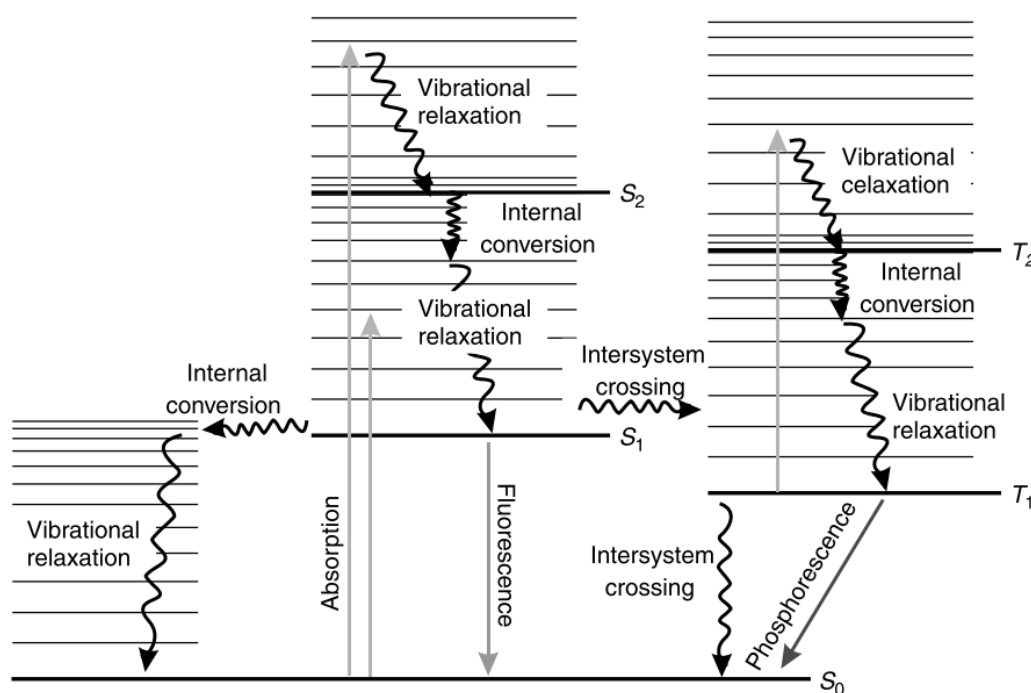


Figure 2-16: Jablonski diagram visualizing the simplified photophysical processes during activation and deactivation of excited organic molecules. Figure from [32]. S_0 is the ground state of the singlet, S_1 , S_2 , and T_1 , T_2 are the first and second excited state of the singlet and triplet.

In the lowest vibrational level of S_1 , non-radiative internal conversion may occur, which transfers the electron into higher levels of the next lower electronic state. Then, non-radiative vibrational and rotational relaxation may take place until electronic ground state (thermal equilibrium) is reached. Another possible pathway is radiative depopulation through emission of photons. The third process can be that the spin of the singlet in the excited state is reversed to a triplet via intersystem crossing. This is very unlikely to happen for organic molecules since it is a “forbidden” spin transition. The probability of intersystem crossing increases if the vibrational levels of the potentials S_1 and T_1 overlap and it has been found that the probability becomes greater for very heavy atoms [32]. Returning from the lowest vibrational level of T_1 to S_0 takes either place through radiative phosphorescence or non-radiative decay via intersystem crossing. Phosphorescence has a much longer lifetime than spontaneous fluorescence. The ratio of the depopulation via spontaneous emission through fluorescence to all other depopulation processes is described by the fluorescence quantum yield ϕ_{fl} shown in Eq. (2-15). [32]

2.8.2 Fuel/air ratio LIF

For weak excitation at a given wavelength and low tracer number density, the detected (e.g. by a camera) fluorescence signal S is given by the linear relation:

$$S = I_{\text{laser}} V n_{\text{tr}}(T, p) \sigma_{\text{abs}}(T) \phi_{\text{fl}}(T, p, n_i) \Pi \eta, \quad (2-14)$$

where I_{laser} is the incident laser intensity, V the probe volume, n_{tr} the tracer number density, σ_{abs} the absorption cross-section, ϕ_{fl} the fluorescence quantum yield (FQY), and Π as well as η are the collection and quantum efficiencies of the detection system, respectively. Apart from the desired quantity n_{tr} (proportional to the fuel number density), also the pressure p , the temperature T , and the number density of all bath-gas species n_i potentially influence the LIF signal. In an engine, only the pressure can be measured directly (see Section 2.2.1) while the local temperature and composition are unknown, the former primarily because in fired operation residual gas mixes with the fresh charge.

For most aromatic fluorophores, the important bath-gas species is oxygen. Quenching by oxygen significantly reduces the FQY of aromatic fluorophores by non-radiative collisional depopulation processes [33-35]. Considering oxygen quenching, the FQY is given by:

$$\phi_{\text{fl}} = \frac{k_{\text{fl}}}{k_{\text{tot}} + \tilde{k}_{\text{q}}^{\text{O}_2} n_{\text{O}_2}}, \quad (2-15)$$

where k_{fl} is the rate of spontaneous emission, $\tilde{k}_{\text{q}}^{\text{O}_2}$ the rate coefficient of quenching by oxygen with oxygen number density n_{O_2} , and k_{tot} the rate of all other deexcitation mechanisms. All these terms are dependent on temperature. If quenching by oxygen is the dominant deexcitation process, $\tilde{k}_{\text{q}}^{\text{O}_2} n_{\text{O}_2}$ considerably exceeds k_{tot} such that k_{tot} can be neglected in the denominator. Substituting this approximated FQY into Eq. (2-14), the measured LIF signal S becomes directly proportional to the fuel/air equivalence ratio ϕ , or inversely proportional to the relative air/fuel ratio λ

$$S \sim \frac{n_{\text{tr}}}{n_{\text{O}_2}} \sim \lambda^{-1} = \phi. \quad (2-16)$$

By Eq. (2-15), the sensitivity of the signal (represented by the FQY) being quenched by oxygen is described by

$$\frac{\phi_{\text{fl},0}}{\phi_{\text{fl}}} = \frac{k_{\text{fl}} (k_{\text{tot}} + \tilde{k}_{\text{q}}^{\text{O}_2} n_{\text{O}_2})}{k_{\text{fl}} k_{\text{tot}}} = 1 + \frac{\tilde{k}_{\text{q}}^{\text{O}_2}}{k_{\text{tot}}} n_{\text{O}_2} \text{ with } k_{\text{SV}} = \frac{\tilde{k}_{\text{q}}^{\text{O}_2}}{k_{\text{tot}}}. \quad (2-17)$$

$\phi_{\text{fl},0}$ is the FQY in the absence of oxygen, and k_{SV} is the Stern-Volmer coefficient, which can be experimentally determined by successively varying the oxygen concentration at otherwise constant conditions. k_{SV} (in unit $\text{bar}^{-1} \text{ mol}^{-1} \text{ m}^{-3}$) then represents the rate efficiency of depopulation by oxygen quenching compared to all other deexcitation processes and thus is relevant in practical systems.

The fuel/air ratio LIF (FARLIF) approach in Eq. (2-16), originally due to Reboux et al. [36], enables measuring λ without knowing the local gas composition, even if fresh charge is mixed with residual gas from the previous cycles. However, since σ_{abs} as well as ϕ_{fl} depend on ambient conditions like temperature or pressure, these variables have either to be measured, too, or appropriately be considered in calibration. E.g., pressure influences are minimized by recording measurements and corresponding calibration images at the same crank angle, although Scholz et al. [37] showed that FARLIF of toluene is almost pressure-independent for absolute pressures larger than 500 mbar. However, temperature is not irrelevant, as will be discussed in the next chapter.

2.8.3 Temperature dependence of LIF

As denoted in Eq. (2-14), the LIF intensity is dependent on temperature. The number density is inverse proportional to temperature $n_{\text{tr}} = x_i p / T$, and the absorption cross-section as well as FQY depend on temperature, which mainly is due to changes of the population of the electronic ground and excited states. If temperature increases higher vibrational levels are populated described by the Boltzmann distribution such that the probability of transitions to even higher vibrational levels in the first excited state increases [32]. Depending on the electronic configuration of the fluorophore the fluorescence spectrum shifts with temperature.

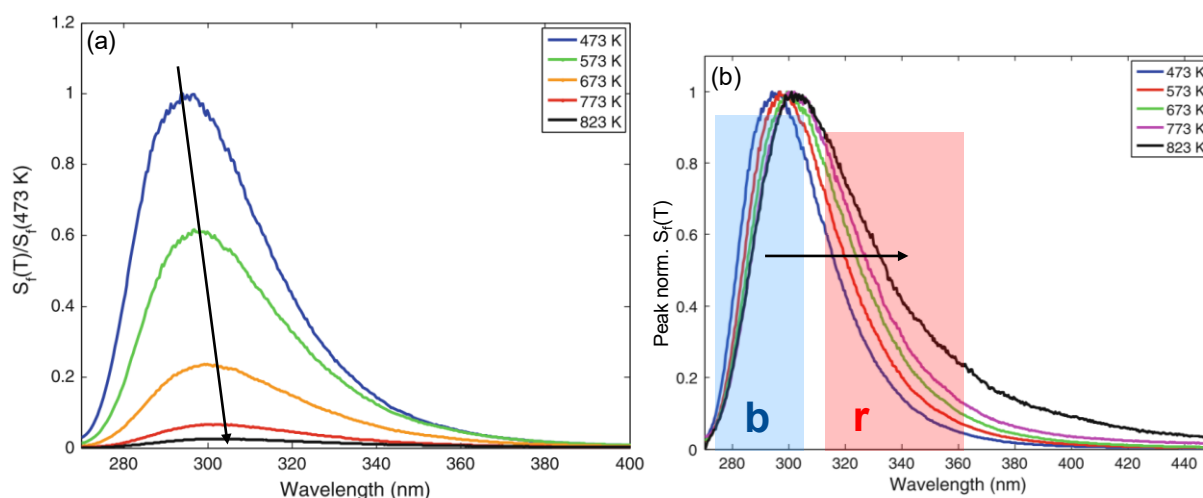


Figure 2-17: At 473 K (a) and peak normalized (b) fluorescence spectra of anisole at elevated temperatures in 1.2 MPa CO₂ and 266 nm excitation. “b” and “r” in (b) represent band-pass filters in that wavelength regions. Spectra from [34].

Figure 2-17 shows the fluorescence spectrum of anisole upon 266 nm excitation in 1.2 MPa CO₂ between 473 K and 823 K [34]. On the one hand, from the temperature dependent fluorescence signal in Figure 2-17a it can be seen that the signal decreases with increasing temperature. From the peak-normalized spectra in Figure 2-17b on the other hand, it can clearly be recognized that the spectrum shifts to longer wavelengths (red-shift) with increasing

temperature. This red-shift can be exploited by spectral separation of the signal at the “short”, $S^{(b)}$, and “long”, $S^{(r)}$, part (in terms of wavelength) of the spectrum by (bandpass) filters as exemplarily shown in Figure 2-17b. By appropriate selection of a suitable filter combination, the temperature sensitivity of the channel ratio R can be increased or decreased. The channel ratio R is described by

$$R = \frac{S^{(b)}}{S^{(r)}} = \frac{I_{\text{laser}} V n_{\text{tr}}(T, p) \sigma_{\text{abs}}(T) \phi_{\text{fl}}^{(b)}(T, p, n_i) \Pi \eta^{(b)}}{I_{\text{laser}} V n_{\text{tr}}(T, p) \sigma_{\text{abs}}(T) \phi_{\text{fl}}^{(r)}(T, p, n_i) \Pi \eta^{(r)}} = \frac{\phi_{\text{fl}}^{(b)}(T, p, n_i) \eta^{(b)}}{\phi_{\text{fl}}^{(r)}(T, p, n_i) \eta^{(r)}} \quad (2-18)$$

for weak excitation at given wavelength. Since the temperature dependence of the absorption cross-section does not affect a spectral shift but rather a change in absolute signal, $\sigma_{\text{abs}}(T)$ cancels out from the equation. The channel ratio in Eq. (2-18) is therefore mainly dependent on the FQY and the collection as well as quantum efficiencies η of each of the detection paths. The deviations in η between both detection channels can be corrected by a homogeneous reference image from each channel. Also, the FQY is mainly influenced by temperature and number density of all bath-gas species. As described in Section 2.8.2, oxygen is the important bath-gas species causing a minor shift of the spectrum to longer wavelengths with increasing partial pressure. The shift becomes less at high oxygen partial pressure and, overall, is small compared to the thermally induced shift of the spectrum. Neglecting the red-shift caused by oxygen, and correcting for deviations between $\eta^{(b)}$ and $\eta^{(r)}$, Eq. (2-18) simplifies to

$$R = \frac{\phi_{\text{fl}}^{(b)}(T)}{\phi_{\text{fl}}^{(r)}(T)} = f(T). \quad (2-19)$$

The relation of temperature and the channel ratio R needs to be calibrated, which may be done in situ or in a separate experiment where the temperature of the mixture in the field of view (FOV) is varied. However, the accuracy in the quantified temperature is therefore strongly affected by the accuracy of the temperature calibration.

2.9 Structured laser illumination planar imaging

Structured laser illumination planar imaging (SLIPI) is a technique to suppress out-of-plane signal generated by multiple scattering of photons [38-41] or re-absorption of fluorescent light [42]. In practical LIF systems, e.g. in optically accessible engines (see Section 3.1), the laser beam enters the probe volume through a transparent medium exciting fluorescent molecules. Optimally, the remaining laser energy is leaving the probe volume and, i.e., is collected by a beam dump. However, in most applications the latter is not possible because of non-transparent boundaries, i.e. the cylinder head surface in optically accessible engines. In that case some portion of the laser light is scattered to the fore- or background where also additional signal is being created (by LIF or scattering), superimposed on the actual signal, and eventually detected by the camera sensor. This additional signal is dependent on the ambient conditions in that region differing from the ambient condition in the light sheet plane. This influences the measurement accuracy.

The basic idea of SLIPI is to spatially modulate the illumination by a fixed frequency. Exciting photons at the laser wavelength that are directly absorbed by molecules or undergo single scattering by droplets keep the information on the modulation while laser photons that undergo multiple absorption or scattering, lose the information on the spatial modulation. Frequencies away from the modulation are then filtered out in the Fourier domain eliminating the additional unwanted signal. This filtering was first described by Neil et al. [43] for 2D images and adapted to planar imaging of engine sprays in e.g. [44].

An example of a SLIPI arrangement is shown in Figure 2-18. The beam from a pulsed Nd:YAG laser is first magnified to fill the area of the grating. Different types of gratings are available with e.g. a rectangular (Ronchi grating) or sinusoidal pattern coated on a transparent substrate. Depending on the frequency of the line pattern, the modulation is superimposed onto the laser beam used for illumination. The damage threshold of the grating substrate limits the instantaneous energy that can be used.

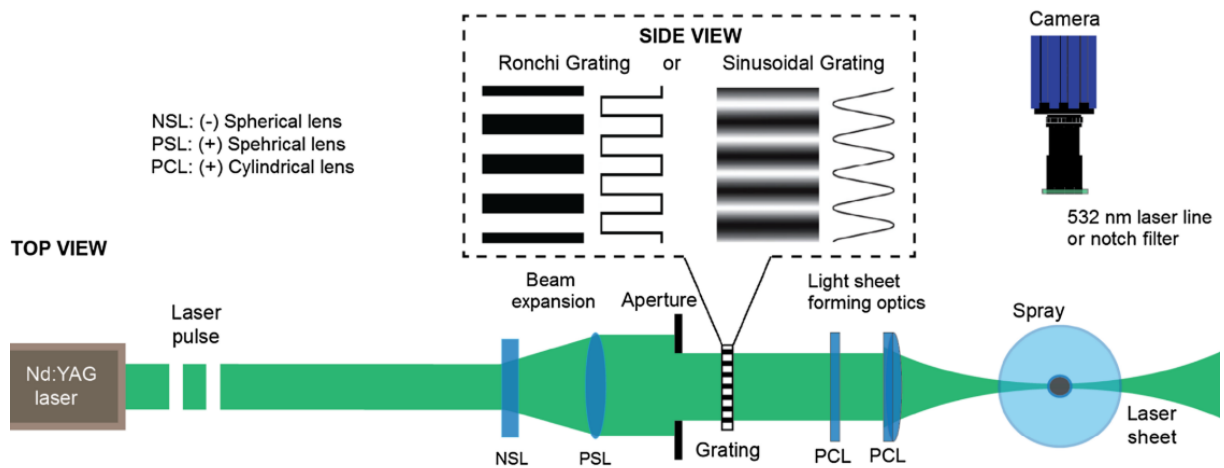


Figure 2-18: Example of an optical setup to create a light sheet for SLIPI to study dense sprays by planar Mie scatter imaging. Figure from [44].

An example of the processing routine of SLIPI is displayed in Figure 2-19. The modulated image in (a) is first transferred into frequency space via Fourier transformation as shown in (b). The 1st order maximum, located at the frequency ν , preserves the information on the SLIPI modulation, but the 0th order maximum, located at around zero, contains information on the unmodulated signal that e.g. was generated by multi-scattering or is the background signal. Other order frequencies may exist and can be because of pattern noise of certain frequencies. The frequencies that represent the modulated signal are separated from other unwanted frequencies. To remove the unwanted frequencies, one of the two 1st order maxima (positive or negative) is shifted to the center of the image as shown in (c). In step (d), a circular two-dimensional profile, e.g. Gaussian or Butterworth, is multiplied with the image in (c) such that only the central part of the image is kept. Everything else is deleted, and after the inverse Fourier transformation the corrected image (e) is the final output in real-space coordinates. [44]

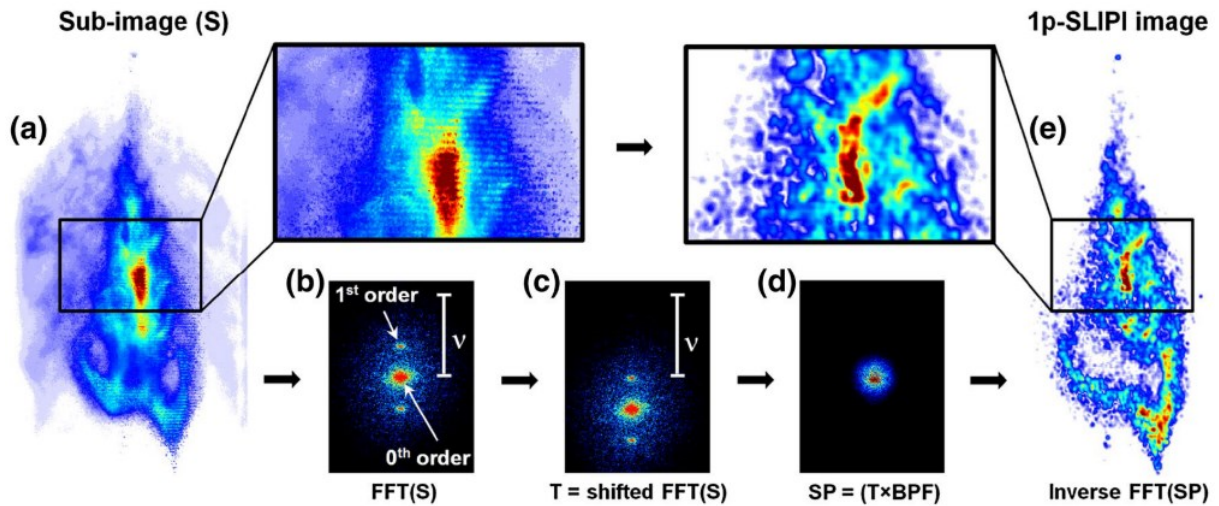


Figure 2-19: One-phase SLIPI processing of a plane through a dense spray. (a) raw image, (b) fast-Fourier transformation (FFT), (c) shifted FFT, and (d) Gauss filtered FFT. (e) shows the inverse FFT of the image in (d). Figure from [44].

Comparing the initial image in Figure 2-19a and the final SLIPI filtered image in (e), it is apparent that the signal outside the spray region is removed, and additionally also some signal within the spray region. However, the spatial resolution is degraded, which is directly connected to the choice of the size of the Gaussian filter. The size of the filter is in turn limited by the spatial frequency ν of the modulation, thus an increase in spatial frequency improves the spatial resolution after SLIPI processing. [44]

2.10 Particle image velocimetry

PIV is a flow measurement technique that uses the shift of particles within a short time period defined by the double illumination by pulsed laser light sources. From the particle shift and the time delay between pulses velocity vectors are calculated within a spatial region. In contrast to other velocity measurement techniques, as with probes in hot-wire anemometry [45], PIV is a minimally intrusive imaging technique. Figure 2-20 shows the general setup of a PIV experiment. Seeding particles are added to the fluid flow and illuminated by the light sheet created from a double-pulsed laser. Usually monochromatic double-pulse Nd:YAG or Nd:YLF lasers are used that consist of two laser cavities temporally synchronized by a delay generator [46]. CCD or CMOS cameras (see Section 2.7.1) acquire two image frames with adjusted exposure time and delay such that the laser pulses at t' and t are within each of the exposures. The user defines the temporal delay $\Delta t = t' - t$ between the laser pulses and the local spatial displacement Δs of the particles is determined from the Mie scattering of each particle detected in each of the camera frames [47]. Both information combined make it possible to estimate the local velocity via $v = \Delta s / \Delta t$.

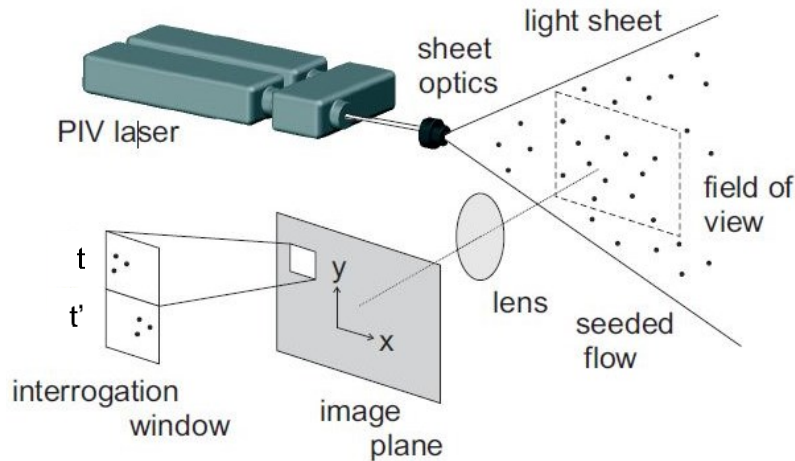


Figure 2-20: General strategy for double frame PIV measurements. Adapted from [48].

2.10.1 Seeding particles

The characteristics of seeding particles are well investigated in literature [49] and the right choice of seeding particles highly depends on the application. The particles should have similar density as the surrounding fluid to represent the local flow velocity, which, however, is only possible to first order. Also, the particles should have reasonable temperature resistance to exist sufficiently long in environments at high temperature. E.g., for the application of PIV in the combustion chamber of an engine, the particles should survive the high in-cylinder temperatures, which is most likely only be the case for certain operating conditions and crank angles. Raffel et al. [50] describe the properties of most common seeding materials for various applications. They provide information on different seeding materials for liquid and gaseous flows of different mean diameters and densities. For gas flows, most commonly synthetic oils with mean diameters on the order of $0.5 - 10 \mu\text{m}$ are used, but also solid seeding materials like polystyrene, phosphors or glass micro-spheres [47] are common.

2.10.2 Vector-field computation

Double-frame PIV is the most common strategy for measuring instantaneous flow fields in combustion engines. Two camera gates are independently illuminated by two laser pulses. Illumination and the camera gates require accurate temporal synchronization. Depending on the flow velocity, magnification, and light-sheet thickness the inter-pulse delay dt needs to be adjusted to minimize out-of-plane losses and achieve reasonable pixel shift of the particles between the two laser pulses. A conservative method to determine the optimal dt is the “one-quarter rule” introduced by Keane et al. [51]

$$ds_{\max} = v_{\max} \cdot dt \leq \frac{1}{4} s, \quad (2-20)$$

where s is the size of the interrogation window in which the particle displacement will be determined in post-processing, ds_{\max} the maximum particle shift, and v_{\max} the maximum flow

velocity within the region of interest (ROI). In other words, the maximum shift ds_{\max} of the particles within dt should not exceed one-quarter of the window size. The particle displacement between frames can be adjusted by de- or increasing the inter-pulse delay dt . However, it is also not advantageous to use a very short dt since the shift of the particles may then be less than one pixel. For flow measurements in the combustion chamber of an engine dt is usually on the order of a few micro-seconds to measure local velocities up to ~ 200 m/s.

The vector field computation from the Mie scatter images is done by cross-correlation of the information from both frames by the mean movement of particles within a finite interrogation window. First, the double frame images are sub-divided into finite interrogation windows usually in quadratic size of 16×16 px, 32×32 px, 64×64 px, etc. The pixel location in each interrogation window of size $2K \times 2L$ is defined as i in x- and j in y-direction and are the running indices in Eq. (2-21). Then the second frame is shifted by (s_x, s_y) with respect to the first frame and the intensities of the first frame I and second frame I' are correlated according to

$$R_{II}(s_x, s_y) = \sum_{i=-K}^{i=K} \sum_{j=-L}^{j=L} I(i, j) I'(i + s_x, j + s_y). \quad (2-21)$$

R_{II} is the correlation value for a fixed shift of s_x and s_y in x- and y-direction, respectively. The shift is varied by the size of the interrogation window, what ally ends up in a correlation map as shown in Figure 2-21. There, R_D represents the shift with highest correlation where identical particles most probably are detected in both frames. Other lower peaks can also be found, which can be reduced with several post-processing steps, filtering bad vectors with bad correlation values to improve the vector quality. Eq. (2-21) is then applied separately to all interrogation windows of the double-frame image. In this work the commercial software *DaVis 8.4* by *LaVision GmbH* is used for PIV recording and processing [48].

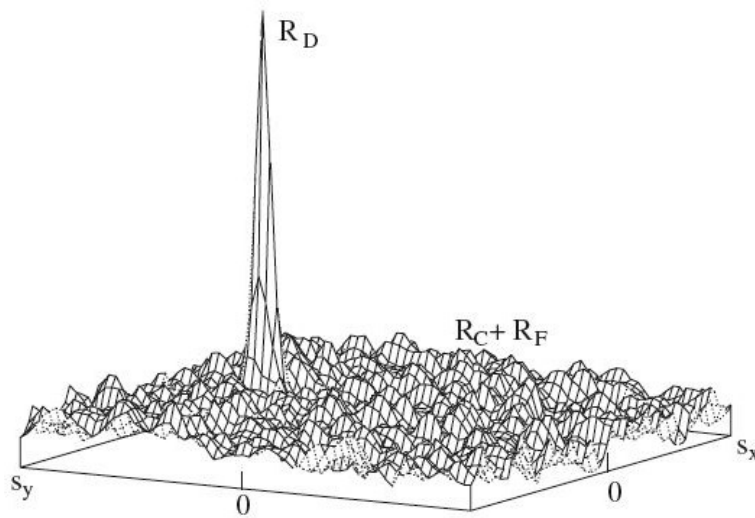


Figure 2-21: Correlation map of peaks in the cross-correlation function. The peak with the highest magnitude is the actual calculated shift in the correlation plane. From [47].

Chapter 3 - Imaging of mixing processes in SI engines

This chapter gives a literature review on optical diagnostics to investigate mixture formation in SI engines. Parts of the content of this chapter have been published as Kranz et al. [52, 53] and Geschwindner, Kranz, et al. [54], in particular Sections 3.2.2, 3.3.1, and 3.3.2. My contributions to the publications are described in more detail in Section 7.1.1.

3.1 Imaging in optically accessible engines

Laser-based imaging in single-cylinder research engines with large windows has proven to be very useful for imaging in-cylinder phenomena. The obvious advantage of optical diagnostics applied to such “optical” engines is the easy optical access to the combustion chamber via large windows. Common optical diagnostics in optical engines are PIV, visualization of combustion and flame luminosity, laser-induced fluorescence (LIF), and laser-induced incandescence (LII) imaging [55, 56]. With these diagnostics, quantitative measurements of fuel distribution, auto ignition, instantaneous flow fields, temperature and qualitatively soot distribution inside the cylinder can be carried out. However, there are two major drawbacks. First, optical engines are often significantly modified from the production engine, cannot operate over the full load-speed range, and are resource-intensive facilities. Second, like every experiment, also optical measurements can only access a small subset of the physically relevant quantities. Already the simultaneous acquisition of two quantities is challenging. To address the first issue, imaging through endoscopes [57, 58] or, even less invasive, point-like measurements via single-port probes have been employed. The second drawback applies much less to multidimensional simulations, which supply information on many quantities throughout the entire computational domain. However, – as in fact in the data evaluation of experiments – simplifying assumptions need to be made, potentially reducing the accuracy of the results.

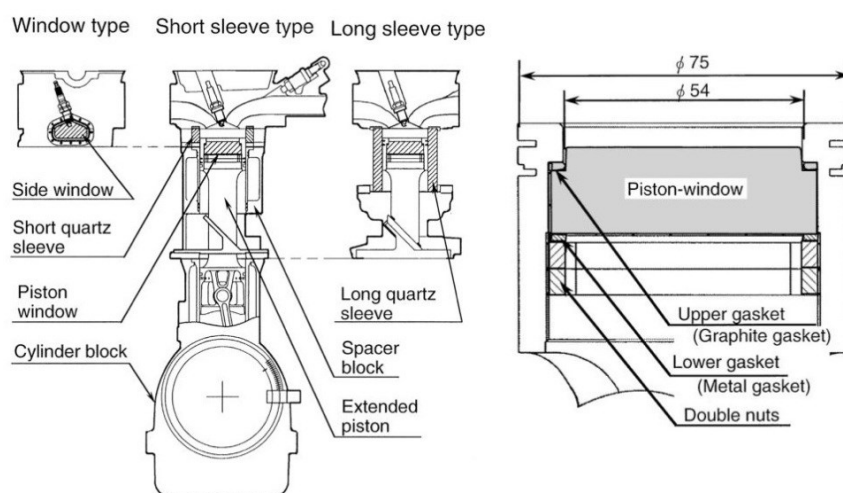


Figure 3-1: Left: Three different types of optically accessible engines; Right: Sectional view of a piston crown with window. From [59].

The evolution of optically accessible research engines is summarized by Miles in [60]. Different layouts of optical engines were developed over the recent years to investigate heat and mass transfer. Kashdan et al. [61] compared the engine performance of an all-metal single-cylinder engine with the performance of a similar-sized engine including large optical access. Various methods to realize optical access to the combustion chamber of engines are discussed by Sasaki et al. [59]. They distinguish three different designs known as window type, short sleeve type and long sleeve type, as shown in Figure 3-1. The three engine types are differing in maximum allowable operation speed, optical accessibility, and peak cylinder pressure. For sleeve type optical engines, optical access is given through the cylinder liner and a piston window. The latter requires an extended piston arrangement as shown in Figure 3-2, known as Bowditch piston assembly [62]. The bottom piston is running in the crank-shaft housing with standard piston rings for all-metal engines and oil. The surface of that piston is connected to the top-piston by a slotted extension. The top-piston keeps a window in the crown. Usually, piston rings made from graphite, Teflon or other synthetic materials without lubrication are used. Fluids for lubrication would influence the optical measurements. A stationary mirror placed into the slot of the piston extension provides optical access to the combustion chamber through the piston window. Designs with a flat piston surfaces allow best access with a camera or laser beam. However, designs with a curved piston-top surface, e.g. for wall-guided injection, complicate the optical access because of strong light refraction and image distortion.

The windows are usually made from fused silica (quartz), but for plane surfaces also sapphire is a common material. Sapphire is harder than fused silica and the heat conductivity is very similar to that of steel. The downside of sapphire is its limited transmittance in the UV.

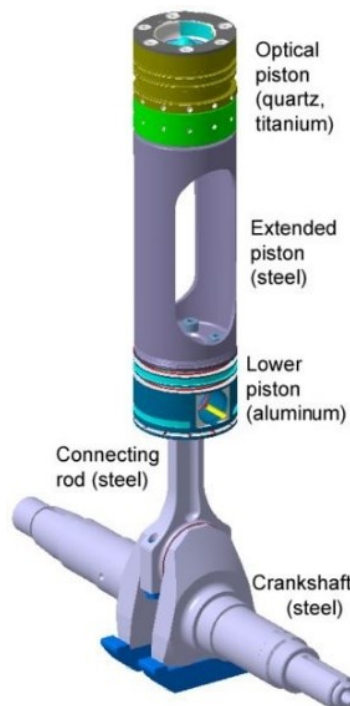


Figure 3-2: Schematic with main components of an optical extended piston assembly from [61].

3.2 Liquid-fuel visualization

3.2.1 Engine Combustion Network

In order to comprehensively investigate GDI and Diesel injection, the *Engine Combustion Network* (ECN) studies the spray from standardized injectors accompanied with well-defined geometries and ambient target conditions [63]. The ECN is an international collaboration of experimental and computational researchers in the field of spray combustion in engines. The experimental results from the ECN serve for model validation of e.g. CFD simulations and the advancement of scientific insights. Results and recent developments are discussed and shared in regularly organized web meetings as well as face-to-face annual meetings. The collaborating institutions utilize standardized injectors from *Delphi Technologies* for GDI, called “Spray G”, and Diesel injectors from *Bosch GmbH*, called “Spray A – D”, operated at engine-relevant target conditions in well-documented experiments. The most well-investigated processes are spray penetration, evaporation, and combustion. Ambient conditions that should be achieved at start of injection are pre-defined. These ambient conditions vary in bulk temperature, pressure, and density such that these represent flash boiling, strong spray collapse, early, late, and double injection in an internal combustion engine. However, Spray G was mainly investigated in spray chambers and not in internal combustion engines. Also, the standardized amount of fuel to inject is 10 mg per cycle, which may only be ignitable in fuel-stratified or throttled operation in an internal combustion engine. The Spray G injector used in the current work is shown in Figure 3-3a. On this particular injector the power connector was replaced by a flat wire to fit into the cylinder head of the optically accessible spark-ignition direct-injection (SIDI) engine at our engine. For CFD simulations, surface geometries as shown in Figure 3-3b are provided by the ECN.

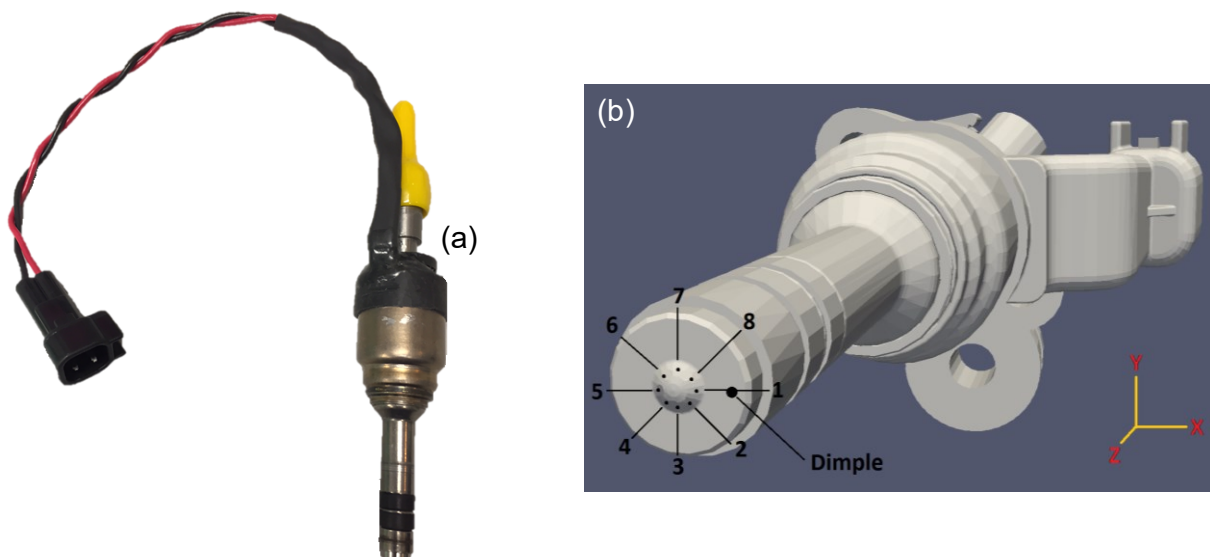


Figure 3-3: (a) modified Delphi injector used by the ECN for GDI called Spray G. (b) surface geometries of the injector showing the location and number convention of the 8 injector holes and the dimple. (b) from [63].

3.2.2 *Liquid-fuel penetration*

In recent years, engine development for passenger car applications has moved towards SIDI as described in Section 2.5. In the beginning of DI in SI engines, wall- and air-guided combustion systems were mainly used, in which the spray was directed towards a shaped piston providing a combustible mixture around the centrally located spark plug [64]. Spray-guided combustion systems have been developed having the potential to reduce particle emissions [65], since one of the most significant causes of such emissions is wall-wetting at the piston surface [66].

The injectors for spray-guided SIDI engines are custom-designed to provide the desired penetration, droplet size distribution, and air-fuel mixing, while avoiding wall-wetting. However, operating parameters such as the bulk-gas pressure and temperature during injection or the in-cylinder flow have strong influence on the spray characteristics. The injection timing, for example, is a critical parameter linked to the interplay between injector and engine operation. Oh and Bae [67] showed that misfire limits the temporal window of injection for stable engine operation using spray-guided stratified combustion. They also showed that a trade-off between efficiency and emissions can be observed, in which retarded injection timing increases the indicated mean effective pressure (IMEP) but also soot emissions.

Even though the spray atomization process is of importance in reducing wall-wetting and hence particulate mass emissions [68], the complex interaction of the fuel injection (injection pressure and injector characteristics) with the in-cylinder flow also needs to be considered, as shown by Stiehl et al. [69] for injection via hollow-cone injectors and by Piock et al. [70] for injection with multi-hole injectors. Fuel injection and mixture preparation have been investigated for fuel-stratified engine operation as summarized in a review article by Fansler et al. [71]. Optical diagnostics have especially been helpful for understanding the in-cylinder processes. Sprays have been visualized using high-speed Mie scatter imaging [72], spark emission spectroscopy can measure fuel concentrations near the spark plug [73], and LIF of a tracer can image fuel distributions [74]. Tracer-LIF, in combination with simultaneous PIV and flame imaging, have helped to understand misfires linked with strong local variations of the equivalence ratio at the spark plug [74]. Even though the average flow features were dominated by the effect of the spray momentum [74], using simultaneous spray visualizations and high-speed PIV, Stiehl et al. [69] showed that the in-cylinder tumble flow directly influences the formation of the spray. Sementa et al. [75] showed differences in the mixture formation for early and late injection strategies, but without decoupling the effects of in-cylinder flow and thermodynamic conditions during injection. Song and Park [76] linked the effect of strong air motion during the intake with spray atomization.

The interaction between spray plumes of multi-hole injectors is of great interest. For the same injector as used in this work (ECN Spray G), Gutierrez et al. [77] found that the interaction between spray plumes as shown in Figure 3-4 is stronger when injection is initiated during the intake stroke than it is in the nearly quiescent environment of a constant-volume chamber (CVC). With injection at 0.5 bar ambient pressure shown in Figure 3-4a flash boiling causes a strong interaction between spray plumes but when the fuel is injected at 1 bar in-cylinder pressure as shown in Figure 3-4b significantly less plume-to-plume interaction occurs.

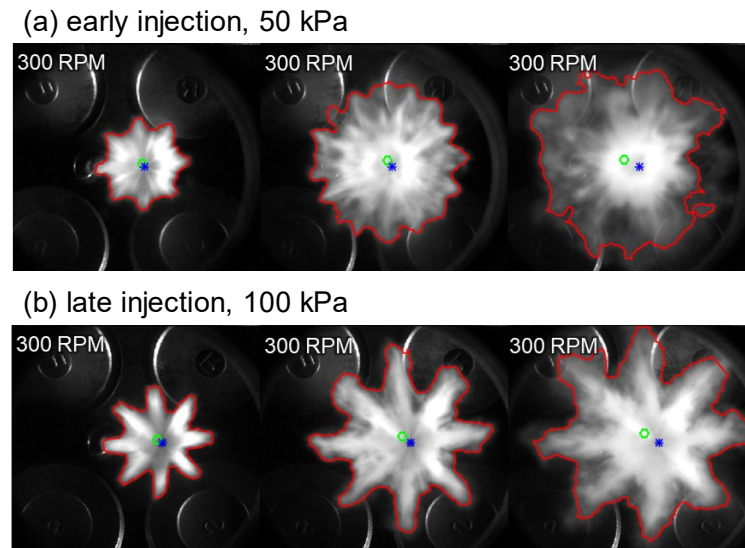


Figure 3-4: Mie scatter imaging through the piston window of the Spray G in an optically accessible engine at the University of Michigan. (a) shows an early injection with provoked flash boiling; (b) injection at 1 bar in-cylinder pressure. Figure from [77].

The spray may collapse not only at low in-cylinder pressures due to flash boiling, but also at increased ambient pressures [78], conditions which are present late during the compression stroke. Mie scattering and Schlieren imaging have been used to quantify the decrease of the angle between the plumes during the injection event indicating spray collapse. A detailed investigation of mixing based on LIF and Rayleigh scattering has shown that the plumes start to merge sooner after the start of injection (aSOI) for increased ambient densities [79]. This transient behavior of the individual plumes during spray collapse was confirmed by Sphicas et al. [80]. They performed time-resolved measurements of the spray-surrounding flow field using PIV and showed that ambient gas is entrained axially from the downstream regions of the spray as well as radially through the gap in-between the plumes. Once the neighboring plumes start to interact, this gap closes and the angle between the plumes quickly decreases until full spray collapse.

In terms of experimental studies, the ECN Spray G injector has been investigated at various research institutions, mainly in CVCs. Light scattering techniques have been used to study the topology of the liquid and vapor phases of the spray. Mie-scatter imaging [80-86] and light-extinction measurements, namely diffuse back-illumination [80, 81, 84, 87, 88], are the most common methods used for imaging the liquid spray, whereas schlieren imaging is used for the visualization of the vapor phase [80, 81, 83, 84, 86, 88]. For example, Hamzah et al. [81] compared the liquid spray penetration determined by DBI with spray penetration via bottom-illumination Mie scatter imaging of propane injected with the Spray G injector. In operating points with severe flash-boiling, they found that the spray penetration extracted from DBI was greater than from Mie scatter imaging due to beam-steering effects.

3.3 Gas-phase LIF imaging

LIF of a “tracer” added in small amounts to a non-fluorescing surrogate fuel has become the tool of choice to image many of the mass and heat-transfer phenomena in IC engines [3]. Most work pertains to liquid fuels with excitation by a pulsed UV laser where it is relatively straightforward to obtain sufficient LIF signal for qualitative visualization of the fuel. Image quantification is much more challenging, because fluorescence depends on pressure, temperature, and bath gas composition. In general, only pressure is known in the cylinder. To quantify e.g. fuel concentration, also the concentration of oxygen and the temperature needs to be known to solve the set of equations related to it, which increases the complexity of the experiment. The following subsections give a review on recent approaches, models, and approximations to quantify fuel components, air-fuel mixing, and temperature.

3.3.1 Imaging of fuel-components

In SIDI engines, fuel evaporation and mixing in the combustion chamber strongly affect ignition, combustion, and pollutant formation. Different volatility classes in the fuel may evaporate differently in the spatio-temporal evolution of the transient injection jet, which may cause mixture inhomogeneity, delayed evaporation, and wall wetting. The light components evaporate first, while heavier components evaporate later. Due to simultaneous convection, the low- and high-volatility components are thus spatially separated after evaporation. Since there is not a suitable optical diagnostic to quantitatively image this effect in internal combustion engines, experimental data are not available to check corresponding simulation models.

LIF imaging of a single-component fuel doped with a tracer has proven to be capable of imaging mixing phenomena in engines [3]. Binary mixtures of e.g. *iso*-octane and a ketone or an aromatic tracer may show preferential evaporation [89, 90], but in this case, preferential evaporation of the tracer is not intentional, but causes measurement errors, since no information on the second component is obtained.

From the pressure-based analysis of engine runs with a sweep in injection timing, Jung et al. [91] found that the engine output optimal mixture formation of *n*-butane is much shorter than that of a multi-component surrogate, which was associated with temporal deviations in mixture preparation of the light, medium, and heavy components in the mixture. A possible approach to optically study the evaporation of liquid multi-component fuels is to add a mixture of tracers of different volatility such that they together match the evaporation characteristics of the fuel [92, 93]. The aim then is to have a single LIF measurement that represents the overall fuel concentration in the gas phase. Alternatively, one could track two or more volatility classes separately. Figure 3-5 shows the mean equivalence ratio of different volatility components of a multi-component fuel from LIF in an optical engine by Ma et al. [92]. The distribution of each component is different most probably because of preferential evaporation. However, the signal from different tracers is differently influenced by temperature, which was not accounted for.

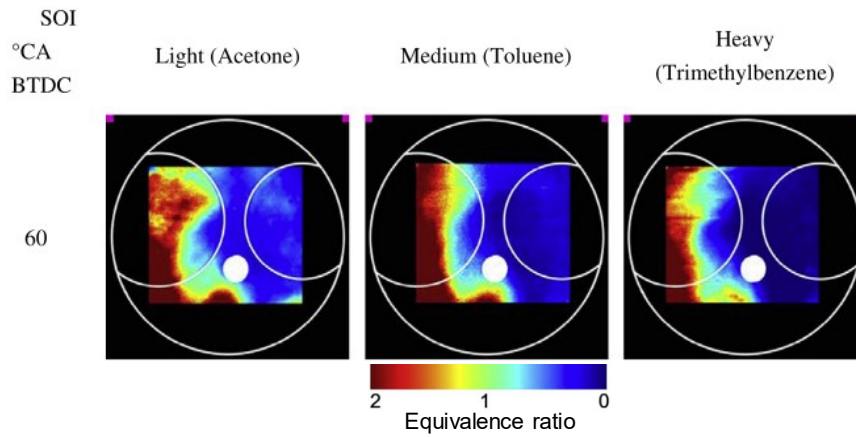


Figure 3-5: Ensemble mean images (view through piston) of the equivalence ratio (fuel component-to-N₂ ratio) of the light, medium, and heavy components of a surrogate of *n*-pentane, *iso*-octane, *n*-octane, *n*-nonane, and *n*-decane. Separate engine runs were carried out with one of the tracers added to the fuel. The GDI engine was motored on N₂. Figure from [92].

Recently, a two-tracer two-color LIF imaging technique was developed to simultaneously image the evaporation of light and heavy surrogate components [94, 95]. However, excited-state energy transfer between the ketones and aromatic species used as tracers was found to interfere with signal quantification [96]. Therefore, Itani et al. [97, 98] and Cordier et al. [99] introduced an LIF technique based on two aromatic tracers. These tracers were added to a transparent surrogate fuel with evaporation properties matching those of the targeted real gasoline fuel as shown in Figure 3-6. Measurements were performed in a high-temperature high-pressure cell. The fuel consisted of *n*-pentane, *iso*-octane (light to medium components), represented by 1,4-difluorobenzene (DFB) [100], and *n*-undecane (heavy component), represented by 1-methylnaphthalene (1MN) [101-103]. The fluorescence spectra of the two tracers are located in distinct wavelength regions, which makes it possible to spectrally separate their LIF.

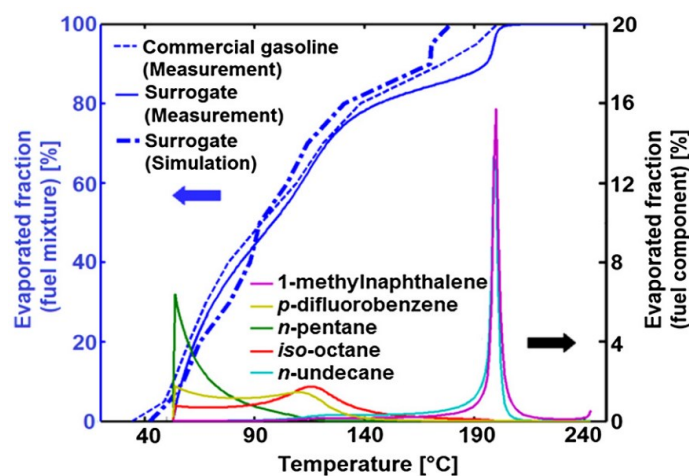


Figure 3-6: Evaporated components as function of temperature of commercial gasoline fuel, three-component surrogate, and fluorescent tracers measured and calculated at 1 bar. Figure from [98].

However, as for all tracers, the (unknown) local temperature influences the fluorescence signal discussed in Section 3.3.3. In fact, Itani et al. [97, 98] included simultaneous temperature imaging in their pressure-vessel study of preferential evaporation. But this increased the complexity of the resulting method and negatively influenced precision.

To relate the tracer-concentration ratio from the two-tracer two-color LIF method to local fuel-component concentration further assumptions are required. Bardi et al. [104] performed a vapor-liquid equilibrium calculation, modeling evaporation as a series of flashes based on the predictive Soave-Redlich-Kwong state equation of Holderbaum et al. [105] to yield the distilled fractions. With this, a conversion of the tracer-concentration ratio into “fuel space” is possible, and the two-tracer LIF technique could be used to investigate the influence of technological parameters, like injection and in-cylinder flow, on the fuel-component distributions resulting from preferential evaporation. Figure 3-7 shows an example of the fuel-mass fractions of the heavy and light components from [99] in a high-pressure high-temperature vessel by applying the model results in [104] onto the *tracer* LIF ratio. Near the injector tip a surplus of the low volatile components of the fuel and downstream of the fuel-vapor jets a surplus of the high volatile components are apparent. Addition of ethanol was found to increase the segregation of fuel-components.

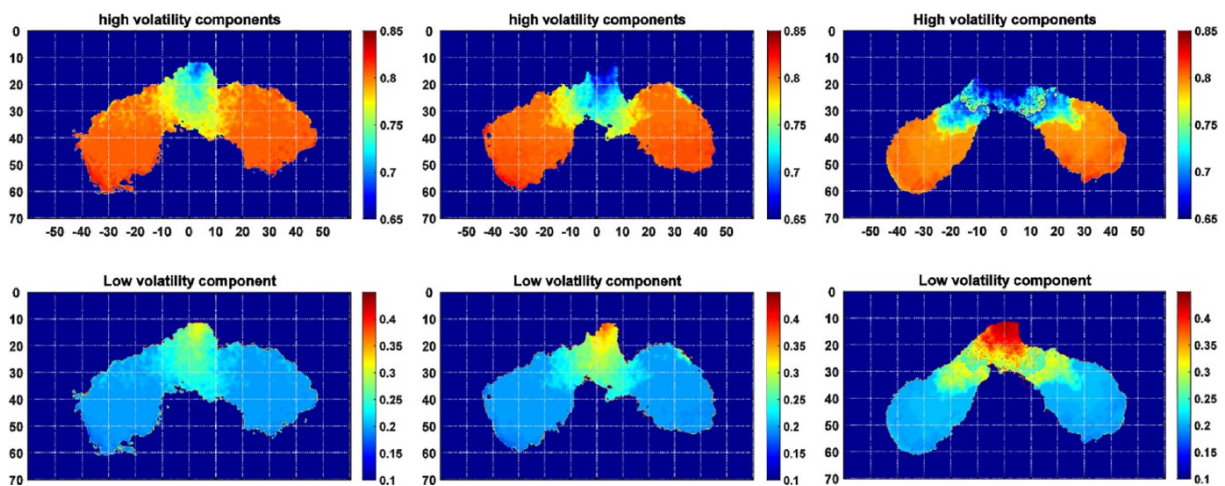


Figure 3-7: Fuel-mass fraction of the high (*n*-pentane, *iso*-octane) and low (*n*-undecane) volatile components of a multi-component fuel after injection into a spray cell at 573 K ambient temperature. In the middle and right column, 20% and 85% of ethanol was added to the fuel. Figure from [99].

3.3.2 Imaging of in-cylinder air-fuel mixing

The air-fuel mixing in SI engines needs to be designed such that a combustible mixture is created. Especially the mixture in the vicinity of the spark plug at the onset of spark influences the early flame kernel, and the air-fuel distribution in the end gas strongly influences further flame propagation. In most optical investigations the tool of choice is qualitative LIF-imaging of fuel tracers, but image quantification is much more challenging, because the fluorescence

depends on pressure, temperature, and bath-gas composition, i.e., concentration of oxygen. The effect of the latter two quantities on the LIF signal of toluene, anisole, naphthalene, and acetone is shown in Figure 3-8 from [106]. The LIF signal per volume is much lower in air than in N_2 , and that an increase in temperature generally strongly decreases the signal in N_2 . In air, the LIF signal is less sensitive to a change in temperature. Anisole has the highest potential to provide strong fluorescence signal also in air, which is, however, significantly influenced by a change in temperature in the absence of oxygen.

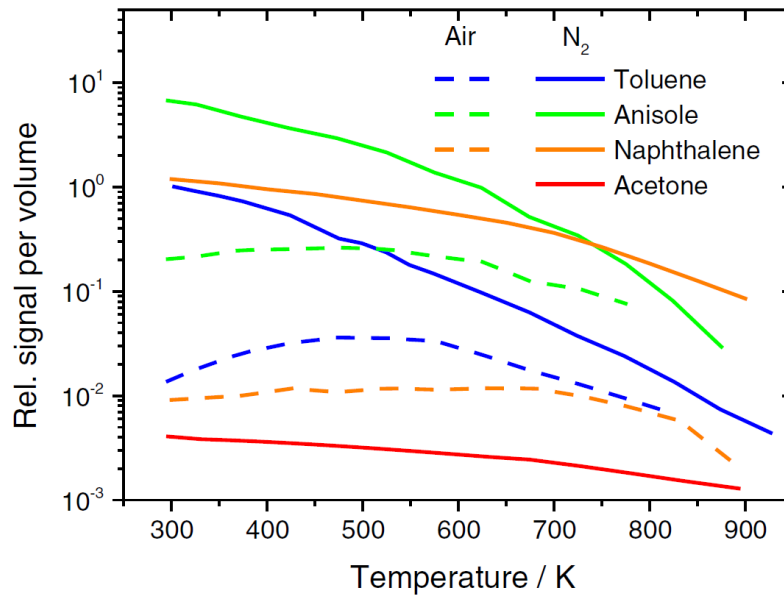


Figure 3-8: Normalized signal per volume of various tracers excited by 266 nm in 1 bar air and N_2 [106].

Less frequently, tracer LIF has been used with gaseous fuels in optical engines. A general challenge is that almost all fluorescent tracers are liquid at room temperature. Thus, at the elevated pressures upstream of the gas injector, only very low concentrations can be evaporated into the gaseous fuel, severely limiting the LIF signal strength. Nevertheless, qualitative visualizations of the fuel distribution in a methane-fueled engine were performed by Medaerts et al. [107] and Rubas et al. [108]. Quantitative LIF imaging of the fuel concentration in a motored hydrogen-fueled engine is documented in [109-111]. At 100 bar fuel pressure, the concentration of the highly volatile tracer acetone was only 0.25 vol.-%. These measurements were also compared to CFD simulations, showing that fuel dispersion was underpredicted by the simulation. Kirchweger et al. [112] used triethylamine (TEA) fluorescence to quantitatively determine the equivalence ratio via the FARLIF approximation as described in Section 2.8.2 in a hydrogen engine.

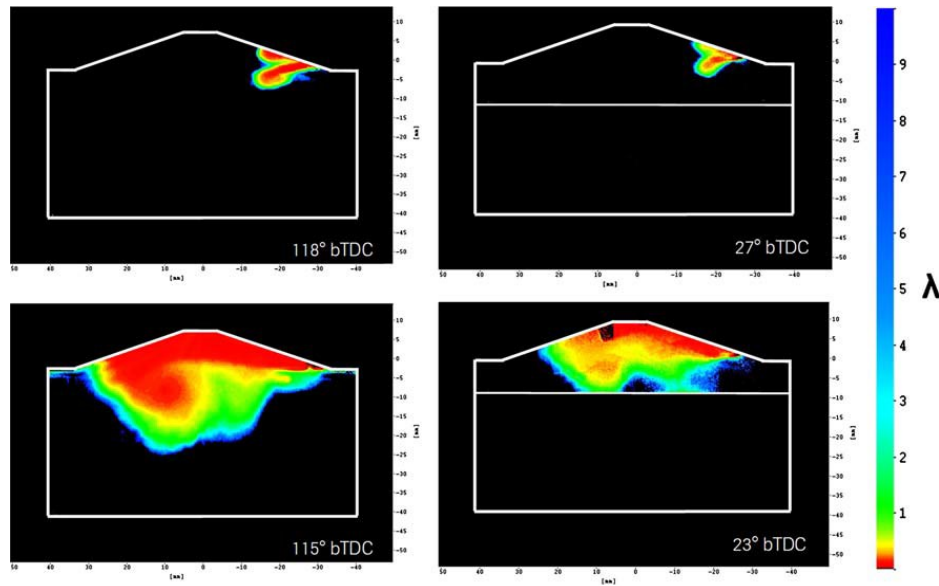


Figure 3-9: Air/fuel ratio imaged via TEA LIF in a hydrogen engine from [112].

Figure 3-9 shows an example of the quantified air/fuel ratio in a hydrogen engine with DI by Kirchweger et al. [112]. However, local temperature deviations between the measurement and the reference field could not be accounted for. More recently, Friedrich et al. analyzed the mixture formation in a CNG-DI engine by simultaneous imaging of TEA fluorescence and IR absorption [113] as well as TEA fluorescence and particle image velocimetry [114]. An example of the ensemble means from IR absorption and LIF imaging are shown in Figure 3-10. The efficacy of TEA for quantifying the equivalence ratio was presented, and IR absorption was used for qualitative visualization of the methane distribution due to line-of-sight imaging technique. However, local variations in temperature were also in [113] and [114] not accounted for.

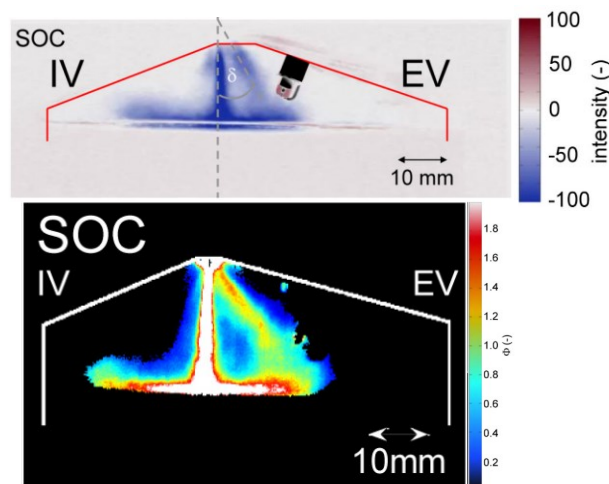


Figure 3-10: Top: Transmitted infrared intensity in line-of-sight imaging through the cylinder of an optically accessible SI engine with DI of methane. Bottom: Equivalence ratio from light-sheet TEA LIF. Images from [113].

In the past, various optical probes based on IR absorption have been used to determine quantitative information on fuel concentration, residual gas concentration, and temperature inside the cylinder of SI engines [115-118]. In the case of CNG-fueled engines accurate quantification can be difficult due to pressure and temperature changes over the cycle. The IR absorption spectrum of methane, the main component of CNG, consists of distinct spectral lines that are affected by pressure broadening and the temperature-dependent distribution of rotational states. Thus, narrowband detection methods are very sensitive to environmental influences. Non-dispersive infrared (NDIR) absorption spectroscopy is capable to quantify fuel density over a short absorption path in the combustion chamber. This method has been applied in gasoline engines using empirical models and requiring in situ calibration [116, 119]. Because of the structural simplicity of the methane molecule, quantification of NDIR absorption spectroscopy based on physical rather than empirical approaches is possible [120, 121].

For CFD simulations the prediction of mixing of two gas flows is challenging, especially in the context of industrial applications with the demand for short simulation times. Recent studies showed acceptable simulation results compared to optical measurements of methane injection by application of the numerical high-resolution method large-eddy simulation (LES). But the RANS approach has the potential for useful results while enabling shorter “wall time” [122-126]. Thus, the experimental LIF-imaging technique developed in this thesis will be compared to results from CFD simulating mixture formation in the engine at a moderate cost level with a commercial code.

3.3.3 *Imaging of temperature*

The accuracy in the quantification of the fuel concentration or the air/fuel ratio via LIF of tracers is negatively affected by deviations in temperature between the calibration and the actual measurement of interest. Therefore, it may be necessary to measure or model the local temperature and correct for its influence on the LIF signal.

Two-color LIF thermometry

In tracer LIF, often a change in the excitation or emission spectrum can be exploited to derive the absolute temperature by imaging in two distinct spectral regions (“two-color thermometry”) as described in Section 2.8.3. Examples of two-color thermometry exploiting a change in emission spectrum are summarized in Table 3-1. Other works use a two-wavelength technique as for example with 3-pentanone [127-129] or with acetone [130]. Figure 3-11 shows the temperature dependence of the fluorescence spectrum of anisole (methoxybenzene) in N₂ and air to address the temperature dependent change in emission spectrum [131].

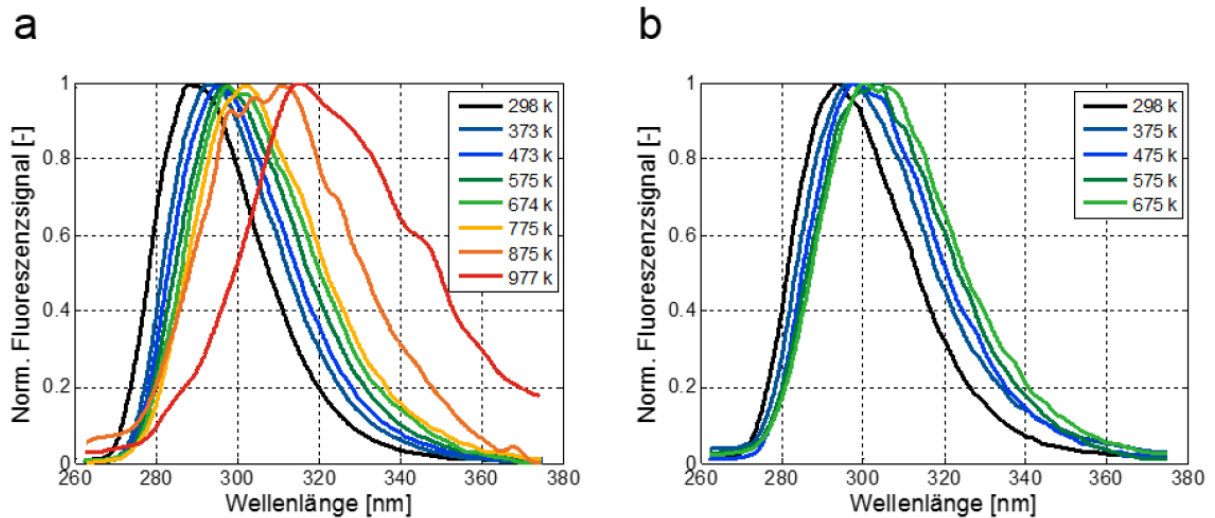
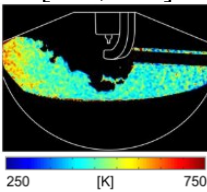
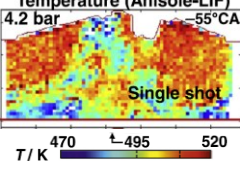
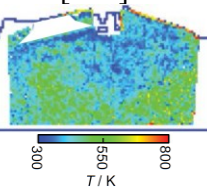
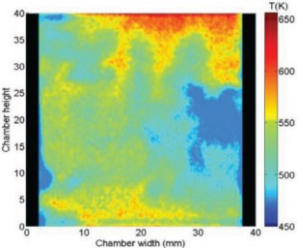
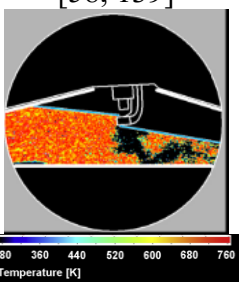
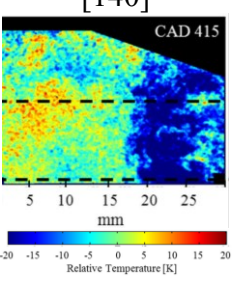
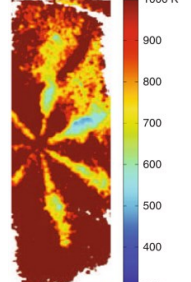
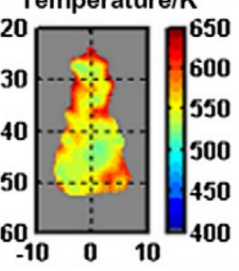
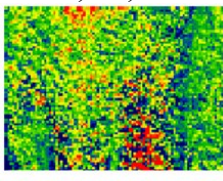
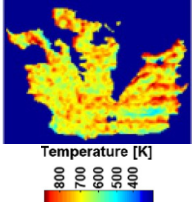
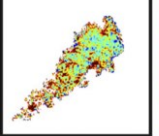


Figure 3-11: Peak-normalized fluorescence spectra of anisole excited at 266 nm at increasing temperature in N₂ (a) and in air (b). Data from Faust [131], figure from Goschütz [132].

Faust [131] reports on photophysical properties of a variety of tracers for practical combustion systems. I.e. he found that the fluorescence spectrum of anisole, excited at 266 nm shifts to longer wavelengths in N₂ and in air, as shown in Figure 3-11. The spectral shift of anisole in air is about 4 nm/100 K, for toluene 2 nm/100 K, for naphthalene 5 nm/100 K [131], and for 1-methylnaphthalene 3 nm/100 K [133]. As shown in Figure 3-8, the expected signal is strongest with anisole, which, in combination with the significant red-shift of the spectrum, is advantageous for the simultaneous measurement of temperature and species concentration. Additional information on photophysical properties of anisole are reported in [34, 35, 103, 134, 135], and it has been used previously for two-color thermometry in engines as summarized in Table 3-1 [53, 132, 136-138]. Shahbaz et al. [137] and Goschütz [132] demonstrated the efficacy of anisole for measuring the local temperature in an endoscopic engine with PFI operated on *iso*-octane. The LIF signal-to-noise ratio (SNR) with 2.5 vol.-% of anisole in the liquid fuel was better than the SNR of LIF from 20 vol.-% toluene in *iso*-octane measured in the same engine [58, 139]. Connected to this, Tran et al. [138] applied two-color LIF thermometry to the reactive flow of a mixture of *iso*-octane, anisole, and air mixture in a rapid-compression machine (RCM).

Table 3-1: Snapshots of temperature fields in engine-related experiments from two-color tracer LIF thermometry with excitation at one line, detection in two spectral regions (colors). * data published by Kranz et al. as part of this work. RCM: Rapid-compression machine; CVC: Constant-volume chamber.

Temperature imaging via two-color LIF thermometry (one-line excitation)		
	Optically accessible engines	Other applications
Anisole, 266 nm	<p>Gasoline PFI, air, 2.5 vol.-% [132, 137]</p>  <p>Gasoline DI, N₂, 0.4 vol.-%, [53]* Temperature (Anisole-LIF) 4.2 bar, 55°CA Single shot</p>  <p>CNG PFI, air, 0.07 vol.-%, [136]*</p> 	<p>Gasoline RCM, air, 1 vol.-%, [138]</p> 
Toluene	<p>Gasoline PFI, air, 266 nm, 20 vol.-% [58, 139]</p>  <p>Motored, air, seeded, 266 nm [140]</p>  <p>Diesel DI, air, 248 nm, 10 vol.-% [141]</p> 	<p>Diesel CVC, inert, 248 nm, 10 vol.-% [142]</p> 
Naphthalene, 266 nm	-	<p>Diesel burner, air, 5 vol.-% [102]</p> 
1-methylnaphthalene	-	<p>Gasoline CVC, 266 nm, 0.1 vol.-% [97, 98]</p>  <p>Diesel CVC, 266 nm, 0.5 vol.-% [101, 133]</p> 

Peterson et al. [140] compared single- with two-color thermometry in a motored engine with toluene seeded into intake flow. They found that single-color thermometry is better at detecting temperature gradients, since the precision in the corresponding temperature is higher

than that from the two-color method. However, they also show that the quantification of temperature by single-color thermometry is only valid in homogeneous operation since the tracer concentration and the temperature is inhomogeneous in engine operation with DI. Two-color LIF thermometry, however, is independent of the local tracer concentration. Toluene was also used in Diesel-fueled systems [141, 142]. Due to the relatively large spectral shift of the fluorescence by naphthalene and 1-methylnaphthalene with temperature, these tracers are also reasonable candidates for two-color thermometry, which was demonstrated on a burner by Kaiser et al. [102] (naphthalene) and in constant-volume chambers [97, 98, 101, 133] (1-methylnaphthalene). Since the latter two tracers are heavy in terms of molecular weight and volatility, they may be either used to dye Diesel-type surrogates or trace the heavy components of a gasoline-type surrogate. Compared to anisole, the fluorescence of naphthalene and 1-methylnaphthalene is quenched stronger by oxygen [106].

Adiabatic mixing model

Another method to determine the local temperature and fuel concentration from LIF imaging in the combustion chamber is to model adiabatic air-fuel mixing. Such models are based on theoretical relations between the quantities LIF signal, fuel concentration, and temperature. A flow diagram of the general procedure from Kokjohn et al. [143] is shown in Figure 3-12. In a first step, a homogeneous temperature distribution, e.g. the adiabatic core temperature, is considered to be valid throughout the combustion chamber. In a next step, the fuel mole-fraction is determined based on the actual intensity, a calibration intensity, and the temperature dependency of these quantities. In a third step, the temperature is calculated based on the fuel mole-fraction via energy conservation taking fluid properties and evaporative cooling into account. Then, the estimated temperature is compared with the temperature determined in step two. If the deviation is greater as a used-defined minimum deviation, the current mixing temperature is used to determine a new fuel mole-fraction and from this a new mixing temperature. The routine is executed iteratively. If eventually convergence has reached after some iteration, the mixing temperature, and the fuel mole-fraction is final output.

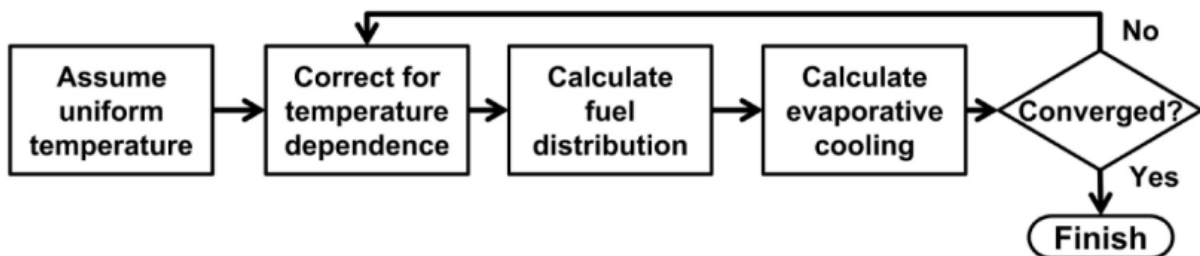
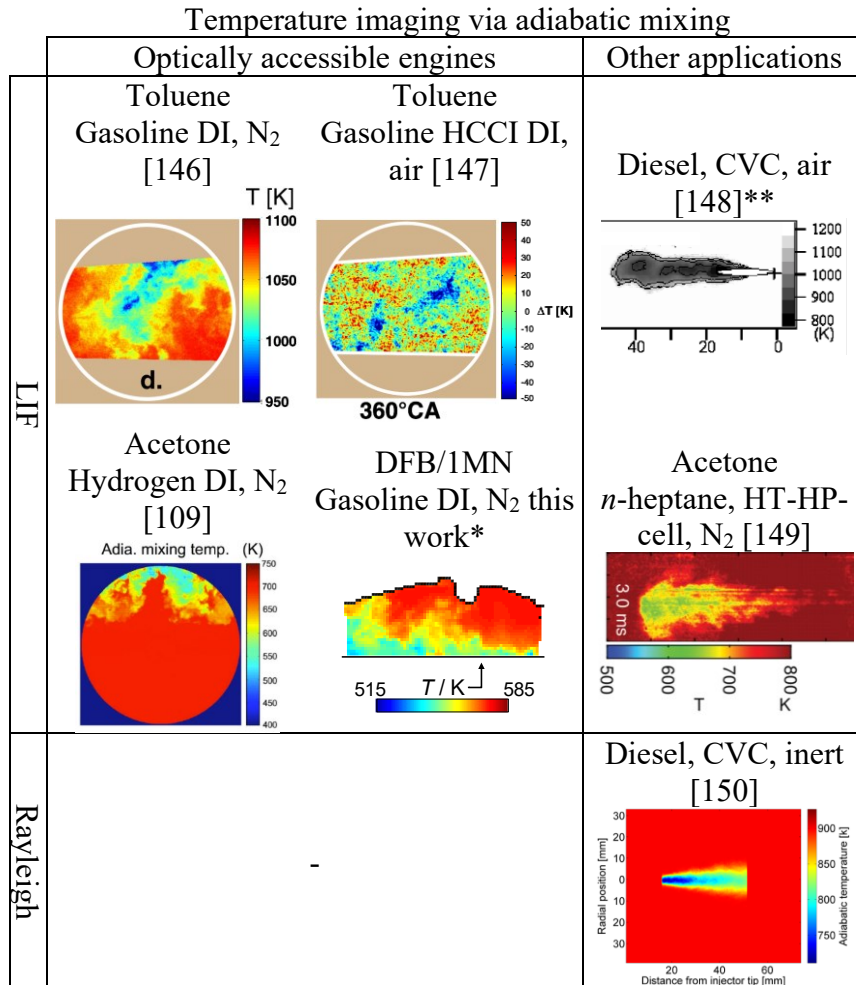


Figure 3-12: Schematic for iterative determination of the adiabatic mixing temperature and fuel concentration via tracer LIF as described by Kokjohn et al. [143].

The advantage with respect to two-color LIF thermometry is that the precision may be increased, since it is a single-color technique, where images are not divided by each other. The disadvantage is that the accuracy may be lower since heat transfer from surfaces is neglected by the adiabatic assumption.

Table 3-2: Snapshots of temperature fields in engine-related experiments from adiabatic mixing. Espey et al. [144], Kokjohn et al. [145], and Tea et al. [142] also report application of adiabatic mixing. * data from Kranz which will be discussed in this work. ** Exciplex LIF.



In previous works, the mixing temperature and fuel concentration was modeled from LIF or Rayleigh signals by assuming adiabatic mixing of the fuel with the bulk flow [109, 146-150]. Table 3-2 shows snapshots of temperature in engine related systems via adiabatic mixing. In adiabatic-mixing models the fuel concentration and temperature are auxiliary variables to solve the energy conservation. Espey et al. [144] showed that with adiabatic mixing can quantify temperature fields with reasonable accuracy and high precision when applied to Rayleigh signal from Diesel. Hwang et al. [146] applied adiabatic mixing on toluene LIF images of GDI in an engine motored on N₂, which was extended by Dec and Hwang [147] to homogeneous-charge compression ignition in the presence of oxygen. In Table 3-2 the decrease in precision due to oxygen quenching in [147] is obvious. Salazar et al. [109] estimated temperature and the

equivalence ratio from adiabatic mixing to gaseous fuels. They applied the model to the LIF signal from acetone vaporized into the hydrogen fuel that was then directly injected to the combustion chamber in the absence of oxygen. Even though only low concentrations of acetone could be vaporized to the gaseous fuel, the precision in the equivalence ratio and temperatures was high. Sahoo et al. [151] derived the equivalence ratio from an adiabatic mixing model applied to toluene seeded to a Diesel surrogate in a light-duty engine. Unfortunately, temperature fields were not shown here. Tea et al. [142] applied two-color LIF thermometry (see Figure 3-1) and adiabatic mixing by single-color LIF to toluene in a diesel spray and homogeneous mixture in a CVC. They found by comparing the mean temperature in a certain region from adiabatic mixing and two-color LIF, that the temperature from two-color LIF is overestimated with respect to the adiabatic temperature at reference temperature exceeding 700 K. However, a field-wide comparison of temperature from two-color LIF thermometry and adiabatic mixing was not carried out.

Even though the experimental technique is easy to implement, and high precision may be achieved compared to two-color LIF thermometry, the processing of the data takes long, and the assumptions in the model may only be valid for adiabatic systems. To address the first point, Manin et al. [150] created a look-up table for all temperature/fuel concentration/signal combinations that was then applied to the images by linear interpolation. This procedure significantly decreased the required time for processing of the data. To address the second point, far from surfaces in a non-reacting system the adiabatic assumption may be reasonably accurate. However, near surfaces the accuracy is expected to be significantly reduced.

This work will discuss the effect of assumptions in the adiabatic mixing model by comparing the temperature fields from adiabatic mixing to temperature fields acquired via two-color anisole LIF thermometry. Additionally, the effect of preferential evaporation will be accounted for in the adiabatic mixing model by utilizing the information on the low and heavy components of a multi-component mixture from LIF of DFB and 1MN, respectively.

Chapter 4 - Preferential evaporation of a multi-component gasoline surrogate in a direct-injection engine

This chapter is on the effect of fuel-component segregation of a multi-component gasoline surrogate due to preferential evaporation, investigated via LIF imaging. Parts of the content of this chapter have been published as Kranz et al. [52, 53], in particular Sections 4.4, 4.5.1, 4.5.3, 4.6.1 - 4.6.3, and as Geschwindner, Kranz, et al. [54], Sections 4.3.3, and 4.3.5. Sections 4.3.2, 4.5.2, 4.5.4, and 4.6.4 contain analysis beyond that already published work. The experiments were carried out in an optically accessible engine at the University of Duisburg-Essen. My contributions are described in more detail in Section 7.1.1.

4.1 Imaging strategy

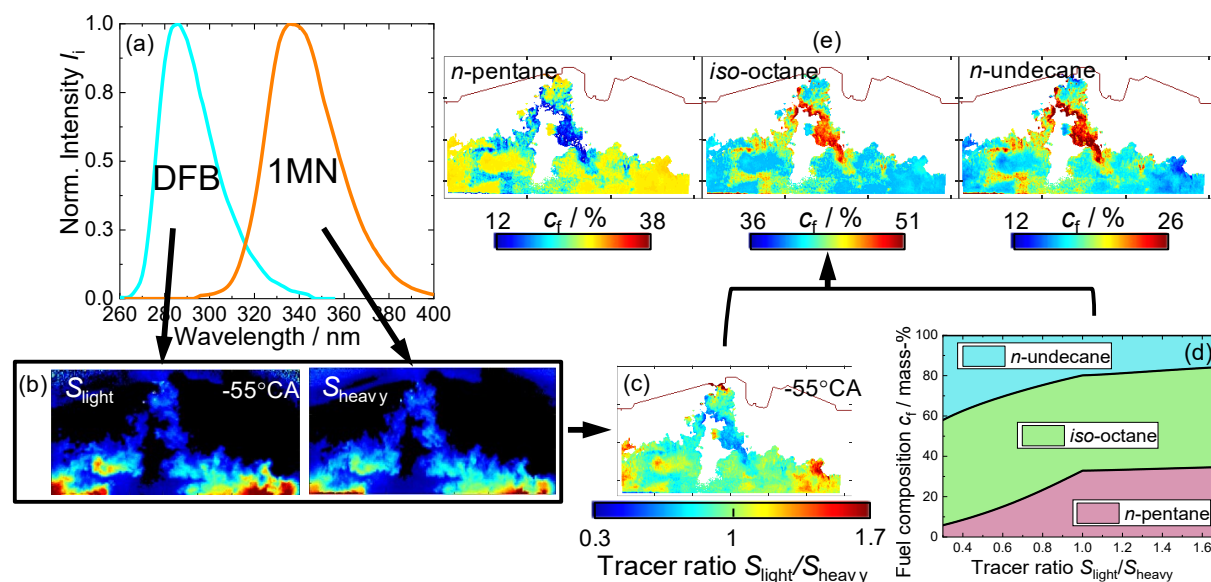


Figure 4-1: Schematic of the measurement strategy for quantifying the effect of preferential evaporation. (a) fluorescence spectra of 1MN and DFB at 525 K in 1 bar N_2 . (b) Images of the light and the heavy tracers' LIF at -55°CA , (c) tracer-concentration ratio, (d) connection between the tracer-concentration ratio and the fuel mass composition from [104]. (e) example images of the fuel mass fraction of each fuel component derived from (c) and (d).

An overview on the LIF imaging strategy to investigate the effect of preferential evaporation is shown in Figure 4-1. The technique is applied to the gas phase after the fuel has evaporated. First (a), a set of two complementary tracers is chosen representing the evaporation of the low and high volatility components in the three-component gasoline surrogate, respectively. The tracers fluoresce in distinct spectral regions making it possible to separate their fluorescence by a suitable filter combination. Second (b), the two LIF images of the fuel vapor are normalized with images taken at homogeneous and known tracer concentration. Then (c), the snapshots of the fuel-vapor are divided by each other to yield the tracer-concentration

ratio $S_{\text{light}}/S_{\text{heavy}}$ (c). Here, ratios greater than 1.0 indicate a surplus of the high-volatility components, and ratios below 1.0 indicate a surplus of the low-volatility components compared to the originally injected mixture. In a last step (d), a look-up table from a thermodynamic calculation modelling component evaporation is used to translate the tracer-concentration ratio (c) to the actual fuel composition as shown in Figure 4-1e.

The overview illustrated in Figure 4-1 does not show every processing step and influence in detail. The accuracy and precision of the technique is also affected by tracer fluorescence crosstalk and deviations in the local temperature, which will be further addressed in the following sections.

4.2 Test bench

4.2.1 Engine, injector, and periphery

The measurements are performed in an optically accessible single-cylinder engine with high-pressure injection of a gasoline surrogate directly into the combustion chamber. Operating parameters and a sketch of the combustion chamber are shown in Figure 4-2. The engine is fed N_2 via a mass-flow controller. The flow is adjusted such that a constant intake pressure of 1.1 bar is achieved. Additionally, the temperatures of coolant, fuel, and intake are adjusted to $80^\circ\text{C} \pm 3^\circ\text{C}$. The engine is equipped with a BMW Valvetronic that allows adjusting the engine's intake-valve lift (IVL). The maximum IVL is 9.7 mm, the exhaust-valve lift is fixed to 3.5 mm.

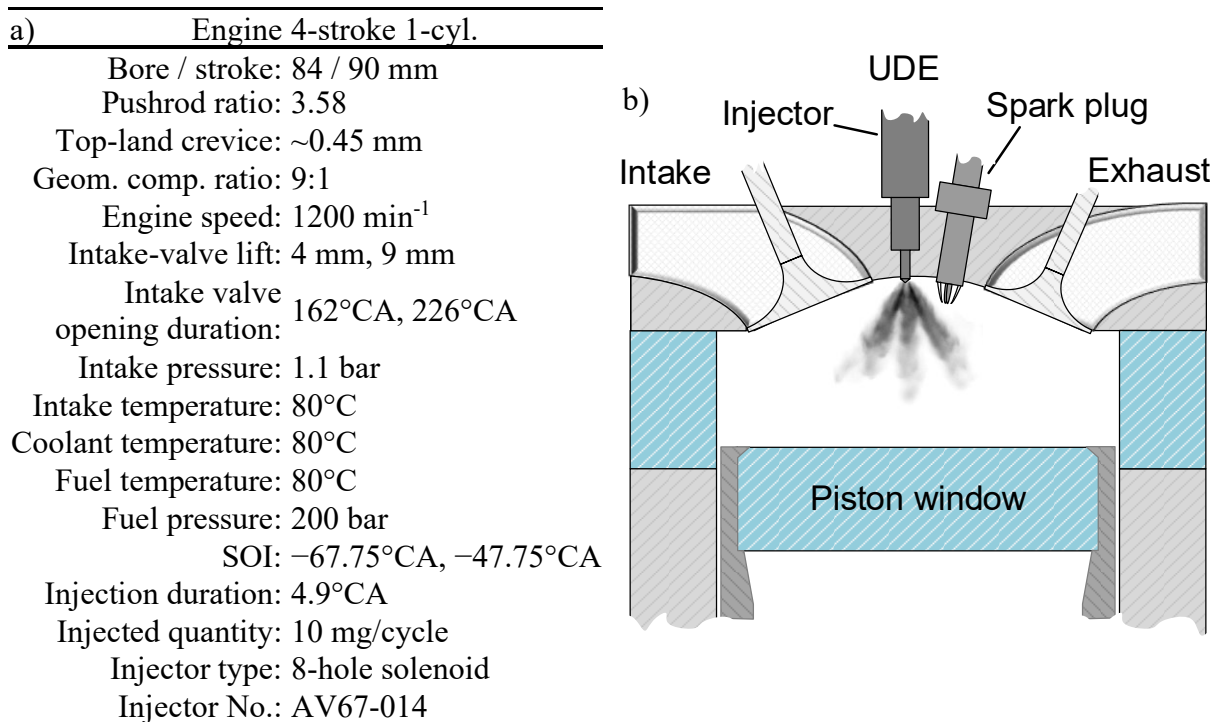


Figure 4-2: (a) Engine and operating properties, (b) sketch of the combustion chamber.

The engine has optical access to the top 28 mm of the stroke plus the pent-roof combustion chamber through a transparent fused-silica cylinder liner as shown in Figure 4-2b. The flat-topped piston is in the FOV after -60°CA . It provides optical access to the combustion chamber through a quartz window of 73 mm in diameter. If the light sheet enters through the piston window, the area near the cylinder liner cannot be illuminated. In all images, the intake valves are located left, and the exhaust valves are located right of the injector nozzle as shown in the schematic in Figure 4-2b.

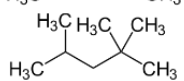
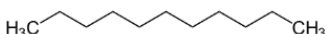
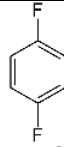
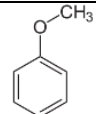
Two injectors are used within one LIF-imaging engine run. A solenoid-activated 8-hole injector (Spray G of the ECN [63]) is used for central DI as shown in the schematic in Figure 4-2b. The ECN provides a standard injection condition approximately reached here when injecting at -47.75°CA with late fuel injection. An earlier injection at -67.75°CA with decreased liquid wall impingement on the piston was also investigated. In addition to DI, a hollow-cone injector can be used to inject fuel at 200 bar about 50 cm upstream of the intake pipe just behind the intake flow heater into a small plenum volume to create a homogeneous mixture for calibrations. Further details on the engine and peripherals can be found in [52, 53, 152, 153].

4.2.2 *Surrogate fuel*

Commercial gasoline-type fuel consists of hundreds of components with different properties, also in terms of fluorescence, which makes it difficult to use for quantitative LIF measurements. Therefore, the preferential evaporation of a three-component surrogate shown in Table 4-1 with evaporation characteristics similar to commercial gasoline-type fuel [97, 98] is studied. The components have very different evaporation characteristics, indicated by their boiling points in Table 4-1. In this work the three-component mixture is referred to as “multi-component surrogate”.

Following Itani et al. [98], the multi-component surrogate has three non-fluorescing components, as shown in Table 4-1, *n*-pentane, the high-volatile component, *iso*-octane (2,2,4-trimethylpentane), the medium-volatile component, and *n*-undecane, the low-volatile component. Additionally, the spray penetration of pure *iso*-octane will be also discussed in this work. For LIF imaging of preferential evaporation, 1,4-difluorobenzene (DFB) and 1-methylnaphthalene (1MN) are added to the surrogate fuel. Alternatively, 1MN and DFB are replaced by anisole (methoxybenzene, ANI) in the multi-component surrogate for temperature imaging via two-color LIF thermometry.

Table 4-1. Fuel surrogate and tracers. ϕ is the liquid volume fraction and BPt the boiling point at 1 bar.

	Component	Structure	Formula	Molar mass / g/mol	BPt / °C	ϕ / vol.-%
Surrogate	<i>n</i> -pentane		C ₅ H ₁₂	72.15	36	36
	<i>iso</i> -octane		C ₈ H ₁₈	114.23	99	46
	<i>n</i> -undecane		C ₁₁ H ₂₄	156.31	196	18
Tracers	DFB		C ₆ H ₄ F ₂	114.09	88	0.02
	1MN		C ₁₁ H ₁₀	142.20	245	0.1
	Anisole		C ₇ H ₈ O	108.14	154	0.4

4.3 In-cylinder velocity and spray morphology

Parts of the content of Section 4.3 have been published by Geschwindner, Kranz et al. [54] in which the spray-flow interactions of Spray G in the optical engines at Technische Universität Darmstadt, TUD and UDE have been compared. This work will focus on the comparison of DBI and Mie scatter imaging, investigations of the spray penetration of the multi- and single-component (*iso*-octane) surrogates, and the influence of in-cylinder flow on the spray.

4.3.1 Gas-velocity imaging

Optical arrangement

As discussed in Section 2.10, PIV is a well-known technique to measure instantaneous velocity fields in engines and other applications [47]. Here, PIV is applied to the bulk flow in motored engine operation and also with DI of *iso*-octane as in Figure 4-2a. Figure 4-3 shows a schematic of the optical arrangement and Table 4-2 summarizes the processing steps.

The beam of a double-pulsed Nd:YAG laser (Litron), frequency doubled to 532 nm, is guided through a combination of a telescope and a negative cylindrical lens to form a divergent light sheet. As shown in Figure 4-3c, the inter-pulse delay Δt is adjusted for each crank angle range and light sheet location to achieve an appropriate particle shift and to minimize out-of-plane losses. The delay Δt is increasing from 2 μ s to 20 μ s towards TDC. Through shifting of the first mirror and light-sheet optics, the position of the light sheet can be easily changed. Then, the light sheet is reflected by a 90°-mirror vertically through the Bowditch piston assembly and the fused-silica piston window. The 1.5-mm thick light sheet is placed either onto the cylinder-center axis $z = 0$ mm or onto one of the valve-center axes at $z = 21$ mm or $z = -21$ mm.

Synthetic silicone oil droplets (Dow Corning) of $\sim 0.5 \mu\text{m}$ diameter are introduced upstream of the intake pipe of the engine scattering the light through the transparent cylinder liner made from fused silica. A polarizing filter is mounted to the lens to suppress some of the light scattered by in-cylinder surfaces. An additional 532 nm bandpass filter is mounted to the camera lens (Nikon $f = 50 \text{ mm } f/5.6 + 52\text{-mm}$ close-up lens) to suppress the room light. The light then passes through the camera lens and is detected on the sensor (PCO Edge 5.5 sCMOS).

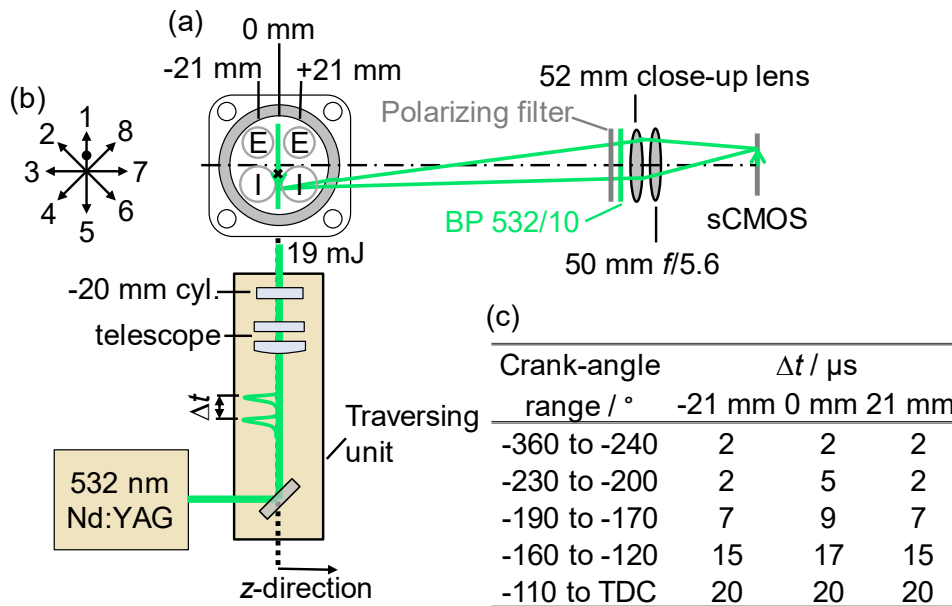


Figure 4-3: (a) Optical arrangement for flow-field measurements via PIV. The three studied imaging planes in z-direction are denoted. (b) injector plume orientation with respect to the camera. The black dot in (b) represents the orientation of the injector dimple, which points towards the spark plug. (c) summary of the inter-pulse delay Δt for each investigated crank angle range and light-sheet position.

Crank-angle synchronized PIV is performed at 10 Hz in two different experiments (A.PIV) and (B.PIV). In experiment (A.PIV), the flow velocity of 75 cycles in motored operation in the cylinder center axis and both valve axes without injection is measured. Vector fields from the intake valves opening at -360°CA through -70°CA in 10°CA -steps are acquired. Between -65°CA and TDC, the time steps are refined to 5°CA . Data later than -25°CA are discarded, because the detected Mie scatter from PIV seeding is on the order of the background signal. Experiment (B.PIV) is performed with injection of pure *iso*-octane at 4 mm IVL. 100 crank-angle synchronized double-frame images at -40°CA , -35°CA , and -30°CA for -47.75°CA SOI and -60°CA to -30°CA in 5°CA -steps for -67.75°CA SOI in the cylinder center axis and at $z = +21 \text{ mm}$ are recorded.

PIV data post-processing

DaVis 8.4 (LaVision) is used to compute the vector fields via a PIV algorithm. First, a background correction is executed according to the methods summarized in Table 4-2. Afterwards, a geometric mask is applied to each image removing the combustion-chamber contours, piston, and strong reflections in the FOV. Then an algorithmic masking is applied, based on the calculation of the local standard deviation over 9 pixels and subsequent thresholding, to mask regions full of fuel droplets. The scattering of the fuel droplets in experiment (B.PIV) cannot be used to compute vectors, since the inter-pulse delay Δt is not adjusted for the high velocities in the spray and the fuel-droplet density is too high. Thus, only the velocity of the bulk gas is represented with the flow fields via PIV.

Table 4-2: Equipment and processing properties used for the PIV experiments.

Processing	Exp. (A.PIV)	Exp. (B.PIV)
Background correction	Sliding high pass (Butterworth) of 9 images	Sliding minimum of 9 images
Vector calculation	Passes 1 and 2: 64 × 64 px with 50% overlap Passes 3 and 4: 32 × 32 px with 50% overlap	Passes 1 and 2: 64 × 64 px with 50% overlap Passes 3 and 4: 32 × 32 px with 75% overlap
Spatial resolution	1.1 mm window size 550 μm vector spacing	1.1 mm window size 275 μm vector spacing

The vector calculations use a multi-pass cross-correlation with decreasing window size as shown in Table 4-2. Vectors with a correlation ratio of the first and second peak less than 1.3 are neglected and a universal-outliner detection (normalized median test) in a window size of 7×7 vectors is applied. Doing so removes “bad”, i.e. unrealistic vectors. Further processing of the computed vectors is carried out without any smoothing. The ensemble average at each crank angle is calculated, rejecting positions with less than 25 valid vectors. In that way, the ensemble average is not biased by a low number of vectors in some regions, especially in the spray.

4.3.2 Spray visualization via diffuse back-illumination and Mie scattering

Optical arrangement

Diffuse back-illumination (DBI) and Mie-scatter imaging have become two of the standard diagnostics of the ECN for liquid-spray visualization [87, 88, 154]. In this work, simultaneous side and bottom illumination as well as DBI for visualization of the liquid spray is carried out by color-coding the illumination and detection.

A schematic of the optical arrangement is shown in Figure 4-5a. It follows the approach of Menser et al. [24]. Six 4-die color LEDs, each with broadband emission at around 600 nm

(red, R), 530 nm (green, G), and 460 nm (blue, B) are used for volumetric illumination of the liquid spray. Individually gated and delayed electronic drivers provide power to each LED die. The duration of each gate is adjusted to achieve approximately the same pulse intensities.

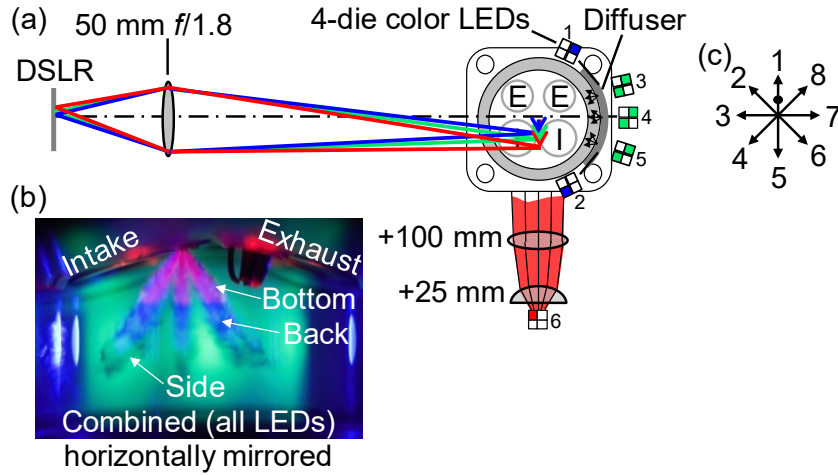


Figure 4-4: (a) Optical arrangement for simultaneous side (blue dies of LEDs 1 and 2), back (green dies of LEDs 3 - 5), and bottom (red die of LED 6) illumination in experiment (A.RGB). The angle of incidence between illumination of LED No. 1 or 2 and the optical axis is 120° . Horizontal mirrored raw image in (b). (c) shows the injector plume orientation with respect to the camera. The black dot in (c) represents the injector dimple that points towards the spark plug.

As labeled in Figure 4-4a, LEDs No. 1 and 2 are used for side illumination at 120° angle of incidence (AOI), LEDs No. 3 – 5 are used for DBI, and LED No. 6 is used to illuminate from the bottom through the piston window in the Bowditch extension. In the case of DBI, a quarter section of a sand-blasted Plexiglas cylinder (diffuser) is placed between LEDs No. 3 – 5 and the fused-silica engine cylinder to achieve a more homogeneous back illumination. For bottom illumination the light of LED No. 6 is guided through a combination of an aspheric lens with $f = 25$ mm and a spherical lens with $f = 100$ mm to condense the light that is then reflected by the mirror in the Bowditch piston assembly through the piston window into the combustion chamber. The light from each LED is then scattered by the liquid spray. This signal is detected through the transparent liner by a commercial color DSLR camera (Nikon D5300) with a $f = 50$ mm, $f/1.8$ lens (Nikon). Since the camera has large jitter in the delay between the start of the trigger and the actual exposure, the image acquisition is initiated at -360°CA with an exposure time of 100 ms (equal to one whole cycle at 1200 min^{-1} , the room light is off). The camera is operated at 2 Hz, i.e., every fifth engine cycle. Between 10 and 47 color images with and without injection are taken phase-locked to a particular crank angle. Each color image includes information from a burst of three corresponding LED die pulses.

Two different experiments were carried out. In experiment (A.RGB) shown in Figure 4-4, simultaneous spray visualization via bottom, side, and diffuse back-illumination by color-coding of the illumination strategies was executed. The red die color-codes bottom (LED No. 6), three green dies code back (LEDs No. 3 – 5), and two blue dies color-code side illumination

(LEDs No. 1 and 2). An example of an RGB raw image is shown in Figure 4-4b, where illumination was initiated at different timings aSOI. However, in the actual experiment (A.RGB) all six illuminations were activated simultaneously ($t_1 = t_2 = t_3$) to compare the spray penetration detected from all three strategies. In experiment (B.RGB) the LEDs are used to color-code the temporal evolution of the spray with one out of the three illumination strategies as shown in Figure 4-5b. Inter-pulse delays of $\Delta t = 138.9 \mu\text{s} \cong 1^\circ\text{CA}$ between red and green, and of $2 \times \Delta t = 277.8 \mu\text{s} \cong 2^\circ\text{CA}$ between red and blue illumination were used. This resulted in a 3-image sequence of 7200 frames per second in each observed engine cycle. The start of illumination was scanned from SOI until $833 \mu\text{s}$ aSOI and was initiated by a master trigger of the engine's timing unit. In all cases background images without fuel injection but illumination turned on, and dark images (injection off, illumination off) were acquired.

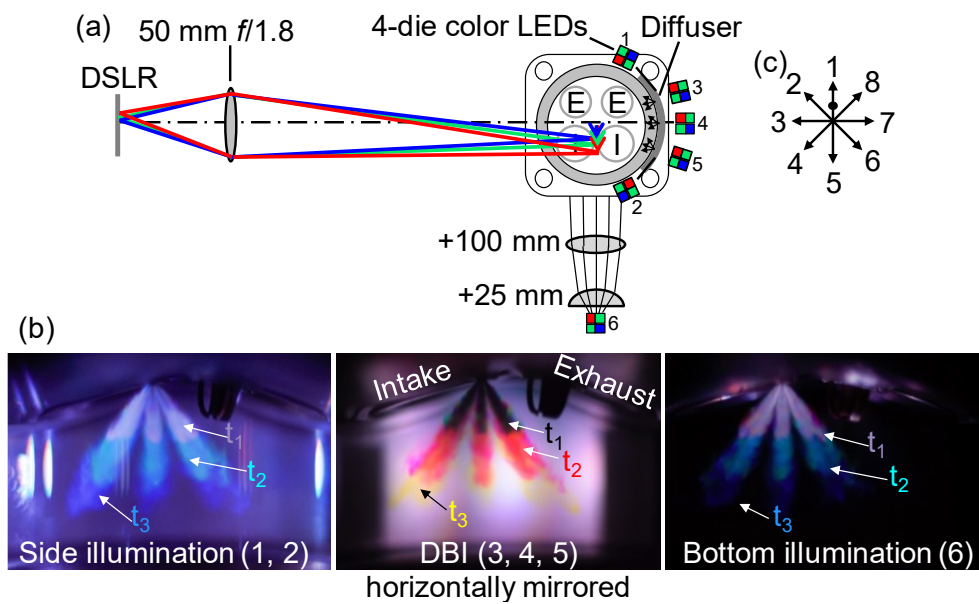


Figure 4-5: (a) Optical arrangement for temporal liquid spray visualization in experiment (B.RGB). The angle of incidence between illumination of LED No. 1 or 2 and the optical axis is 120° . Horizontal mirrored raw color images in (b) including LED numbering. Red illumination is initiated at time t_1 , green at $t_1 + 138.9 \mu\text{s} = t_2$, and blue at $t_2 + 138.9 \mu\text{s} = t_3$. (c) Shows the injector plume orientation with respect to the camera including the location of the dimple represented by the black dot.

Image pre-processing

As shown in Figure 4-5b, in a first step the raw images are horizontally mirrored to be consistent with other experiments in this work. Plume 1 is pointing to the exhaust side and plumes 3 and 7 are in the center. Then, the overlapping transmittances between channels of the color filter array on the Bayer sensor are de-mixed [24], de-mosaiced, and three instantaneous images $I^{(R)}$, $I^{(G)}$, and $I^{(B)}$ corresponding to time steps t_1 to t_3 are extracted from the three-channel color image. The images are dewarped and translated into real-world coordinates using a target calibration plate. All reflective engine features including the cylinder head, intake valves and

the piston are masked out to guarantee that the remaining intensity is generated by Mie scattering of the injected spray. Finally, the images are binned 4×4 , i.e. the values of 16 pixels are averaged to form one super pixel, increasing the projected pixel size to $57.5 \mu\text{m}$. From here on, images with injection are denoted as I , and images without injection (background images) as I_0 .

DBI data processing

Images from DBI are first corrected by subtracting a mean dark image. Then, analogously to Manin et al. [84], the Beer-Lambert's law for light extinction

$$\frac{I}{I_0} = e^{-\tau} \quad (4-1)$$

is applied to each image. The pixel-wise division of the measurement I by the background (baseline) I_0 corrects for inhomogeneities in the illumination and detection path. Then the optical thickness τ is related to the integrated liquid volume fraction $\int_{-y_\infty}^{y_\infty} LVF \, dy$ as

$$\tau = \int_{-y_\infty}^{y_\infty} C_{\text{ext},i}^* \frac{LVF}{\pi d^3/6} \, dy \Leftrightarrow \int_{-y_\infty}^{y_\infty} LVF \, dy = \tau \frac{\pi d^3/6}{C_{\text{ext},i}^*}. \quad (4-2)$$

A droplet diameter d of $7 \mu\text{m}$ is assumed for the calculations based on measurements of the Sauter mean diameter by Parrish et al. for the same injection parameters [63]. The effective extinction cross-section $C_{\text{ext},i}^*$ is then calculated for the three center wavelengths of the color LEDs based on Mie theory as implemented in *MiePlot* [155] for an *iso*-octane droplet of size d . Here, * denotes a finite collection angle of 350 mrad determined from the optical arrangement. Extinction cross-sections are estimated to be $C_{\text{ext},460 \text{ nm}}^* = 41.7 \cdot 10^{-6} \text{ mm}^2$, $C_{\text{ext},530 \text{ nm}}^* = 43.2 \cdot 10^{-6} \text{ mm}^2$, and $C_{\text{ext},600 \text{ nm}}^* = 44.4 \cdot 10^{-6} \text{ mm}^2$ for each emission center wavelength. Spray contours are determined by segmenting the images according to Payri et al. [88] with a threshold of $0.2 \cdot 10^{-3} \text{ mm}^3/\text{mm}^2$. Binarization fills the area enveloped by the spray contour with ones and outside the contour with zeros. An example of the spray contour is overlaid onto the integrated LVF in Figure 4-6a.

Mie-scatter data processing

The images I from Mie scattering are corrected by subtracting a mean background I_0 obtained without injection. Following the general idea of Siebers [156], the segmentation threshold is taken as the intensity at the position of the steepest negative gradient in the vertical direction of each frame. To this end, a line of 1 mm width (17 pixels) through the injector tip in the axial direction is extracted in each frame. Image noise is estimated as three-standard deviations calculated in a region of $5 \times 5 \text{ mm}$ of a background-corrected snapshot without injection. Pixels with intensities below 3σ are rejected in the line plot. The data is averaged in the y -direction (parallel to the piston surface) and the derivative in the x -direction (perpendicular to the piston surface) is calculated. Then, the intensity at the position of the

steepest gradient in the axial direction is extracted for each frame. The threshold intensities (between 2.5% and 10% of the maximum spray intensity) are used to binarize the spray in each image. Finally, 6-pixel erosion followed by 6-pixel dilation is applied to each binarization, and spurious areas of the foreground smaller than 17 mm² are deleted. An example of the contour of the spray is shown in Figure 4-6b.

Extraction of geometrical parameters

Geometric parameters of the spray are extracted from the binary images generated with the processing methods for DBI and Mie-scatter imaging. Figure 4-6 illustrates the definitions of the investigated spray features for both experimental approaches. The axial penetration x is defined as the maximum distance of the liquid spray boundary to the injector tip in x-direction. Note, this is not restricted to the central geometric spray axis. The spray angle α is extracted by a method similar to the one of Payri et al. [88]. The spray contour between 1% and 50% of the axial penetration is extracted and a linear least-squares fit is found. Subsequently, α is the angle between the two fitted lines.

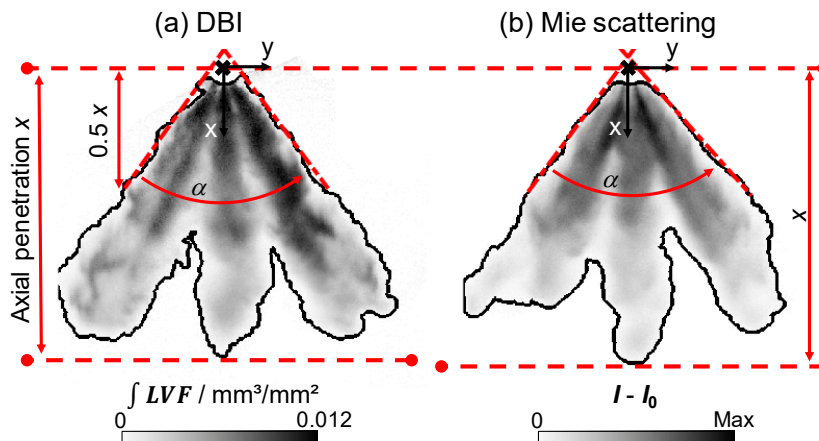


Figure 4-6: Example single shot from (a) DBI and (b) Mie scattering including detected spray contours depicted as a dark black outline. A black \times marks the location of the injector tip with the origin of the x-y coordinate system. The spray angle α and the axial penetration x are shown by red lines and arrows.

Comparison of DBI and Mie-scatter imaging

Figure 4-7 shows the polar plot of the expected Mie-scatter signal $|S(\Omega)|$ at 460 nm, 530 nm, and 600 nm for an *iso*-octane droplet of 7 μm in diameter. As shown in the optical arrangement in Figure 4-5, illumination takes place under different AOI Ω with respect to detection. For a droplet located in the optical axis of the detection path, side illumination takes place at approximately 120°, DBI at 180°, and bottom illumination at 90°. These angles are indicated by colored arrows in Figure 4-7. In general, the plots for different illumination wavelengths show minor deviations in scatter intensity $|S|$. However, $|S|$ increases for angles

between 90° and 180° with some small-scale fluctuations along Ω . For a single droplet at the same incident intensity, the intensity detected at 120° is 6-times greater than at 90° and the expected Mie signal at 180° is 160-times stronger than at 90° . However, light extinction because of the line-of-sight arrangement may be superimposed.

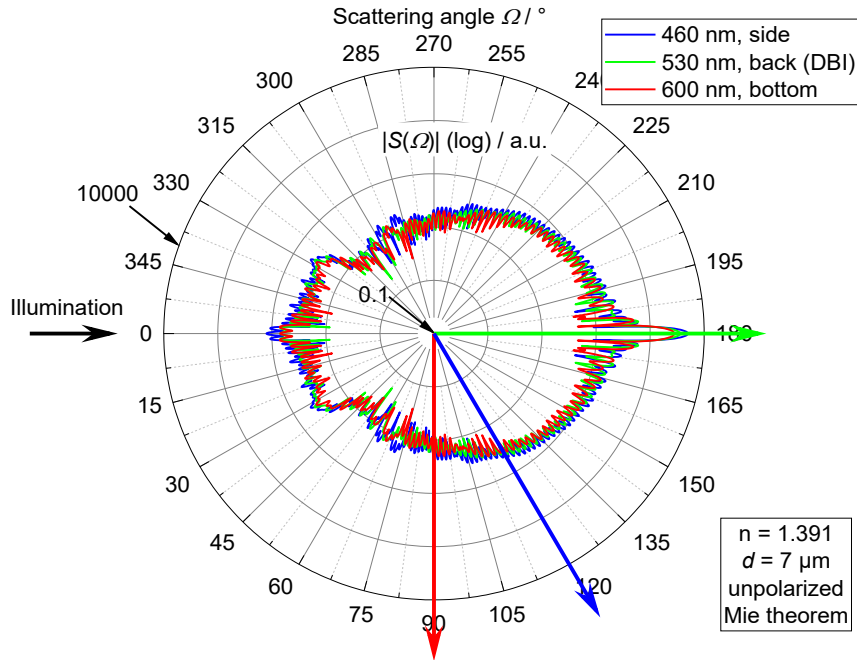


Figure 4-7: Polar plot of Mie scattering $|S|$ for an $7\text{-}\mu\text{m}$ *iso*-octane droplet calculated via the Mie theorem included in *MiePlot* [155]. The calculations were carried out for three different wavelengths with unpolarized light.

To compare the strategies of bottom illumination, DBI, and side illumination, all are performed simultaneously in experiment (A.RGB) via color-coding of each technique according to the schematic in Figure 4-4. Now, illumination of every die is activated at the same time. The signal after scattering and extinction is detected by the R, G, and B channels of the camera sensor. Figure 4-8a shows raw images from the combustion chamber of the motored engine with -67.75°CA SOI and 4 mm IVL. Figure 4-8b shows the images after de-mixing according to Menser et al. [24]. Parts (c) and (d) show color images after processing by following routine: First, images from channels R and B are processed according to the Mie-scatter data processing on page 58. However, the DBI data in channel G is processed as $1 - I/I_0$. Then, the white balance is adjusted by dividing each channel by the field-wide spatial mean of the channels of a snapshot, neglecting values below 0.01% of the maximum value. Here the white balance was determined from the de-mixed snapshot at -66°CA with injection of *iso*-octane shown in Figure 4-8b. The same white-balance adjustment is applied to all snapshots. This makes it possible to compare inhomogeneities and gradients in intensity (or extinction in the green channel) after processing of all image channels. Finally, the channels are recombined to a 16-bit color image. Row (c) shows processed single and (d) shows ensemble means of 10

single shots after processing. The image in (e) shows a snapshot of the spray from *iso*-octane at -66°CA including overlaid spray outlines determined from each of the RGB channels according to the methodology discussed on page 58. The additive color circles visualize the meaning of the color in the images, i.e., if the RGB values in all three channels are the same, this results in shades of gray, but if side illumination is weaker compared to the other illumination then the color will be yellowish. Thus, any deviation from gray means a surplus or deficit in some illumination (color).

Since all techniques are applied simultaneously, a comparison on a single-shot basis is possible. In the raw RGB images in Figure 4-8a the spray region appears magenta because of the addition of red and blue from bottom and side illumination. Green from back illumination, however, is mostly extinct in that region. De-mixing (b) increases the visually perceived color saturation, i.e. the greenish color outside the spray region in (a) looks deeper green in (b). Single shot and mean images after processing in (c) and (d) show that in some regions the illumination from any of the techniques is less than the others resulting in inhomogeneities in color. The region just below the injector tip appears yellowish indicating a deficit in intensity of side illumination compared to the other illumination techniques. This is because the spark plug blocks some of the light from LED No. 1 (see Figure 4-5a). Along the spray axes the color is slightly cyan indicating a deficit in bottom illumination and approximately the same signal from DBI and side illumination.

Between injection of *iso*-octane and the multi-component only minor deviations in the color images can be seen. At the tip of the spray the color in Figure 4-8d appears more blueish with *iso*-octane compared to the multi-component surrogate, and the spray region of the multi-component surrogate appears to be broader than the one from *iso*-octane. Both effects may indicate differences during the temporal evolution of atomization, evaporation, and droplet sizes.

If the liquid spray boundaries shown in Figure 4-8e are compared, side illumination and DBI coincide but a significant deviation in bottom illumination is apparent. In addition to the latter, DBI and side illumination reveal deeper spray penetration than Mie scattering from bottom illumination in that single shot. The contours in Figure 4-8e also display that the angle between the two outer plumes obtained from DBI or side illumination is broader than from bottom-illumination. Moreover, the spray penetration is deeper, which may have several reasons: First, DBI images are corrected for local non-uniformities in illumination and detection (see Eq. (4-1)) affecting the subsequent image segmentation (for detection of the spray outlines) applied with a global threshold. However, such a correction is not possible for Mie scattering images. Second, the method for determining the thresholds is necessarily different for both diagnostics. Third, it appears that DBI can detect smaller droplets than bottom-illumination Mie scattering. Beam steering is likely negligible in the DBI channel as determined from the geometrical relations given by Westlye et al. [87]. In the current arrangement the emission angle of the light source is greater than the collection angle of the system.

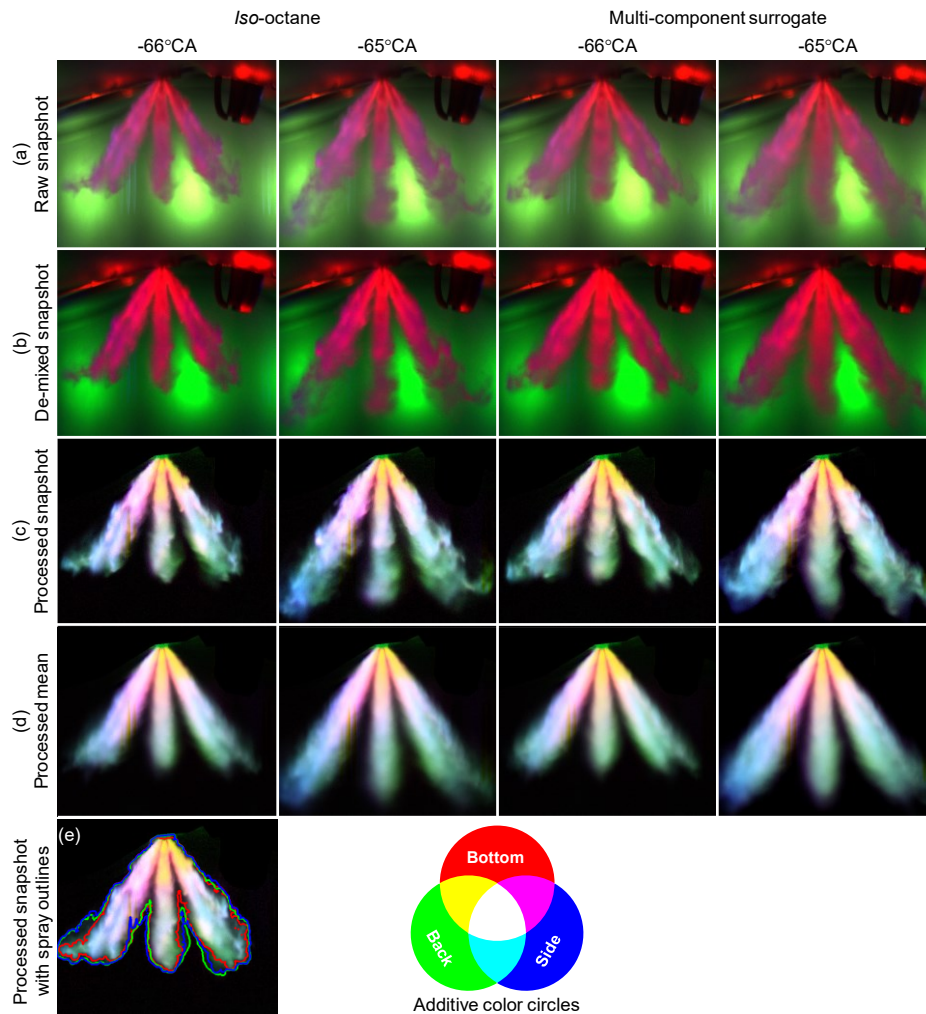


Figure 4-8: (a) Raw, (b) de-mixed, (c) and processed RGB snapshots of the spray at -66°CA and -65°CA from simultaneous bottom (red), back (green), and side illumination (blue). Each frame was processed according to the post-processing routines, normalized to its maximum value, and recombined to an RGB image in (c). (d) shows the ensemble mean after processing, (e) snapshot at -66°CA of iso-octane with overlaid spray outlines. Additive color circles visualize mixtures of the RGB colors. The back illumination was processed as $1-I/I_0$. The engine is operated at 1200 min^{-1} , 4 mm IVL, and $-67.75^{\circ}\text{CA SOI}$.

To further compare influence of the differences from each method on the measured spray penetration, Figure 4-9 shows the correlation of the single-cycle axial penetrations x from simultaneous RGB imaging by bottom illumination and DBI in (a), and side illumination and DBI in (b). The correlation shows solely the influence in illumination and thresholding, while differences in real spray penetration do not influence the correlation since illumination via all three techniques was carried out on the same injection event. Ideally, the data points would be on the straight line labeled in Figure 4-9 as “Best”. However, as a consequence of the differences in illumination and thresholding, compared to DBI, bottom illumination systematically reveals of about 0.5 mm shorter penetration lengths at -66°CA and -65°CA . The correlation of x from DBI and side illumination instead is above the unity-slope line. At -66°CA and -65°CA there are only minor deviations from the ideal correlation. At -65°CA ,

side illumination finds about 0.25 mm deeper penetration than DBI. The deficit in x from bottom illumination may come from the 90° scattering angle that is 160-times less efficient than under 180° , as shown in Figure 4-7.

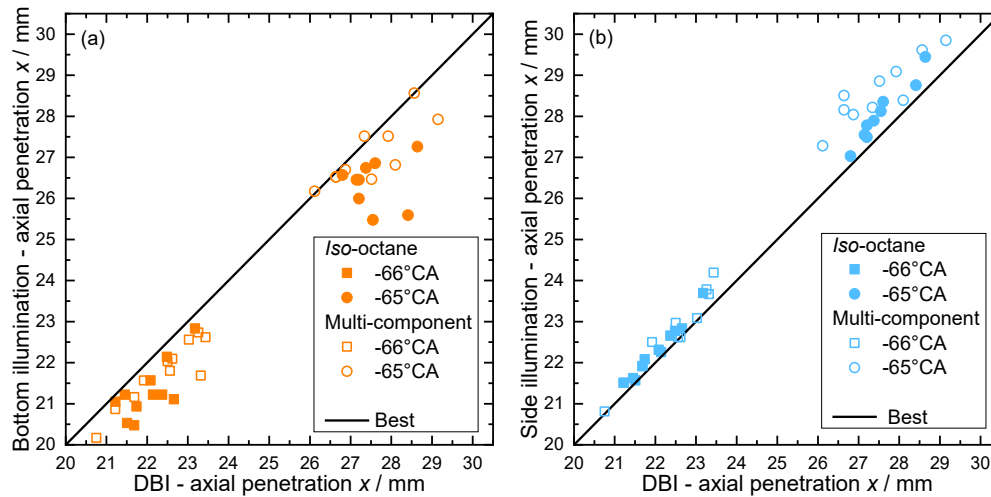


Figure 4-9: (a) Correlation of the axial penetration x from simultaneous DBI and bottom illumination, (b) correlation of x from DBI and side illumination.

4.3.3 In-cylinder bulk flow

Figure 4-10a shows the crank-angle evolution of the average of 75 velocity fields in motored operation without injection at 4 mm IVL and, in Figure 4-10b, at 9 mm IVL from experiment (A.PIV). Velocity fields in both valve center planes and in the cylinder center axis while the intake-valve is open (-260°CA) as well as in mid and late compression are displayed. The blue-yellow colormap represents the velocity magnitude and the flow directions are displayed by vectors of same length. Regions with strong reflections are geometrically masked and displayed in white. Thick black lines depict the position of the piston and the silhouette of the cylinder head including both the Spray G injector and the spark plug. At -90°CA , the lower edge of the FOV is limited by the optical access (compare with Figure 4-2). This means that at -90°CA the piston surface is located about 22 mm below the FOV.

Fresh charge is entering the combustion chamber through the intake valves. At -260°CA , when the maximum valve lift has reached, an increase in IVL causes a decrease in velocity magnitude and a clockwise rotation of the inclination of the incoming flow as shown at $z = -21$ mm and $+21$ mm. With 4 mm IVL the incoming flow is almost parallel to the closed exhaust valves. Compared to the latter, at 9 mm IVL the incoming flow points stronger towards the piston surface. At -90°CA , the flow velocity fields with 4 mm IVL shows low velocity magnitudes and the absence of an apparent tumble vortex but with 9 mm IVL there is a clockwise tumble flow with higher velocity magnitudes on the intake side compared to the exhaust side of the combustion chamber. Overall, the strength of the tumble flow significantly increases with increasing IVL.

Using the 3-dimensional information from all three measured planes, the tumble center axis is not oriented perpendicular to the cylinder center axis at 9 mm IVL, and the trajectory of the tumble axis though seems to be curved, as also seen by Janas et al. [157] in an LES of a similar optical engine. At $z = -21$ mm and -90°CA , the core of the vortex is located approximately 8 mm higher and at $z = +21$ mm about 2 mm higher in vertical direction than the core of the vortex in the central tumble plane at $z = 0$ mm. The highest velocity magnitude just before SOI at -70°CA and -50°CA is located near the piston surface. At 4 mm IVL, the velocity decreases almost linearly from the piston to the cylinder head surface, while at higher IVL the velocity magnitude from the piston surface first de- and then increases towards the cylinder head. Late in the compression stroke, at -40°CA in the last row of Figure 4-10a and (b) the velocity magnitudes are low, not showing any apparent tumble flow with 4 mm IVL, but a tumble flow with 9 mm IVL.

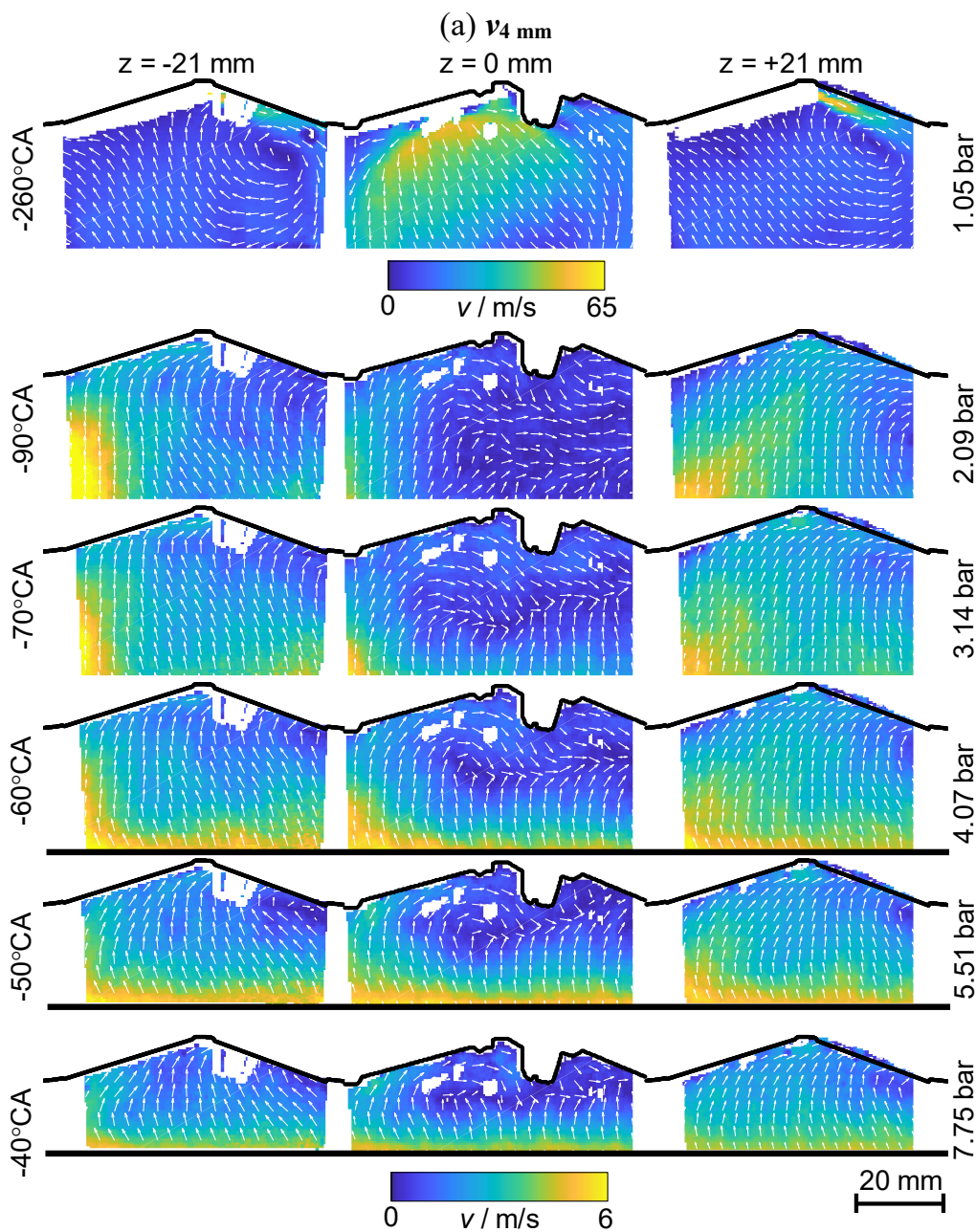


(figure continues next page)

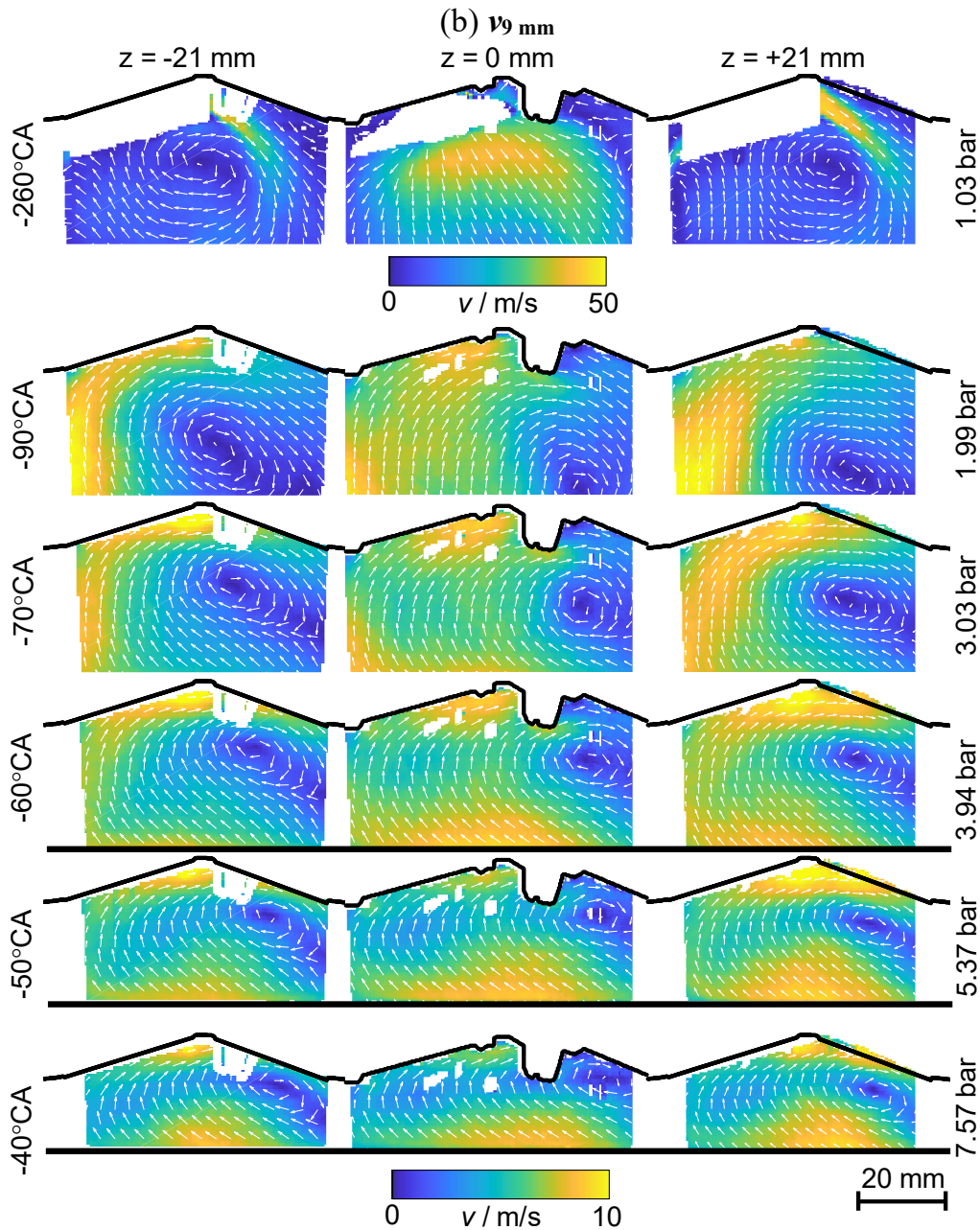


Figure 4-10: Ensemble average of 75-vector fields at (a) 4 mm (on previous page) and (b) 9 mm IVL from motored engine runs without injection in experiment (A.PIV). Vector fields in both exhaust-intake valve planes, $z = -21\text{ mm}$ and $z = +21\text{ mm}$, and in the center plane of the combustion chamber for intake open, middle of compression, around SOI, and late during the compression stroke. Every 6th vector is displayed.

For 4 mm IVL at -50°CA , the spatially averaged velocity magnitude is 2.2 m/s. The near-wall velocity, obtained as the mean value of the first 2 mm of velocity data above the piston, though, is 5.0 m/s, which coincides with the kinematic piston velocity of 5.1 m/s. This shows that the tumble energy, initially induced by incoming flow (-260°CA) through the intake valve, has almost entirely dissipated late in the compression stroke, as can also be seen in the vector fields late during compression in all planes. Instead, the flow at 4 mm IVL is mainly induced

by the piston movement. At 9 mm IVL and -50°CA , the velocity near the piston surface increases to 7.4 m/s, 48% more than in the 4 mm case. Increased IVL causes a strong tumble flow preserving the momentum of the initial incoming flow (see planes $z = -21$ mm and $z = +21$ mm at -260°CA in Figure 4-10) in its rotation as the flow is compressed by the piston. Therefore, the in-cylinder velocities for 4 and 9 mm IVL are both affected by the piston motion but for 9 mm IVL, the tumble is a significant part of the bulk flow. Relative to 9 mm IVL, the 4 mm-IVL case is more similar to experiments in a CVC.

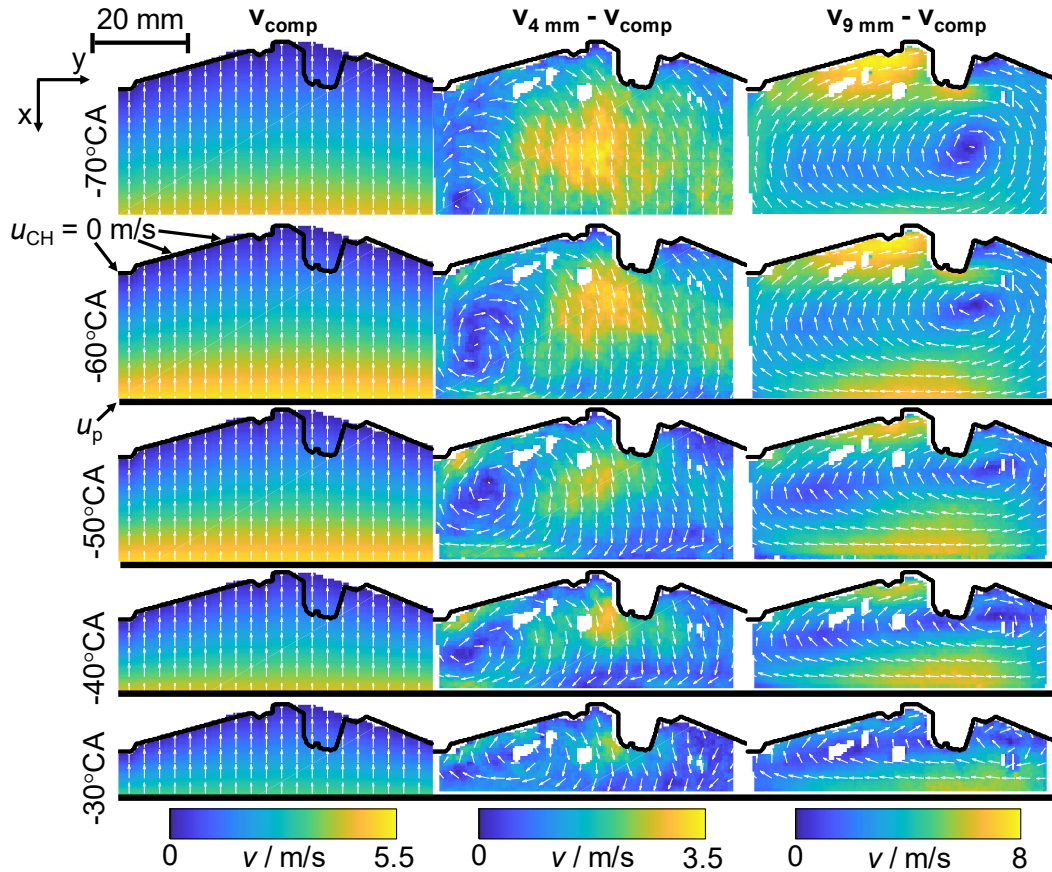


Figure 4-11: Ensemble averages of 75 velocity fields v_i at 4 mm and 9 mm IVL subtracted by the compression velocity v_{comp} at $z = 0$ mm for 4 mm and 9 mm IVL. v_{comp} is artificially created. The black horizontal line marks the piston location, which is below the FOV at -70°CA . Note that the x -direction is vertical and y is horizontal to be consistent with the direction of spray penetration.

From the compression flow induced by the piston and the information on the initially incoming flow, it might be assumed that the in-cylinder flow is a mixture of different flow patterns. If one of the patterns predominates in magnitude, e.g. the flow induced by the piston motion, then the other patterns are hidden. This may be seen with 4 mm IVL, where the initial influence of the incoming flow is not existent later in the compression stroke. One obvious pattern is the flow induced by the piston movement. Thus, the flow induced by compression v_{comp} shown in the first column of Figure 4-11, is subtracted from flow fields in Figure 4-10 for

each crank angle. The decomposition into different flow patterns is based on studies of Borée and Miles [158].

The theoretical vector fields reflecting the compression flow are created by assuming a linear decrease of the piston-induced flow from the piston surface to the flame deck computed via

$$u_{\text{comp}}(y, x, CA) = m(y, CA) \cdot (x - x_{\text{CH}}(y)), v_{\text{comp}} = 0 \frac{m}{s}, \quad (4-3)$$

$$\text{with slope } m(y, CA) = \frac{u_p(CA)}{x_p(CA) - x_{\text{CH}}(y)}, x_{\text{CH}} \leq x \leq x_p.$$

In Eq. (4-3) the velocity component in horizontal direction v_{comp} is zero throughout the whole FOV and the component in vertical direction u_{comp} is dependent on the location in x , y dimensions and the crank angle CA . x_{CH} is the location of the cylinder head surface with respect to the origin parametrized as a function of y (see cylinder head silhouette in Figure 4-11). The piston position x_p and velocity u_p are determined by the piston motion equation using the geometrical parameters listed in Figure 4-2. The spark plug is neglected here. It is assumed that the flow velocity induced by the piston motion linearly decreases from the piston surface to the cylinder head surface from $u_p > 0$ m/s to $u_{\text{CH}} = 0$ m/s with the slope $m = u_p / (x_p - x_{\text{CH}})$. The slope is therefore different at each crank angle and y -location.

The first column of Figure 4-11 shows the theoretical velocity fields $\mathbf{v}_{\text{comp}} = [v_{\text{comp}}, u_{\text{comp}}]$ of the compression-induced flow during the compression stroke in the cylinder center axis. The subtraction of the compression flow from the average flow fields is shown in the second and third columns for both IVLs in Figure 4-11. After subtraction, the 4 mm-IVL case also shows a tumble vortex, but of lower velocity magnitude compared with 9 mm IVL. Because of the different incident angles of the initial incoming flows through the intake valves (see -260°CA in Figure 4-10), the center of the tumble at 4 mm IVL is located near the intake valve, while at 9 mm it is located close to the exhaust valve. Now also late in the compression stroke tumble can be observed for both IVLs.

4.3.4 Thermodynamic condition of the bulk gas

Figure 4-12a displays the in-cylinder pressure p_{cyl} and adiabatic core temperature T_{core} . Figure 4-12b shows the velocity $\langle v \rangle$ spatially averaged over the FOV and the bulk-gas density ρ_b during compression for 4 mm and 9 mm IVL. Except for $\langle v \rangle$, the traces of all other quantities show only marginal deviations between 4 mm and 9 mm IVL. p_{cyl} and T_{core} develop slightly differently when changing IVL, and the bulk-gas densities ρ_b are therefore also slightly affected by the IVL. The maximum in-cylinder pressure is 25 bar and the adiabatic core temperature at TDC is 840 K. Significant influence on the in-cylinder flow magnitude can be observed. Overall, a change from 4 mm to 9 mm IVL causes an increase in $\langle v \rangle$ by a factor of 3 to 4 between -90°CA and -35°CA .

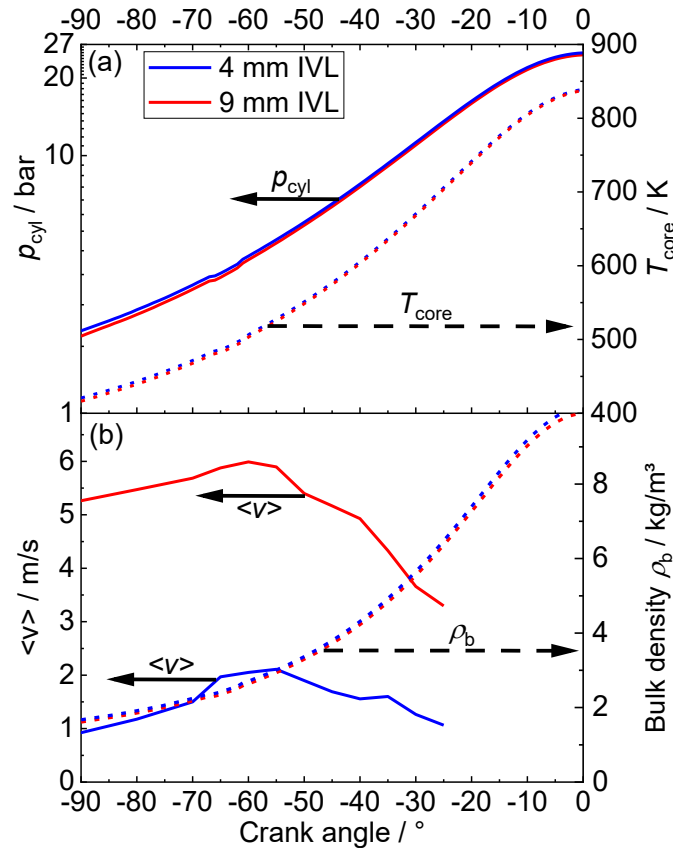


Figure 4-12: (a) Adiabatic-core temperature T_{core} (dashed lines) and in-cylinder pressure p_{cyl} (solid lines) for an IVL of 4 mm and 9 mm motored at 1200 min^{-1} on N_2 , (b) bulk density (dashed lines) and FOV-averaged flow velocity $\langle v \rangle$ (solid lines) of the multi-cycle mean flow fields for both IVLs.

4.3.5 Spray-flow interaction

Next, the interaction of the in-cylinder flow and the spray is discussed. First, spray visualization data from experiment (B.RGB) are presented and compared with the bulk-flow velocity fields to gain knowledge of the interdependency of the IVL and the spray morphology. Then, PIV data obtained during injection are examined to investigate the spray-flow interaction.

Table 4-3 summarizes the in-cylinder conditions studied here. Early injection takes place at lower in-cylinder temperature, pressure, and bulk-gas density compared to injection later during compression. Different from what was expected, an increase in IVL causes a slight decrease in overall in-cylinder pressure, temperature, and bulk density – probably due to the increase of convection and heat transfer in the combustion chamber (the intake pressure was always 1.1 bar, the intake temperature 80°C). Late injection at -47.75°CA was chosen to fit the ECN Spray G standard condition, Spray G1. The bulk density fits almost perfectly with Spray G1 but, temperature and pressure are a little lower than ECN specification.

Table 4-3: In-cylinder pressure p_{cyl} , adiabatic-core temperature T_{core} , and bulk density ρ_b at the injection timing of each test, and the Spray G1 specification [63] for ambient conditions at injection.

SOI / °CA	IVL / mm	p_{cyl} / bar	T_{core} / K	ρ_b / kg/m ³
-47.75	4 mm	5.7	550	3.53
	9 mm	5.5	544	3.46
-67.75	4 mm	3.3	478	2.33
	9 mm	3.2	475	2.26
ECN, Spray G1	-	6.0	573	3.50

The spatial probability distributions of the projected liquid spray area for injection of *iso*-octane and multi-component surrogate by means of DBI and bottom illumination in experiment (B.RGB) are illustrated in Figure 4-13. Side illumination is left out since no standalone data could be acquired due to engine problems. However, Figure 4-8 shows that the liquid-spray boundary in single shots from side illumination coincides with DBI almost perfectly. The distributions in Figure 4-13 are generated by adding up the binary images for multiple cycles at the same time aSOI and dividing by the number of cycles. The resulting 2D-probability map displays the probability of the liquid spray occurring at a certain pixel, visualizing the outlines of the liquid spray as well as cycle-to-cycle variability (CCV). The distributions are generated from 10 to 47 non-consecutive injections depending on the observed crank angle.

The sprays injected with 4 mm and 9 mm IVL keep their symmetrical shape throughout the observed timespan with minor CCV. Due to the late-injection strategy, wall impingement can be observed as the spray expansion is interrupted by the piston top. Contact between spray and the piston surface occurs sometime between 521 μs aSOI and 660 μs aSOI.

As already discussed with Figure 4-8, the probability maps demonstrate that the angle between the two outer plumes obtained from DBI is broader and indicates deeper spray penetration than Mie-scatter imaging via bottom illumination. Comparing the injection of different fuel surrogates, it is noticeable that the projected spray region is greater with the multi-component surrogate than with *iso*-octane. This also expresses itself through a broader spray angle of the multi-component surrogate. Moreover, linking the spatio-temporal evolution of the probability maps with fuel evaporation (e.g. at 4 mm IVL in Mie scattering), the multi-component surrogate overall evaporates slower than *iso*-octane, indicated by the stronger fading of the spray region at 799 μs aSOI in Mie scatter imaging. Evaporation is probably slower with the multi-component surrogate because of *n*-undecane's of low volatility.

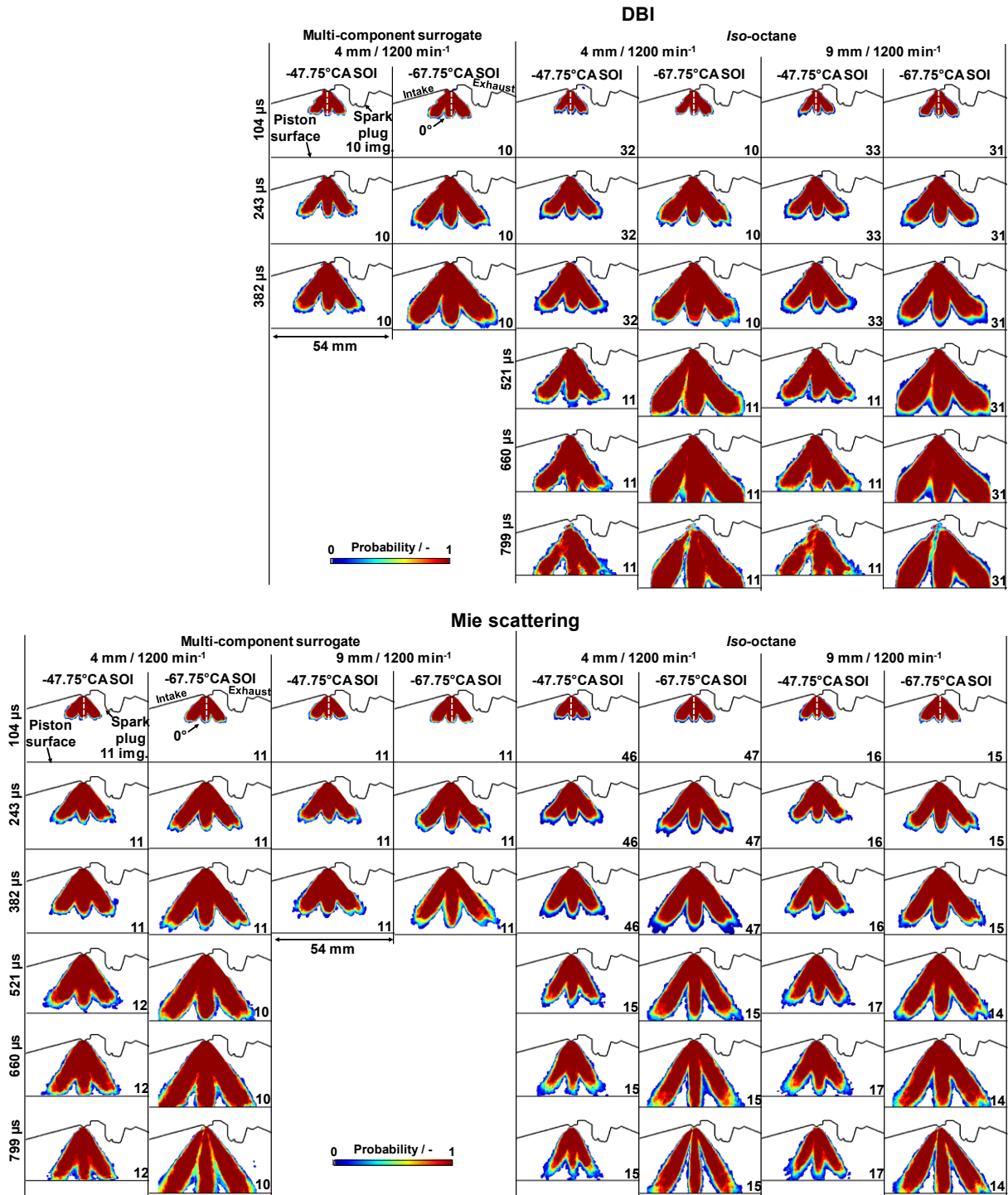


Figure 4-13: Evolution of liquid-spray probability maps from DBI and Mie scatter imaging by bottom illumination in experiment (B.RGB). The bottom right of each image shows the number of single shots used.

At 9 mm IVL it can be observed that the spray is pushed slightly more towards the spark plug than in the 4 mm-IVL case. In [54], by comparing the data displayed in Figure 4-13 with data from the TUD engine, it was shown that an increase in either IVL or engine speed causes a clockwise movement of the liquid spray region. An observation of the CCV of the spray

injection by analyzing the probability map at the spray outlines in Figure 4-13 shows four noticeable effects:

- *Overall spatio-temporal evolution:*

Looking at the temporal evolution of the probability distribution for each combination of IVL and fuel in Figure 4-13, CCV increases over the course of the spray injection. Early in the injection process the spray outlines only vary slightly, while with ongoing evaporation at the edge of the liquid spray the probability distribution broadens, indicating increased cyclic fluctuations of the outlines of the spray.

- *Iso-octane versus multi-component surrogate:*

The spatial gradient at the edge of the spray probability maps are overall flatter (increased CCV) with *iso*-octane due to overall faster evaporation compared to multi-component surrogate.

- *-47.75°CA versus -67.75°CA SOI:*

A shift in SOI to earlier crank angles slows evaporation, thus reduces CCV in all cases.

- *4 mm versus 9 mm IVL:*

The decrease of the probability at the edges of the spray broadens spatially with increasing flow velocity magnitude, indicating higher CCV in the outlines of the liquid spray with increasing IVL. In general, an increase in in-cylinder flow magnitude leads to more pronounced cyclic fluctuations of the spray region.

The axial penetration x extracted from DBI and bottom illumination Mie scattering is displayed in Figure 4-14. In the left column, DBI data are compared with DBI data from CVC experiments obtained by Payri et al. [88] and a Reynolds averaged Navier-Stokes (RANS) simulation (ITV RWTH Aachen, Hinrichs, FVV project M0714, unpublished) of this engine with injection of *iso*-octane at -47.75°CA . In the early stages of injection, both axial penetrations at different IVLs coincide with the penetration measured in the CVC. In the vicinity of the piston surface, the upward flow driven by the piston movement shown in Figure 4-10 and the temporally increasing bulk-gas density decelerate the spray expansion in axial direction stronger than in the CVC. The deviations between both penetrations with different IVLs are marginal even in the late stages of the injection. Injection at -67.75°CA causes faster spray penetration compared to injection at -47.75°CA because of the lower bulk-gas density, and overall deeper penetration because of greater distance to the piston surface. Comparing the penetration of *iso*-octane and the multi-component surrogate, *iso*-octane penetrates shorter. Especially at 4 mm IVL the penetration of the multi-component surrogate is deeper. The simulation initially coincides, but from 0.1 ms the simulation predicts deeper penetration than the experimental data. From 0.25 ms aSOI the penetration speed in the simulation decreases such that it again coincides with the penetration from the DBI data.

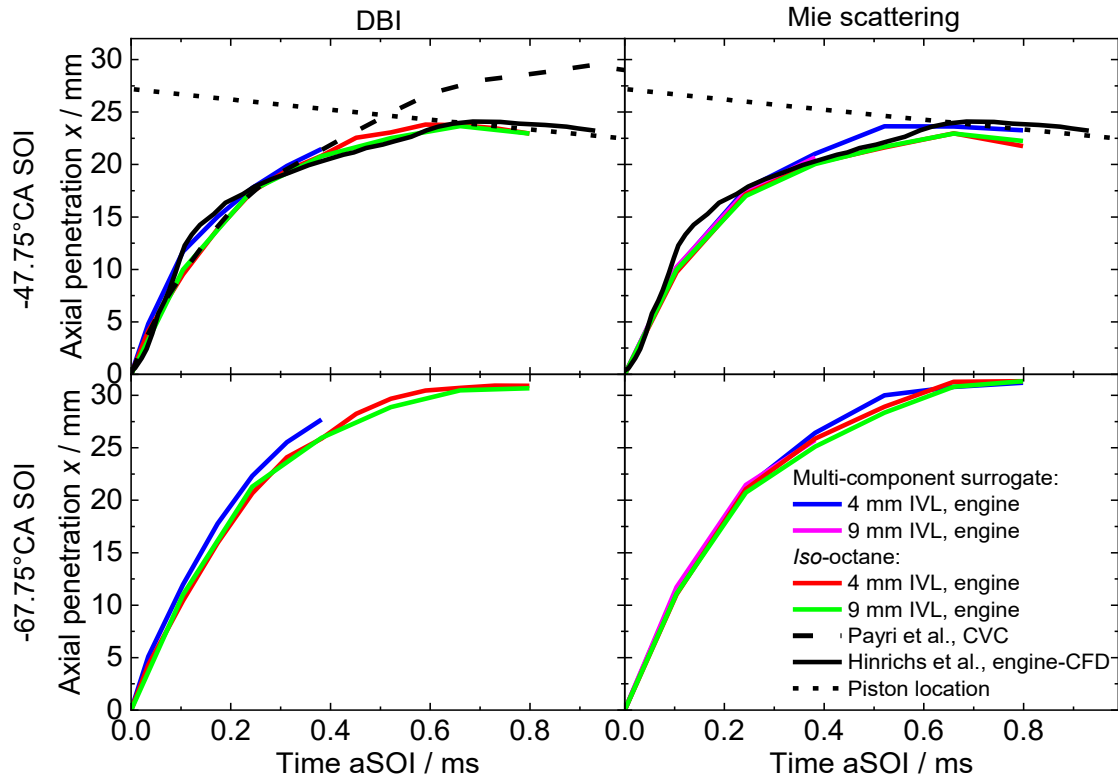


Figure 4-14: Axial penetration x from DBI and Mie scatter imaging for the Spray G standard condition (top row) and injection 20°CA earlier (bottom row) from experiment (B.RGB). DBI results are compared with spray penetration data from the CVC of Payri et al. [88]. Preliminary RANS-CFD results from RWTH Aachen (ITV, Hinrichs, FVV M0714) at 4 mm IVL and injection of *iso*-octane at -47.75°CA are included.

In [54] the data measured at UDE were compared to data measured at the optical engine at TUD. The engine at TUD was operated at 800 min^{-1} and 1500 min^{-1} with a fixed IVL of 9.5 mm. The fuel was injected centrally with 8° -inclination as opposed to the vertically mounted injector at UDE. The images were thus rotated by 8° before extracting the penetration length. Further details can be found in [54].

The axial penetration x and penetration velocity $\Delta x/\Delta t$ extracted from bottom illumination Mie scatter imaging at TUD and UDE in experiment (B.RGB) are displayed in Figure 4-15. The diagram includes UDE data with injection at -47.75°CA at which the ambient conditions are comparable to the ECN Spray G standard condition (see [54]). Initially, the axial penetrations in the UDE engine are greater due to lower bulk-gas density ρ_b compared to TUD as explained in [54], which results in higher axial spray velocities compared to the TUD engine. In this early injection phase, the spray's penetration and velocity are mainly controlled by the influence of ρ_b on the aerodynamic drag of the spray (see Section 2.5.2). Afterwards, at 0.28 ms aSOI, the penetration curves of the TUD and UDE data intersect and the spray penetrations in the TUD engine subsequently remain greater. Although the bulk-gas densities for both operating conditions from this work are lower than in the TUD engine for most of the duration of the injection, the penetrations show a different trend to what was found in CVC experiments

[80], where an increase of the bulk-gas density for the Spray G standard condition generally translates into a decrease of the spray penetration. For example, the spray penetration of the operating condition 9.5 mm IVL / 800 min^{-1} , although having a higher bulk-gas density, subsequently remains deeper than at 9 mm IVL / 1200 min^{-1} . As the latter shows a larger upward velocity magnitude than in [80] it was concluded that the counter flow decelerates the spray expansion and therefore decreases penetration.

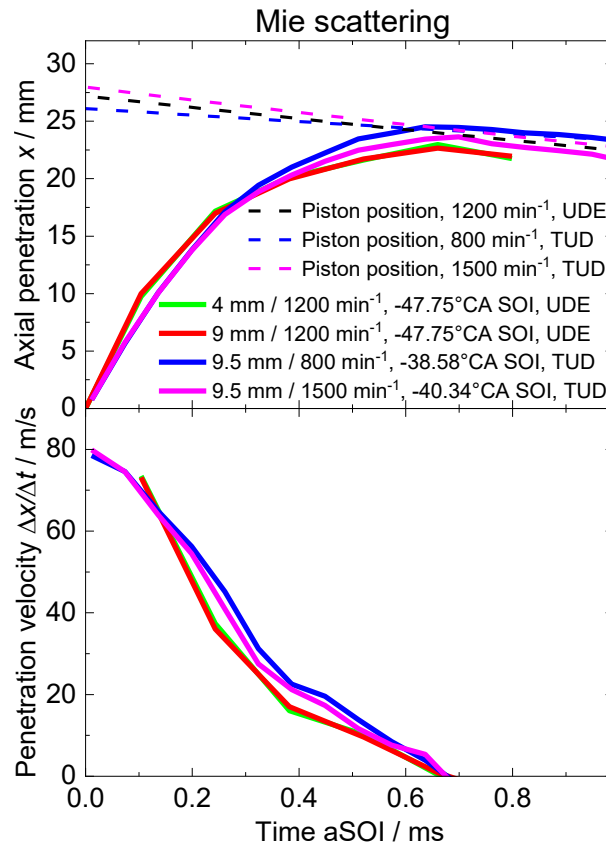


Figure 4-15: Axial penetration x and velocity $\Delta x/\Delta t$ from DBI and Mie scatter imaging for the Spray G standard condition from experiment (B.RGB). Mie scattering data is compared to penetration data by Mie scattering in the optical engine at TUD. *Iso*-octane was injected. Data are published in [54].

After discussing the spray imaging data in combination with in-cylinder flow velocity fields in motored operation, the flow structure in the vicinity of the spray will now be investigated. This allows for a more detailed analysis of the spray-flow interaction. Figure 4-16 displays the mean velocity fields of the bulk flow after injection of *iso*-octane. Similar to the flow fields in Figure 4-10, the velocity magnitude is represented by a colormap while the flow directions are displayed by vectors of fixed length. Engine features are displayed by thick black lines. Masking is applied to regions with strong reflections within the FOV and the spray itself since the scattering intensity of the spray droplets exceeds the scattered intensity of the seeding droplets significantly.

Observing the flow fields in the first row of Figure 4-16, a distinctive flow structure develops caused by the influence of the injected fuel. Fuel injection exhibits distinct fluid entrainment significantly seen at -40°CA with -47.75°CA SOI and at -60°CA with -67.75°CA SOI outside of the spray plumes generating large vortical structures in the tumble and valve plane of the combustion chamber. The vortices in the cylinder center plane point clockwise on the intake and counterclockwise on the exhaust side of the combustion chamber. The entrainment has higher velocity magnitudes when injecting at -47.75°CA compared to the early-injection case.

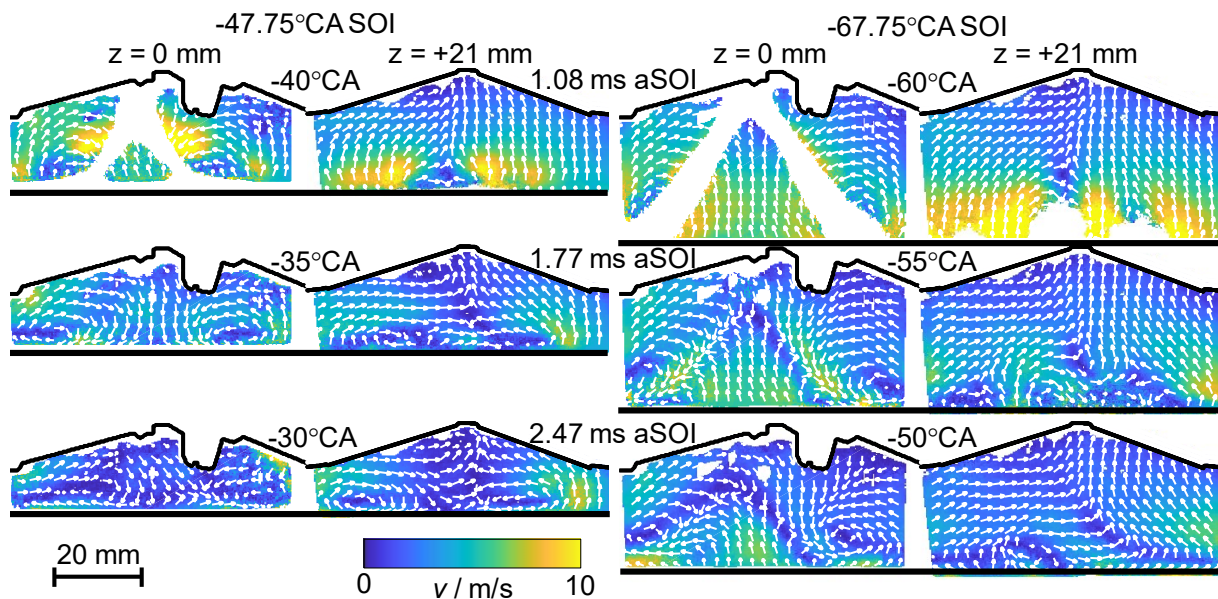


Figure 4-16: Ensemble average of 100 vector fields at 4 mm IVL with injection of iso-octane at -47.75°CA and -67.75°CA . Vector fields in the center, $z = 0$ mm, and in the valve plane at $z = +21$ mm are displayed. The scattering of the fuel droplets is masked out in each single shot and a minimum of 25 source vectors are required in each position to calculate the mean. Every 10th vector is displayed.

In-between spray plumes, an upward flow is visible in the first row of Figure 4-16 and $z = 0$ mm. The velocity magnitude in that region does not significantly differ between injection at -47.75°CA and -67.75°CA . The upward flow between spray plumes is preserved at least until 2.47 ms aSOI for the early injection but is not visible from 1.77 ms aSOI in the late injection case due to strong interaction with the piston surface. When the velocity induced by the piston is subtracted, as shown in Figure 4-17, it is apparent that at -67.75°CA SOI the flow between plumes starts to change its direction by rotating approximately 40° counter clockwise between -60°CA and -50°CA . In [54] the vector fields with injection at -47.75°CA SOI are compared with data from the optical engine at TUD at similar ambient conditions but different engine speed and IVL. A change of engine speed has a significant effect on the velocity magnitude in-between spray plumes. The magnitude increases with engine speed. Spiccas et al. [18] investigated the flow field between plumes at the Spray G standard condition (comparable

to -47.75°CA SOI and 4 mm IVL) in a high-pressure vessel and found that the existence of an upward recirculation zone between spray plumes is vital for preventing spray collapse.

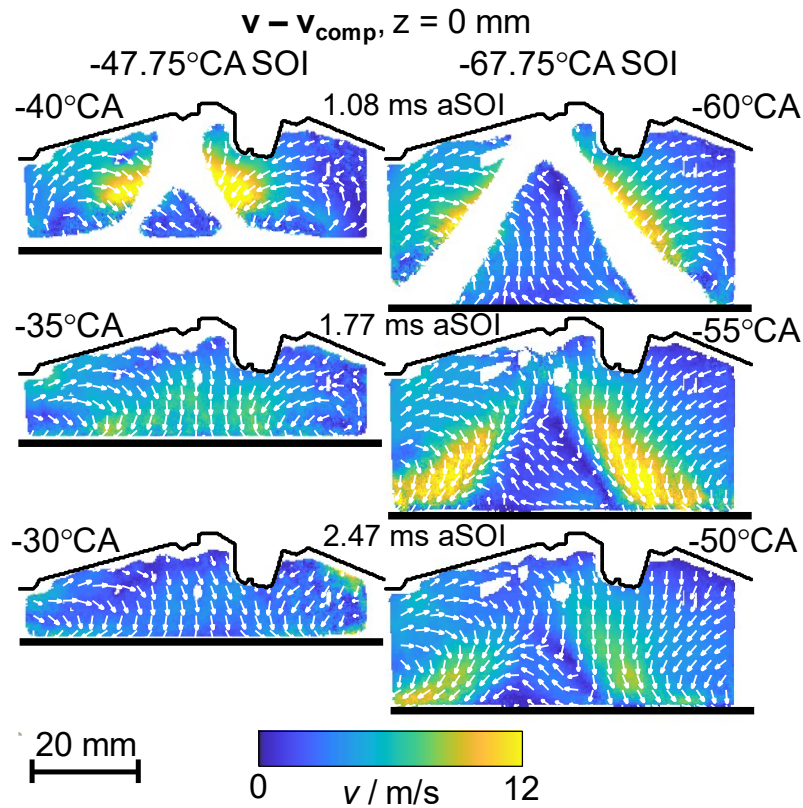


Figure 4-17: Ensemble averages of 100 velocity fields with the compression-induced velocity subtracted. 4 mm IVL and $z = 0$ mm with iso-octane injection at -47.75°CA and -67.75°CA . The black horizontal lines mark the piston location in each field. Every 10th vector is shown.

After the fuel has evaporated, a strong influence of the spray-induced flow field is still visible in the PIV data. This is apparent when comparing velocity fields without injection (see Figure 4-10) with velocity fields after injection has taken place (last two rows of Figure 4-16 and Figure 4-17). At 4 mm IVL, the flow fields without injection show a uniformly upward-facing velocity distribution with slight deviations close to the cylinder head. After injection took place at -47.75°CA , most of the velocity vectors reverse their orientation, following the injection direction of the spray, causing a stagnation point a few millimeter above the piston surface. In that region the piston-induced flow clashes with the spray-induced fluid entrainment even after the spray has already evaporated. Injecting at -67.75°CA does not show this behavior, at least to -50°CA (2.47 ms aSOI). Unfortunately, there is no data available to see if the vectors change direction later in the cycle with injection at -67.75°CA . At $z = +21$ mm and -67.75°CA SOI the wall impingement of the outer three spray plumes (No. 6, 7, 8 in Figure 4-3) can be detected by the lack of vectors near the piston surface displayed in white. Here, the upward pointing flow near the piston surface in the motored case (see Figure 4-10a, $z = +21$ mm) is strongly influenced by the created aerodynamic motion by the injection.

Injection at -47.75°CA also causes entrained bulk flow in the valve center plane at -35°CA , which is less pronounced with -67.75°CA SOI.

To analyze spray-flow interaction in greater depth, the temporal evolution of the spray angle with injection at -47.75°CA is depicted in Figure 4-18 and compared to data acquired in the TUD engine [54]. In the left column, DBI data from this work (UDE) is compared with CVC data from Payri et al. [88]. The spray angle in the CVC undergoes heavy collapse. Its initial spray angle begins at a greater value than measured at both IVLs in the engine from the current work and decreases by 37% to 0.52 ms aSOI. Meanwhile, the spray angles in the UDE engine both begin at lower initial values and decrease by 13% for 9 mm IVL and 17% for 4 mm IVL in the same time duration indicating a reduced spray collapse at higher in-cylinder flow velocities. Similarly, when comparing the angles derived from Mie scatter imaging in the right column of Figure 4-18, the same trend can be observed when comparing the temporal evolution of both spray angles for each engine separately. In [54] it was found that the influence of the flow field on the spray shape is more pronounced as the spray is injected at an angle as done in the TUD engine. The combined analysis of the temporal evolution of the spray angle and the inter-plume flow for engine operation shows that the upward flow field during the compression stroke of an engine supports fluid entrainment and is fundamentally important to prevent collapse of the spray plumes.

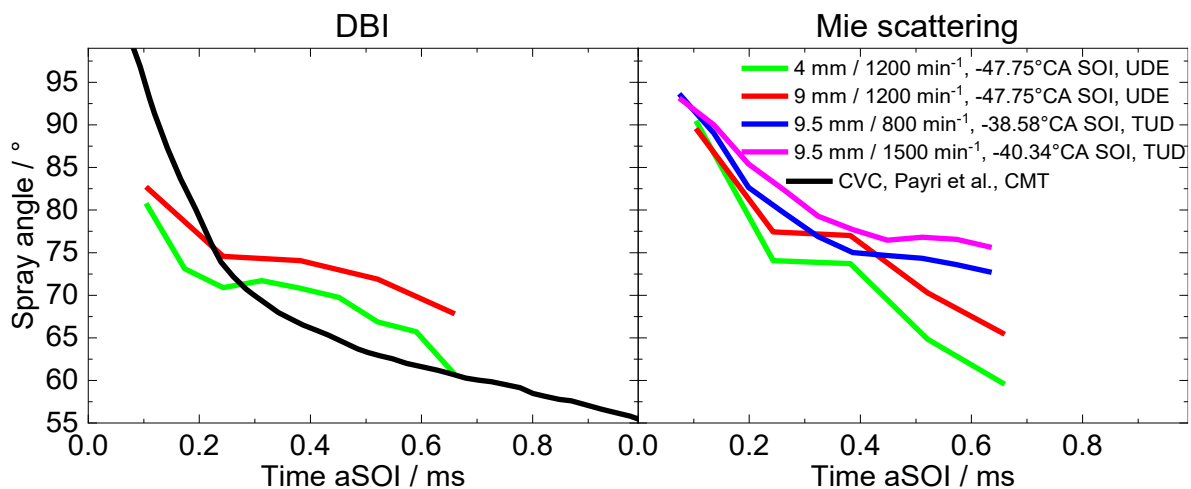


Figure 4-18: Spray angle from DBI and Mie scatter imaging for the Spray G standard condition. DBI results are compared with spray angle data from the constant volume chamber CVC [88]. Data published in [54].

4.4 LIF experiments

Preferential evaporation of the multi-component gasoline surrogate was investigated by LIF imaging of fuel tracers in an optically accessible SIDI engine. In this section, the experimental technique is described including correction of signal crosstalk. Temperature uncertainty and the influence of ambient flow as well as injection timing are discussed. Parts of the following content and data have been published by Kranz et al. [4, 52, 53].

4.4.1 Tracer-fluorescence characteristics

The multi-component surrogate has three non-fluorescing components, as shown in Table 4-1. For LIF imaging of the effect of preferential evaporation a pair of fluorescent tracers DFB and 1MN are added in a 1:5 ratio (by volume) to the multi-component surrogate, which was anticipated to provide similar fluorescence signal strength. The tracers then represent different volatility components of the multi-component surrogate. As shown in Figure 4-20a upon 266 nm excitation DFB and 1MN emit fluorescence in distinct spectral regions, but there is some overlap at about 315 nm. The expected relative camera signals can be estimated by convoluting the area-normalized spectra with the transmittance of the detection system and multiplying by FQY, ϕ_f , and absorption cross-section, σ_{abs} . The latter two quantities are either known or can be estimated as a function of temperature and pressure from the literature [97, 100]. For the filter combination used in this work, the expected signal crosstalk of 1MN and DFB is shown in Figure 4-20b. At 525 K, the ratio of undesired crosstalk to desired signal in each channel is about 7.6% for DFB and 1.3% for 1MN. Crosstalk was minimized as much as possible by optimizing the filter selection.

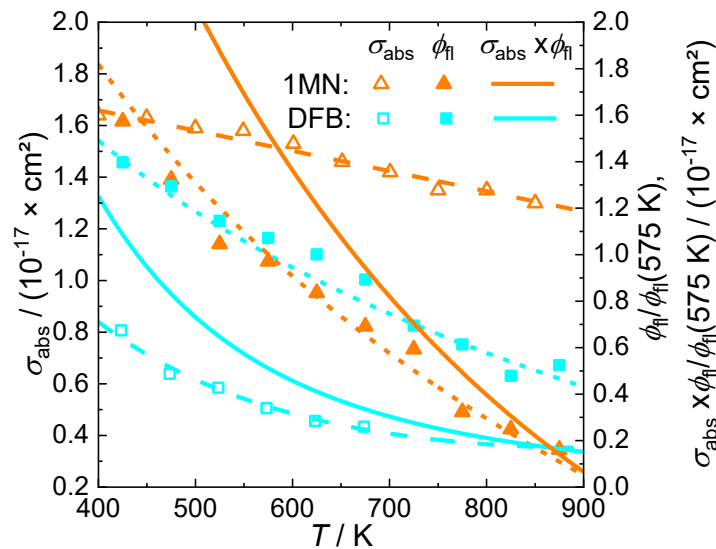


Figure 4-19: Absorption cross-section σ_{abs} at 266 nm, normalized fluorescence quantum yield ϕ_f and the multiplication of both for DFB and 1MN in 1 bar N_2 over temperature. The DFB data were measured at the IVG, DFB absorption cross-section are from [100], FQY was calculated from fluorescence lifetime measurements in the same reference. Data for 1MN from [5].

At 293 K the absolute FQY in nitrogen is similar, with $\phi_{\text{fl,DFB}} = 0.43$ [100] and $\phi_{\text{fl,1MN}} = 0.40$ [159]. As for most aromatic tracers in N_2 , ϕ_{fl} and, less strongly, σ_{abs} decrease with increasing temperature but, as shown in Figure 4-19, differently for DFB and 1MN, what may induce errors in the LIF tracer-concentration ratio. The LIF measurements in this study are performed at adiabatic in-cylinder temperatures from approximately 500 K to 740 K, where the signal of DFB decreases by a factor of 2.7 and the signal of 1MN decreases by a factor 3.3 as estimated from $\phi_{\text{fl}} \times \sigma_{\text{abs}}$ (the red-shift of the spectrum was neglected here). The true local temperature is unknown, but in this range, the combined changes in ϕ_{fl} and σ_{abs} of both tracers are quite similar, which indicates that temperature-induced variations in their signal ratio might be small. To assess the potential error, ratiometric two-color LIF thermometry of anisole is performed in a separate experiment. There, 0.4 vol.-% of anisole are added to the surrogate replacing DFB and 1MN. The properties of anisole are shown in Table 4-1 and fluorescence spectra, lying between those of DFB and 1MN, are displayed in Figure 4-20a. At 318 nm, the spectrum shifts to longer wavelengths with increasing temperature by about 4 nm/100 K.

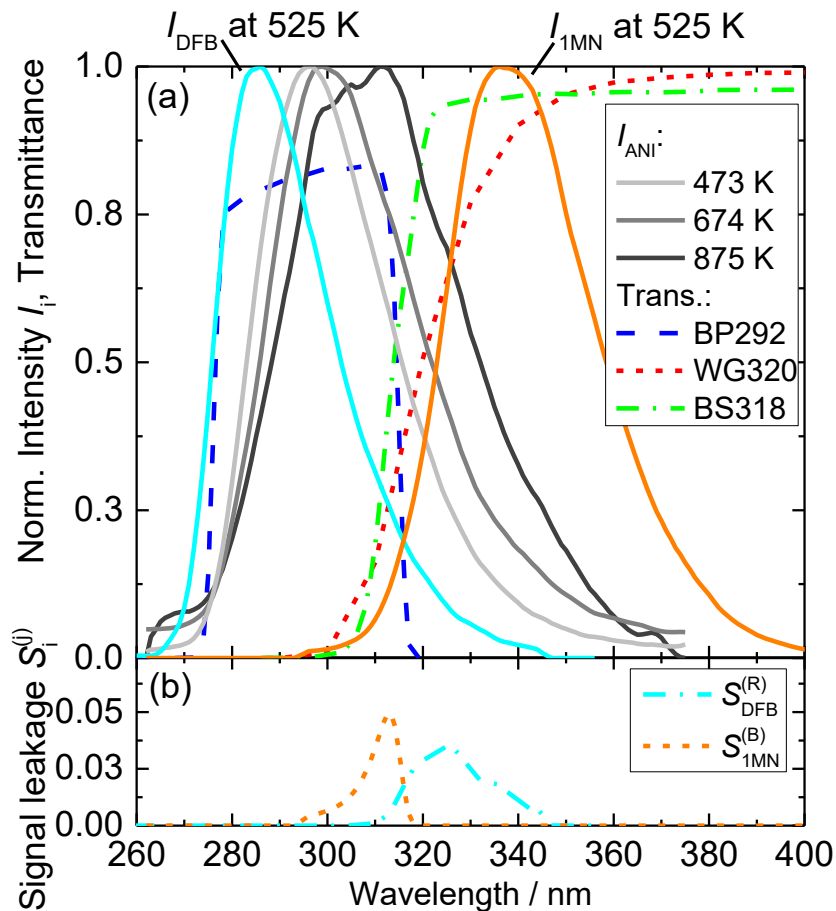


Figure 4-20. (a) Fluorescence spectra of anisole [134] for different temperatures, DFB [100] and 1MN (measured similarly to DFB in [100], private communication with T. Benzler) at 525 K and 1 bar in nitrogen, all upon excitation at 266 nm. Also shown are the transmittances of the filters used in this work. (b) Predicted crosstalk from DFB and 1MN in each detection channel. Figure published in [53].

4.4.2 Optical arrangement

The optical arrangement and a schematic of the side view of the combustion chamber are shown in Figure 4-21. Pulses from an Nd:YAG laser, frequency-quadrupled to 266 nm at 10 Hz repetition rate, are stretched in time by a single-loop passive cavity [22] with a beam splitter of 63% reflectivity and 37% transmittivity to a pulse duration of 21 ns. The extended pulse duration decreases the laser irradiance to prevent damage of optical parts. An energy monitor measures shot-to-shot fluctuations. A combination of a positive and a negative cylindrical lens then forms a light sheet. This divergent sheet is reflected 90° upwards by a mirror through the center axis of the Bowditch piston assembly. After passing the fused-silica piston window the light sheet has a thickness of about 1.5 mm and a width of 70 mm and two of the eight fuel jets are located in the light sheet's plane. The average fluence before the piston window is 25 mJ/cm² which corresponds to an irradiance of 1.2 mJ/(cm² ns).

For LIF detection, a dichroic beam splitter angle-tuned to 30° AOI spectrally separates the signal at 318 nm into a “blue” and “red” part. A band-pass filter BP292 ± 13 nm (Semrock) and a Schott-glass filter WG320 (see Figure 4-20a) further narrow the emission spectra before detection on two identical intensified CCD cameras (LaVision, Imager Intense + IRO) with UV lenses (Cercos, $f = 100$ mm, $f/2.8$). Since the LIF signals cannot be quantified if significant amounts of liquid phase are present [97, 98], also Mie scatter at 266 nm from fuel droplets is imaged to determine the time of full evaporation. This is done in separate engine runs, replacing the BP292 with a neutral density filter.

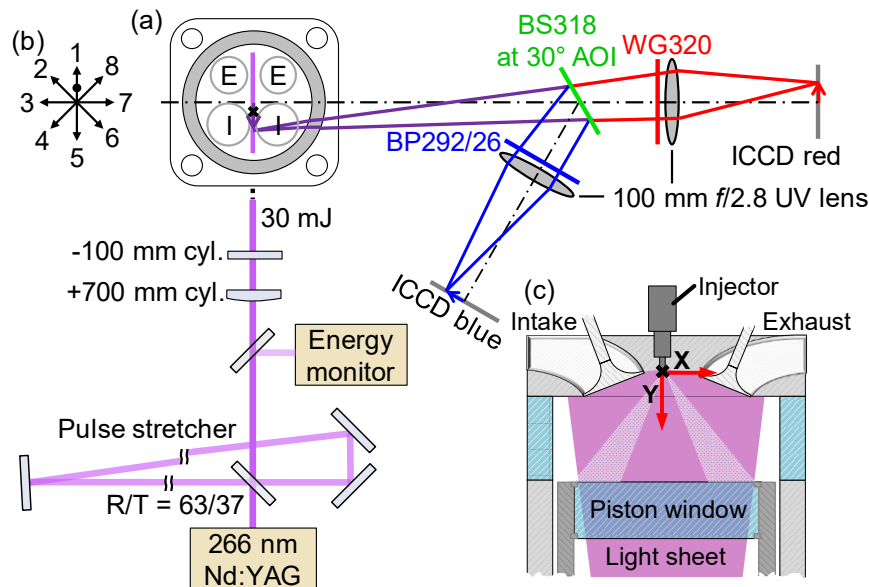


Figure 4-21: Optical arrangement in (a) with field of view inset in (c). The pulse stretcher's beam splitter has a reflectivity of 63% and transmission of 37%. (b) shows the injector plume orientation with respect to the camera. The black dot in (b) represents the orientation of the injector dimple, which points towards the spark plug. An version of this figure was published in [53].

To determine if the LIF signal is proportional to the laser fluence, a preliminary experiment was carried out by successively increasing the laser pulse energy and measuring the LIF from a homogeneous mixture (injection far upstream of the intake) while the engine was motored. Figure 4-22 shows the normalized DFB and 1MN fluorescence intensity upon 266-nm excitation and 8 ns pulse duration over the laser irradiance. The laser irradiance was varied by attenuation of the pulse energy after the exit of the laser head. Each of the 4 data points for DFB and 1MN correspond to the 20-cycle mean in a ROI far from surface. Fluctuations in pulse energy were determined from the reading of the shot-to-shot energy monitor (see Figure 4-21) and the mean pulse energy was determined by an energy meter before each engine run. The coefficients of determination R^2 of the least square fit of a linear function through the origin are greater than 0.99, which indicates a high linear correlation between irradiance and fluorescence signal. However, using 8-ns pulses, Itani [97] found that 1MN and DFB fluorescence is linearly proportional to the laser fluence lower than 28 mJ/cm², which is equal to an irradiance of 3.5 mJ/(cm² ns). Therefore, a fixed laser irradiance of 1.2 mJ/(cm² ns) at 21 ns pulse duration which corresponds to a laser fluence of 25 mJ/cm² is chosen in this work to achieve sufficient LIF signal and to be below the limit of 28 mJ/cm² determined by Itani [97].

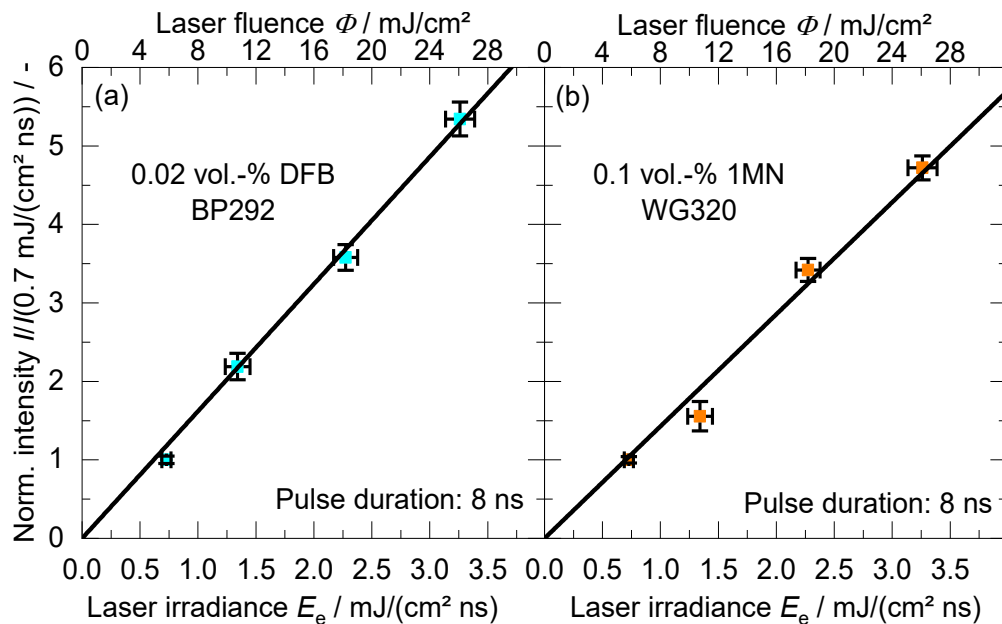


Figure 4-22: (a) DFB and (b) 1MN intensity over the laser irradiance upon 266-nm excitation by 8 ns pulses at -55°CA in homogeneous fuel- N_2 operation at 1200 min^{-1} . Mean intensity in a $3 \times 3 \text{ mm}$ region is extracted and normalized by the 20-cycle mean intensity at $0.7 \text{ mJ/(cm}^2 \text{ ns)}$. The error bars in intensity are the one standard deviation over 20 values, the bars in irradiance the shot-to-shot fluctuations. The data are fitted by linear functions.

4.4.3 Measurements

LIF imaging is performed in three different experiments (A, B, and C), with identical filter configuration as shown in Figure 4-20. In experiment (A), images of a homogeneous

mixture (“flatfields”), via injection upstream of intake port) are acquired, injecting surrogate with one tracer at a time to determine the crosstalk in each channel. LIF from either DFB or 1MN only is imaged in two separate engine runs. In the absence of one tracer, crosstalk from the other can be determined as discussed below.

Experiment (B) is the actual DI experiment, with both DFB and 1MN in the multi-component surrogate. From the Mie-scatter images, it had been concluded that almost all liquid fuel is evaporated 12°CA (1.66 ms) aSOI for injection at –67.75 and 10°CA (1.39 ms) aSOI for injection at –47.75°CA. In this work, LIF images from –55°CA to –35°CA for –67.75°CA SOI, and from –37°CA to –15°CA for –47.75°CA SOI are considered. At every crank angle, 20 images with DI and, in a separate engine run, with homogeneous mixture were taken. Additionally, 200 images with DI and, also in a separate engine run, 50 images with homogeneous mixture were taken at –55°CA / –67.75°CA SOI and –37°CA / –47.75°CA SOI.

In experiment (C), DFB and 1MN were replaced by anisole for single-tracer two-color thermometry at the same engine operating condition as in (A) and (B). As apparent from Figure 4-20, the filters do not need to be changed, since the LIF spectrum of anisole is in between that of DFB and 1MN, such that the BS318 can separate anisole LIF into a “blue” and “red” channel. Flatfields and images with DI at –67.75°CA into a homogeneous background mixture were acquired. Having the tracer also present outside of the DI jet allows determining the temperature in the whole field of view.

4.5 LIF data post-processing and quantification

4.5.1 Tracer-concentration ratio

First, spatial image registration is performed based on a dot target. Then, images are pixel binned 4×4 to a spatial resolution of 0.24 mm/pixel and corrected for background and shot-to-shot energy fluctuations (although the latter would cancel in the tracer-concentration ratio). Next, channel crosstalk needs to be corrected.

Figure 4-23 shows an example of the crosstalk correction. $\mathcal{S}_i^{(j)}$ is defined as the signal in channel j from tracer i . In the blue channel, the measured signal $\mathcal{S}^{(b)}$ consists of the desired signal from DFB, $\mathcal{S}_{\text{DFB}}^{(b)}$, plus unwanted signal from 1MN, which can be expressed as a fraction $\chi^{(b)}$ of the red channel’s desired signal $\mathcal{S}_{\text{1MN}}^{(r)}$ as in

$$\mathcal{S}^{(b)} = \mathcal{S}_{\text{DFB}}^{(b)} + \chi^{(b)} \cdot \mathcal{S}_{\text{1MN}}^{(r)}. \quad (4-4)$$

Analogously for the red channel,

$$\mathcal{S}^{(r)} = \mathcal{S}_{\text{1MN}}^{(r)} + \chi^{(r)} \cdot \mathcal{S}_{\text{DFB}}^{(b)}. \quad (4-5)$$

In vector notation, the solution of this linear system of equations is

$$\begin{bmatrix} \mathcal{S}_{\text{DFB}}^{(b)} \\ \mathcal{S}_{\text{1MN}}^{(r)} \end{bmatrix} = \frac{\begin{bmatrix} 1 & -x^{(b)} \\ -x^{(r)} & 1 \end{bmatrix}}{1 - x^{(b)}x^{(r)}} \begin{bmatrix} \mathcal{S}^{(b)} \\ \mathcal{S}^{(r)} \end{bmatrix}, \quad (4-6)$$

where now the desired signals $\mathcal{S}_i^{(j)}$ depend on measured values only. The relative signal crosstalk $x^{(i)}$ can be determined directly from the single tracer flatfield (FF) pairs in experiment (A):

$$x^{(b)} = \frac{FF_{\text{1MN}}^{(b)}}{FF_{\text{1MN}}^{(r)}}, \quad (4-7)$$

$$x^{(r)} = \frac{FF_{\text{DFB}}^{(r)}}{FF_{\text{DFB}}^{(b)}}. \quad (4-8)$$

In Figure 4-23, images of the fieldwide relative signal crosstalk show an apparent gradient in horizontal direction due to the angular dependent transmittance of the dichroic beam splitter. Over the investigated crank-angle range the average crosstalk is measured to be $x^{(b)} = 4.3\%$ of 1MN signal in the blue channel $\mathcal{S}^{(b)}$ and $x^{(r)} = 8.2\%$ of the DFB signal in the red channel $\mathcal{S}^{(r)}$ after intensifier gain was accounted for as shown in the last bottom row in Figure 4-23. For DFB, this is consistent with the theoretically calculated crosstalk, discussed in Section 4.2.2, while for 1MN it is greater than predicted.

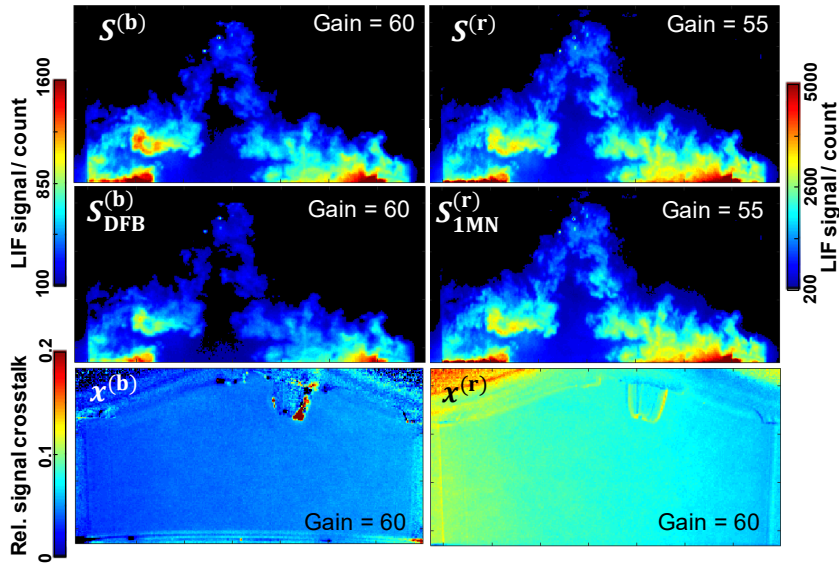


Figure 4-23: Effect of crosstalk correction. The first row shows the detected signal, the second images after correction, and the third the relative signal crosstalk.

With these images, both flatfield and DI images from experiment (B) can be corrected for crosstalk on a pixel-basis via Eq. (4-6). Since the images are now free of crosstalk, from here on superscripts indicating the detection channel are suppressed as: \mathcal{S}_{DFB} and \mathcal{S}_{1MN} . For a given

crank-angle, images in both channels are then divided by the ensemble-mean flatfield at the same crank-angle, such that to first order also the influence of pressure is accounted for. Example single shots after crosstalk and flatfield correction are shown in Figure 4-24a.

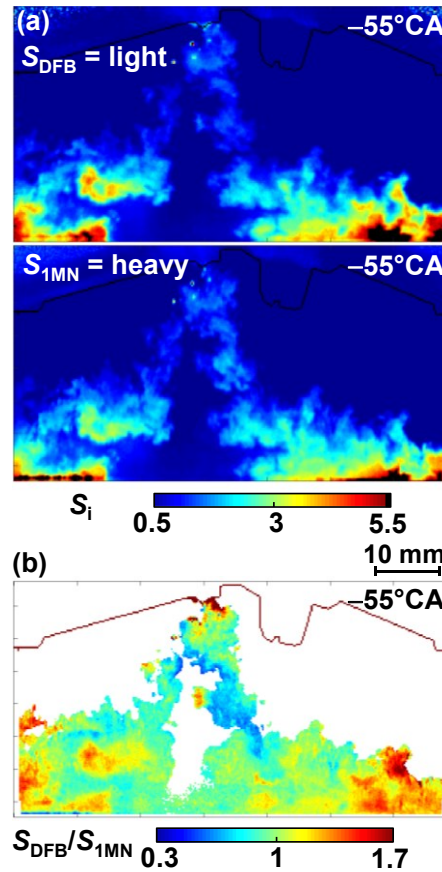


Figure 4-24: (a) Flatfield and crosstalk corrected single-shot images of the fuel-vapor jet at -55°CA (1.77 ms aSOI), (b) ratio of light and heavy components $S_{\text{DFB}}/S_{\text{1MN}}$ after masking. Figure published in [53].

After flatfield correction, shot-specific binary masks are created by thresholding at 20% of the maximum value to suppress regions with low signal that cannot be evaluated accurately. The suppressed regions are filled with “Not a number”. Finally, the image ratio $S_{\text{DFB}}/S_{\text{1MN}}$ represents the relative concentration ratio of light to heavy components. An example is shown in Figure 4-24b. A ratio of unity means that the tracers are present in the gas phase in same proportions as in the originally injected liquid surrogate. Greater values mean there are more light components, lower ones more heavy components.

The ensemble average and standard deviation at each crank angle are calculated by rejecting positions with more than 80% invalid pixels which are filled with “Not a number”. By doing so, the average is not biased by a low number of valid pixels in some regions, especially on the edge of the fuel region.

4.5.2 Fuel-mass composition

Figure 4-24 shows the relative tracer-concentration ratio. However, the local *fuel composition* is not known yet. To close this gap, further assumptions are needed. Two different ways can be followed: Either the CFD simulation includes the tracer within the simulation, such that a comparison with the relative tracer-concentration ratio S_{DFB}/S_{IMN} is possible or the tracer-concentration ratio is translated into *fuel composition* using thermodynamic-based model assumptions. Addressing the latter, Bardi et al. [104] developed a model to connect the tracer-concentration ratio with the fuel-mass fraction of the multi-component surrogate and tracers used in this work. They developed a vapor-liquid equilibrium calculation, modeling evaporation as a series of flashes based on the predictive Soave-Redlich-Kwong state equation of Holderbaum et al. [105] to yield the distilled fractions. Their results, exemplarily shown in Figure 4-25, imply that a relative S_{DFB}/S_{IMN} ratio of 1.3 at 10 bar, as found in regions of the fuel jet, corresponds to 34% *n*-pentane, 48% *iso*-octane, and 18% *n*-undecane by mass, whereas $S_{DFB}/S_{IMN} = 1$ corresponds to a mass ratio of 32/47/21. A ratio of 0.7 implies a mass ratio of 23/51/26. Increasing the system pressure p_{sys} reduces the effect of preferential evaporation (slope decreases for $S_{DFB}/S_{IMN} < 1$) but the component segregation remains significant.

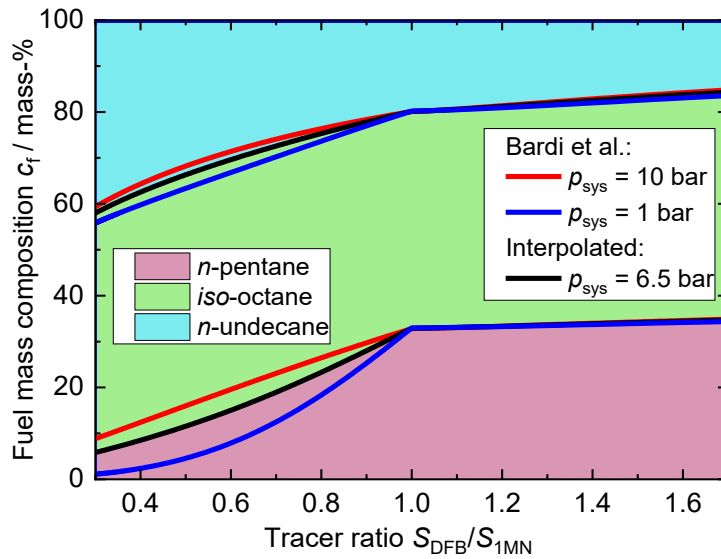


Figure 4-25: Fuel map relating the tracer-concentration ratio S_{DFB}/S_{IMN} with the fuel mass-concentration c_f for system pressures p_{sys} of 1 bar, 6.5 bar, and 10 bar. 6.5 bar is the result of the linear interpolation between 1 bar and 10 bar. Data from Bardi et al. [104].

The S_{DFB}/S_{IMN} -images can be translated into fuel component concentration c_f interpolating the fuel maps from [104] at 1 bar and 10 bar (also included in Figure 4-25) to the in-cylinder pressure at the observed crank angle. However, the restrictive assumptions made in the model may not apply for the complex situation of droplet evaporation in an engine spray. Additionally, the linear interpolation may not represent the actual dependence of pressure but is intentionally a reasonable assumption.

4.5.3 Temperature via two-color LIF thermometry

Two-color LIF thermometry (2CT) was carried out to determine the temperature in the FOV. Flatfield image pairs of anisole-LIF in experiment (C) were recorded from -180°CA to TDC in steps of 20°CA in three engine runs with different intake temperatures T_{in} . The images were spatially registered, 4×4 pixel binned, corrected for background, and ensemble averaged. Finally, $S_{\text{ANI}}^{(\text{B})}/S_{\text{ANI}}^{(\text{R})}$ was calculated. The adiabatic core temperature T_{core} away from the walls was calculated by isentropic compression using the in-cylinder pressure trace with an isentropic coefficient of $\kappa = 1.36$. The start temperature at intake-valve closing at -200°CA was estimated as the arithmetic mean of intake and coolant temperature. Figure 4-26 shows the temperature versus $S_{\text{ANI}}^{(\text{B})}/S_{\text{ANI}}^{(\text{R})}$ averaged over a small ROI below the injector. The function $T = T_0 + \beta \cdot \xi^{r_c}$, with $r_c = S_{\text{ANI}}^{(\text{B})}/S_{\text{ANI}}^{(\text{R})}$ was least-squares fitted to the data, yielding $T_0 = 327$ K, $\beta = 950$ K, and $\xi = 0.227$.

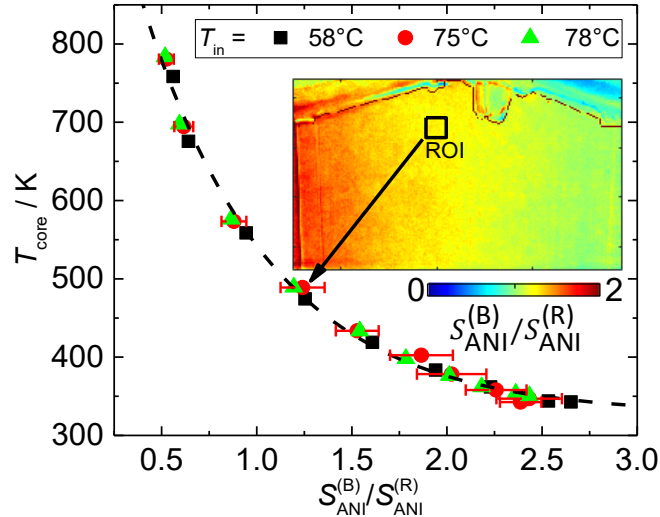


Figure 4-26: Parametrization of the relationship between anisole-LIF signal ratio $S_{\text{ANI}}^{(\text{B})}/S_{\text{ANI}}^{(\text{R})}$ and temperature based on isentropic compression. The error bars at 75°C indicate noise (one standard deviation) within the $3.6 \times 3.6 \text{ mm}^2$ ROI. The insert shows a background corrected signal-ratio image at -120°CA with the ROI used to extract the data in the plot. Figure published in [53].

The DI images were dewarped, spatially registered, 4×4 pixel binned, corrected for background, and divided by their corresponding mean flatfield image. Besides accounting for the influence of pressure to first order, the latter also removes the horizontal gradient created by the angular transmission dependence of the dichroic beam splitter that is so prominent in the insert of Figure 4-26. By multiplication with the flatfield signal in the ROI the relevant absolute signal is preserved. A similar correction procedure was described by Peterson et al. [140] and further extended by Kranz et al. [136]. Then, temperature images $T_{2\text{CT}}$ were computed using the fit function. To increase precision, the temperature snapshots were again binned 4×4 to a final spatial discretization of 0.96 mm/pixel .

4.5.4 Temperature and fuel concentration via adiabatic mixing

Adiabatic mixing (AM) is applied to the DFB/1MN-LIF images from experiment (B) to derive the temperature from actual experiment investigating preferential evaporation. This section describes the current implementation following the methods introduced in [146] and [150].

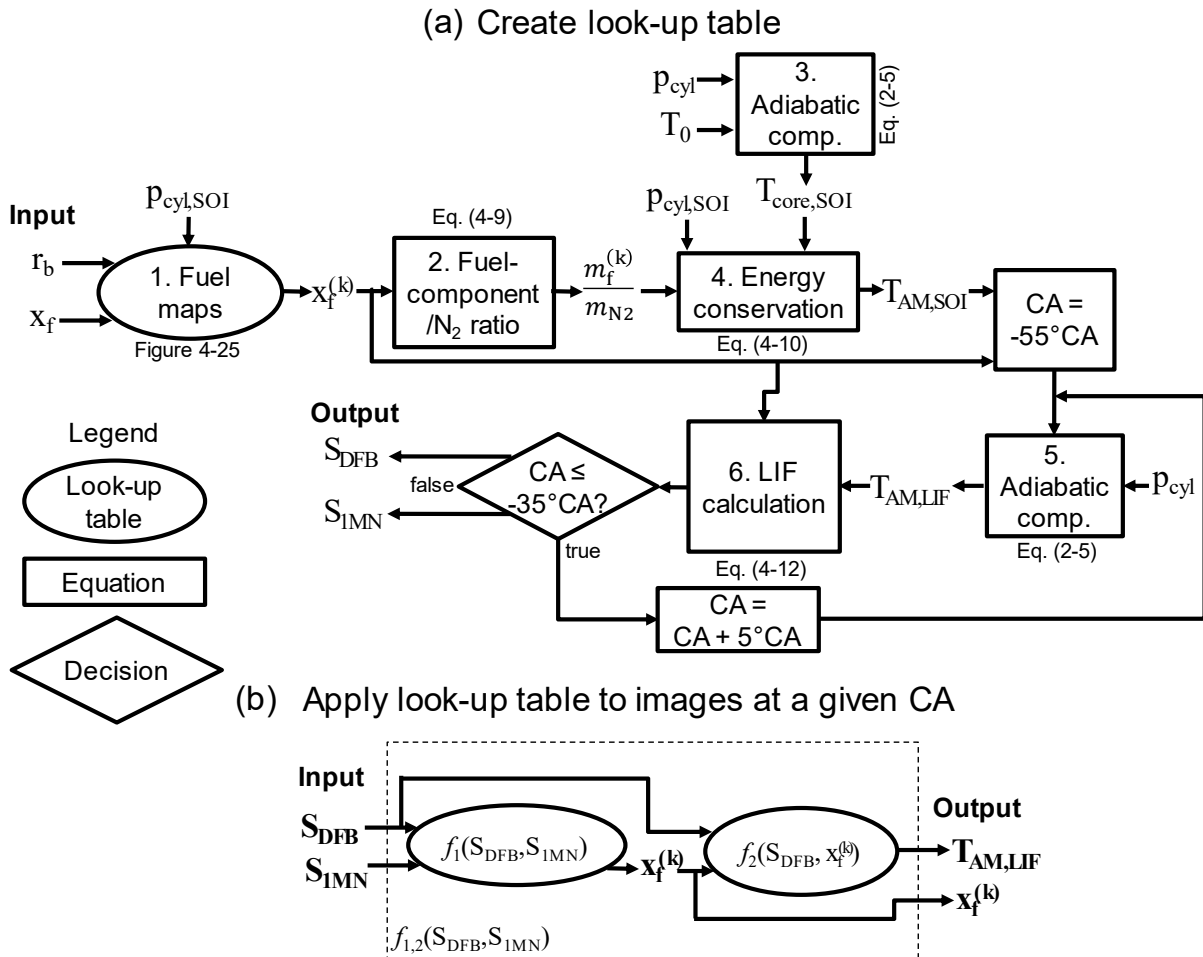


Figure 4-27: (a) Flow chart of how to create a look-up table connecting the LIF signals with the fuel mole-fraction x_f and mixing temperature T_{AM} via adiabatic mixing. (b) flow chart for applying the look-up table to the images. CA: Crank-angle.

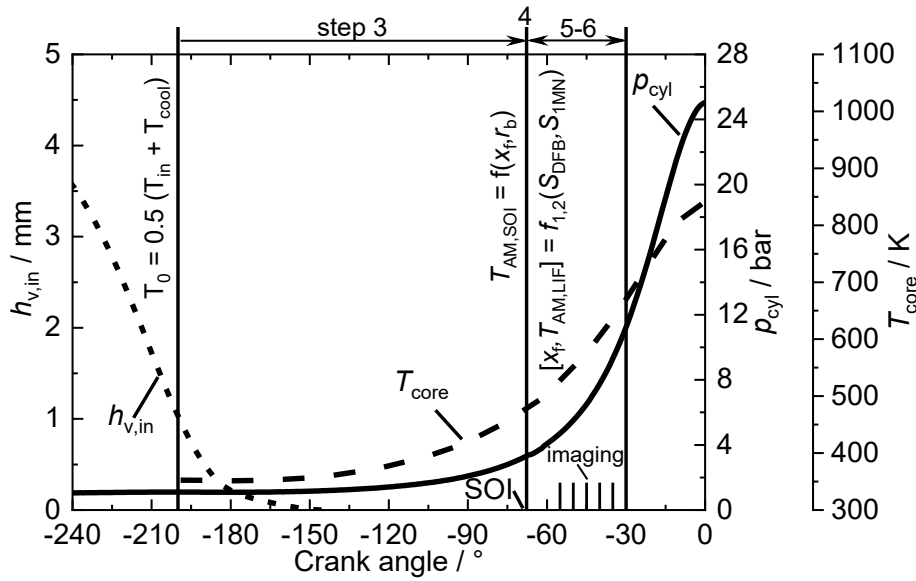


Figure 4-28: In-cylinder pressure p_{cyl} , intake-valve lift $h_{v,in}$, and adiabatic core temperature T_{core} including labels for each of the processing steps. SOI is at -67.75°CA . CA: Crank-angle.

The following paragraphs describe each step in creating and applying the look-up table in more detail.

(a) Create look-up table (Figure 4-27a):

Input:

The fuel mole-fraction x_f is discretized between 0 mol.-% and 0.03 mol.-% and the tracer-concentration ratio r_b is discretized in the range of 0.3 and 3, both into 10 equally spaced parts, resulting in a “stack” of two 10×10 matrices as shown in Figure 4-29, containing all possible combination of r_b and x_f . The ranges of the two quantities were chosen based on a preliminary test with broader range in fuel mole-fraction. It was found that the fuel mole fraction does not exceed 0.025 mol.-% and, as stated in [104], the practical range of r_b is between 0.3 and 3.0.

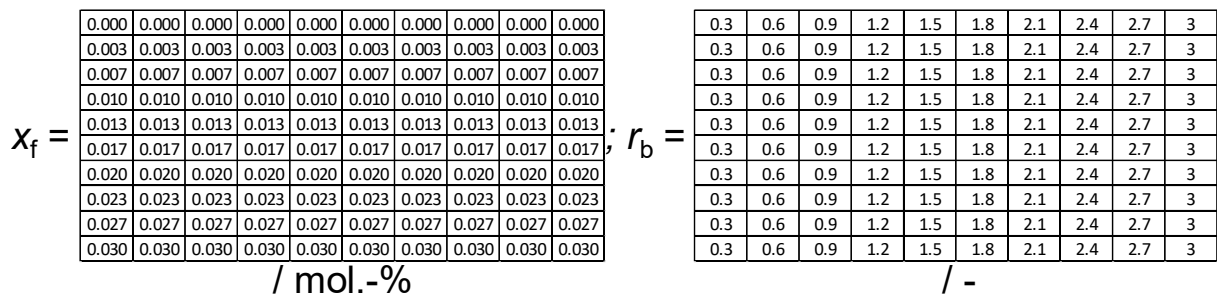


Figure 4-29: x_f and r_b as matrix inputs to the adiabatic mixing model.

Step 1: Fuel maps

For every combination of x_f and r_b , the fuel-component mole-fractions $x_f^{(k)}$ are determined via interpolation of the fuel maps of the in-cylinder pressure at SOI $p_{cyl,SOI}$. Figure 4-25 shows the fuel map at 6.5 bar from the interpolation of the fuel maps at 1 bar and 10 bar. Here, the superscript (k) indicates each of the fuel components, i.e., *n*-pentane, *iso*-octane, and *n*-undecane.

Step 2: Fuel-component/N₂ ratio

The fuel-component mole-fraction is transformed into the fuel-component to N₂ mass ratio ($m_f^{(k)}/m_{N_2}$) via

$$\frac{m_f^{(k)}}{m_{N_2}} = \frac{M_f^{(k)} x_f^{(k)}}{M_{N_2} (1 - x_f)}. \quad (4-9)$$

$m_f^{(k)}$: Mass of fuel component (k)

m_{N_2} : Mass of nitrogen

$M_f^{(k)}$: Molar mass of fuel component (k)

M_{N_2} : Molar mass of nitrogen

$x_f^{(k)}$: Mole fraction of fuel component (k)

The mass ratio is passed on to the equation for energy conservation in step 4.

Step 3: Adiabatic compression

The adiabatic core temperature at SOI ($T_{core,SOI}$), is determined via adiabatic compression along the in-cylinder pressure trace (Figure 4-28). It is assumed that the temperature prior to start of injection is equal to the adiabatic core temperature throughout the entire FOV. The pressure and adiabatic core temperature at SOI are passed on to the equation representing energy conservation in the next step.

Step 4: Energy conservation

With the mass ratio of each of the fuel components to nitrogen as an input, the equation for energy conservation (4-10) including evaporation is solved for the mixing temperature $T_{AM,SOI}$ at SOI.

$$\int_{T_{AM,SOI}}^{T_{amb}} c_{p,N_2} dT = \sum_{k=1}^{N=3} \frac{m_f^{(k)}}{m_{N_2}} \left(\int_{T_{f,l,ini}}^{T_b^{(k)}} c_{p,f,l}^{(k)} dT + h_{v,Tb}^{(k)} + \int_{T_b^{(k)}}^{T_{AM,SOI}} c_{p,f,v}^{(k)} dT \right). \quad (4-10)$$

$\int_{T_{AM,SOI}}^{T_{amb}} c_{p,N_2} dT$: Change in thermal enthalpy of bulk gas (N₂)

$\int_{T_{f,l,ini}}^{T_b^{(k)}} c_{p,f,l}^{(k)} dT$: Change in thermal enthalpy of the liquid-fuel component (k)

$h_{v,Tb}^{(k)}$: Latent heat of vaporization of fuel component (k)

$\int_{T_b^{(k)}}^{T_{AM,SOI}} c_{p,f,v}^{(k)} dT$: Change in thermal enthalpy of the fuel-vapor component (k)

$m_f^{(k)}/m_{N_2}$: Mass ratio of fuel-vapor component (k) to nitrogen

The energy conservation in Eq. (4-10) consists of four parts: $\int_{T_{AM,SOI}}^{T_{amb}} c_{p,N_2} dT$ is the change in thermal enthalpy of the bulk gas. This change is equal to the sensible heat described by the change in thermal enthalpy of each liquid fuel component (k) from the initial fuel temperature $T_{f,l,ini}$, to the boiling temperature $T_b^{(k)}$, the latent heat of vaporization $h_{v,Tb}^{(k)}$, and the change in thermal enthalpy of the evaporated fuel from $T_b^{(k)}$ to the adiabatic mixing temperature $T_{AM,SOI}$. Functional parametrizations for the constant-pressure heat capacity c_p , and latent heat of evaporation $h_{v,Tb}$, at $p_{cyl,SOI}$ for each fluid depending on temperature are taken from the VDI Heat Atlas [9].

The principal applicability of Eq. (4-10) for determining the mixing temperature was tested with data published by Zigan et al. [129]. Using two-line-excitation tracer LIF of 3-pentanone, they simultaneously measured the fuel-vapor mass fraction and temperature distribution after injection of *iso*-octane into a high-temperature high-pressure chamber. Figure 4-30 shows a radial profile of fuel-vapor fraction and temperature perpendicular to the spray plume axis 40 mm from the injector tip. The fuel-vapor mass fraction (dashed line in Figure 4-30) is inserted into Eq. (4-10) and solved for the mixing temperature at constant pressure.

The adiabatic mixing temperature T_{AM} (black solid line in Figure 4-30) agrees well with the temperature from two-line LIF. However, a significant deviation occurs in the center of the jet between -3 mm and 3 mm, where Zigan et al. found a mostly constant temperature of 525 K. The adiabatic mixing temperature, however, follows the profile of the vapor mass fraction. This results in a deviation in temperature at 0 mm from two-line excitation LIF of 20 K. This may indicate that the gas phase in center of the spray is not adiabatic, as a considerable number of droplets may be in that region.

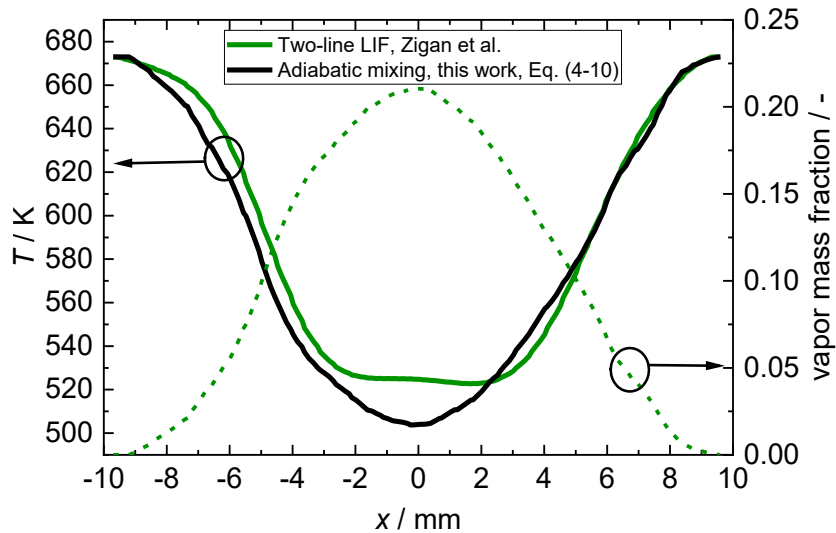


Figure 4-30: Comparison of the temperature by means of two-line excitation tracer LIF by Zigan et al. [129] and calculated via Eq. (4-10). Shown are the radial profiles 40 mm far from the injector tip of temperature and vapor-mass fraction in the fuel jet after injection of *iso*-octane. Ambient pressure 8 bar, ambient temperature 673 K, injection pressure 100 bar.

Step 5: Adiabatic compression

Steps 5 and 6 are executed in a loop over the CA of image acquisition as shown in the flow chart in Figure 4-27a. Taking the reduction of compression heating into account, in step 5, $T_{AM,SOI}$ is input to adiabatic compression to calculate the mixing temperature at the pressure at CA of LIF image acquisition. As denoted in Figure 4-27a and Figure 4-28, CA starts at $-55^{\circ}CA$ and is changed in steps of $5^{\circ}CA$ in every loop until $-30^{\circ}CA$ has reached. At this point, $T_{AM,LIF}$ is a function of x_f and r_b (and thus of the component concentrations $x_f^{(k)}$), but the absolute fuel concentration x_f is not known not allowing for direct quantification of $T_{AM,LIF}$ from the measured LIF signals. $T_{AM,LIF}$ and $x_f^{(k)}$ are passed on to the next step. The index “AM,LIF” denotes quantities at the CA of image acquisition.

Step 6: LIF calculation

To determine the relation between the fuel-component mole-fractions and the LIF signals, the temperature and pressure dependencies of the fluorescence signal of DFB and 1MN are used in step 6. The LIF intensity is described by

$$I_i(T, p) = C_i \cdot \tilde{I}_i(T) \cdot x_i \cdot \rho(T, p). \quad (4-11)$$

I_i : LIF intensity from tracer i

\tilde{I}_i : Density-corrected LIF intensity from tracer i

x_i : Mole-fraction of tracer i

ρ : Vapor density

The index i denotes the tracer representing the light-to-medium volatile components (DFB) and heavy component (1MN) in the multi-component fuel. In Eq. (4-11) I_i is dependent on temperature and pressure. All other presumably constant influences on the detected signal are included in the calibration constant C_i .

The density-corrected intensity \tilde{I}_i from each tracer is determined from a series of flatfields of DFB/1MN LIF in experiment (B), in which the tracers are present at known and constant ratio over a range of temperatures. Flatfield-image pairs of DFB/1MN LIF were recorded from -180°CA to TDC in steps of 20°CA in one engine run to determine the temperature sensitivity of the fluorescence signal of each tracer. Similar to the processing of the anisole-LIF images, the images are dewarped, spatially registered, 4×4 pixel binned, corrected for background, and ensemble averaged. T_{core} away from the walls is again calculated by isentropic compression based on the in-cylinder pressure trace of the experiment with homogeneous fuel-nitrogen mixture with an isentropic coefficient of $\kappa = 1.36$. The start temperature for isentropic compression at intake-valve closing is 78°C .

Figure 4-31 shows the ad-hoc parametrization of the density-corrected intensity \tilde{I}_i of DFB and 1MN averaged over a $3 \times 3 \text{ mm}^2$ ROI below the injector tip versus the adiabatic-core temperature. The Boltzmann function shown in Figure 4-31 is least-squares fitted to the data yielding the values of the constants $A_{1,i}$, $A_{2,i}$, $T_{0,i}$, and dT_i as listed in the figure.

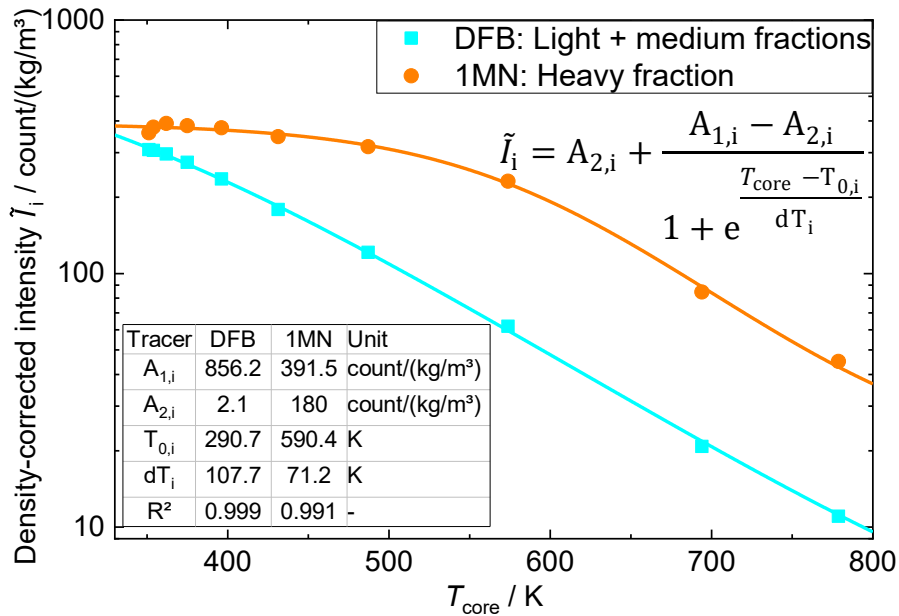


Figure 4-31: Density-corrected DFB and 1MN signal extracted from a small ROI in DFB/1MN-LIF flatfields from -180°CA to TDC parameterized as a Boltzmann function of T_{core} . The density at each crank angle is calculated via adiabatic compression taking the change in isentropic coefficient into account.

Normalizing the LIF intensity $I_{\text{LIF},i}$ (DI measurement) in Eq. (4-11) at unknown temperature $T_{\text{AM,LIF}}$ by the calibration intensity $I_{\text{cal},i}$ (flatfield) at known temperature T_{cal} , the calibration constant C_i cancels out:

$$\frac{I_{\text{LIF},i}}{I_{\text{cal},i}} = S_i = \frac{\tilde{I}_i(T_{\text{AM,LIF}}) \cdot x_{f,i}}{\tilde{I}_i(T_{\text{cal}}) \cdot x_{f,\text{cal},i}} \cdot \frac{p_{\text{cyl,LIF}} T_{\text{cal}}}{p_{\text{cyl,cal}} T_{\text{AM,LIF}}}. \quad (4-12)$$

$I_{\text{cal},i}$: LIF intensity of tracer i in calibration (flatfield)

T_{cal} : Core temperature in calibration (flatfield)

$p_{\text{cyl,cal}}$: In-cylinder pressure in calibration (flatfield)

$x_{f,\text{cal},i}$: Mole-fraction of fuel i in calibration (flatfield)

$I_{\text{LIF},i}$: LIF intensity of tracer + fuel i at CA of image acquisition (DI)

$T_{\text{AM,LIF}}$: Mixing temperature at CA of image acquisition (DI)

$p_{\text{cyl,LIF}}$: In-cylinder pressure at CA of image acquisition (DI)

$x_{f,i}$: Fuel mole-fraction of volatile fraction i in actual measurement (DI)

Now, the normalization allows to replace the tracer concentration x_i by the fuel concentration $x_{f,i}$ of the light-to-medium (n -pentane + iso -octane) and heavy (n -undecane) volatile components of the mixture. Also, the density in the measurement with DI and during calibration (flatfield) is now expressed by the in-cylinder pressure $p_{\text{cyl,LIF}}$ and $p_{\text{cyl,cal}}$ and temperature $T_{\text{AM,LIF}}$ and T_{cal} . T_{cal} is the adiabatic core temperature and $x_{f,\text{cal},i}$ is the fuel mole-fraction of either the light plus medium (n -pentane + iso -octane) or the heavy component (n -undecane) of the fuel during calibration in homogeneous operation. $x_{f,\text{cal},i}$ was calculated from the injected mass of fuel per cycle (far upstream of the intake) and the mass flow of N_2 that was measured by an MFC. In the current experiments, the fuel mole-fraction of the light to medium components is $x_{f,\text{cal,light}} = 0.69$ mol.-% and of the heavy component is $x_{f,\text{cal,heavy}} = 0.1$ mol.-%.

Output:

Eq. (4-10) and (4-12) created in steps 4 and 6, respectively, yield the desired look-up table relating the fuel mole-fraction and adiabatic-mixing temperature to the normalized LIF signals of DFB and 1MN, $[x_f, T_{\text{AM,LIF}}] = f_{1,2}(S_{\text{DFB}}, S_{\text{1MN}})$. In the course of the calculations the energy conservation only needs to be solved once, but adiabatic compression in step 5 and the calculation in step 6 need to be applied for every CA of image acquisition.

(b) Apply look-up table to images at a given CA (Figure 4-27b)

Figure 4-27b shows a block diagram for the application of the look-up table. Inputs to the look-up table are the crosstalk corrected DFB/1MN images S_{DFB} and S_{1MN} after 4×4 -pixel binning. Matrices of S_{DFB} , S_{1MN} , $T_{\text{AM,LIF}}$, and x_f each with 10×10 elements are available, which form the overall look-up table $[x_f, T_{\text{AM,LIF}}] = f_{1,2}(S_{\text{DFB}}, S_{\text{1MN}})$. The entries of $T_{\text{AM,LIF}}$ and x_f in the look-up table are linearly interpolated to S_{DFB} and S_{1MN} from the DI experiments.

Figure 4-32 shows an example of operations in the look-up table $[x_f, T_{\text{AM,LIF}}] = f_{1,2}(S_{\text{DFB}}, S_{\text{1MN}})$ created for images acquired at -35°CA . Figure 4-32a represents

the sub-level look-up table $x_f = f_1(S_{DFB}, S_{IMN})$ and Figure 4-32b $T_{AM,LIF} = f_2(S_{DFB}, x_f)$ visualized by the block diagram in Figure 4-27b with $x_f = \sum_{k=1}^3 x_f^{(k)}$. First, in (a) S_{DFB} and S_{IMN} are used to determine the fuel mole-fraction x_f . Then, in (b), x_f and S_{DFB} (S_{IMN} could also be taken) are applied to estimate $T_{AM,LIF}$. E.g., if $S_{DFB} = 4$ and $S_{IMN} = 5$, x_f will be 1.8 mol.-% and $T_{AM,LIF}$ will then be 565 K. This procedure is applied to all pixels in the FOV.

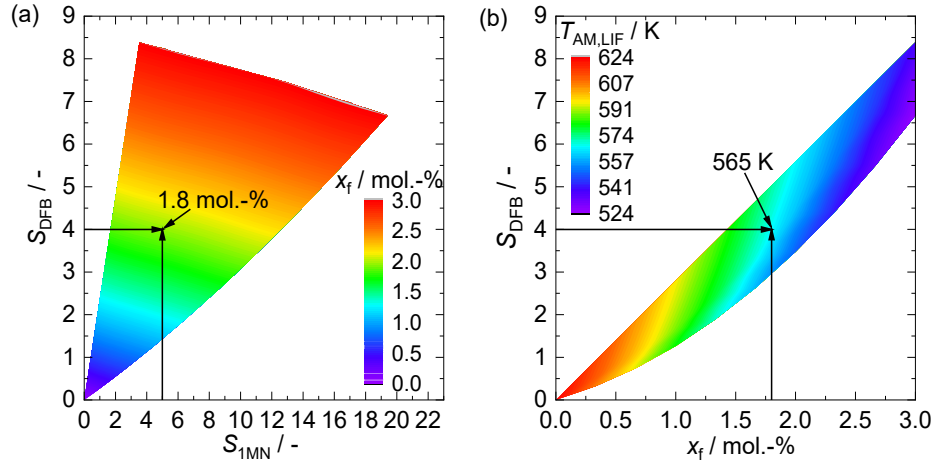


Figure 4-32: Example of a look-up table for -35°C A . (a) shows x_f as function of S_{DFB} and S_{IMN} , (b) $T_{AM,LIF}$ as function of x_f and S_{DFB} .

As mentioned in Section 3.3.3, the procedure was first applied to each pixel of each single shot in other publications and then extended to the procedure with the look-up table as used in the current thesis. Using a look-up table shortens the “wall-time” by orders of magnitude compared to solving the equation for every single shot and pixel separately. Solving of the energy conservation is significantly reduced. E.g., with the current MatLab code processing a set of 200 single shots with a total of $7.68 \cdot 10^6$ valid pixels using a look-up table of 10×10 elements takes in total 70 min per processor. If each image is processed in an iterative manner, which takes approximately 8 iterations (8 times solving energy equation) per image in the current study, then the wall-time is approximately 160-times greater. Thus, using a look-up table increases computational cost by approximately two orders of magnitude with minor numerical errors. If some of the computing were parallelized, then the overall wall-time could be reduced further.

4.6 Results and discussion

4.6.1 Preferential evaporation

Variation of injection timing

Figure 4-33 shows images of Mie scattering and tracer-concentration ratio S_{DFB}/S_{IMN} from experiment (B). Mie scattering shows the spray penetration and that the liquid spray

impinges on the piston top causing film evaporation. Although further crank angles are not included here, droplets were clearly visible until 10°CA aSOI. Since signal contribution from liquid-phase LIF currently cannot be quantified, LIF measurements were started after that time. In the first set of images at -55°CA and -35°CA in Figure 4-33a and (b), respectively, high-volatility components are preferentially found downstream, near the piston surface. These components evaporated first and were pushed forward by spray's flow. This convective effect can also be seen in the measurements of Itani [97, 98]. In contrast to those measurements in a large vessel, the jet in the engine interacts with piston-top and cylinder walls. Impinging on the piston top, the vaporized fuel is directed towards the cylinder walls outside of the FOV. At later crank angles, $S_{\text{DFB}}/S_{\text{1MN}}$ differs less from unity compared to earlier image timings due to mixing with the surrounding gas and of the fuel components. Injection at -67.75°CA results in more pronounced segregation of fuel components than injection at -47.75°CA because of slower evaporation at lower temperatures. Nevertheless, over the entire crank-angle range investigated here, the effect of preferential evaporation is significant. As expected in turbulent mixing, the inhomogeneity in typical single shots (top rows of Figure 4-33a and b) exceeds that of the multi-cycle mean (bottom rows).

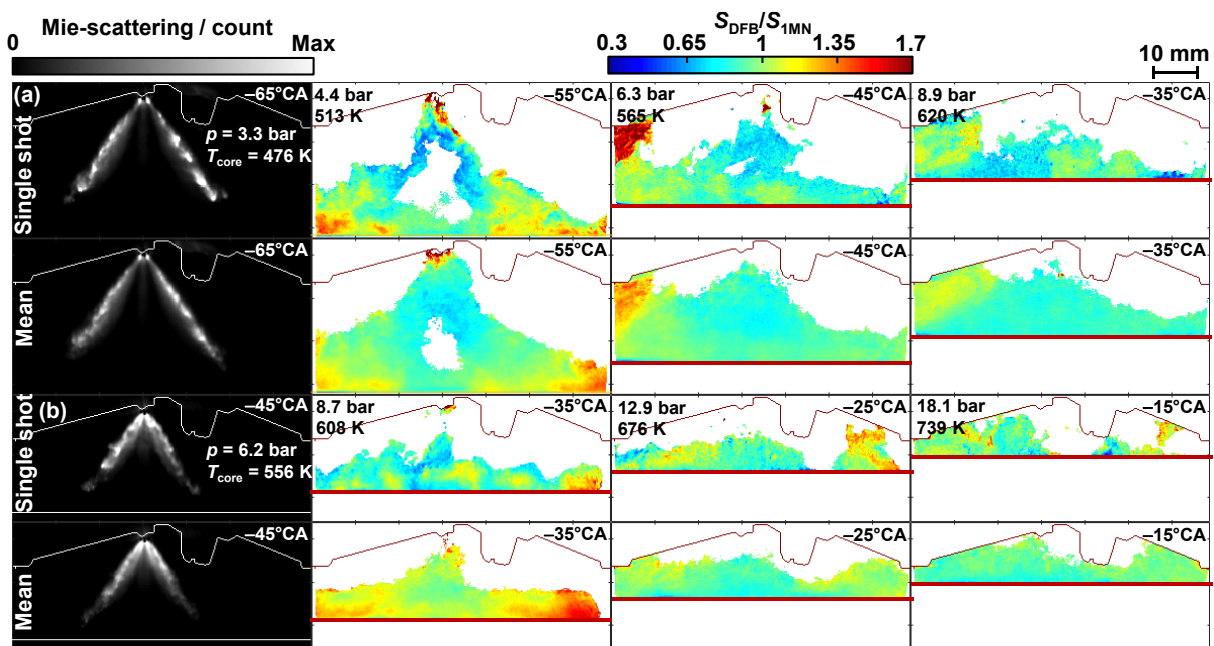


Figure 4-33: Mie-scattering images (gray scale) from the liquid phase and tracer concentration-ratio images (color scale) at different crank angles, (a) for injection at -67.75°CA , (b) for injection at -47.75°CA . Ratios greater than unity indicate a surplus of the high-volatility components, values lower than unity of the low-volatility component. Figure published in [53].

Variation of intake-valve lift

The magnitude of the tumble flow during the compression stroke may influence the fuel and component distribution. Figure 4-34 shows a comparison of snapshots of $S_{\text{DFB}}/S_{\text{1MN}}$ in

panels (a), (b), (c) and the 200-cycle ensemble averages in (d) from engine runs with 4 mm and 9 mm IVL at -37°CA upon SOI at -47.75°CA . The images were computed as described in Section 4.5.1.

Ensemble average images of $S_{\text{DFB}}/S_{\text{1MN}}$ show that the fuel evaporates from the piston top surface with a significant surplus of light components, while heavy components are predominantly located upstream in the fuel vapor cloud. The snapshots in Figure 4-34a-c show that cycle-to-cycle variability affects the location and fraction of the fuel components. In some snapshots a surplus of high volatility components can also be found upstream in the fuel vapor cloud closer to the injector and spark plug than at the piston. But upstream, the probability of finding $S_{\text{DFB}}/S_{\text{1MN}} > 1$ is low, since the 200-cycle average ratio is lower than unity in that region.

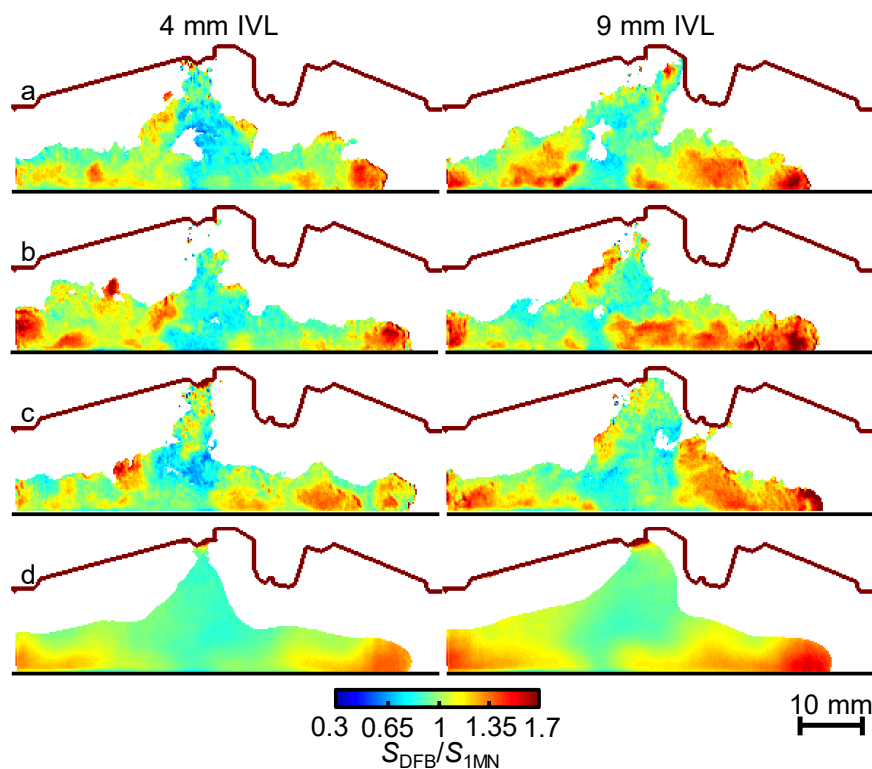


Figure 4-34: Example results of $S_{\text{DFB}}/S_{\text{1MN}}$ at -37°CA with 4 mm and 9 mm IVL. Injection at -47.75°CA . Rows a, b, and c show three snapshots and d shows the 200-snapshot average.

Comparing the influence of a change in IVL, it can be seen that the symmetry of the fuel vapor cloud is affected. The tumble flow at 4 mm IVL weakly affects the symmetry of the two fuel-vapor plumes, but at 9 mm IVL the plumes are significantly rotated in clockwise direction following the direction of the tumble flow shown in Figure 4-10 at $z = 0$ mm. Also, it seems that a larger area with tracer-concentration ratios greater than unity is present at 9 mm IVL than at 4 mm IVL. This may be due to an increase in convective transport due to higher velocity magnitudes at 9 mm compared to 4 mm IVL as demonstrated in the velocity fields in Figure 4-10. Hence, an increase in the magnitude of the tumble flow causes a more pronounced

separation of light and heavy components during the spatio-temporal process of droplet evaporation.

4.6.2 Temperature imaging

In this section the temperature results from adiabatic mixing, and two-color LIF thermometry are discussed. Since now the temperature at image acquisition is discussed, the nomenclature of “ $T_{AM,LIF}$ ” is reduced to “ T_{AM} ”. In general, AM is valid only for an adiabatic system, i.e. without heat transport through boundaries. In the combustion chamber of an engine, AM may only be accurate far away from surfaces and in non-reactive operation, e.g. without combustion. 2CT may reflect a more realistic temperature, independent from mass and/or heat transport. The accuracy of the temperature computed via 2CT is primarily influenced by errors in the calibration.

Two data sets with similar engine operation, from 2CT with anisole and AM with DFB and 1MN, will be compared. Table 4-4 summarizes the boundary conditions of those engine runs to discuss the deviations in ambient parameters. The adiabatic mixing temperature T_{AM} is computed from the measurement of preferential evaporation in experiment (B), while the temperature images via two-color LIF T_{2CT} are determined from anisole-LIF images in experiment (C) in a separate engine run. The major differences in both experiments are the tracers, and that for 2CT additionally to DI also fuel is injected upstream of the intake port. The additional fuel causes a decrease in the isentropic coefficient from $\kappa = 1.39$ in the AM experiment (B) to $\kappa = 1.36$ in the 2CT experiment (C) at -68°CA . Thus, in the latter the overall in-cylinder temperatures are expected to be lower than that in the AM experiment.

Table 4-4: Boundary conditions of two engine runs with two temperature methods, two-color thermometry (anisole, 2CT) and adiabatic mixing (DFB/1MN, AM). For case *, additionally to DI fuel is also injected upstream of the intake.

Parameter	Value	Unit
Method	2CT	AM
Experiment	(C)	(B)
Tracer	Anisole	DFB/1MN
Fuel	Multi-comp.	Multi-comp.
SOI	-67.75	-67.75 / $^\circ\text{CA}$
T_{core} at SOI	465	468 / K
T_{core} at -35°CA	608	619 / K
p at SOI	3.31	3.28 / bar
κ at -68°CA	1.36	1.39 / -
N_2 mass flow	4.97	5.00 / g/s
Injected mass FF	14.53	14.26 / mg/cycle
Fuel fraction FF	0.81	0.79 / mol.-%
Injected mass DI	10 (+ 14.32*)	10 / mg/cycle

Figure 4-35a shows the crank-angle evolution of snapshots and the 20-cycles means of T_{2CT} and T_{AM} . Additionally, row (b) in Figure 4-35 shows the subtraction of the ensemble means as $T_{2CT} - T_{AM}$. T_{AM} was additionally 4×4 -pixel binned to fit to the spatial resolution in T_{2CT} which is 0.96 mm/px. Overall, both techniques reveal a lower temperature along the spray jet-axes than in the adiabatic core. In addition to the latter, single shots of T_{2CT} show noise that is much higher than the noise in T_{AM} . In other words, the single-shot precision in images of T_{2CT} is considerably worse than in images of T_{AM} .

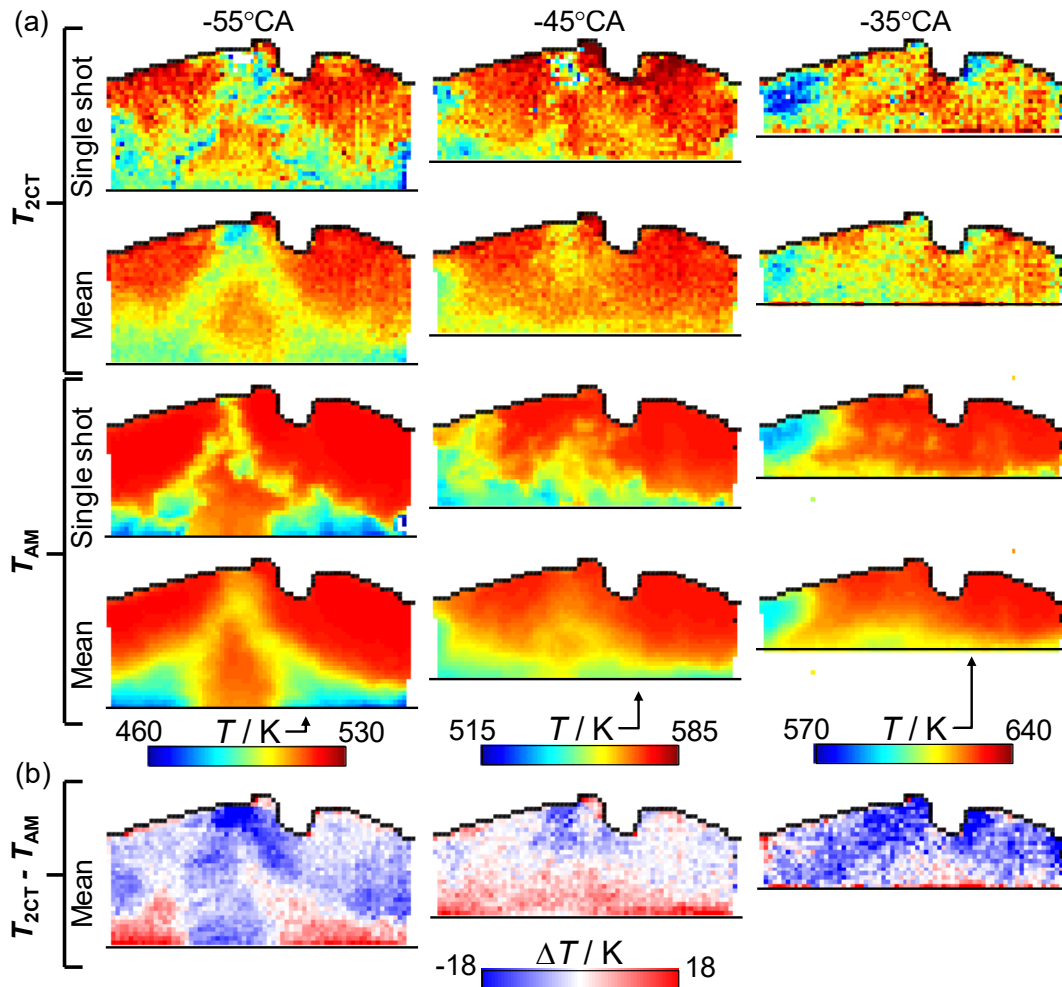


Figure 4-35: Crank-angle evolution of temperature fields determined by means of anisole 2CT, T_{2C} , and AM, T_{AM} . (a) crank-angle evolution of single shot and mean temperature images. (b) temperature deviation $T_{2CT} - T_{AM}$ of the ensemble means.

At -55°CA the mean of T_{2CT} shows that the temperature in the fuel region is overall about 20 K lower than the adiabatic core. Due to heat transfer to the piston surface, the lowest temperature is reached near where the fuel impinges. Looking at T_{AM} in Figure 4-35a and the difference to T_{2CT} in (b) shows that the temperature gradient along the spray-jet axes at -55°CA is steeper in T_{AM} than in T_{2CT} . The lowest temperature is found near the piston surface where at -55°CA T_{AM} is about 35 K and T_{2CT} is about 25 K lower than T_{core} .

A major influence on the temperature near the surface is the location where the liquid fuel has been evaporated. If heat is transferred from the fuel film to the piston or vice versa, then the phenomenon is not adiabatic, and AM hence inaccurate. The 2CT method, however, does not neglect heat transfer from or to the piston material, thus it is a direct measurement of the temperature. Overall, it is expected that 2CT has higher accuracy close to surfaces compared with AM.

Single shots of T_{2CT} in Figure 4-35a at -55°CA also show temperature gradients outside the fuel region, e.g. right of the spark plug. Here some stratification in temperature is detected that cannot be seen in T_{AM} , since there the LIF signal is zero that region.

Later in the cycle, at -45°CA the temperature deviation shown in (b) reduces, but T_{AM} near the piston surface is still lower than T_{2CT} in that region. Near the injector tip the situation is the other way around, T_{2CT} is lower than T_{AM} . Towards TDC, at -35°CA the deviation in temperature in (b) is almost flat with minor gradients near the piston surface. Overall, the temperature from T_{2CT} is about 8 K lower in most regions of the FOV, probably due to the reduction in compression-induced temperature increase by the additionally injected fuel.

4.6.3 Measurement uncertainty

Errors in terms of precision and accuracy appear due to several effects. Spatial mismatch after registration, inaccurately corrected tracer crosstalk, and, in particular, temperature differences between calibration (flatfield) and actual measurement (with DI) can affect the accuracy of the measurements.

Single-shot precision is estimated from series of ratios of flatfield images corrected with the mean flatfield, where theoretically S_{DFB}/S_{1MN} should be unity throughout every shot. However, the standard deviation among pixels in an area of $4 \times 4 \text{ mm}^2$ of a typical single shot is $\sigma_{\text{area}} = 0.08$. Photon noise and systematic errors in laser-profile correction are likely sources for this error. The standard deviation in one pixel over a series of single shots is $\sigma_{S2S} = 0.04$. Since this shot-to-shot deviation is statistically uncorrelated from the spatial variation, the overall precision is estimated according to $\sigma = \sqrt{\sigma_{\text{area}}^2 + \sigma_{S2S}^2} = 0.09$. Thus, preferential presence of heavy or light components is determined with a single-shot precision of 9% at a relative tracer-concentration ratio of 1.0 and 0.24-mm resolution.

The bulk-gas core temperature can be calculated from adiabatic compression, but the local temperature is unknown and implicitly assumed to be homogeneous and identical in flatfield and DI images. In reality, due to the fuel's latent heat of vaporization, the temperature in the jet $T_{\text{jet}} = T_{\text{core}} + \Delta T$ is lower than in the bulk-gas core as shown in Figure 4-35a. Additionally, there may be increased wall heat transfer where the fuel-vapor jet interacts with the piston. However, similar to the temperature-dependency of the DFB and 1MN intensity shown in Figure 4-31, with the flatfields from DFB/1MN-LIF in experiment (B) a series of images are available, in which the two tracers are present at known and constant ratio over a wide range of temperatures. Thus, this image series can also be used to estimate the relationship between tracer signal ratio

$S_{\text{DFB}}/S_{\text{1MN}}$ and temperature. Figure 4-36a shows $S_{\text{DFB}}/S_{\text{1MN}}$, extracted in a small region of the ensemble-average flatfields, as a function of T_{core} . Parametrizing the data with an ad-hoc fit function, the relative error ε as a function of T_{core} and the deviation ΔT from it is shown in Figure 4-36b. If for example $T_{\text{core}} = 560$ K and $\Delta T = -30$ K, the LIF measurement would measure $S_{\text{DFB}}/S_{\text{1MN}}$ 10% too high.

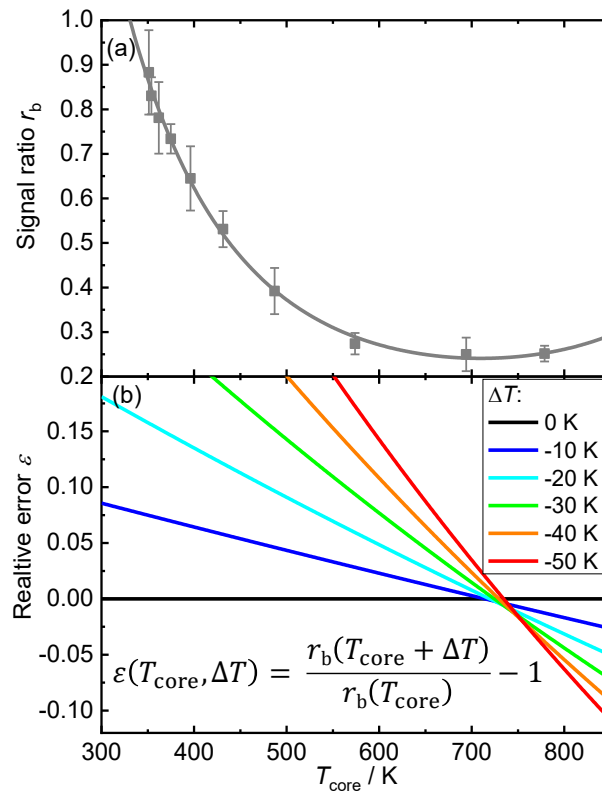


Figure 4-36: (a) Signal ratio $r_b = S_{\text{DFB}}/S_{\text{1MN}}$ extracted from a small region in DFB/1MN-LIF flatfields in experiment (B) from -180°CA to TDC parameterized as a function of T_{core} . (b) Relative error ε in $S_{\text{DFB}}/S_{\text{1MN}}$ induced by temperature deviation ΔT from T_{core} . ε is calculated by the equation given in the figure. The error bars indicate the noise (one standard deviation) in the evaluated small region. Figure published in [53].

Now an estimate of the actual local temperature in the DI experiment is needed, which is why the two-color anisole-LIF thermometry, experiment (C), had been performed, and adiabatic mixing had been applied on the actual DFB/1MN data in experiment (B), as described in Sections 4.5.3 and 4.5.4. Example images from 2CT for injection at -67.75°CA are shown in Figure 4-37. At -55°CA , the temperature on the jet axis is about 20 K lower than the adiabatic core temperature of 510 K, which translates to $\varepsilon \approx 0.09$. Near the piston surface the deviation increases to $\Delta T = -25$ K, or $\varepsilon \approx 0.12$. The positive error means that in the DI experiment (B), the concentration of DFB is overestimated with respect to 1MN.

For later crank angles the error should be smaller. Not only does T_{core} increase towards TDC, which decreases ε until $T_{\text{core}} = 730$ K is reached (Figure 4-36b), but also temperature

deviations should decrease due to mixing. However, at -35°CA on the left side of the combustion chamber, Figure 4-37 shows a zone that anisole-LIF measures to be 35 K colder than the bulk gas. This is probably due to fuel-rich mixture that already was outside of the field of view at -55°CA and has been convected back into the imaged area by the combined action of tumble flow and cylinder wall. As expected from Figure 4-36b, this relatively large temperature “deficit” results in a smaller error ($\varepsilon \approx 0.10$), because at the now higher overall temperatures LIF from DFB and 1MN are more similar in their temperature sensitivities.

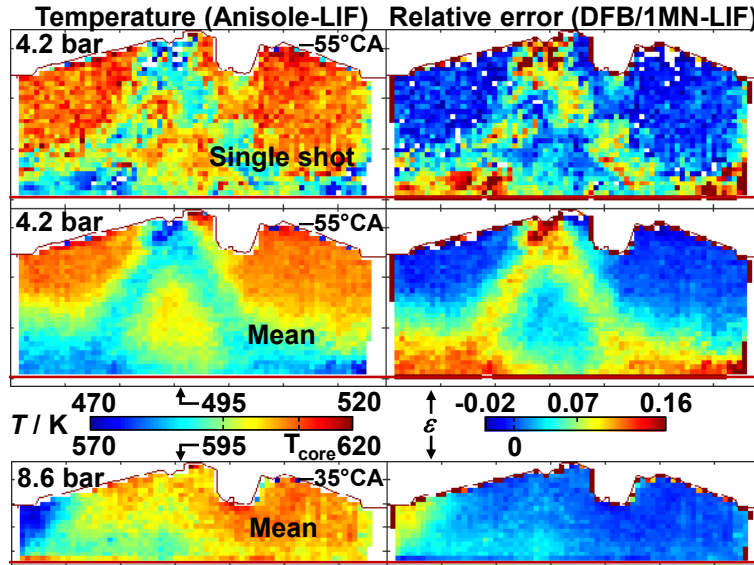


Figure 4-37: Left column: Single shot and ensemble-mean temperature distribution with DI at -67.75°CA derived from anisole 2CT. The mean temperature is shown for -55°CA ($T_{\text{core}} = 510 \text{ K}$) and -35°CA ($T_{\text{core}} = 610 \text{ K}$). Right column: Corresponding temperature-induced error ε incurred in the relative ratio $S_{\text{DFB}}/S_{\text{1MN}}$. Figure published in [53].

4.6.4 Fuel composition and concentration

In a next step, $S_{\text{DFB}}/S_{\text{1MN}}$ is translated into fuel-component fractions using the fuel maps (see Figure 4-25) provided in Bardi et al. [104]. First, the influence of the deviation between the temperature in the calibration and the actual DI experiment (B) on the tracer-concentration ratio r_b is corrected via

$$r_b = \frac{r_{b,i}}{(1 + \varepsilon(T_{\text{core}}, \Delta T))} \quad (4-13)$$

In Eq. (4-13) the relative error ε shown in Figure 4-36b is used to correct the initial tracer-concentration ratio $r_{b,i}$ in each pixel. This means if ε is positive then the initial ratio is overestimating the concentration of DFB with respect to 1MN. The relative error ε is dependent on T_{core} and the deviation ΔT from T_{core} in the DI experiment. ε is parametrized as an ad-hoc function as shown in Figure 4-36. To apply the correction, the temperature deviation ΔT is a necessary input that can be determined in three ways: First, by assuming that the spray is

isothermal and the is temperature equal to T_{core} throughout the combustion chamber such that $\Delta T = 0$ K, hence no correction is applied. Second, via the ensemble mean temperature from 2CT, such that $\Delta T = T_{\text{core}} - T_{2\text{CT}}$. However, $T_{2\text{CT}}$ is from experiment (C) and was measured in a different engine run than the two-tracer LIF in experiment (B) quantifying $S_{\text{DFB}}/S_{\text{1MN}}$. Thus, the boundary conditions slightly differ. Thirds, from AM in single shots of experiment (B), such that $\Delta T = T_{\text{core}} - T_{\text{AM}}$.

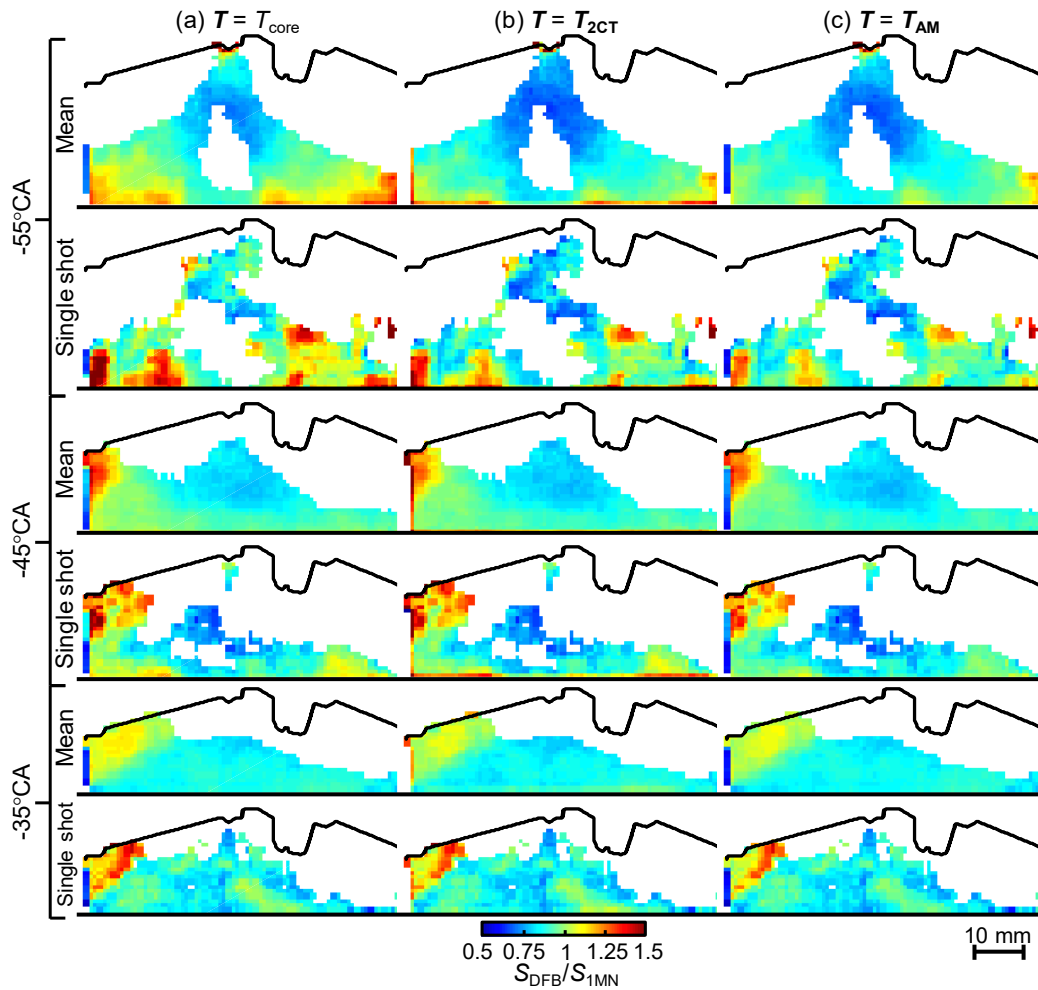


Figure 4-38: (a) Uncorrected tracer-concentration ratio (isothermal, $T = T_{\text{core}}$), (b) ratio corrected via ensemble average temperature from anisole-LIF 2CT ($T = T_{2\text{CT}}$), and (c) corrected via temperature snapshots from DFB/1MN-LIF AM ($T = T_{\text{AM}}$). All images are binned to a spatial resolution of 0.96 mm/pixel.

Figure 4-38 shows the crank-angle evolution of the 20-cycle ensemble means and single shots of $S_{\text{DFB}}/S_{\text{1MN}}$ corrected with different temperature deviations. Data from the test with injection at -67.75°CA and 4 mm IVL are shown. All images were binned to a spatial resolution of 0.96 mm/pixel. Figure 4-38a shows the uncorrected tracer-concentration ratio ($T = T_{\text{core}}$), (b) shows the ratio corrected by $T_{2\text{CT}}$, and (c) the ratio $S_{\text{DFB}}/S_{\text{1MN}}$ corrected via T_{AM} .

Corrections of $S_{\text{DFB}}/S_{\text{1MN}}$ by $T_{2\text{CT}}$ and T_{AM} cause an overall decrease in the tracer-concentration ratio. The strongest change in $S_{\text{DFB}}/S_{\text{1MN}}$ occurs if the uncorrected ratio, Figure 4-38a, is corrected via T_{AM} . At -55°CA in (c) $S_{\text{DFB}}/S_{\text{1MN}}$ decreases up to 16% in the mean image compared to the uncorrected image in (a). Towards 730 K the temperature sensitivities of DFB and 1MN fluorescence become similar (see Figure 4-36b). Therefore, $S_{\text{DFB}}/S_{\text{1MN}}$ decreases to less than 5% at -35°CA , even though the deviation of the measured temperature from T_{core} becomes larger. Also, as expected, the change in the tracer-concentration ratio in single shots is stronger using single shots of T_{AM} instead of the mean temperature via 2CT.

From the corrected tracer-concentration ratio the fuel-mass composition is determined. Here, T_{AM} is used to correct the temperature influence on the ratio. Figure 4-39 shows the overall mass fraction $\omega = m_f/(m_{\text{N}_2} + m_f)$ of the fuel via AM and the fuel-mass composition c_f determined from the temperature-corrected tracer-concentration ratio via interpolation of the fuel maps shown in Figure 4-25. Crank-angle evolutions of ω and c_f with -67.75°CA SOI and both IVLs are shown. The homogeneous composition $c_{f,h}$ is 33 mass-% *n*-pentane, 47 mass-% *iso*-octane, and 20 mass-% of *n*-undecane, with a homogeneous (global) total fuel-mass fraction of $\omega_h = 2$ mass-%. These homogeneous reference compositions are denoted in each of the color scales in Figure 4-39.

At -55°CA and 4 mm IVL, the highest fuel-mass fraction of about 8 mass-% is located near the piston surface, but near the injector tip the fraction of fuel is slightly lower than the homogeneous fuel fraction $\omega \leq \omega_h$. When the IVL is increased, the location of the highest fuel fraction is relocated in direction of the tumble flow, which is more pronounced for the fuel-vapor plume located left from the injector tip. Additionally, preferential evaporation causes an inhomogeneous distribution of the fuel-components as apparent in c_f . Significant component segregation remains until late during the compression stroke when ignition would occur in fired operation. At -55°CA preferential evaporation is more pronounced at 9 mm IVL than with 4 mm IVL. The highest fraction of *n*-pentane is located near the piston surface. Contrary to that, the less volatile components (*iso*-octane and *n*-undecane) are preferentially found near the injector tip. At later crank angles, the overall fuel fraction homogenizes in the fuel region and the component segregation becomes less pronounced. In the case of 9 mm IVL, it can be seen that the tumble motion of the bulk (see Figure 4-10) causes the plumes to rotate clockwise, which is less pronounced with 4 mm IVL.

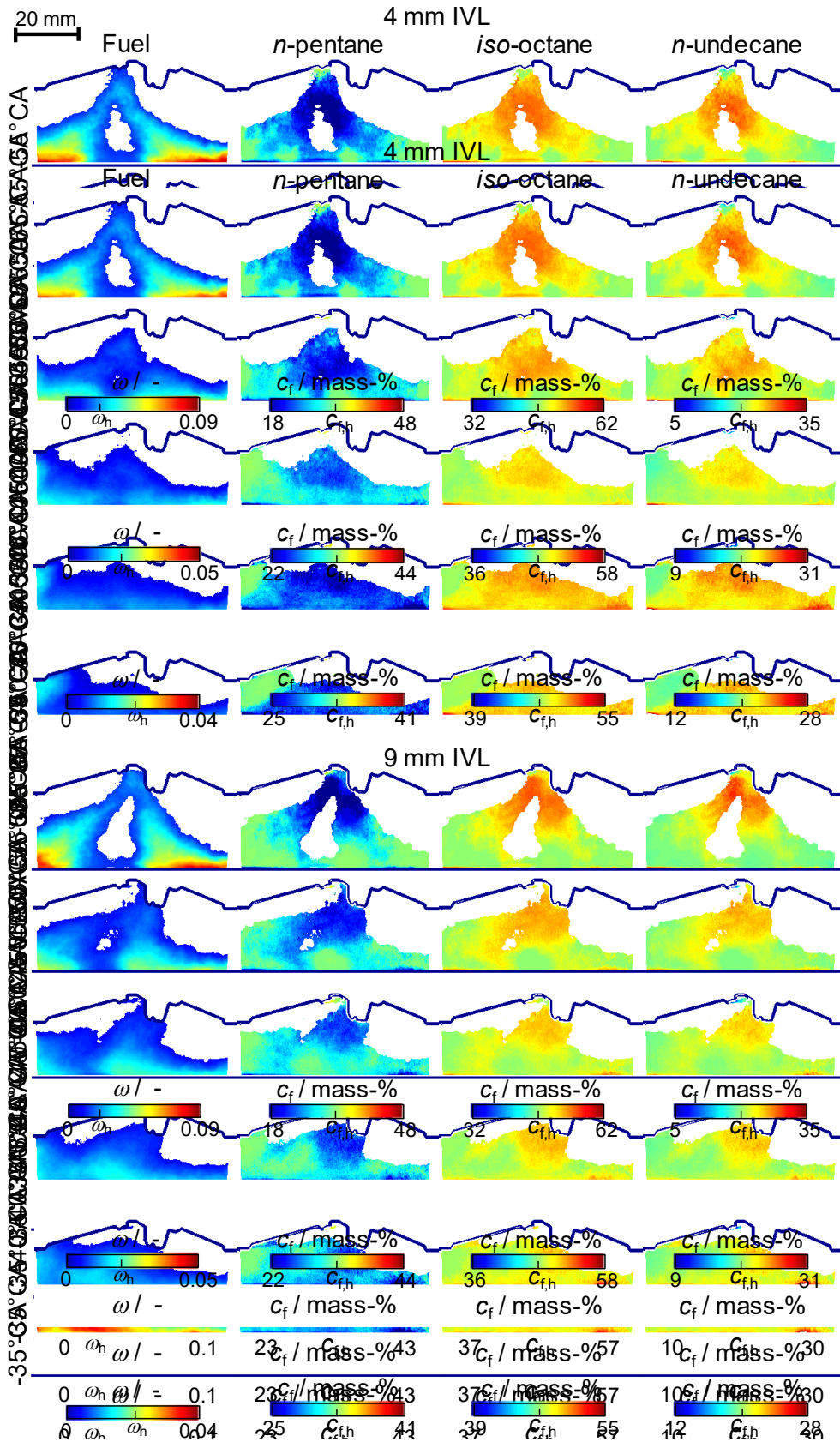


Figure 4-39: Evolution of the 20-cycle mean of fuel-mass fraction ω and fuel-component composition c_f , determined using the evaporation model in [104]. 4 mm and 9 mm IVL with -67.75°CA SOI are shown. The composition in a perfectly homogeneous mixture ($S_{\text{DFB}}/S_{\text{IMN}} = 1$) is at ω_h and $c_{f,h}$ as marked in each of the color scales.

From the crank-angle evolution of ω and c_f between -55°CA and -35°CA with 9 mm IVL it can be noticed that a fuel mixture of nearly homogeneous fuel-component composition is convected from the exhaust side along the piston surface towards the intake side of the combustion chamber. In contrast to the latter, the fuel-component composition near the spark plug has a surplus of *iso*-octane and *n*-undecane but is poor of *n*-pentane with respect to $c_{f,h}$. Also, it is apparent that the overall fuel mass does not correlate with the fuel-vapor composition, e.g. in regions of great ω the fuel composition can be close to homogeneous but in other regions overall heavy. Also, towards TDC the component segregation becomes less because of mixing.

With 4 mm IVL the situation is different: The fuel region near the piston surface probably caused by the left spray plume, is convected to the left side, outside the FOV, and then moved back into the FOV from around -45°CA . This region of high ω has a surplus of *iso*-octane as seen in the fuel-component distribution c_f . The movement of the fuel coincides with the tumble flow shown in Figure 4-11 after subtraction of the compression-induced velocity. The fuel region, which was initially caused by the right spray jet, however, is not transported and stays near the piston surface at least until -40°CA . Overall, with 9 mm IVL the effect of preferential evaporation is initially more pronounced compared to with 4 mm IVL. An increase in turbulent air-fuel mixing causes earlier homogenization shown by the larger region close to the homogeneous mixture $c_{f,h}$ at -35°CA . The latter also applies to ω .

In the vicinity of the spark plug, late in the compression stroke at -35°CA and 9 mm IVL a fuel-composition of 28 mass-% *n*-pentane, 50 mass-% *iso*-octane, and 23 mass-% of *n*-undecane is present. The inhomogeneous composition may affect ignition, combustion, and, in worst case may cause engine knock (autoignition) or flame extinction. It is not intuitive to tell from the images in which regions autoignition could occur since this is dependent on the local temperature and mixture in fired operation. However, from literature it is known that *n*-undecane has an autoignition temperature of 195°C , *n*-pentane of 260°C , and *iso*-octane of 410°C at 1 bar [160]. Even though the pressure also has an influence on autoignition, high concentration of *n*-pentane and/or *iso*-octane tend to lower the onset of autoignition.

To further discuss the influence of a change of the IVL, Figure 4-40 shows the fuel-component composition c_f of two single shots, the ensemble means, and the one-standard deviation σ of 200 consecutive cycles at -55°CA / -67.75°CA SOI comparing 4 mm with 9 mm IVL. At -55°CA the first images after fuel evaporation are available.

Single shots of c_f in Figure 4-40 show even more pronounced component segregation compared to the ensemble mean. In large regions near the piston surface c_f of *n*-pentane slightly exceeds $c_{f,h}$, and *iso*-octane mainly surpluses near the injector tip. Close to the injector tip, the spatial occurrence is quite intermittent due to the turbulent mixing with the surrounding gas, which is compensated in the ensemble mean, by neglecting regions without fuel in the calculation (see explanations in Section 4.5.1). Contrary to this, *n*-pentane has the widest spread in c_f of 33 mass-% near the piston surface down to 18 mass-% near the injector tip, or, with 9 mm IVL 21 mass-% near the spark plug. An increase in IVL convects all fuel-components closer to the spark plug and increases the effect of preferential evaporation at -55°CA slightly.

Cyclic variability, visualized by one standard deviation in each pixel of each fuel component over 200 snapshots, is the strongest near the injector tip and the spark plug. In that region CCV in the fuel-component fraction is more pronounced with 4 mm IVL compared to 9 mm IVL. Relative to the mean in each pixel, the fraction of *n*-pentane near the injector tip varies overall the most. Near the piston surface, the variability increases with IVL, but the variability between the two fuel-vapor plumes significantly decreases at higher IVL. As discussed in Section 4.3.5, an increase in velocity magnitude between spray plumes is vital for preventing spray collapse. The decreased CCV in that region may indicate that spray collapse might be lower with 9 mm IVL.

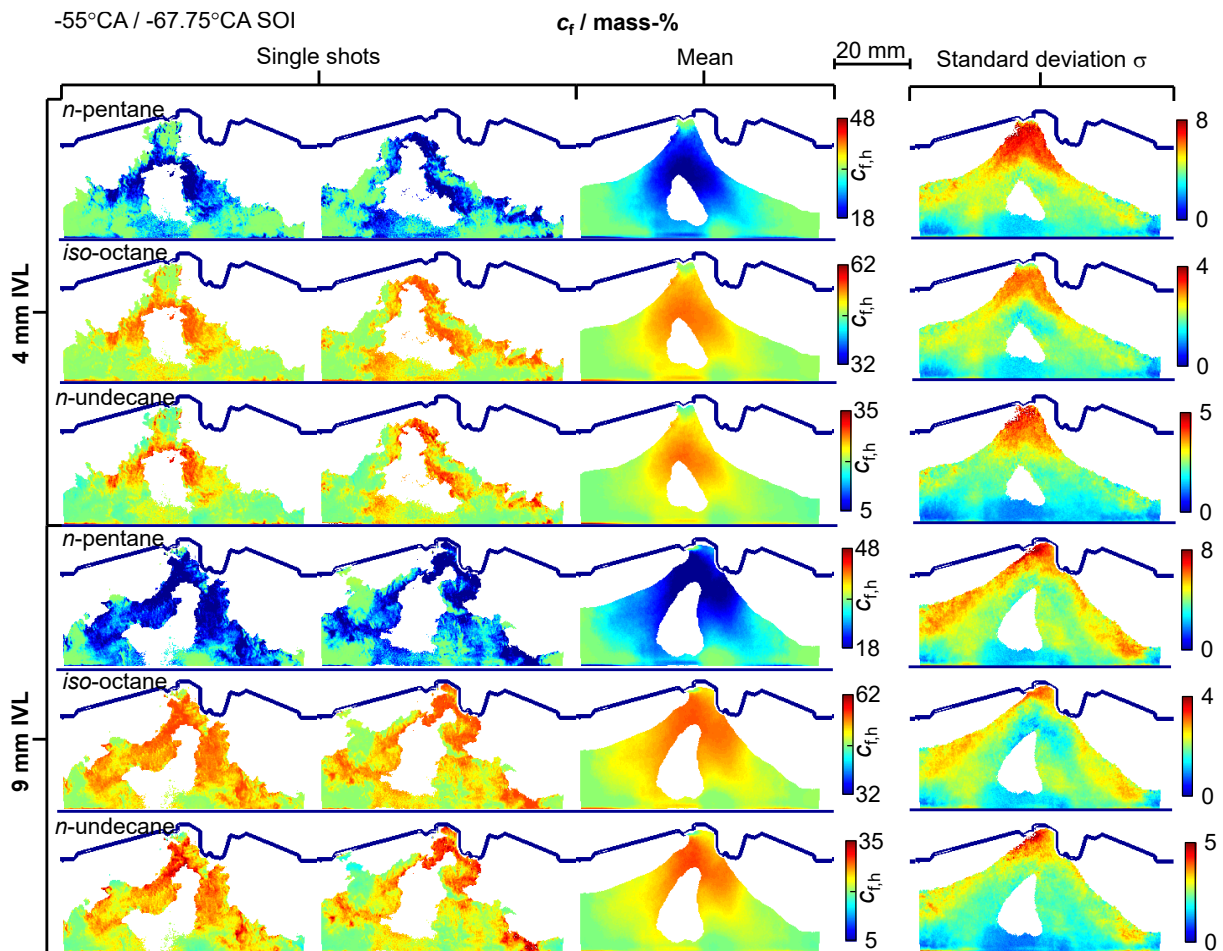


Figure 4-40: Two single shots, 200-cycle mean, and standard deviation of the fuel-component distribution at -55°C . Injection at -67.75°CA SOI. IVL: 4 mm and 9 mm.

Figure 4-41 shows the fuel-component composition c_f of two single shots, the ensemble means, and the one-standard deviation σ of 200 consecutive cycles at -37°C / -47.75°CA SOI with each of the IVLs. At -37°C the first images after fuel evaporation are available for late fuel injection.

Again, an increase in IVL does increase the fuel-component segregation, and an increase in IVL overall lowers cyclic variability in c_f . The overall standard deviation is about half of that of 200 snapshots 13°CA aSOI when injection is initiated at -67.75°CA shown in Figure 4-40. For injection at -47.75°CA the spread in fuel-mass fraction of n -undecane is between 16 mass-% and 22 mass-% at -37°CA , which is quite consistent with the spread of c_f from n -undecane in Figure 4-39 at -35°CA with injection at -67.75°CA . As already addressed in Section 4.6.1, one possible explanation for the decrease in fuel-component segregation between the two injection timings is that the spray evaporates faster when injection takes place later in the compression stroke at higher ambient temperature and density. Thus, the fuel components have less time for segregation if injection occurs late during compression compared to injection taking place 20°CA earlier in the cycle.

The reader is reminded that the simplifying assumptions made in the model calculations of [104] may not apply for the complex situation of droplet evaporation in an engine spray. The dominating droplet evaporation processes in engine sprays are discussed in literature [161-163] where the dimensionless Peclet number is used to describe the ratio of the surface regression rate (evaporation rate) to the liquid diffusion coefficient. If the Peclet number is greater than 1 then the process is limited by liquid diffusion and is not distillation like. In the current study it is assumed, that for 4 mm IVL and injection at -67.75°CA the evaporation most possible is distillation like. However, the accuracy of the results shown in Figure 4-39, Figure 4-40, and Figure 4-41 cannot be addressed yet.

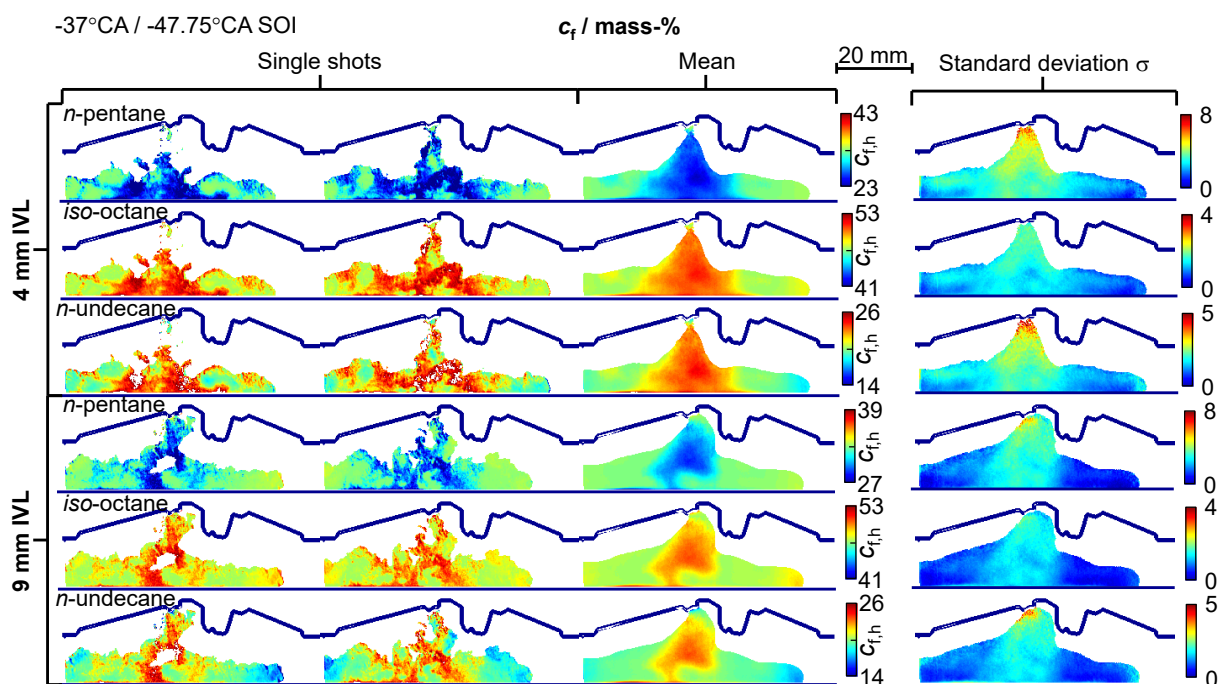


Figure 4-41: Two single shots, 200-cycle mean, and one-standard deviation of the fuel-component distribution at -37°CA . Injection at -47.75°CA SOI. IVL: 4 mm and 9 mm.

4.7 Section conclusions

The effect of preferential evaporation upon late GDI of a multi-component surrogate was investigated with a two-color two-tracer LIF imaging technique in an optically accessible engine motored on nitrogen. Before the actual LIF gas-phase imaging, the liquid penetration of *iso*-octane and the three-component surrogate consisting of *n*-pentane, *iso*-octane, and *n*-undecane were studied via Mie scatter and diffuse back-illumination imaging color-coded by a combination of RGB-LED illumination and detection by a Bayer array. Additionally, the influence of the in-cylinder flow field, measured by PIV, on the spray penetration was studied. Data were compared to spray-penetration data in an optical engine at TU Darmstadt and to results of a CFD simulation at RWTH Aachen. For LIF imaging a pair of aromatic tracers, 1,4-difluorobenzene (DFB) and 1-methylnaphthalene (1MN), were added to the multi-component surrogate representing the light-to-medium and heavy components, respectively. Measurement uncertainties and in particular the error induced by variations in temperature were assessed by means of two-color anisole LIF thermometry and an adiabatic mixing calculation. An adiabatic-mixing model was developed, partially validated against data from FAU Erlangen, and the mixing temperature from the model was compared to the temperature determined via two-color LIF thermometry in a separate experiment. To increase the accuracy in the final fuel-component fractions, the temperature deviation between calibration and the DI experiment was corrected for. Finally, the fuel-vapor composition was calculated from results of a thermodynamic model provided by collaborators at IFPen [104].

Imaging was performed after late fuel injection by a centrally mounted 8-hole injector. Injection at -47.75°CA takes place at conditions close to the ECN Spray G standard condition. To reduce wall wetting, earlier injection at -67.75°CA was also investigated. The engine speed was 1200 min^{-1} , and two intake-valve lifts – 4 mm and 9 mm – were used to affect a change in in-cylinder bulk flow. The combination of spray imaging via DBI and Mie scattering, flow-velocity measurements via PIV, and fuel-vapor imaging via LIF allows for an analysis of mixture formation affected by the interaction between the liquid-fuel penetration, fuel-component segregation, and in-cylinder flow.

Visualization of the liquid fuel penetration and measurements of the in-cylinder velocity fields yielded several insights. Spatial spray probability distributions showed that cyclic variation increase both over the course of the injection and with an increased magnitude of in-cylinder bulk flow. These observations were explained by increased turbulent mixing of the spray with the surrounding flow structures. The temporal evolution of the axial spray penetration is marginally influenced by a variation of bulk-flow velocity magnitude. Only a minor decrease of the spray expansion with increased flow-field velocity was observed. A comparison with experiments in a constant-volume chamber showed deviations as the piston approaches the spray, causing wall impingement. Nevertheless, in addition to the increase in bulk-gas density, the influence of the in-cylinder flow on the spray development must be considered in engines operating with late fuel injection. In comparison with the spray penetration of *iso*-octane in the engine at TUD [54], it was found that the upward recirculation flow in-between spray plumes is enhanced with increased in-cylinder tumble. This stabilizes the spray shape and prevents an unwanted spray collapse induced by plume-to-plume

interaction as previously reported by Sphicas et al. [18]. With the late injection strategy investigated here, the in-cylinder flow is heavily disturbed by the spray that induces a strong aerodynamic motion of the surrounding gas. The weak tumble can hardly preserve its initial momentum, resulting in a flow structure that is characterized by two counter-rotating vortices caused by fluid entrainment during the spray development.

Taking the measurement uncertainty of the two-tracer, two-color LIF imaging into account, tracer segregation and thus preferential evaporation of the fuel components were significant for all investigated conditions. Just after the fuel has completely evaporated, low-volatility components were preferentially found near the injector tip, high-volatility components primary downstream at the tip of the vapor cloud. This is consistent with previous results in a high-pressure vessel [97, 98]. Spatio-temporal mixing of the fuel with the bulk gas decreases the effect of preferential evaporation towards TDC, and injection later in the compression stroke also decreases the overall segregation. Also, it was found that increased tumble in the bulk flow decreases the effect of preferential evaporation. However, in contrast to measurements in a high-pressure vessel, the in-cylinder flow significantly influences the location of the fuel components, and the change in gas temperature and density with crank angle influences the obtainable LIF signal.

Two-color anisole-LIF thermometry in a separate experiment showed that after complete evaporation the ensemble-mean temperature in the injection jet at -55°CA is about 20 K to 25 K lower than the adiabatic core temperature. This corresponds to a relative error induced by temperature inhomogeneities in the tracer-concentration ratio of less than 11% throughout the measured crank-angle range, which seems reasonable given the unfavorable conditions of experiments in IC engines. Simultaneous thermometry is in principle possible [97] but was not attempted in the engine experiments here in favor of lower uncertainty. But with anisole a tracer was available that allowed at least temperature imaging in separate experiments without touching the detection optics. This is very useful because two-color LIF thermometry is sensitive to the pixel-level registration of the two detection paths. The temperatures determined by adiabatic air-fuel mixing from the DFB/1MN-LIF experiment agree reasonably well with those from anisole LIF but are too low by about 10 K near the piston surface just after complete fuel evaporation. Towards TDC, the deviation between the two temperatures becomes less. The presented adiabatic mixing model assumes quasi-instantaneous fuel-bulk mixing and does not consider the spatio-temporal evolution of mixture preparation, especially the location of droplet evaporation. By definition adiabatic mixing neglects heat transfer between the fluid and the cylinder and surfaces, which negatively affects the accuracy near boundaries. However, the precision in the temperature from two-color LIF thermometry is significantly worse than in that from adiabatic mixing.

One of the obvious last steps in the DFB/1MN-LIF technique's data processing is to relate tracer-concentration ratio to local fuel-component concentration. To do so, further assumptions are needed. At IFPen, Bardi et al. [104] implemented a vapor-liquid equilibrium calculation, modeling evaporation as a series of flashes based on the predictive Soave-Redlich-Kwong state equation of Holderbaum et al. [105] to yield the distilled fractions. With these model calculations yielding "mapping into fuel space", the actual fuel-component distribution was

computed from the tracer-concentration ratio. It was seen that the strongest segregation occurs close to the injector tip and spark plug where the overall fuel mass-fraction is low. In regions of high fuel mass-fractions, e.g. near the piston surface, the segregation is less pronounced but still significant. An increase in intake-valve lift accelerates fuel-bulk mixing and the homogenization of the fuel-component. Initially, just after the start of injection, segregation with 4 mm is slightly less than with 9 mm intake-valve lift, but close to TDC segregation is less pronounced with higher intake-valve lift. However, the restrictive assumptions made in the model may not apply for the complex situation of droplet evaporation in an engine spray. Alternatively, if the LIF-based imaging data are to be compared with CFD simulations, it may be preferable to include the tracers in the simulation's evaporation model, which would then allow a direct comparison to the experimental data to evaluate the accuracy of that particular evaporation model applied to the data. The downside of this approach is that a model may differ in accuracy with which it predicts major fuel components versus sub-percent trace species.

Chapter 5 - Mixture formation in a port-fueled natural gas engine

This chapter describes the investigation of the mixture formation in a natural-gas engine with PFI via LIF imaging. Parts of this chapter have been published as Kranz et al. [136], particular Sections 5.2, 5.4, 5.5.2 and 5.5.3, while Sections 5.4.1, 5.5.1, 5.5.4 to 5.5.6 contain analysis beyond that already published work. The experiments were performed at Volkswagen AG, together with the project partners Laser Laboratorium Göttingen e.V. (LLG) and LaVision GmbH. My contributions are described in more detail in Section 7.1.1.

5.1 Imaging strategy

The goal of this study is to quantify the air/fuel ratio in an optically accessible engine operated on methane with spark ignition. Here, a tracer is chosen whose fluorescence signal is quenched by oxygen, such that the LIF signal, under certain conditions, can be seen as proportional to the ratio of the number density of the tracer and oxygen, which is the inverse of the air/fuel ratio, the desired quantity. This so-called FARLIF strategy [36] is discussed in more detail in Section 2.8.2. Since the LIF signal is also influenced by temperature, in particular by the deviation of temperature between the calibration and the actual measurement this needs to be accounted for to increase the accuracy in the estimated air/fuel ratio. Therefore, the temperature is simultaneously measured by means of two-color LIF thermometry to correct its influence on the signal. In Section 5.5.3 the results from LIF imaging are compared to results from an point-like infrared absorption measurement near the spark electrodes by LLG and results from a Reynolds-averaged Navier-Stokes (RANS) CFD simulation by Volkswagen AG, both further described in [136].

5.2 Test bench

5.2.1 *Engine and periphery*

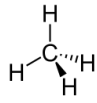
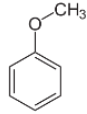
The LIF experiments were performed in an optically accessible single-cylinder engine at Volkswagen's corporate research center. Engine parameters and operating conditions are summarized in Table 5-1. The crank-angle resolved pressure was measured in intake, exhaust, and cylinder with 0.5°CA resolution (kHz sampling frequency), while intake and exhaust temperatures were always acquired at 4 Hz.

The custom engine head is typical for a four-valve spark-ignition engine, with the pent roof and the cylinder sleeve as well as the piston partly made from fused silica. This enables optical access to the top 55 mm of the stroke and the pent-roof combustion chamber. A fused silica window (diameter 65 mm) in the flat piston top provides additional optical access via a Bowditch-type piston extension (similar to the extension in Figure 3-2) and a 45°-mirror. For

IR absorption measurements, a sensor with its integrated spark electrodes was mounted in the centrally located M12 spark-plug bore.

Table 5-1: (a) Engine parameters and (b) test matrix including operating conditions. * these data sets were measured via SLIPI.

(a)

Engine		4 valves, pent-roof	
Cylinders	1		
Geometric compression ratio	8		
Displacement / cm ³	374		
Bore / stroke	74.5 mm / 85.9 mm		
Fuel	CH ₄		+ 0.07 vol.-% anisole 
Intake oxygen concentration / vol.-%	21 (air)		
Intake valve opens / °CA	-334		
Intake valve closes / °CA	-184		
Exhaust valve opens / °CA	+167		
Exhaust valve closes / °CA	+347		

(b)

Label	A				B		C
Speed / min ⁻¹	1500				1200		2500
Experiment ID	07_02, 08_02*	07_01	08_01*	03_02	09_03	09_04	13_01
λ_{FF}	1.10	1.00	0.95	0.95	1.28	0.98	1.05
λ_{PFI}	1.09	1.01	0.97	0.86	1.23	1.05	1.14
IMEP p_{ind} / bar	3.8	4.4	4.2	3.7	1.7	2.3	4.6
COV in IMEP / %	1.1	1.1	1.2	1.6	4.8	3.0	5.4
Elec. SOI / °CA	297	290	285	256	345	335	165
Elec. EOI / °CA	-334			-345	-334		-334
Ignition timing / °CA	-10			-12	-15		+5
In. pressure p_{in} / bar	0.82				0.60		1.58

5.2.2 Fuel supply

The engine was fueled with methane of 99.995% purity (grade 4.5). The fuel pressure was regulated down to 5 bar and the fuel was supplied to the mass-flow controlled intake air flow by one of two possible procedures: A controller calibrated for methane provided a well-known fuel-mass flow that was continuously injected far upstream of the engine into a Venturi-type flow constriction. Mixing was further promoted by four static mixing elements downstream of this injection point. The air-fuel mixture is expected to enter the combustion chamber spatially and temporally homogeneous, and thus allows computing a “global” air/fuel ratio λ_{FF} . The calculated λ_{FF} were verified by an exhaust gas analyzer. This air-fuel mixing procedure was used for calibration purposes. Alternatively, for the actual mixing measurements,

a commercial CNG injector (Bosch NG 2) injected the fuel approximately 20 cm upstream of the intake valves into the intake pipe. Figure 5-1 shows the geometries of the computational domain of the engine including the injector mount position labeled with “I/O injector”. This is similar to current production engines, where PFI is implemented. For the PFI measurements the exhaust-gas analyzer determined the injection duration that yielded the desired mean air/fuel ratio λ_{PFI} in fired operation.

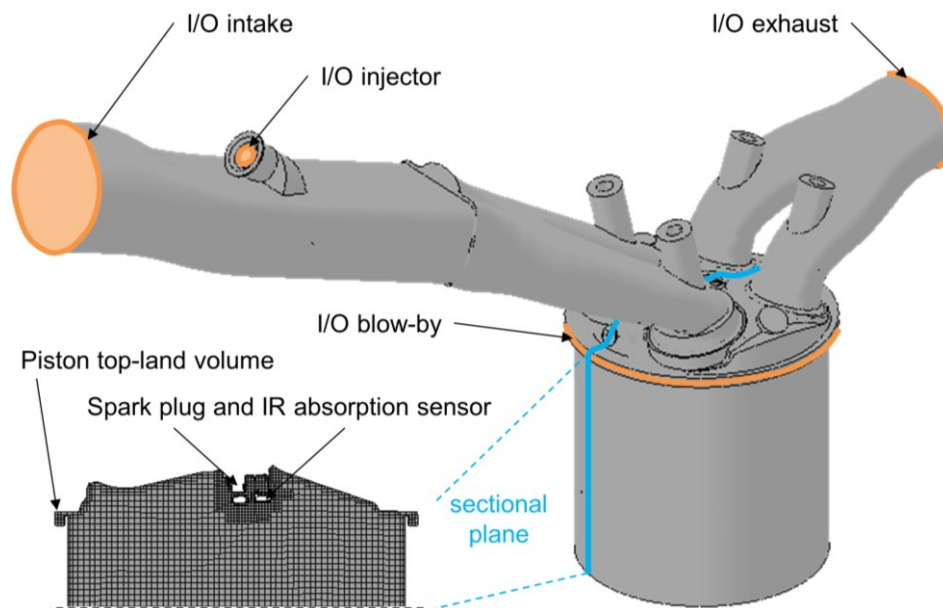


Figure 5-1: Geometry of computational domain with inlet and outlet boundaries (I/O) marked in orange color. The inset on the bottom-left shows the central cut plane that will be used to visualize the results. Figure published in [136].

5.2.3 Operating conditions

Several injection timings and air/fuel ratios were investigated. This work reports on 7 operating conditions at engine speeds of 1200 min^{-1} , 1500 min^{-1} , and 2500 min^{-1} with air/fuel ratios λ_{PFI} varying between fuel rich and fuel lean, and intake pressures p_{in} of about 820 mbar, 600 mbar, and 1580 mbar as listed in Table 5-1. Ignition of the mixture close to TDC resulted in IMEPs between 1.7 bar and 4.6 bar with a maximum in-cylinder pressure of 24 bar. The engine was fired for about 50 cycles before starting the optical measurements, which were then also performed in continuously fired operation. Continuously fired operation was stopped after 45 to 90 seconds (depending on engine load) to prevent damage to the optical engine because of high thermal stress. The global air/fuel ratio λ_{FF} in homogeneous operation was adjusted such that it approximately corresponded to λ_{PFI} of each experiment.

5.3 LIF experiment

5.3.1 Tracer seeding

Methane was seeded with anisole for LIF imaging. Experiments in an all-metal engine at full load and high boost had shown that the concentration of anisole used here did not lead to abnormal combustion like knocking or pre-ignition. The photophysical aspects of anisole as a tracer are discussed below. To mix the gaseous fuel with the normally liquid tracer, a high-performance liquid-chromatography pump metered anisole into the nozzle of a carburetor-like evaporator upstream of a pressure vessel. This allowed keeping the anisole concentration constant for different fuel flows when operating the engine at different speeds. The methane flowing through the evaporator's Venturi nozzle was slightly pre-heated to 30°C and its mass flow controlled to maintain a pressure of 7 bar in the vessel. The vapor pressure of anisole at 30°C is 6.8 mbar, corresponding to a volume fraction of 0.1% at 7 bar. To prevent condensation, the anisole flow was controlled to 0.07 vol.-% (0.5% by mass) in methane. For comparison, in previous engine experiments with liquid fuel, 2.5 vol.-% anisole in *iso*-octane were used, the limitation being excessive laser absorption for higher concentrations [137, 138].

5.3.2 Anisole-fluorescence characteristics

Anisole is used as a fluorescent tracer to image air-fuel mixing in the CNG engine. Its physical properties are provided in Table 4-1, and photophysical properties at elevated temperatures and pressures are documented in [34, 134, 135]. A recent theoretical and experimental comparison with toluene indicated the potential of anisole as a brightly fluorescing tracer [106], and first experiments in an endoscopically accessed engine confirmed that indeed much higher signal than with toluene was possible [58, 137]. Additionally, Tran et al. [34] showed for anisole excited at 266 nm that the fluorescence is inversely proportional to n_{O_2} for a temperature range of 473 K to 573 K at elevated pressure.

Figure 5-2 shows anisole fluorescence spectra after 266-nm excitation for different temperatures at 1 bar absolute pressure in air. Each spectrum is normalized to its maximum intensity. The peak of the fluorescence spectrum shifts about 14 nm to longer wavelengths from 298 K to 675 K. As with other aromatic tracers [106], this red-shift can be exploited by detecting the fluorescence in two separate spectral windows ("colors") and then relating the ratio of these two measurements to temperature. Figure 5-2 additionally shows the transmission characteristics of the dichroic beam splitter and the two bandpass filters that were used in this study for this purpose. After suitable calibration, the temperature information then can be used to correct its influence on the LIF signal.

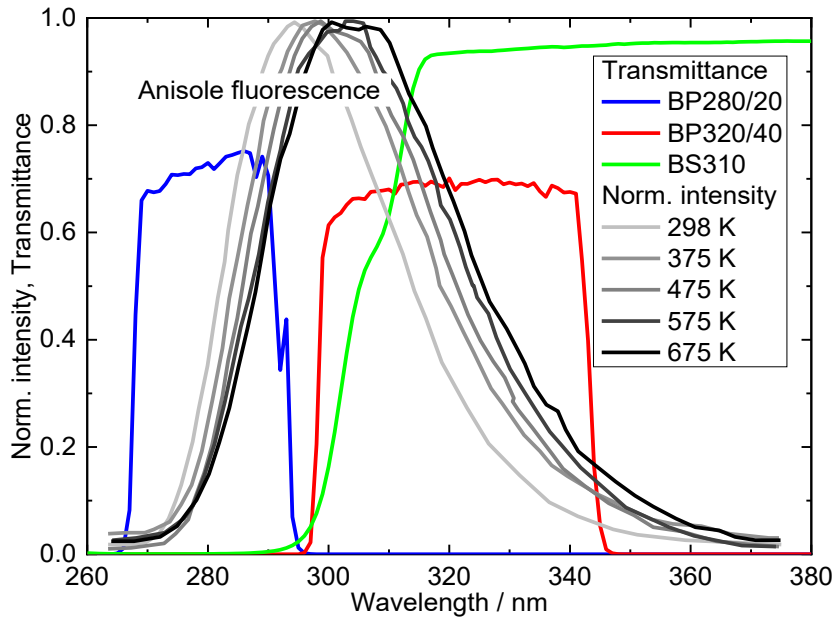


Figure 5-2: Normalized anisole fluorescence spectra after 266-nm excitation for different temperatures in 1 bar air measured by Faust et al. [134]. The transmittances of the filters and beam splitters used here are plotted.

5.3.3 Optical arrangement

A schematic drawing of the imaging system is shown in Figure 5-3. The beam of a frequency-quadrupled Nd:YAG laser at 266 nm is guided through an energy monitor reflecting 8% of the laser light onto a detector to measure shot-to-shot fluctuations. The relative shot-to-shot energy fluctuations measured by this device typically are 6% (one standard deviation). A combination of cylindrical and spherical lenses then forms a light sheet that was reflected 90° upwards by the mirror in the Bowditch-piston assembly. After passing the fused silica piston window, the sheet has a thickness of about 1 mm and is placed in the central symmetry plane of the combustion chamber as shown in Figure 5-3b. The average laser shot energy in the observation area is 27 mJ. Because the piston window is only 65 mm in diameter, some of the 74.5-mm bore cannot be illuminated, as indicated in Figure 5-3b. Also, the flat-top piston is in the field of view after -90°CA .

Optionally, a reflective-transmissive Ronchi grating can be placed between the sheet-forming optics and the Bowditch-piston mirror, creating a periodic, lateral intensity modulation in the light sheet. With the SLIPI post-processing as described in Section 5.4.1, this modulation can be utilized to reject fluorescent out-of-plane background at the expense of spatial resolution. In the current work, SLIPI is used for temperature calibration in the standing engine and applied in two engine experiments as denoted in Table 5-1.

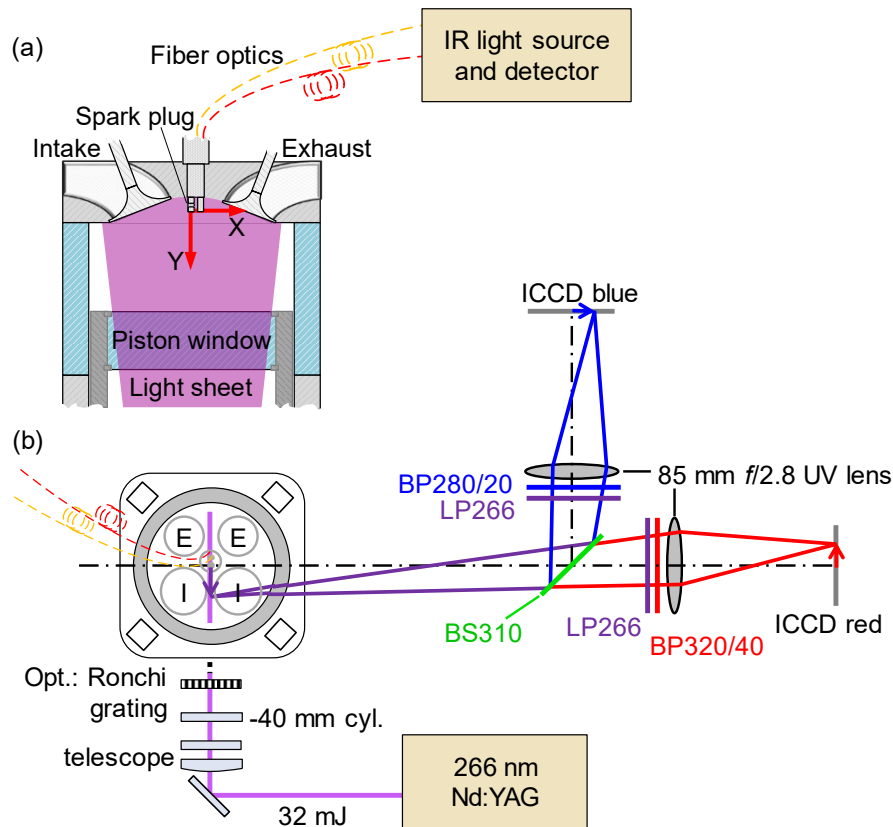


Figure 5-3: Arrangement of optics and engine cylinder for LIF imaging and IR absorption measurements (the latter by the LLG) (a) Side view of the combustion chamber, (b) top view of cylinder and optics. Figure published in [136].

Following the two-color strategy for measuring the temperature in addition to the air/fuel ratio, the anisole fluorescence is spectrally separated into a “blue” and a “red” part by means of a 310 nm dichroic beam splitter (see BS310 in Figure 5-2). A 266-nm longpass edge filter in front of each camera lens suppresses remnants of laser light. In addition, bandpass filters at $280 \text{ nm} \pm 10 \text{ nm}$ and $320 \text{ nm} \pm 20 \text{ nm}$ further narrow the “blue” and “red” spectral range of detection, respectively. Two ICCD cameras (LaVision IRO and Imager E-lite CCD) with UV camera lenses (LaVision, $f = 85 \text{ mm}$, $f/2.8$) image the field of view at a projected pixel size of 0.07 mm/pixel .

5.3.4 Measurements

PFI measurement and calibration are performed in two consecutive steps: First, the engine is operated in fired PFI mode to image mixture formation under realistic engine conditions. Second, the engine is motored and supplied with a homogenous air-fuel mixture serving as quantitative calibration as well as a correction for inhomogeneity in illumination and detection (flatfield correction) in the PFI measurements of step one. These images are captured in motored operation in order to prevent inhomogeneities caused by residual burnt gas from previous cycles.

Phase-locked to a particular crank-angle, images of 20 consecutive cycles for PFI and for flatfields from -360°CA to TDC are taken, respectively. The laser is operated at 25 Hz. The cameras are operated at integer parts of the laser's repetition rate (12.5 Hz or 5 Hz) depending on the engine speed. In order to prevent damage to the optical engine caused by high temperatures in fired operation, PFI data are recorded in sets of a certain number of crank angles each, with enough time in motored operation in between to cool down the engine. In between sets flatfield images are recorded in motored operation. Also, background images (motored operation without fuel injection) over the full crank angle range are recorded after PFI and flatfield imaging at each operating condition has finished.

5.4 Data post-processing and quantification

This section outlines the basic concept of the image quantification in Section 5. Details are provided in subsequent sections. Figure 5-4 shows a schematic of the LIF data processing.

As described in Section 2.8.2, the fluorescence signal of aromatic tracers is strongly quenched by oxygen via collisional depopulation of the excited state. Thus, according to Eq. (5-1), the relative air/fuel ratio λ is approximated to be inversely proportional to the LIF signal. The measured PFI images \mathbf{S} are corrected for background via SLIPI (see Section 5.4.1) or by subtraction of images without fuel injection. Then the resulting images are corrected for inhomogeneities in illumination and detection by dividing them by flatfield images \mathbf{S}_{FF} taken at the same crank angle. $\mathbf{S}/\mathbf{S}_{\text{FF}}$ is then calibrated by the global air/fuel ratio λ_{FF} that was set during the flatfield acquisition. This yields a first estimate of the local λ of the PFI measurements

$$\lambda = \left(\frac{\mathbf{S}}{\mathbf{S}_{\text{FF}}} \right)^{-1} \cdot \lambda_{\text{FF}}. \quad (5-1)$$

However, the fluorescence signal depends on temperature, and the flatfield images were taken in motored operation, where the in-cylinder temperature level before ignition is on the order of 100 K lower than in fired operation (see Figure 5-8b). Additionally, there is local temperature inhomogeneity. Hence, all images need to be corrected for temperature. This is done based on temperature correction functions, which must be determined first. Finally, λ is computed by Eq. (5-1) using one of the temperature-corrected images of the two cameras.

In detail, inputs of the processing are the PFI LIF signals $\mathbf{S}^{(\text{b})}$, $\mathbf{S}^{(\text{r})}$ and the flatfield images $\mathbf{S}_{\text{FF}}^{(\text{b})}$, $\mathbf{S}_{\text{FF}}^{(\text{r})}$, where indices “b” and “r” label the signals in the “blue” and “red” channel, respectively. In a first step, all images are binned 10×10 pixels corresponding to a spatial resolution of 0.7 mm. After this, the images are corrected for background and shot-to-shot laser energy fluctuations. Then, a beam-splitter correction is applied to all images used for the determination of the local temperature T . This temperature information is used to correct the temperature-caused signal differences in flatfields $\mathbf{S}_{\text{FF}}^{(\text{j})}$ and PFI measurements $\mathbf{S}^{(\text{j})}$. After these steps, FARLIF, Eq (5-1), is used to compute the temperature-corrected local relative air/fuel ratio λ for the PFI measurements.

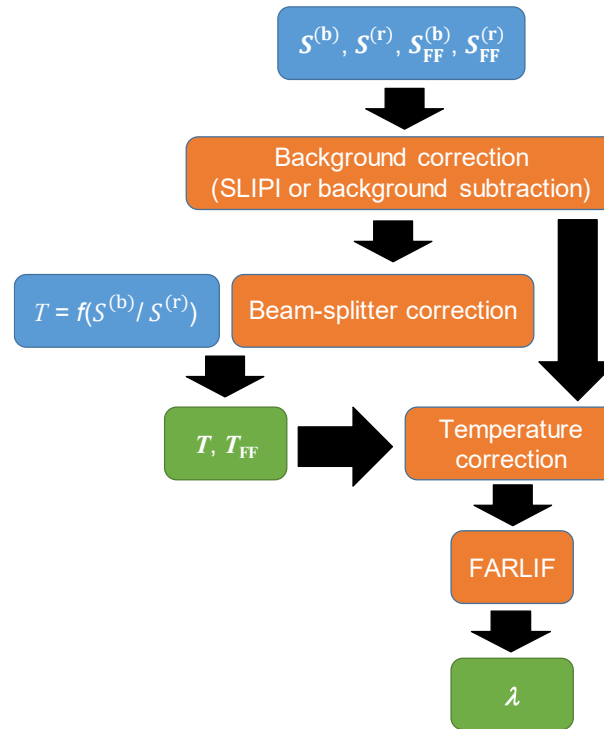


Figure 5-4: Schematic overview of the data processing for LIF imaging. This figure has been published in Kranz et al. [136].

5.4.1 Dynamic-background elimination via SLIPI

The quantification of λ might be influenced by out-of-plane LIF signal due to reflection of the laser light from surfaces. This background may change from shot to shot because of density gradients such that a constant background image taken without fuel injection may not be sufficient for correction. To see if this is the case some experiments were carried out with transverse modulation of the light sheet using a Ronchi grating with 8.33-line pairs per 10 mm. The background is then not corrected by images without fuel injection, but as part of the SLIPI image processing as already described in Section 2.9.

SLIPI experiments and processing were carried out as following: The Ronchi grating is placed in the laser path just before the 45°-mirror of the Bowditch-piston assembly, as shown in Figure 5-3. The modulated light sheet is reflected by the engine mirror into the center axis of the combustion chamber where LIF takes place. Figure 5-5 shows the SLIPI processing. The grating in the light sheet causes a modulated intensity as shown in the raw image in Figure 5-5a. Because of the diverging light sheet, the period p_s as show in (b) of the modulation changes in the vertical direction from 40 px (2.8 mm) near the piston surface to 46 px (3.2 mm) near the spark plug.

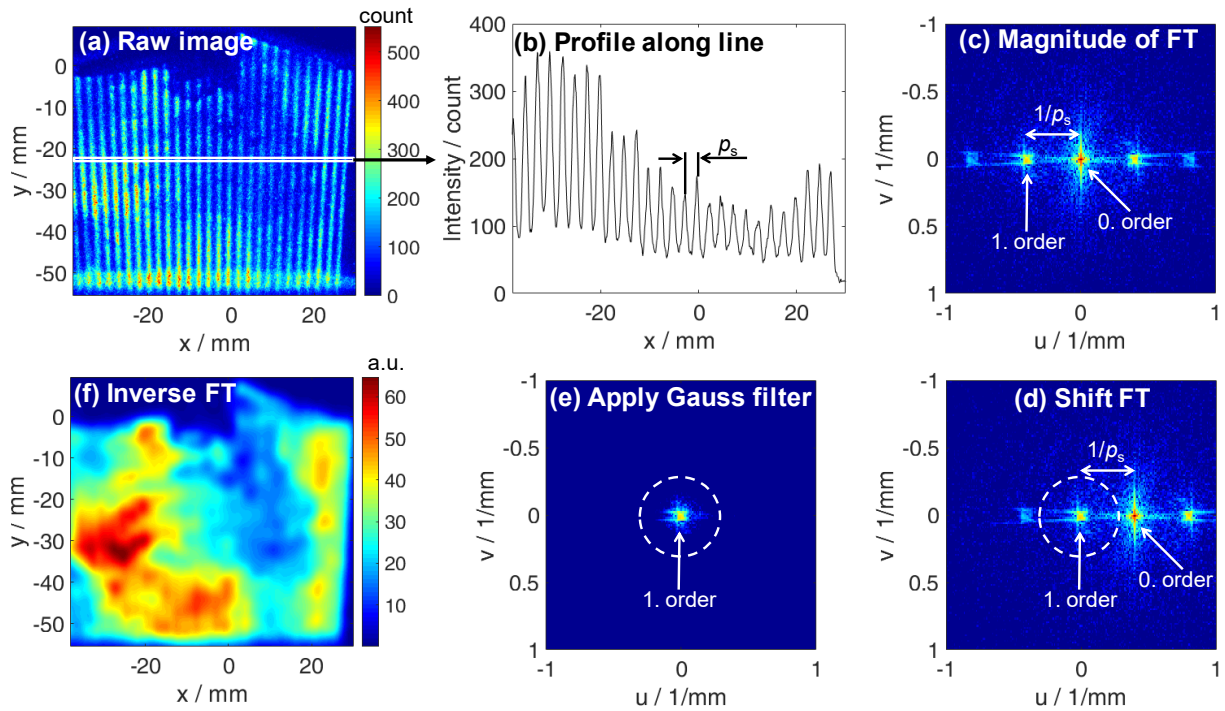


Figure 5-5: SLIPI processing steps explained on a single shot at -240°C A from dataset 08_02. (a) raw LIF image I and (b) profile along horizontal line. (c) Fourier transform (FT, clipped at 1 mm^{-1} in both dimensions) of image in (a). (d) the image is shifted by $1/p$. (e) multiplication of image in (d) with symmetrical 2D Gaussian profile. (f) inverse FT of image in (e).

In step (c), the image is transformed to frequency space using a fast Fourier transform. Only the magnitude of the Fourier transformed image is shown and the axes of the diagram are spatial frequencies of unit “ $1/\text{mm}$ ”. The zeroth, first, and second order maxima are visible in (c), with the first order maximum (0.332 1/mm) corresponding to the inverse of the average period $p = 3\text{ mm}$ generated by the Ronchi grating. Because of the transverse modulation, the amplitude of the frequencies in v -direction is low compared to the u -direction. In step (d) the image is shifted by $1/p_s$ such that one of the two first order maxima is located in the origin. In step (e), the image in (d) is multiplied with a symmetrical 2D Gauss profile with a full-width at half maximum of 0.12 1/mm . Finally, the inverse FT is applied to the image in (e), yielding image in real-space coordinates as shown in Figure 5-5f.

In Figure 5-5f only the modulated part of the signal is kept and the unmodulated part of the signal discarded. Because of the modulation and the Gaussian filtering of the FT, the resolution of the corrected images is significantly reduced compared to an uncorrected image, but SLIPI processing does not require any additional background correction. Therefore, in data with SLIPI (08_01 and 08_02), only flatfield (S_{FF}) and PFI (S) images were acquired. The corrected images serve as inputs to the FARLIF processing as shown in Figure 5-4.

5.4.2 Temperature calibration

Temperature calibration is done in situ in the standing engine, similarly to [58]. The spark plug is removed, and a heated fused silica nozzle is fitted into the bore as shown in the inset of Figure 5-6. For safety, the methane flow was replaced by air for this calibration. This means that the calibration is carried out at an oxygen partial pressure of about 210 mbar. Hence, a mixture of air and anisole continuously flows through the heated nozzle, enters the combustion chamber and exits through an opened exhaust valve. The gas temperature T_{TC} was measured by a thermocouple where the mixture exits the nozzle in the field of view of the cameras. T_{TC} was varied between 300 K and 870 K with 100 images averaged for each temperature.

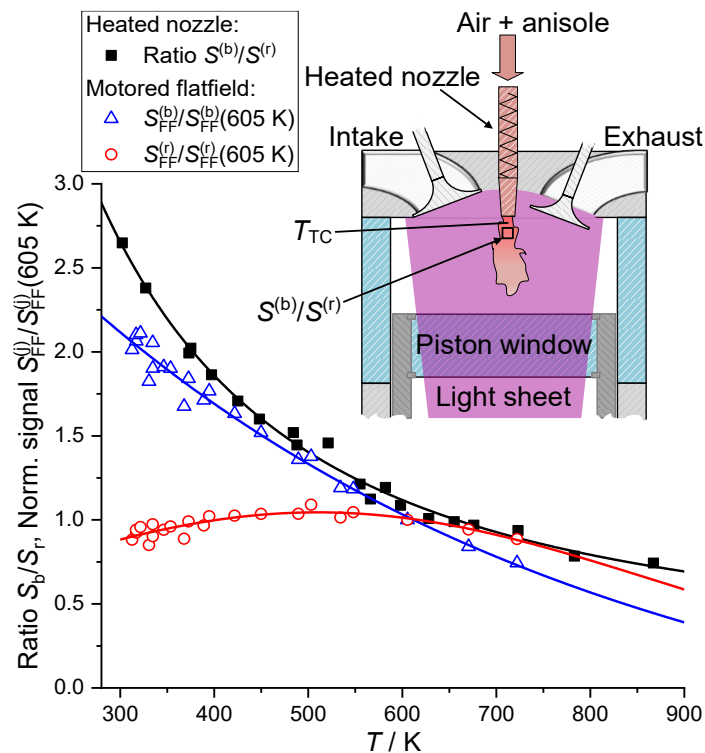


Figure 5-6: Parametrization of the relationship between LIF signal ratio and temperature based on a heated nozzle flow. The inset shows the principle of the in-situ calibration with the heated nozzle. In addition, for both channels the temperature dependence of the LIF signals, determined from motored engine operation and normalized to the signal at 605 K, is plotted. Figure published in [136].

Since in particular these heated-nozzle images were found to suffer from out-of-plane fluorescence, the Ronchi grating, indicated in Figure 5-3b, was placed in the laser path, and SLIPI procedures as described in Section 5.4.1 were used to correct all images for background. The dependence of the signal ratio $S^{(b)}/S^{(r)}$, averaged over the region indicated in the inset of Figure 5-6, on T_{TC} was measured (see diagram in Figure 5-6). The data were phenomenologically parametrized by a three-parameter exponential function, allowing pixel-wise computation of the local temperature from the signal ratio $S^{(b)}/S^{(r)}$.

5.4.3 Beam-splitter correction

The angular dependence of the transmittance of the dichroic beam splitter BS310 displayed in Figure 5-7 significantly affects the relative assignment of the fluorescence signal to a specific channel. Even in case of uniform temperature and illumination, a variation in signal ratio will occur over the FOV, since every pixel receives light at slightly different angles with respect to the beam splitter. In fact, the example raw images in Figure 5-8a show that both the PFI and flatfield images differ between red and blue channel, with a systematic horizontal shift in intensity. A correction for such beam-splitter effects was already implemented in [140]. The procedure is extended here by considering also the temperature information in the correction functions, since the temperature influences the magnitude of the angular dependence through the red shift of the anisole fluorescence spectrum.

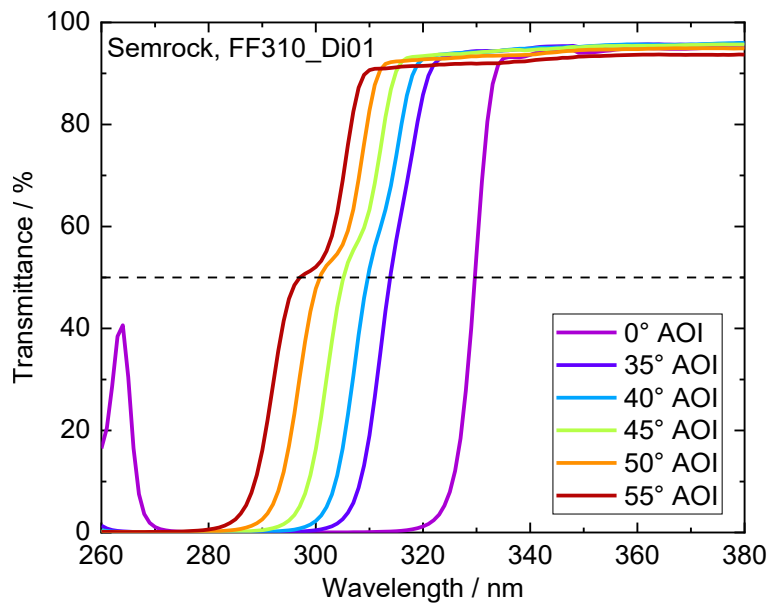


Figure 5-7: Angular dependence of the transmittance of the BS310 dichroic beam splitter (Semrock, FF310_Di01) measured in a UV spectrometer (Bruker). At 0° AOI the surface of the beam splitter is perpendicular to the path of light.

5.4.4 Temperature correction

After beam-splitter correction of the channel ratio images, the field-wide temperature is determined. Using this temperature, PFI and flatfield images are corrected to signal values that would be expected if the images had been recorded at uniform and equal temperature. In Figure 5-6, the temperature dependence of the LIF signals, normalized to the signal at 605 K (arbitrarily chosen) is plotted for both channels. The tracer concentration in the mixture flowing through the heated nozzle fluctuated, since the tracer metering system was inaccurate at the low flow rates used then. This did not affect the signal ratio, but the absolute signals needed to determine the temperature correction functions. Thus, for this latter purpose flatfields from the motored engine are used. The absolute signals originate from averaging the flatfield signal for

both channels separately over the area indicated in the inset of Figure 5-6. The temperature is determined based on the ratio method applied to the flatfields in that very region.

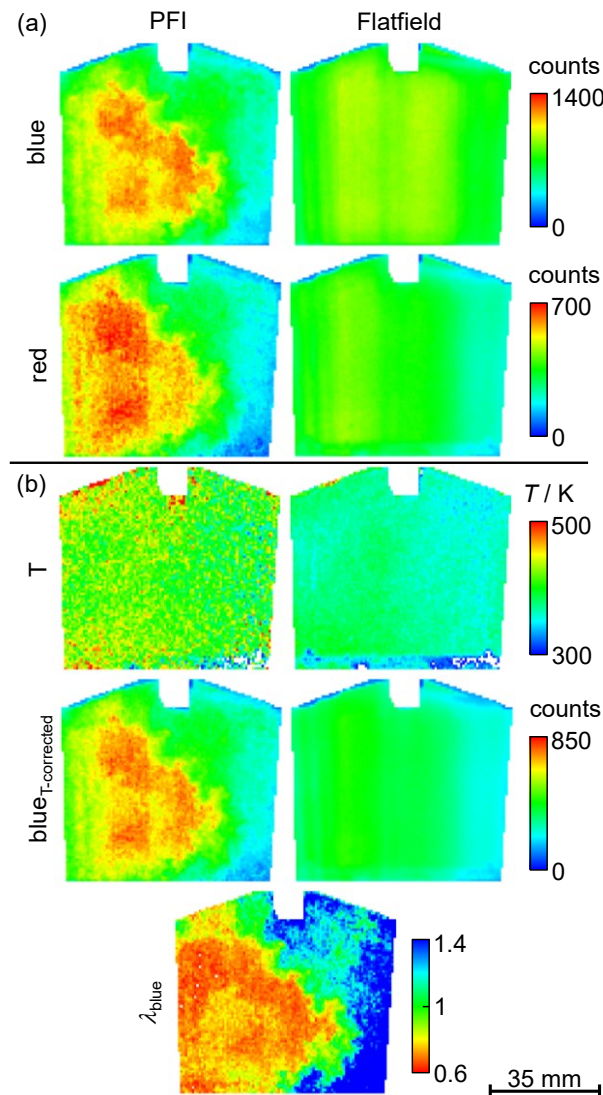


Figure 5-8: Demonstration of the temperature correction for a single shot at -160°C . (a) shows the uncorrected flatfield and PFI images for the blue and the red channel. (b) shows the calculated temperature as well as the temperature-corrected image in the blue channel and the deduced (temperature corrected) air/fuel ratio. Figure published in [136].

For the example PFI and flatfield image pairs shown in Figure 5-8a, the resulting temperature images are shown in the top row of Figure 5-8b. Although there is a – presumably real – horizontal temperature gradient across the field of view, this is much less than what would have been expected from the blue/red image pairs in Figure 5-8a, meaning that much of that visually obvious difference was due to the beam splitter. Figure 5-8b also shows that the average temperature in the motored flatfield is significantly lower than with continuously fired PFI. The temperature correction accounts for both the spatial temperature variation within the flatfield and the overall underestimation with respect to fired conditions.

After temperature correction, the corresponding λ images can be determined based on either of the two channels. While the variation in signal ratio caused by the beam splitter influences the temperature determination, and thus has to be corrected in this case, in the FARLIF-quantification of λ according to Eq. (5-1), this influence is already eliminated by the flatfield correction.

5.5 Results and discussion

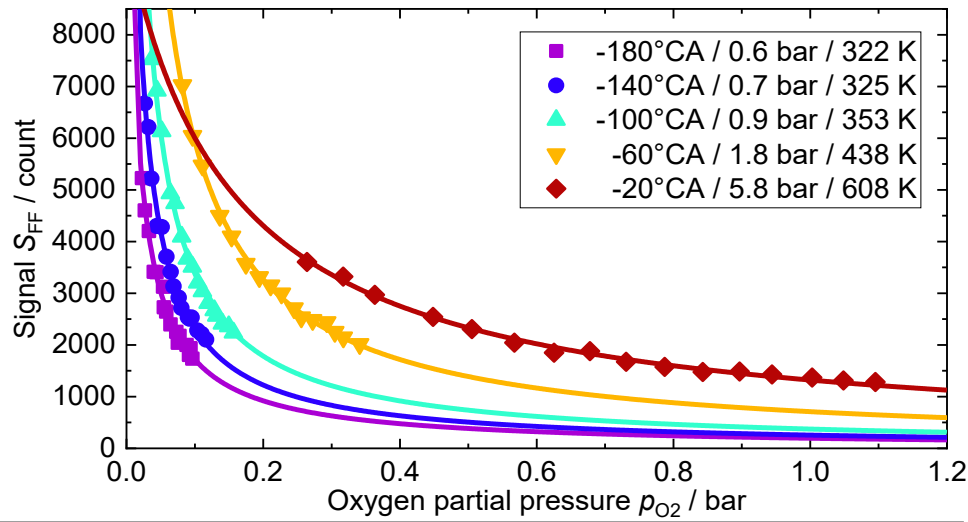
5.5.1 Linearity between fuel/air ratio and LIF signal

To assess the accuracy of FARLIF described by Eq. (2-16) and (5-1) at relevant temperatures and pressures, λ is varied in the motored engine by substituting air by N_2 , while keeping the fuel-mass flow and overall mass flow constant. Flows of air, N_2 , and CH_4 are controlled by MFCs calibrated for each fluid. The fluids were mixed far upstream (~ 0.7 m) of the intake valves. The overall mass flow of air and N_2 was 10 kg/h and the CH_4 mass flow was $0.68 \text{ kg/h} \pm 0.05 \text{ kg/h}$ continuously recorded by the data computer such that the mass flows can be assigned to the recorded set of images. The O_2 mole-fraction was varied from 4 mol.-% to 19 mol.-% by changing the N_2 dilution.

Image series of 20 cycles, synchronized to a particular crank angle, were acquired with the filter combination from the actual experiment shown in Figure 5-2. The crank angle of image acquisition was varied from -180°CA to -20°CA in 40° steps. Image pairs are background corrected, averaged for each N_2 dilution and at each crank angle. Then, the mean signal in a $3 \times 3 \text{ mm}^2$ region far from surfaces is extracted. The difference in gain between both channels is adjusted using white images taken at different gains. Then, the core temperature corresponding to each signal is then estimated by adiabatic compression along the in-cylinder pressure trace. The compression causes different temperature-pressure combinations, from 322 K and 0.6 bar to 608 K and 5.7 bar late in the cycle. The resulting O_2 partial pressures were between 25 mbar and 1045 mbar depending on the N_2 dilution and in-cylinder pressure.

Figure 5-9 shows the relation between the O_2 partial pressure p_{O_2} and the detected LIF signal at different temperature-pressure combinations. Generally, the signal at constant temperature and pressure decreases with increasing O_2 partial pressure. Also, the signal first increases to 438 K and then decreases to higher temperature. Temperature affects the population of the molecule in the ground and excited state described by the Boltzmann distribution altering the ratio of the depopulation by oxygen quenching to all other depopulation processes (see Stern-Volmer coefficient in Section 2.8.2). However, just the change of density at constant temperature to first order does not produce a change in signal since the ratio of fuel to oxygen remains the same. This is consistent with the findings of Faust et al. [106] (shown in Figure 3-8). They found that the anisole LIF signal in air upon 266 nm excitation increases up to ~ 500 K followed by a decrease in signal to higher temperatures. However, because of the different transmittance of each detection path (see Figure 5-2) a change in temperature affects the detection of LIF signal differently in each channel.

In a next step, the Stern-Volmer relation Eq. (2-17) was least-squares fitted to the O_2 partial pressure and the LIF signal. Figure 5-9 shows the fit of p_{O_2} and the sum of the signal from both channels $S_{FF} = S_{FF}^{(b)} + S_{FF}^{(r)}$ after gain correction. The signal in the absence of oxygen S_0 and the Stern-Volmer coefficient k_{SV} (per bar oxygen) were optimized to fit Eq. (2-17). Theoretically, S_0 may be directly extracted from the LIF signal, for example from a pure N_2 - CH_4 mixture ($p_{O_2} = 0$ bar). Unfortunately, measurements in the absence of oxygen were not possible, because the N_2 pre-pressure for the MFC was not great enough for mass flows exceeding 7.5 kg/h. The solid lines in Figure 5-9 show the result of the parameter fitting. The estimated k_{SV} and S_0 at each temperature-pressure combination are summarized in the table in Figure 5-9.



Model	Stern-Volmer				
Equation	$S_{FF} = S_0 / (p_{O_2} k_{SV} + 1)$				
Plot	-180°C	-140°C	-100°C	-60°C	-20°C
\dot{m}_f / kg/h	0.65	0.73	0.71	0.66	0.63
S_0 / count	12839	22079	32369	32478	9908
k_{SV} / bar ⁻¹	64.8	85.1	85.7	44.8	6.5
R^2	0.990	0.990	0.996	0.998	0.994

Figure 5-9: Fluorescence signal $S_{FF} = S_{FF}^{(b)} + S_{FF}^{(r)}$ extracted in a 3×3 mm² ROI as a function of the equivalence ratio λ^{-1} and adiabatic-core temperature T_{core} . The engine was motored at 2000 min⁻¹ on an air- N_2 - CH_4 mixture. Air was replaced step-wise by N_2 , while the overall mass-flow was constant at $\dot{m}_{N_2} + \dot{m}_{Air} + \dot{m}_f = 10$ kg/h. The table lists the estimated signal S_0 in pure N_2 , the Stern-Volmer coefficient k_{SV} , and \dot{m}_f .

Faust et al. [134] provide k_{SV} of anisole at 1 bar total pressure with 266 nm excitation measured in a steady-state flow cell by successively diluting an air flow by N_2 while varying the temperature. Additionally, Tran et al. [34] determined k_{SV} of anisole with 266 nm excitation at 20 bar total pressure measured in a high-pressure high-temperature cell. Figure 5-10 shows the comparison of k_{SV} from literature with the values determined in this work. Overall, k_{SV} from this work agrees reasonably well with the literature. In all cases, a decrease in k_{SV} with

increasing temperature is seen. However, quantitatively the data from Faust et al. [134] agrees with the current data at 325 K and 440 K. At higher temperatures, k_{SV} from this work is lower than measured by Faust et al. but exceeds the coefficient from Tran et al. [34] at 20 bar.

The deviations may have several reasons: At -180°C A (0.6 bar) the intake valves are still open, which might cause a non-homogeneous mixture at this time of image acquisition and therefore might affect the measured k_{SV} at low temperature. Also, in this work pressure increases with temperature influencing the efficiency of oxygen quenching. If the Stern-Volmer coefficients at 1 bar and 20 bar are compared, an increase of pressure at constant temperature causes a decrease in k_{SV} . Also, in the current work only a limited part of the fluorescence spectrum is detected by each of the detection paths (see Figure 5-2), such that the LIF signal may have a different sensitivity to oxygen quenching than with detection of the whole spectrum, which may be because of a shift in the fluorescence spectrum with oxygen concentration. Also, the techniques to approximate k_{SV} are different. Faust et al. [134] determined k_{SV} from the fluorescence life-time in the spectral range of 260 nm to 370 nm. In the current work, however, k_{SV} is determined from the integrated LIF signal in ranges of 270 nm to 290 nm ($S_{FF}^{(b)}$, BP280) and from 310 nm to 340 nm ($S_{FF}^{(r)}$, BS310 + BP320).

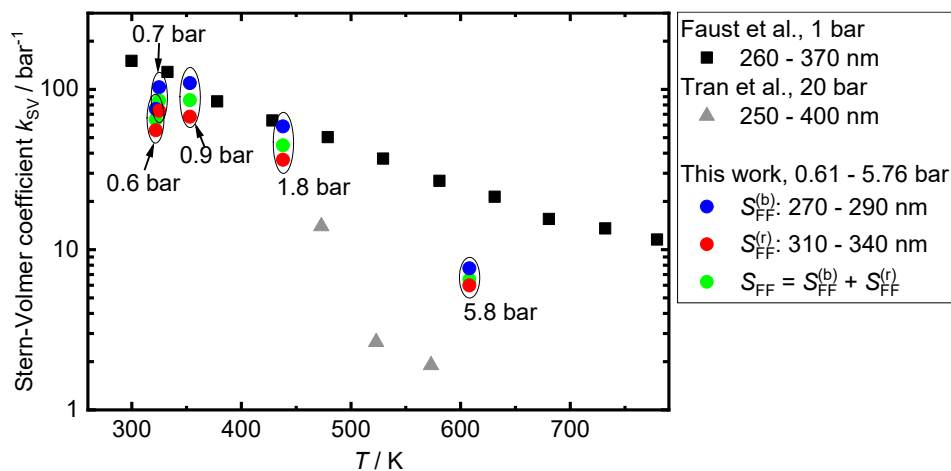


Figure 5-10: Stern-Volmer coefficient k_{SV} of anisole fluorescence at different temperatures, determined from different spectral regions with 266-nm excitation in N_2 dilution series. The in-cylinder pressure is given for each data set. Data from Faust et al. [134] measured in a flow cell, from Tran et al. [34] measured in a high-pressure high-temperature cell.

With the Stern-Volmer relation Eq. (2-17), an estimate of the accuracy of the linear approximation in FARLIF can be drawn. Figure 5-11a shows the signal from the blue channel, (b) the signal from the red channel, and (c) the sum of both, all normalized by S_0 from each detection path at each temperature-pressure combination. For each dataset, the Stern-Volmer curve and its linear approximation according to FARLIF are plotted. The linear approximation deviates significantly from the Stern-Volmer curve in all cases. The relative error in the air/fuel ratio from FARLIF can be defined as $(\lambda_{LA} - \lambda_{SV})/\lambda_{SV}$ with λ_{SV} being the air/fuel ratio according

to the Stern-Volmer relation and λ_{LA} being the air/fuel ratio from the linear approximation (FARLIF).

In general, the error increases with decreasing λ . (A plot of the relative error is provided in Appx. 8-2.) For $\lambda_{SV} = 1$ and 325 K the relative error in λ_{LA} is 7%, at 438 K it is 5%, and at 608 K it is 12%. At $\lambda_{SV} = 2$, the relative error is 3% at 325 K, 2% at 438 K, and 9% at 608 K. For $\lambda_{SV} = 0.2$, the relative error is 37% at 325 K, 29% at 438 K, and 70% at 608 K. Thus, the strongest deviation from linearity occurs at very rich mixtures where the relative oxygen content is low, and thus $\tilde{k}_q^{O_2} n_{O_2}$ is smaller compared to fuel-leaner mixtures. Therefore, only in presence of large fractions of residual gas or in very fuel-rich regions, for example just after the intake valve opens, FARLIF may yield grossly inaccurate results, but for most conditions in an engine, Eq. (2-16) yields a reasonable estimate for λ .

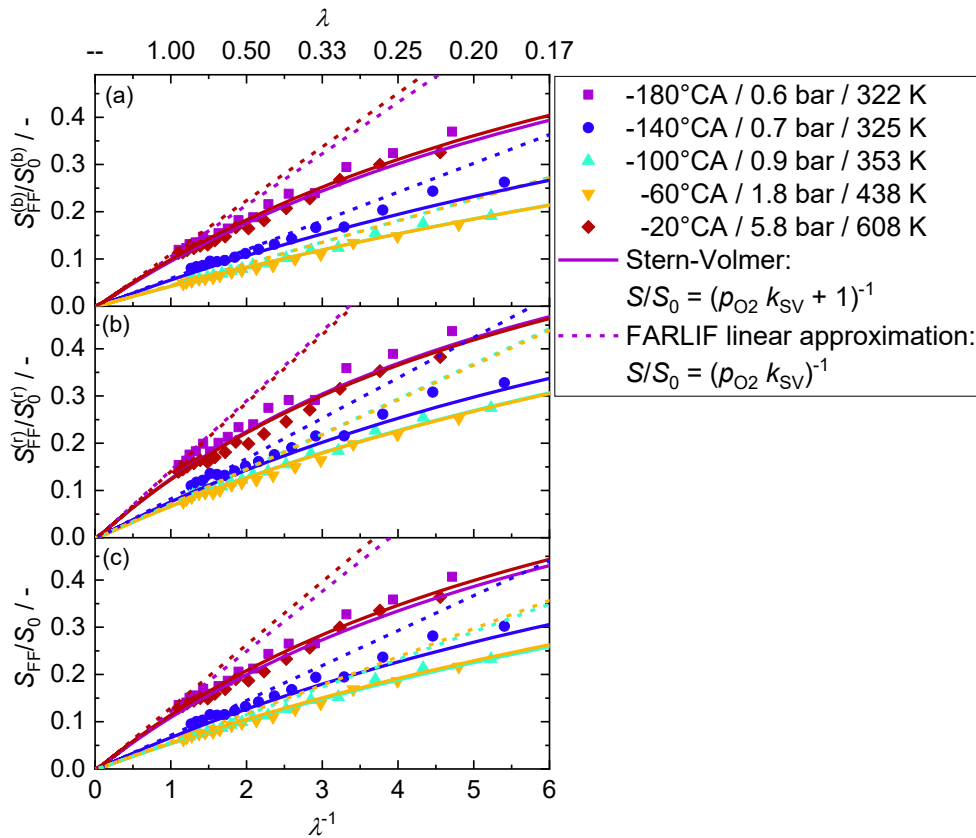


Figure 5-11: Dependence of the normalized anisole LIF signal on the fuel/air ratio λ^{-1} for series of approximately same tracer number densities (i.e., crank angles). Each trace is normalized by the estimated signal in absence of O_2 . Solid lines: Fit to the data according to the Stern-Volmer relation; Dashed lines: Assuming a linear approximation according to the FARLIF approximation. (a) $S_{FF}^{(b)}$, BP280; (b) $S_{FF}^{(r)}$, BS310 + BP320; (c) $S_{FF} = S_{FF}^{(b)} + S_{FF}^{(r)}$.

As shown in Figure 5-2, the peak of the fluorescence spectrum shifts into the BP320-channel with increasing temperature. Besides the temperature-induced red-shift, there is also a

red-shift with increasing oxygen partial pressure as shown by Faust et al. [134]. The oxygen-induced red-shift may also be an explanation for the differences in k_{SV} determined from the LIF signal of each channel. k_{SV} from $S_{FF}^{(r)}$ is lower than from $S_{FF}^{(b)}$ at constant temperature and pressure. The shift of the fluorescence spectrum to longer wavelengths with increasing p_{O_2} partially counteracts to the decrease in signal due to increasing oxygen quenching in $S_{FF}^{(r)}$. This effect is the other way around for $S_{FF}^{(b)}$ causing a greater k_{SV} than in $S_{FF}^{(r)}$.

To check the influence of oxygen partial pressure p_{O_2} on the signal ratio in the current experiment, Figure 5-12 shows the channel ratio $S_{FF}^{(b)}/S_{FF}^{(r)}$ at constant temperature and increasing oxygen partial pressure due to the increasing total pressure. The range in O_2 -partial pressure increases towards TDC. At 325 K and below 0.15 bar the channel ratio is significantly sensitive to a change in O_2 -partial pressure indicating a pronounced red shift of the fluorescence spectrum. However, with increasing pressure and temperature the channel ratio becomes less sensitive to a change in O_2 -partial pressure. If the ratio is approximated as a linear function of p_{O_2} , then the slope at 325 K between 0.03 bar and 0.11 bar O_2 is -1.29 bar^{-1} , but at 608 K and p_{O_2} between 0.26 bar and 1.10 bar O_2 the slope decreases to -0.04 bar^{-1} .

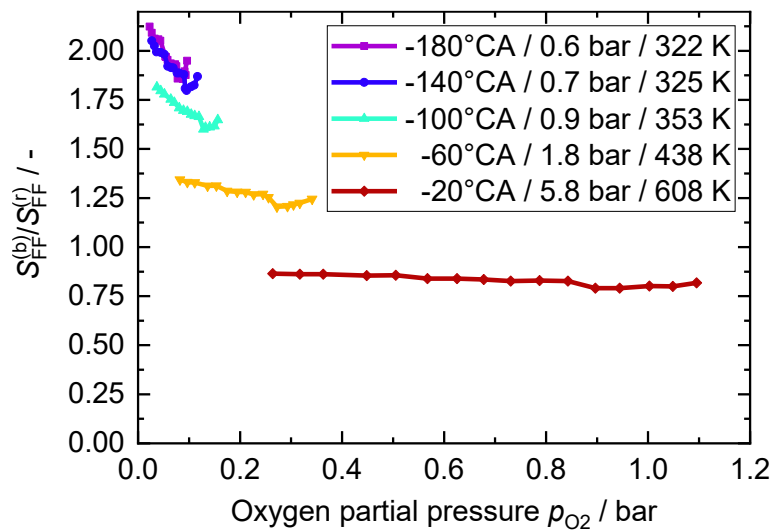


Figure 5-12: Channel signal ratio $S_{FF}^{(b)}/S_{FF}^{(r)}$ as function of the oxygen partial pressure at different temperature/total pressure combinations.

Connecting the findings from Figure 5-11 and Figure 5-12 to the issue of quantifying the air/fuel ratio in the engine measurements, at low temperature ($\sim 325 \text{ K}$, 0.7 bar, early compression) the error in fuel-lean mixtures ($\lambda > 1$) is low, i.e., for $\lambda = 4$ the error is about 2%. For $\lambda = 1$ (e.g. 75% residual gas) the error increases to about 7% while at 438 K and 1.8 bar the error at $\lambda = 1$ is 5%. If the air/fuel ratio decreases towards 0 (no O_2) the error increases significantly. Part of the error is due to the red shift of the fluorescence spectrum at low oxygen partial pressure, but most of the error is induced by significant deviation from the linear

approximation in FARLIF. At high temperature (~ 608 K, 5.8 bar, late compression), the error for $\lambda = 4$ is on the order of 3%, while for $\lambda = 1$ the error is about 11%. However, at $\lambda = 0.2$ and 325 K the deviation is about 37%, increasing to 70% at 608 K. It is to mention, that the combination of $\lambda = 0.2$ at 608 K (late during compression) is not realistic in engines operated with PFI, but during gas-exchange, when the temperature is low, very fuel-lean regions may exist.

5.5.2 Temperature and air/fuel ratio

Figure 5-13 shows examples of single-shot and ensemble-averaged images of λ and temperature during gas exchange (-300°CA), early compression (-140°CA), and close to ignition (-40°CA). At -300°CA fuel-rich mixture enters the combustion chamber from the intake valves. In the single shot, small-scale structures due to turbulent mixing can clearly be seen. The boundary of the fresh charge gas appears sharper here than it really is because for clarity the color palette is clipped at $\lambda = 3$. However, beyond $\lambda = 5$ the background signal dominates over the anisole-LIF signal such that this value represents the upper detection limit at this crank angle.

The corresponding temperature images suffer from more noise, originating from the division of two noisy images, the limited sensitivity of the channel ratio to temperature, and pixel-level inaccuracies in the mapping of the two images. However, at -300°CA temperature structures are still apparent, though with reduced resolution compared to λ . The inhomogeneity in temperature is consistent with that in λ , the incoming fresh charge being much colder than the surrounding gas.

At -140°CA , in the single shots fine-scale structures from turbulent mixing are still visible in λ , but not in temperature anymore. Since the overall temperature level is still like that at -300°CA , noise at a given λ is also similar. However, mixing has increased λ in the fuel-rich zone and thus decreased the LIF signal there and the contrast to the surrounding leaner gas. Both in λ and in temperature, horizontal stratification of the mixture is discernable, from rich and hotter on the left side to lean and cooler on the right. At first, it might be surprising that the presumably rich fresh charge is associated with higher temperatures, but as will be seen later, due to the closed-valve PFI timing, the fresh charge is only rich for the earlier part of the intake stroke, followed by nearly pure air. The earlier, rich part of the charge encounters the hot residual gas, partially mixes with it, and becomes warmer than the lean remainder of the charge. Simultaneously, convection in tumble motion yields the spatial distributions that were measured. However, this level of detail would have been difficult to conclude from the LIF imaging alone since the contrast in the temperature images is simply too low. Instead, consulting also the CFD simulation [136] (e.g., Figure 5-17) reconciled what first appeared to be measurement inaccuracy.

At -40°CA , when temperatures are high, the LIF signal in the blue channel is much lower than in the early compression as shown in Figure 5-6, lowering the SNR in temperature and λ .

The grainy small-scale structures visible in the single shots are due to noise, but the average λ field still shows large-scale inhomogeneity. λ ranges from values of about 1.2 at the very left end of the field of view to values slightly lower than 1.0 in most parts of the remaining area. Inhomogeneity in temperature is hard to distinguish from noise even in the 20-shot ensemble average. Overall, at crank angles late in the compression, it may be advantageous to reduce resolution further in favor of noise reduction, since at least in λ small-scale structures are not expected anyway.

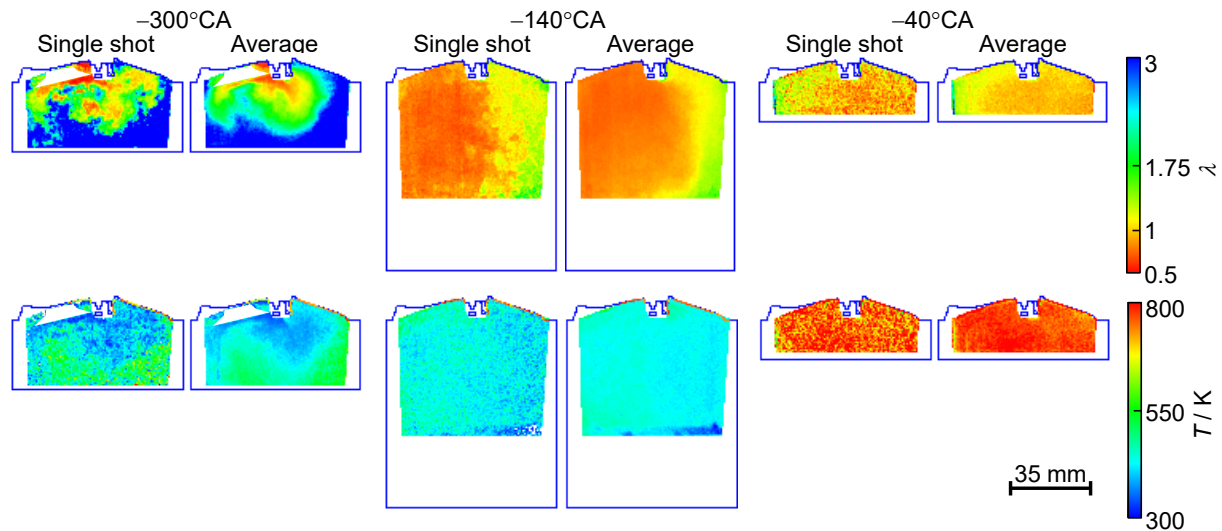


Figure 5-13: Single cycle and ensemble-average over 20 cycles of temperature-corrected air/fuel ratio and temperature distributions from LIF imaging for three selected crank angles. The boundary of the combustion chamber and intake valve is also shown. Figure published in [136].

5.5.3 Comparison with IR-absorption measurements and CFD simulation

LIF imaging was performed simultaneously together with IR absorption measurements carried out by the LLG [120, 121, 136, 164] on the same engine at stoichiometric operation and 1500 min^{-1} (data set 07_01 in Table 4-4). Subsequently, a CFD simulation was executed by the Volkswagen AG of that specific engine run. Details on the IR absorption methodology and explanations about the RANS-type CFD simulation are given in [136]. While from IR absorption the average λ is determined over a short line in the optics cage next to the spark plug, LIF imaging yields λ at almost any point in the field of view, but unfortunately not in the sensor cage. Therefore, the evolution of λ determined by LIF imaging is examined in four different ROIs located around the spark plug sensor and is compared to the results of the IR absorption measurement. The location of the ROIs and the resulting crank-angle series of λ are shown in Figure 5-14. ROIs 1, 2 and 3 are located close to the sensor to reflect the IR results, while ROI 4 was placed further away to check if background in the LIF images in the immediate vicinity of the reflective spark-plug sensor influenced the measurements. At $2.1 \times 2.1 \text{ mm}^2$ each, the ROIs were chosen to fit approximately the projected area of the probe volume of the IR sensor.

As discussed above, closed-valve PFI causes charge stratification: First, very lean mixture enters the combustion chamber for a short time after the intake valves open at -334°CA , followed by fuel-rich fresh charge, ending again with a lean mixture just before the intake valve closes, with homogenization during compression. In the early, lean phase and while the fuel-rich “plug” from PFI passes through the probe volumes, only small differences between all four ROIs and the IR absorption can be seen, but at about -250°CA , ROI 2 starts to significantly lag the other locations and the IR absorption measurement. The lag with respect to the other ROIs persists until mid-compression. It is consistent with the expected flow in the upper center of the combustion chamber, where valve and tumble flows are expected to produce convection from left (ROI 3) to right (ROI 2) in both intake and compression stroke.

ROI 3, upstream of the sensor cage, best matches the IR absorption measurement during the rapid leaning around -240°CA , with ROIs 2 and 4 having lower peaks than 1 and 3. In the case of ROI 2, this may be due to additional mixing in the wake of the sensor and spark electrode. The coefficient of variation (COV), which is here the ratio of the 20-cycle one standard deviation to the mean value in ROI 1, at -220°CA is 0.35. After intake-valve closes (-184°CA) and the in-cylinder flow presumably becomes much slower, ROI 4 yields very similar λ as ROIs 1 and 3, indicating that also in the immediate vicinity of the sensor the LIF imaging is not significantly affected by background. After -140°CA , λ from IR absorption is in between the values extracted from the different ROIs. At -40°CA in ROI 1 the COV is 0.11. Therefore, cyclic variability in the late compression stroke is lower than at -220°CA , but still significant against the single-shot precision of the LIF measurements. Based on these results, it was decided to average λ over ROIs 1 to 3 and to use this mean value for the further comparisons. ROI 4, being farther away from the region of IR absorption measurements, was neglected. If CFD simulations are presented spatially averaged, also ROIs 1 to 3 are used.

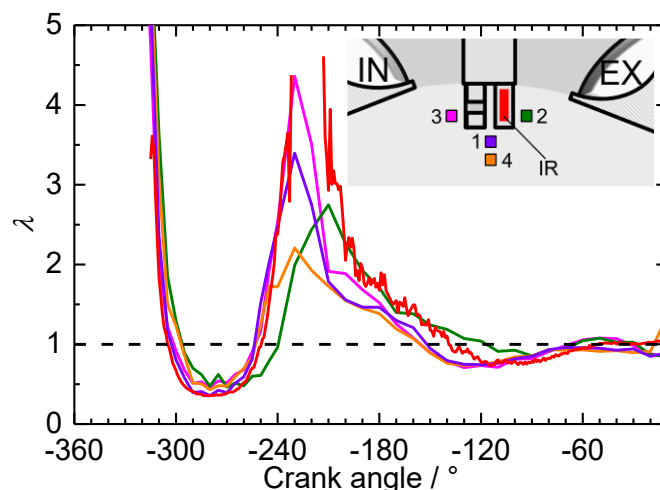


Figure 5-14: Evolution of the relative air/fuel ratio λ from LIF imaging extracted from four different $2.1 \times 2.1 \text{ mm}^2$ regions of interest (ROIs) surrounding the IR absorption sensor (red), compared to the results from the IR absorption measurement (all ensemble-averaged data). The locations of the ROIs and the color-coding of the corresponding traces are indicated in the inset. Figure published in [136].

Based on this spatial averaging around the spark plug sensor, Figure 5-15 compares the evolution of λ and temperature from LIF imaging and CFD simulation with that from the IR absorption sensor. The experimental results are ensemble averaged. In addition, Figure 5-16 shows a field-wide comparison of λ from ensemble-averaged LIF imaging and from the CFD simulation for selected crank angles. Also, six single LIF shots from consecutive cycles at -180°CA are shown to illustrate CCV. For orientation, the contour of the combustion chamber is indicated in the LIF-based images, and the FOV of the LIF imaging in the CFD results. In LIF imaging, one of the open intake valves obscures parts of the field of view, while from the CFD information is available for the corresponding region.

Overall, in λ the two experiments and the simulation agree well. In particular, the spatio-temporal evolution from LIF imaging and the CFD simulation largely coincide. Both clearly show that in-cylinder mixture formation consists of clockwise tumble convection with gradual mixing. Figure 5-15 shows that the three-region-average λ from the LIF data agrees well with the IR absorption measurement. In temperature, there are greater differences with significant disagreement at all crank angles.

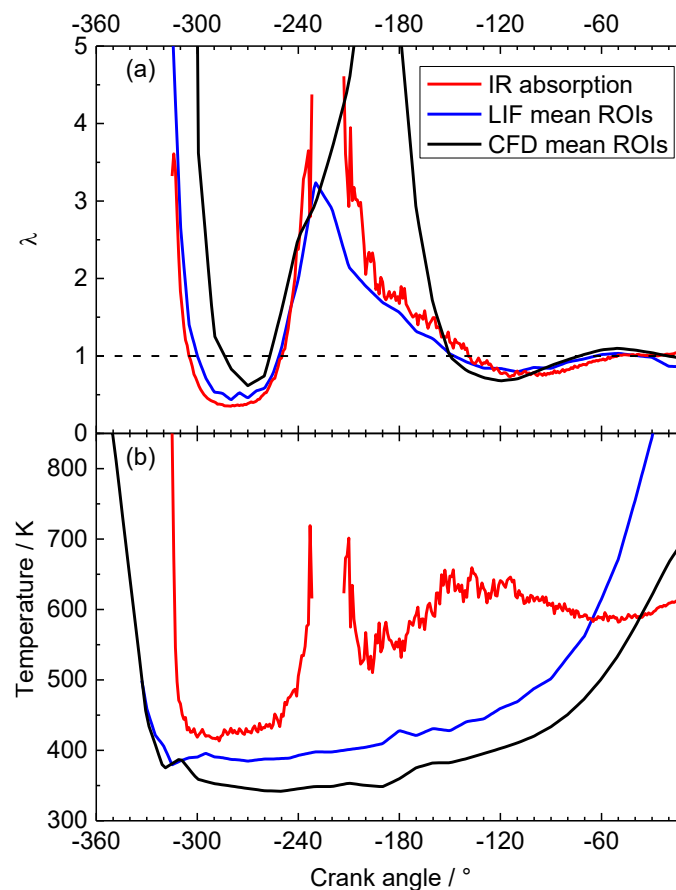


Figure 5-15: Comparison of λ and temperature from LIF imaging, IR absorption, and CFD simulation. LIF and CFD data were extracted from three ROIs around the spark plug sensor and then averaged. LIF data are taken from averages of 20 consecutive cycles, IR absorption from averages over three runs with 100 cycles each. Figure published in [136]. IR-absorption was carried out by LLG, CFD simulation by Volkswagen AG.

At gas exchange TDC (-360°CA), λ is ill-defined, since apart from crevice outgassing only the products of stoichiometric combustion are present. From -330°CA to -240°CA , all methods yield qualitatively consistent λ showing the lean-rich-lean sequence during intake that already had been discussed in Figure 5-14. However, while LIF imaging and IR absorption agree in the timing of the fresh gas arriving at the probe volume, this event occurs about 15°CA later in the CFD. Figure 5-16 also shows this lag, but additionally it can be seen that the fresh charge penetrates into the cylinder faster in the CFD simulation, such that by -290°CA the prediction from CFD fits to the other results. The initial offset may be due to inaccuracies in the CFD's domain geometry or the simulation itself in the intake pipe. In particular, there are some areas of flow detachment in the intake pipe that may not be captured accurately by this RANS-type simulation. The distance between injector and port is relatively long. Therefore, small differences in the calculated flow here can lead to the observed differences in the arrival time of the fuel at the valve. (15°CA offset correspond to 7.5 mm distance at the mean flow velocity in the intake pipe.)

Figure 5-15 illustrates that between -240°CA and -150°CA , roughly corresponding to the lean phase of the intake flow, IR absorption and LIF imaging yield qualitatively similar results, with differences in maximum λ . Due to the very lean mixture, both experimental methods suffer from signals close to background at these crank angles, reducing the accuracy in λ , in addition to the differences caused by the locations of the sensor and the ROIs. CFD simulation, not affected by detection limits, predicts significantly larger λ , with the maximum ($\lambda = 9.5$ at -190°CA) shifted by about $+30^{\circ}\text{CA}$ with respect to the experimental techniques. The “falling edge” of the lean phase (high λ to low λ) is much steeper in the CFD than it is in LIF imaging and IR absorption. This difference in temporal gradient apparent in Figure 5-15 is consistent with the fact that the CFD simulation yields higher spatial gradients as seen in Figure 5-16. The single-shot λ fields at the bottom of Figure 5-16 demonstrate that on an instantaneous basis, the gradients are in fact pronounced, but the CFD cannot capture the large-scale cyclic variability that smooths out the ensemble mean, an effect that is well-known for RANS-type engine simulations [111, 122, 126].

During compression, beyond -150°CA , Figure 5-15 shows λ given by all three techniques to be quite similar. Again, consistent with steeper spatial gradients, the slight lean-then-rich modulation during mid and late compression is stronger in the CFD simulation. At ignition, the CFD simulation yields $\lambda_{\text{CFD}} = 0.97$, close to $\lambda_{\text{ign}} = 1.01$, while IR absorption and LIF imaging yield $\lambda_{\text{IR}} = 1.08$ and $\lambda_{\text{LIF}} = 0.86$, respectively. The actual value is unknown, but this is some indication that LIF may underestimate and IR absorption overestimate λ . A possible explanation for the latter is that residual gas was neglected in the data evaluation of the IR absorption measurement. The residual gas concentration was estimated by the gas-exchange model (see section “CFD simulation”) to be 11%, reducing the amount of fresh air by a factor of 0.89. This can be applied to the IR absorption results by multiplication with the total gas density when calculating λ , resulting in $\lambda_{\text{IR,corr}} = 0.95$ and thus close to the value from CFD. LIF imaging is, in first approximation, not influenced by residual gas since it directly measures the tracer/oxygen (i.e., fuel/air) ratio. However, in the LIF data evaluation, inaccuracies in the simultaneously measured temperature may affect λ .

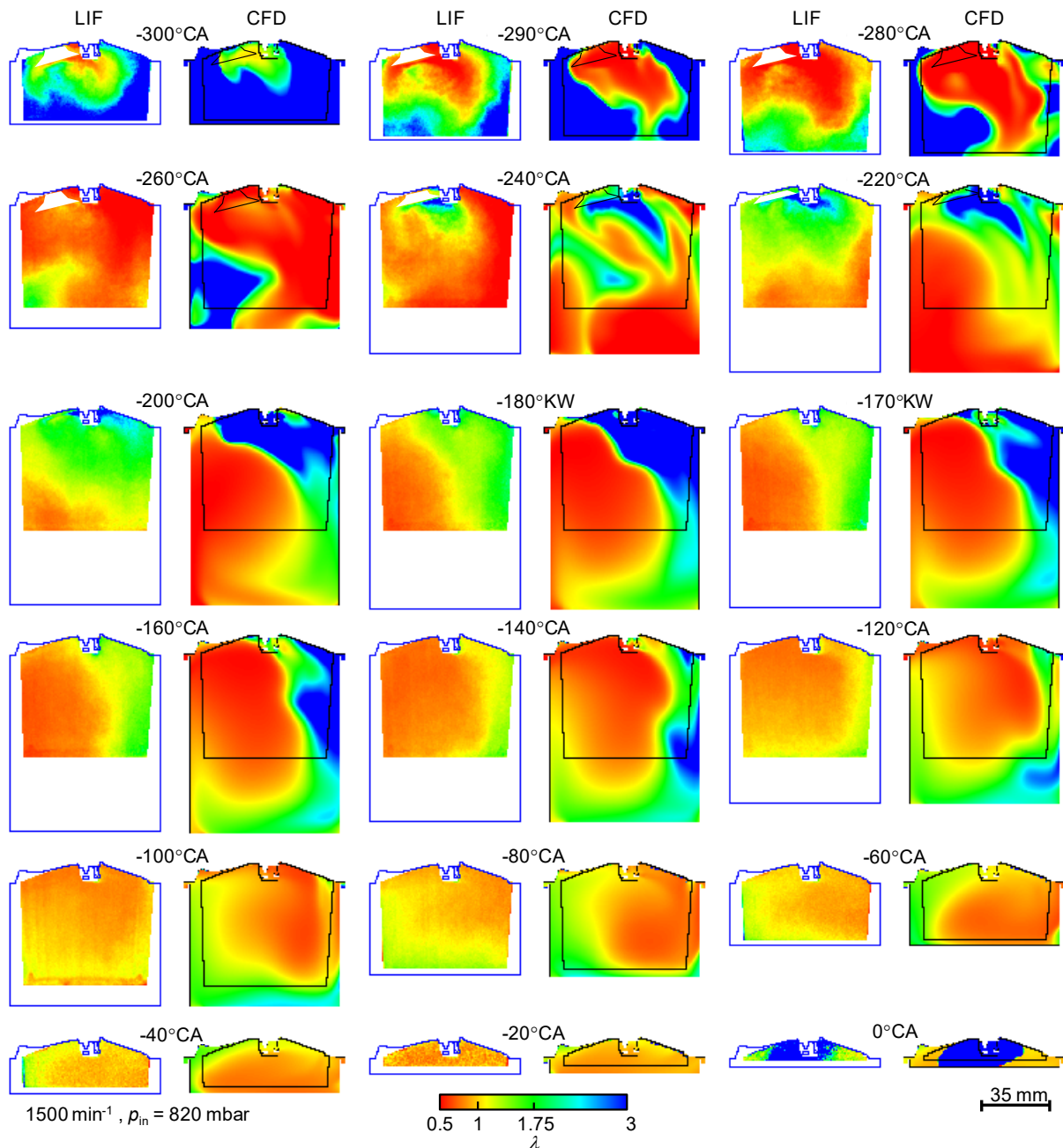


Figure 5-16: Comparison of the λ -images as crank-angle evolution from LIF imaging and CFD simulation. LIF images, data from experiment 07_01 at 1500 min^{-1} with $\lambda_{\text{PFI}} = 1.01$, at each crank angle are ensemble averages of 20 consecutive cycles. Figure published in [136]. CFD simulation by Volkswagen AG.

In Figure 5-16 at TDC, the burnt area can be identified in LIF imaging by its local lack of signal. The direction of flame propagation is consistent with that predicted by the CFD simulation. Figure 5-16 shows the ensemble-averaged image, but because of the strong contrast between burnt and unburnt area, the burnt area is also clearly delineated in single shots.

In terms of temperature, Figure 5-15 shows that after -330°CA , there is a nearly constant offset of about 50 K between LIF imaging and CFD simulation, increasing close to ignition.

Since it is such a systematic deviation, it might originate from errors in the temperature calibration of the two-color LIF imaging. The heated-nozzle method described in Section 5.4.2 for example does not take into account spectral changes with increasing pressure. However, underestimated wall temperatures in the boundary conditions of the CFD simulation might also contribute to the discrepancy.

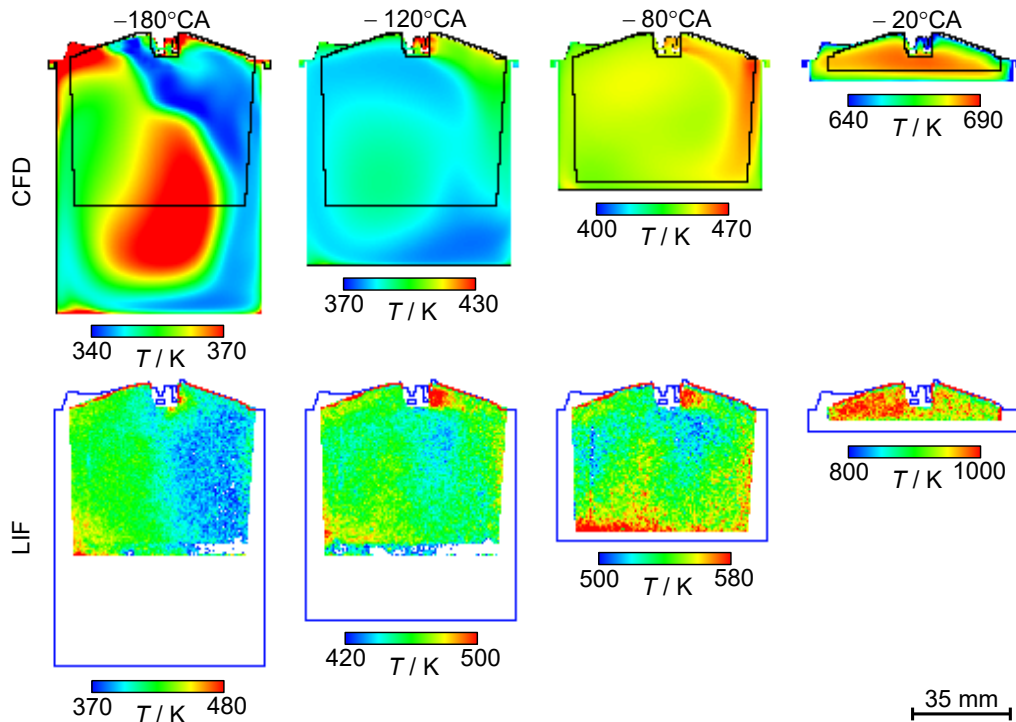


Figure 5-17: Crank angle evolution of temperature during compression from CFD simulations and ensemble-averaged from LIF measurements. LIF data from experiment 07_01. Figure published in [136]. CFD simulation by Volkswagen AG.

For further confirmation of the observed thermal interaction of the spark-plug probe with the surrounding gas, the center-plane temperature fields from the CFD simulations and LIF imaging were extracted and displayed in Figure 5-17. Even if the LIF temperature images suffer from noise and the temperature appears to be overestimated, CFD and LIF agree qualitatively. They both show that temperature around the spark plug differs significantly from the temperature in the rest of the cylinder. Downstream of the spark plug it is higher during early compression, and in the vicinity of the spark plug it is lower close to ignition (in fact the CFD shows higher temperatures at -20°CA than the polytropic compression model). This is the same behavior as measured with the IR absorption sensor (see Figure 5-15b). Thus, a physically consistent picture emerges: The sensor cage heats up during combustion and expansion. While the intake valve is open, the cage is still hot, but because of the fast flow through it, the temperature of most of the gas volume in the cage is nevertheless close to the temperature of the incoming charge. When the charge motion slows down after intake-valve closure, the still hot cage heats up the gas in it. The temperature of the gas in the probe volume is now

significantly higher than that of the bulk gas. Finally, during late compression, this difference reverses as the bulk gas is compressed to temperatures above the cage temperature.

5.5.4 Variation of engine operating parameters

This section reports on the effects of changes in engine operation on the mixture formation. Engine operation was varied by changing engine speed, intake pressure, and air/fuel ratio. Figure 5-18 shows crank-angle evolutions of λ from around the spark plug of five engine runs at 1500 min^{-1} with 820 mbar intake pressure and two engine runs at 1200 min^{-1} with 600 mbar intake pressure. Detailed information on the parameters are listed in Table 5-1. Except for experiment 03_02, injection ends at intake valve opening at -334°CA . In experiment 03_02, the end of injection is 11°CA after the intake valves have closed, engine operated at 1500 min^{-1} , and $\lambda_{\text{PFI}} = 0.86$. Similar to Figure 5-10, λ is averaged over the three ROIs around the spark-plug sensor.

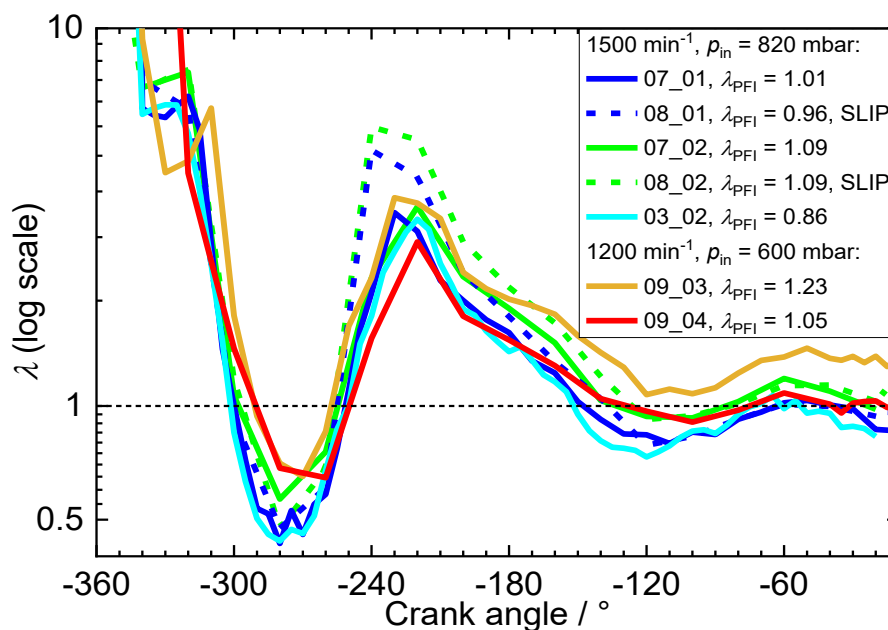


Figure 5-18: Comparison of λ from LIF imaging of different engine runs. Data from three ROIs around the spark plug sensor from 20-cycle averaged images were extracted and averaged. The black dashed line marks $\lambda = 1$.

Qualitatively all traces show the same trend: In the very beginning of the cycle between -340°CA and -300°CA a fuel-lean mixture with $3.5 < \lambda < 8$ is present in all cases followed by fuel-rich mixture passing the spark plug between -320°CA and -250°CA . In the vicinity of the spark plug, slower engine speed and lower intake pressure (see Table 5-1) cause greater λ during the fuel-rich phase. At around -280°CA all λ -traces have a local minimum. At that minimum λ is lower the lower λ_{PFI} . At 1200 min^{-1} in fuel-lean operation (09_03), λ exhibits

a 10°CA-shorter fuel-rich phase (from -290°CA to -260°CA) than in fuel-rich operation (09_04). In 09_04 injection was initiated 10°CA earlier than in 09_03 which coincides with the 10°CA-delay in the arrival of the second fuel-lean phase. A field-wide comparison of λ from these two experiments is shown in Appx. 8-3.

Between -250°CA and -120°CA, the most significant changes in λ occur. In all cases significantly fuel-lean ($\lambda > 3$) mixtures are seen with a peak at around -220°CA. Fuel-lean operation at 1500 min⁻¹ examined with SLIPI (08_02), has a maximum of $\lambda = 5.5$ at -200°CA, while λ via conventional LIF (07_02) at a similar engine speed and λ_{PFI} does not exceed 3.3. Additionally, the peak in 07_02 is reached 20°CA later than seen in 08_02 via SLIPI. From the field-wide comparison in Figure 5-20 it can be seen that the estimated fuel-lean region at -220°CA is broader by SLIPI than by conventional LIF imaging. However, the fuel-rich regions at -220°CA estimated via SLIPI and conventional LIF imaging coincide. Similar characteristics can also be seen in the comparison of experiments 07_01 and 08_01.

From the local maximum at approximately -220°CA λ decreases towards stoichiometric, followed by a slight increase from about -110°CA. During compression, λ in images with SLIPI quantitatively coincides with the corresponding λ from conventional LIF. Fuel-rich operation, experiment 03_02 ($\lambda_{\text{PFI}} = 0.86$), is subject to an oscillation in λ that does not exceed stoichiometric later than -160°CA, finally reaching $\lambda = 0.84$ at around -20°CA. In contrast to the latter, λ in overall fuel-lean operation 09_03 ($\lambda_{\text{PFI}} = 1.23$) at 1200 min⁻¹ does not fall below stoichiometric after -260°CA and reaches $\lambda = 1.32$ close to TDC in the vicinity of the spark plug.

5.5.5 Effect of SLIPI and Gaussian filtering

Figure 5-19 shows four single shots, the 20-cycle mean, and coefficient of variation (COV, ratio of the one-standard deviation σ to the mean μ) of λ at -280°CA from SLIPI, conventional LIF imaging, and a Gaussian filter applied to the images from conventional LIF imaging. The engine was operated at $\lambda_{\text{PFI}} = 1.09$ and 1500 min⁻¹. Gaussian filtering was applied with a similar kernel as in the SLIPI processing describe in Section 5.4.1 neglecting the shift of the image in Fourier space. Conventional LIF imaging resolves smaller structures than SLIPI as apparent in single shots of λ in Figure 5-19. The Gaussian filtered images from conventional LIF imaging degrades the resolution of the images such, that approximately structures of similar size as from SLIPI are resolved. The loss in resolution can also be recognized in the mean images by the smoothing in the image after Gaussian filtering. However, the overall distribution of λ in the mean image apparently is not different with or without Gaussian filtering, but the estimated fuel-rich region in the mean SLIPI images is larger than estimated from conventional LIF imaging. The latter may be due to the more accurate corrected background with SLIPI compared to conventional background subtraction in the other data. The COV in λ from SLIPI is greater compared to the relative variability from conventional LIF imaging. Especially in the region where the fresh charge mixes with the residual gas the COV in λ is 25% higher in the SLIPI images compare to the others indicating an increased detection limit in λ with SLIPI.

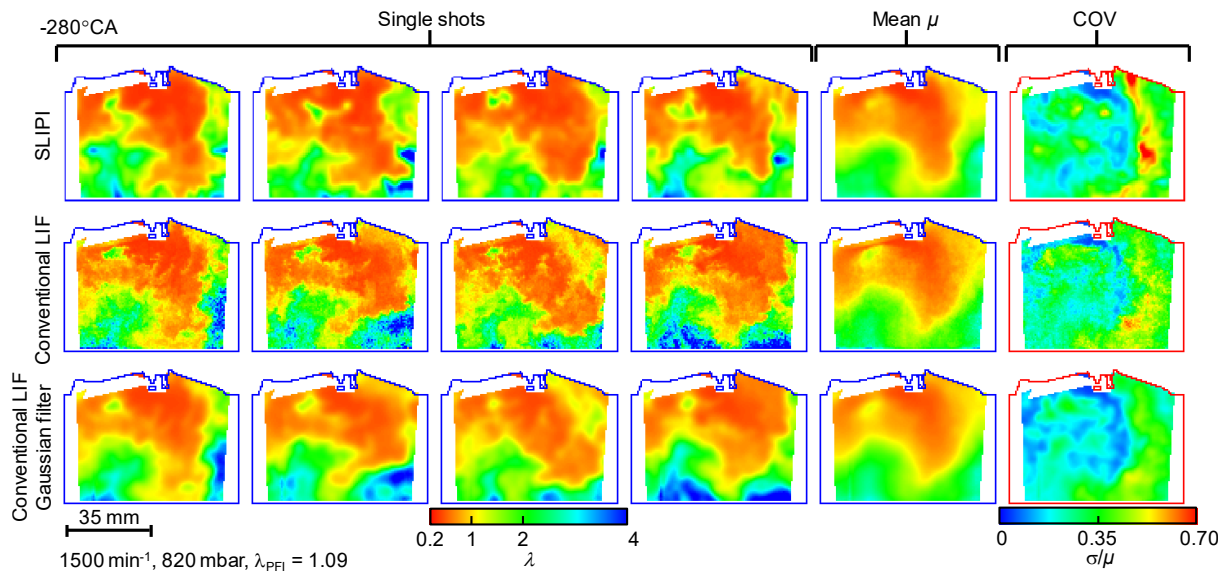


Figure 5-19: Single shots, 20-cycles mean, and local COV of λ at -280°CA at 1500 min^{-1} engine speed and $\lambda_{PFI} = 1.09$. The data in the top row (08_02) were acquired via SLIPI, the data in the middle row (07_02) via conventional LIF imaging, and the data in the bottom row (also 07_02) shows the data from conventional LIF imaging after Gaussian filtering. The mean images and COVs are calculated from 20 single shots in consecutive cycles.

Figure 5-20 shows a field-wide comparison of the spatio-temporal evolution of the 20-cycle mean λ via SLIPI, conventional LIF imaging, and conventional LIF imaging with Gaussian filtering with the engine operated at $\lambda_{PFI} = 1.09$ and 1500 min^{-1} . The images from SLIPI show greater λ compared to the images from conventional LIF imaging in fuel-lean regions near the spark plug during the gas-exchange stroke. Therefore, SLIPI seems to increase the dynamic range towards higher λ -values. Additionally, local gradients are slightly steeper in the SLIPI data, which may be due to an increase in sensitivity in measuring λ for low LIF signal. Also, especially late in the compression stroke, the mean images from conventional LIF imaging with Gaussian filtering and SLIPI look smoother than the images without filtering, since small grainy structures associated with noise are filtered. However, after intake-valve closing at -184°CA , the evolutions of λ agree temporally and spatially, all showing clock-wise tumble convection with gradual mixing. At -40°CA the results quantitatively match showing a slight decrease in λ from left to right.

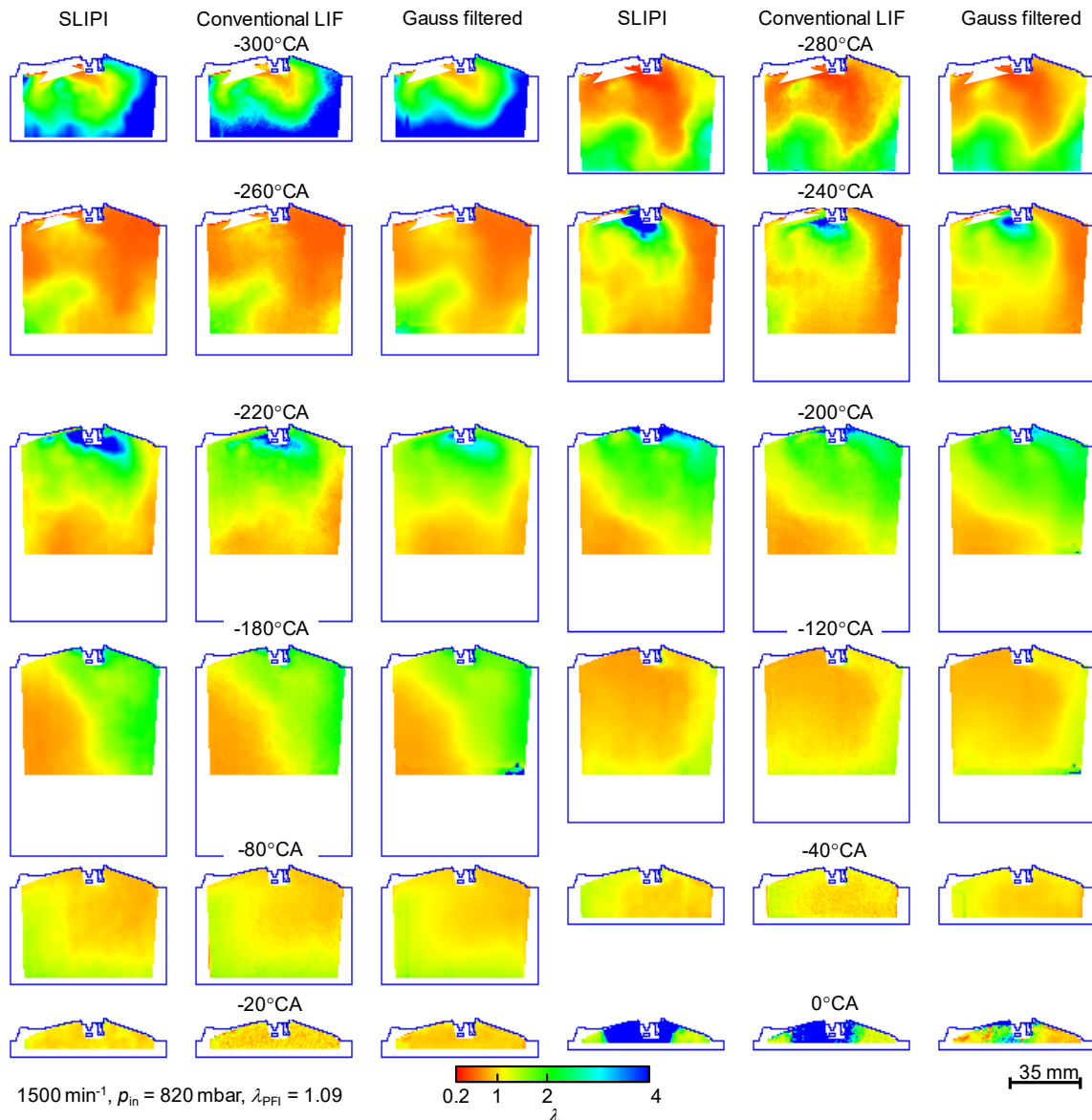


Figure 5-20: Field-wide comparison of λ as crank-angle evolution from LIF imaging of engine operation at $\lambda_{PFI} = 1.09$ measured via SLIPI (set 08_02) and conventional LIF (set 07_02) as well as at $\lambda_{PFI} = 0.86$ (set 03_02). Engine speed is 1500 min⁻¹, intake pressure 820 mbar. LIF images at each crank angle are ensemble averages of 20 consecutive cycles.

Figure 5-21 shows four single shots, the 20-cycle mean, and standard deviation σ in λ at -40°CA from SLIPI, conventional LIF imaging, and a Gaussian filter applied to the images from conventional LIF imaging. SLIPI processing and Gaussian filtering decreases the standard deviation by a factor of 2 compromised by the degradation of the spatial resolution due to the line structures (one line pair per 3 mm) in the SLIPI raw images. The decrease in spatial resolution is directly connected to the size of the low-pass Gaussian filter applied to the SLIPI data. The size of the Gaussian filter, in turn, is limited by the spatial frequency of the modulation. The effect of SLIPI filtering on spatial resolution has been discussed by Mishra et al. [44]. They state that a modulation of the light sheet at high spatial frequency is crucial to resolve small-scale structures via one-phase SLIPI.

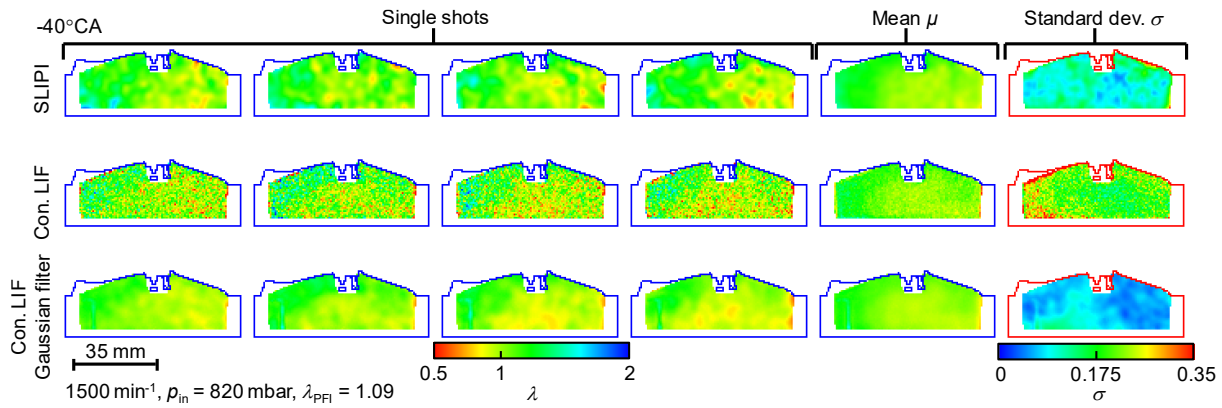


Figure 5-21: Single shots, 20-cycles mean, and local standard deviation σ of λ at -40°CA at 1500 min^{-1} engine speed and $\lambda_{\text{PFI}} = 1.09$. The data in the top row (08_02) were acquired via SLIPI, the data in the middle row (07_02) via conventional LIF imaging, and the data in the bottom row (also 07_02) shows the data from conventional LIF imaging after Gaussian filtering. The mean images and COVs are calculated from 20 single shots in consecutive cycles.

5.5.6 Cyclic variability

Figure 5-22 shows four snapshots, the 20-cycles mean and coefficient of variation COV in every pixel of λ in (a) and the corresponding temperature-fields in (b) during intake-valve open at -280°CA at 1200 min^{-1} , 1500 min^{-1} , and 2500 min^{-1} in fuel-lean operation. As discussed with Figure 5-18, λ reaches a global minimum at -280°CA near the spark plug in all data. From the mean images in at -280°CA in Figure 5-22 it can be seen that an increase in engine speed with additional increase in intake pressure does affect the λ and temperature distribution. The fuel-rich region is the largest at 1500 min^{-1} and 820 mbar intake pressure. At 1200 min^{-1} and 2500 min^{-1} the mean λ images in Figure 5-22a look largely the same, but the mean at 1500 min^{-1} shows shorter penetration of the fuel-rich fresh charge compared other engine speeds. This may have two reasons: At lower engine speed, the mixture has more time to propagate from SOI until -280°CA , and an increase in intake pressure might also increases the fluid velocity through the intake valves affecting fuel propagation. However, the influence of intake pressure on the fluid velocity cannot be determined from Figure 5-22.

The temperature in the images in Figure 5-22b that correspond to the λ -images in Figure 5-22a, however, decreases monotonically with the simultaneous increase in engine speed and intake pressure. At 1200 min^{-1} the temperature near the piston surface is 20 K higher than at 1500 min^{-1} and 60 K higher than at 2500 min^{-1} . The local temperature near the spark plug electrode, near where the fresh charge is entering the combustion chamber, is 340 K in all cases.

Cyclic variability can be seen from the series of individual single shots of λ and temperature. A measure for CCV of each data set is the 20-cycle COV in every pixel. The highest COVs of up to 65% are located in the fuel-lean region where the mixing of the fresh charge with the hot residual gas takes place. It seems like that the location of highest COV in λ rotates further clockwise with increasing engine speed and intake pressure, while the strongest cyclic variability occurs at 1500 min^{-1} . Contrary to this, the COV in IMEP over 200 cycles is

1% at 1500 min^{-1} , but 5% at 2500 min^{-1} and 3.5% at 1200 min^{-1} , even though far from ignition exactly the opposite trend to that seen from the COV of λ at -280°CA . One possible explanation might be that higher COV in λ early in the cycle indicates stronger turbulent mixing yielding a more homogeneous mixture later in the cycle, and thus lower cyclic variability in IMEP. From snapshots of T and λ it can be seen that hotter regions are preferentially fuel-lean and colder regions are more likely to be fuel-rich which is expected since the incoming air-fuel mixture is cold and mixes with the hot residual gas.

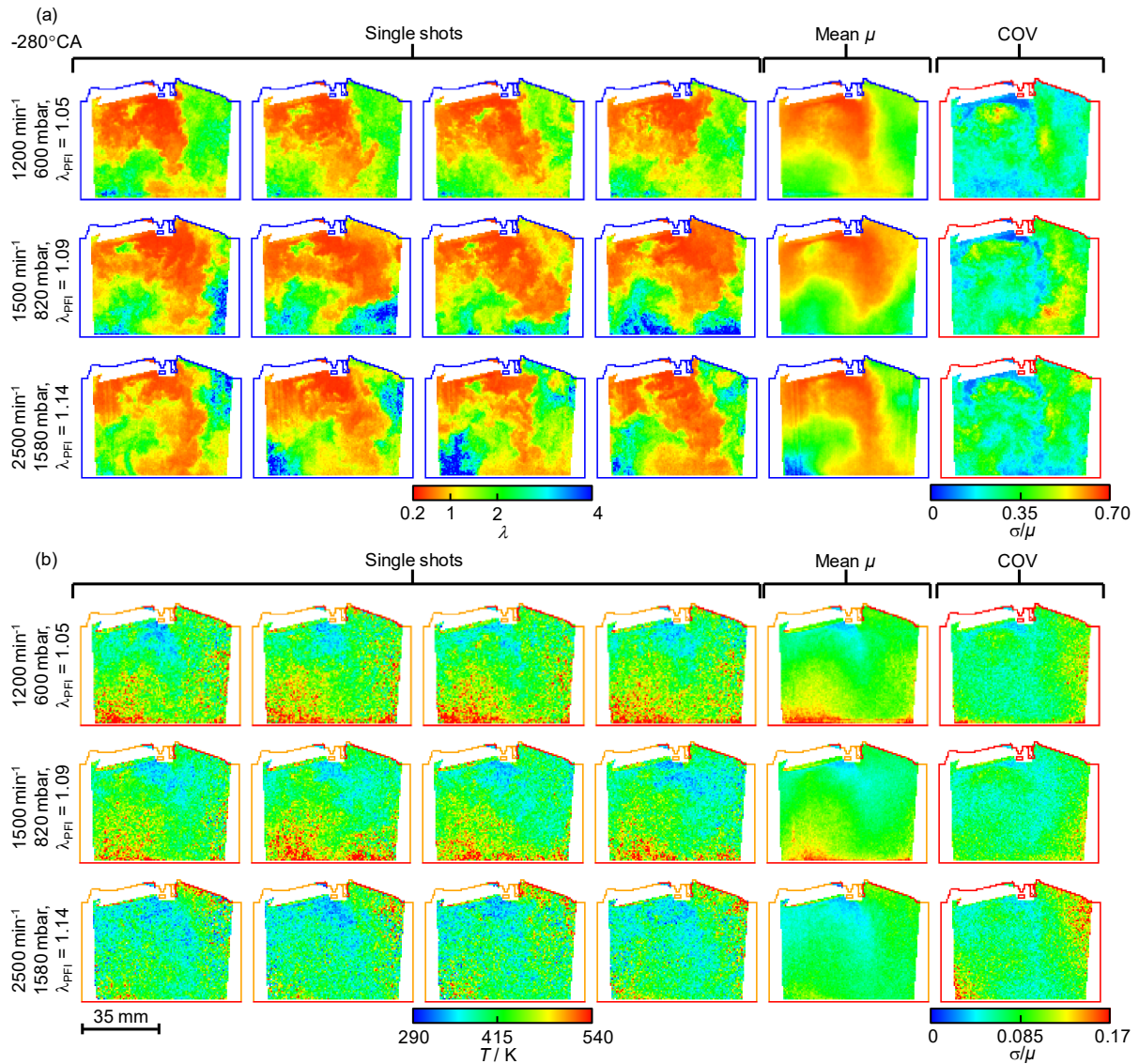


Figure 5-22: Single shots, 20-cycles mean, and local COV of λ in (a) and T in (b) at -280°CA from four engine runs (Top to bottom: 09_04, 07_02, and 13_01) at different engine speeds, intake pressures, but similar $\lambda_{PFI} \approx 1.1$. The mean images and standard deviations are calculated from 20 single shots in consecutive cycles in the experiments at 1200 min^{-1} and 1500 min^{-1} , and from 15 single shots in every 2nd cycle at 2500 min^{-1} .

To discuss the effect of engine speed and intake pressure on the cyclic variations in λ close to ignition, Figure 5-23 shows images of λ at -40°CA , again four single shots, the 20-cycles ensemble mean, and one-standard deviation in each pixel at 1200 min^{-1} and 1500 min^{-1} in fuel-lean operation. The images from conventional LIF imaging are Gaussian filtered with a kernel size equal to the one from SLIPI to improve the SNR. Because of an engine failure, unfortunately data are not available at 2500 min^{-1} for crank angles later than -280°CA . Instead, results at 1200 min^{-1} with $\lambda_{\text{PFI}} = 1.23$ are shown.

The in-cylinder temperature is high late in the compression stroke, causing a significant decrease in signal negatively affecting the SNR compared to SNR in images at earlier crank angles as already discussed in Section 5.5.5. At 1500 min^{-1} and $\lambda_{\text{PFI}} = 1.09$ the temperature is about 70 K higher than at 1200 min^{-1} and $\lambda_{\text{PFI}} = 1.05$, which slightly lowers the precision. Also, when operating at $\lambda_{\text{PFI}} = 1.23$ the one-standard deviation shown in Figure 5-23 at is slightly higher than the standard deviation when operated at $\lambda_{\text{PFI}} = 1.05$, which coincides with the fact, that the COV in IMEP of 3% at $\lambda_{\text{PFI}} = 1.05$ is lower than the COV in IMEP of 4.8% at $\lambda_{\text{PFI}} = 1.23$. However, because of the superposition of measurement noise and cyclic variations in λ , the standard deviations in Figure 5-23 do not evidently correlate with the COVs in IMEP listed in Table 5-1b.

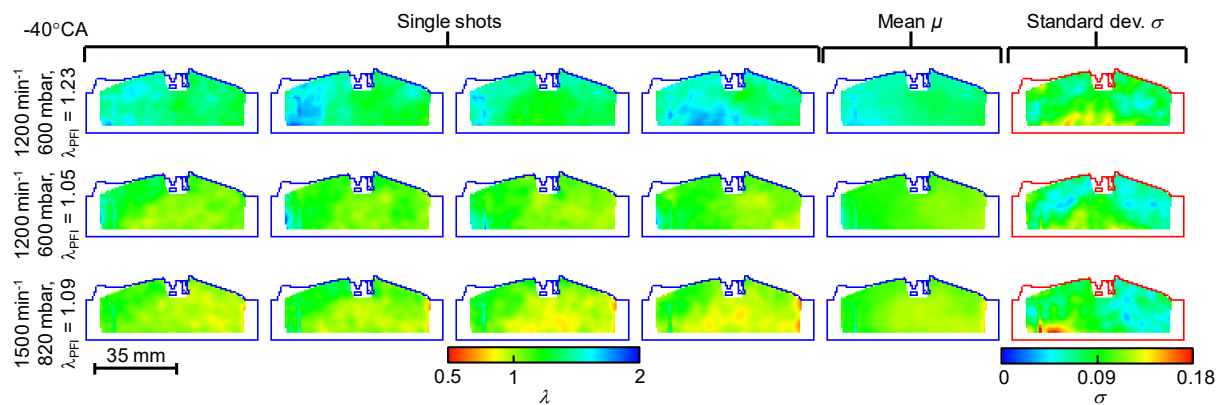


Figure 5-23: Single shots, mean, and standard deviation of λ from conventional LIF imaging after Gaussian filtering at -40°CA from three different engine runs (Top to bottom: 09_03, 09_04, and 07_02) at different engine speeds, intake pressures, and λ_{PFI} . Mean images and standard deviations in each pixel are calculated from 20 single shots in consecutive cycles.

5.5.7 Single-shot precision and accuracy

In all flatfields, λ is thought to be spatially homogeneous and equal to the set λ_{FF} . Hence, the scatter of λ around unity in the temperature-corrected flatfields reflects the precision of the measurements at $\lambda = 1$. The relative standard deviation of λ_{FF} among pixels in an area of $4.2 \times 4.2\text{ mm}^2$ of a typical single shot is $\sigma_{\text{area}} = 4.6\%$ until -100°CA , increasing to $\sigma_{\text{area}} = 11.5\%$ at -20°CA . Photon noise and non-uniformities in laser-profile are likely sources for this error. The standard deviation of one binned super-pixel (an area of $0.7 \times 0.7\text{ mm}^2$) over 20

consecutive single shots is $\sigma_{S2S} = 4.9\%$ and $\sigma_{S2S} = 11.6\%$. A typical overall precision at $\lambda = 1$ and 0.7-mm resolution is again estimated according to $\sigma = \sqrt{\sigma_{\text{area}}^2 + \sigma_{S2S}^2} = 6.7\%$ for crank angles before -100°CA and $\sigma = 16.3\%$ at -20°CA . Equivalent to this, precision in the temperature at 0.7-mm resolution is $\sigma = 8.9\%$ for crank angles before -100°CA (T below 405 K) and $\sigma = 10.4\%$ at -20°CA (at 771 K).

The accuracy in λ is more difficult to address. As already discussed in Section 5.5.1, the linear approximation in FARLIF causes an overestimation of λ on the order of 5% to 12% at stoichiometric air/fuel ratio. To cross-check the findings from Section 5.5.1, fired engine runs in homogeneous operation were carried out where the field-wide λ should be equal to λ_{FF} before ignition. Especially the differences with and without correction of the deviations in temperature in fired and motored operation are of interest. Therefore, Figure 5-24a shows the λ -evolution from the average of ROIs 1 to 3 near the spark plug of operation at $\lambda_{\text{FF}} = 1.1$ and 1500 min^{-1} . The air/fuel ratio was computed from experiment 07_02 with conventional LIF and 08_02 with SLIPI. Figure 5-24 includes λ estimated with and without temperature correction. Because the transmission of each detection channel (blue vs. red) has different temperature sensitivities, additionally to the temperature corrected λ also the air/fuel ratios without temperature correction from both channels are shown.

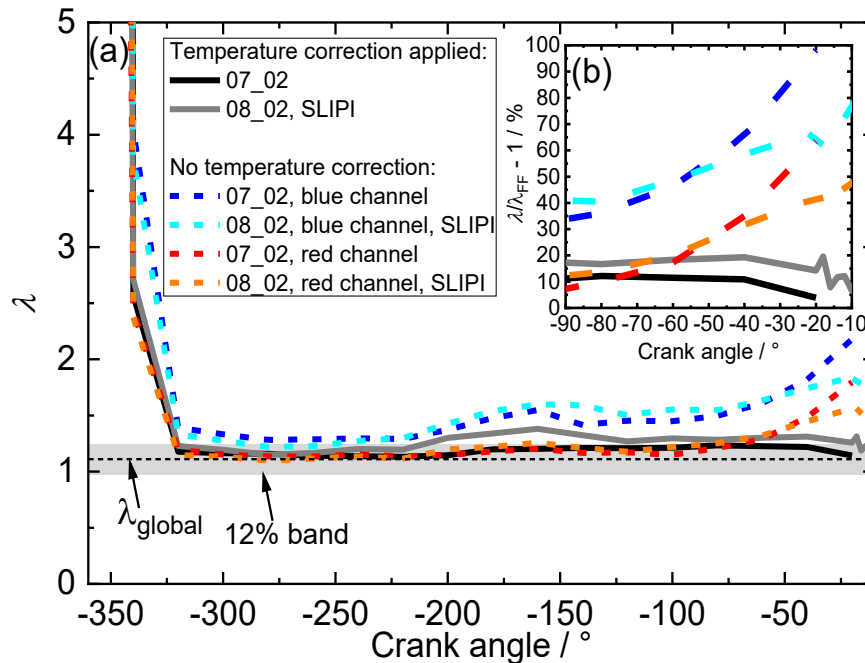


Figure 5-24: Crank-angle evolutions of λ in (a) at $\lambda_{\text{FF}} = 1.1$ and 1500 min^{-1} with the engine running on a homogeneous mixture in fired operation. Insert: the error $\lambda/\lambda_{\text{FF}} - 1$ for late crank angles. Datasets with SLIPI are compared with conventional LIF imaging processed with and without correction of the influence of the local temperature.

Differences between fired and motored operation with homogeneous charge are expected. Compared to the motored case, the in-cylinder temperatures are higher due to the mixing of the fresh gas with the hot residual gas. However, regions reached by the intake air-fuel mixture should always be at an air/fuel ratio equal to λ_{FF} .

Even though the engine was operated with continuous fuel supply far upstream of the intake pipe, the λ -evolutions shown in Figure 5-24a reflect similar characteristics as with PFI, but not that pronounced. A steep decrease towards stoichiometric ($\lambda \approx 1.13$) takes place when the intake valves open. Then a slight increase in λ towards a local maximum at around -180°CA occurs. The λ -trace from the blue channel without temperature correction shows greater values than the evolution of λ from the red channel without temperature correction and both temperature-corrected air/fuel ratios. As already seen in the PFI case shown in Figure 5-18, also in homogeneous operation λ from SLIPI is greater than λ from conventional LIF. Also, the λ -evolution of the red channel without temperature correction agrees well with the corrected λ -trace without SLIPI until mid of the compression stroke. However, the λ -evolution of the blue channel without correction mismatches the expected λ_{FF} at every crank angle.

Figure 5-24b shows the relative deviation of λ from λ_{FF} , $\lambda/\lambda_{FF} - 1$. From -70°CA the strongest deviations between the corrected and uncorrected λ -evolutions in both channels arise. At -40°CA , the deviation of λ estimated without temperature correction from λ_{FF} without of the red channel is about 30% and of the blue channel is 70%, (greater than λ_{FF}), while with correction the deviation is on the order of 10% to 15%. At -20°CA , which is 10°CA before ignition, λ after temperature correction from λ_{FF} deviates less than 10% while without correction of the temperature influence a relative error between 40% and 100% remains. Hence, the accuracy in λ from the red channel (BP320) during gas-exchange and early compression until approximately -90°CA is better than 10% and similar to the accuracy of the temperature-corrected λ . From -70°CA ($\sim 500\text{ K}$) the accuracy is improved from at least 40% relative error to better than 10% if the influence of the temperature deviation between motored and fired operation on the LIF signal is corrected. The remaining 10% error at $\lambda = 1.1$ may stem from the deviation from the linear assumption in FARLIF as discussed in Section 5.5.1. Overall, in a trade-off with the resulting degradation in precision, the LIF signal needs to be corrected for temperatures greater than 500 K and $\lambda > 1.1$ to achieve an accuracy of about 11%.

5.6 Section conclusions

Two-color LIF imaging of temperature and air/fuel ratio in an optically accessible engine fueled by natural gas was reported. Snapshot images of λ were computed from LIF imaging of anisole as a tracer added to the methane fuel. In the current implementation, LIF provides spatially resolved two-dimensional data on the mixture formation once per cycle. Temperature deviations between the calibration and the fired PFI measurement were corrected to improve the accuracy of the technique. λ in the vicinity of the spark plug was compared to λ derived from simultaneously measured broadband IR absorption over a short path in a spark-plug integrated sensor. Additionally, a field-wide comparison of λ and T at 1500 min^{-1} and $\lambda_{\text{PFI}} = 1$ from LIF imaging and a RANS-type CFD simulation was presented. All three methods (LIF imaging, IR absorption measurements, and CFD simulation) are capable of determining λ and give complementary results. IR absorption is restricted to a point-like measurement, but at a high repetition rate delivering continuous crank-angle resolved measurements over consecutive cycles. The CFD simulation involves simplifying models of turbulence and mixing but delivers three-dimensional results in all relevant scalars and velocity. In practical use, application of the IR absorption sensor in production engines is straightforward, whereas LIF is much more resource intensive. The effort for CFD is in between, depending partly on which models are already available to estimate the boundary conditions.

The temperature in the probe volume is a crucial auxiliary variable to quantify λ via LIF imaging. Therefore, the technique exploits the change of spectral features with temperature via a two-camera LIF optical setup. This additional experimental complexity significantly improves accuracy. As a result, the LIF experiment agrees well with the IR absorption experiment and the simulation in the measured or calculated λ . Visually, the spatio-temporal evolution from LIF imaging and the CFD simulation coincide very well. Both clearly show that in-cylinder mixture formation consists of clockwise tumble convection with gradual mixing. The CFD shows sharper spatial gradients, which is due to the RANS approach. Sampling around the spark-plug in LIF images and CFD simulation, the crank-angle evolution of λ agrees well with the IR absorption measurement. The CFD simulation also agrees, except for an offset in the time at which the fuel-rich portion of the fresh gas enters. However, in temperature there is significant disagreement between the three methods at all crank angles. IR absorption predicts a temperature evolution that is qualitatively different from LIF and CFD. With the extra spatial information available from the (LIF cross-checked) simulation, it was shown conclusively that this temperature evolution is due to heat transfer to the spark-plug sensor's metal cage from the cylinder charge. It is "a feature, not a bug" and can be accounted for in data evaluation. Temperature from LIF imaging, however, is systematically about 50 K higher than that from the CFD simulation, which could not be attributed to any particular experimental issue.

After this comparison of LIF imaging with other methods at one engine operating condition, the mixture preparation at 1200 min^{-1} , 1500 min^{-1} , and 2500 min^{-1} in fuel-lean and fuel-rich operation - mainly at low load - was investigated further via LIF imaging only. For the presented LIF imaging technique, to first order, higher load at approximately stoichiometric equivalence ratio is inconsequential. The resulting higher wall and thus charge temperatures are

taken into account by the temperature correction. It was shown that fuel-lean operation (e.g. $\lambda_{\text{PFI}} = 1.3$ versus stoichiometric operation) does not cause a significant decrease in signal-to-noise ratio, even late in the compression stroke, when in-cylinder temperatures are high. This negatively affects the measurement precision, which was recognizable in the local coefficient of variation over a set of cycles. At -280°CA a simultaneous increase of engine speed and intake pressure increases the penetration depth of the fresh charge into the combustion chamber and overall decreases the temperature. From the combination of single shots of temperature and λ , the cooling of the residual gas by the fresh charge during gas exchange was examined. Initially, the incoming fuel-rich fresh charge mixes with the hot residual gas and is then followed by almost pure air during the late part of the intake stroke but ends up warmer than the leaner part of the charge at start of compression. The observed effect is driven by spatio-temporal convection of the fresh charge and residual gas by the bulk flow. Close to TDC, the temperature images are noisy without large-scale gradients, but some gradients in λ were found.

The linearity between the LIF signal and λ^{-1} is crucial for the FARLIF approximation and was addressed in Section 5.5.1 by sets of flatfields acquired at different oxygen concentrations by successively replacing air with nitrogen while keeping the overall and fuel-mass flow (tracer-mass flow) constant. Here, it was seen that the deviation from a linear approximation increases towards low λ . At $\lambda = 1$, the deviation from linearity is below 11% up to 608 K, but at $\lambda = 0.2$ and 325 K the deviation is about 37%, increasing to 70% at 608 K. Thus, in very fuel-rich regions the accuracy in λ is expected to be poorer than in fuel-leaner regions. Since with PFI λ is mainly low early in the cycle, when temperatures are also low, the overall relative error is estimated to be on the order of 11%. However, it was also found that the current imaging system can detect a maximum of $\lambda \approx 3.3$ due to low signal-to-noise ratios in very fuel-lean regions. Related to that, it was also shown that SLIPI improves the detection limit to $\lambda \approx 5.5$ but reduces spatial resolution.

In LIF imaging with a gaseous fuel the main obstacle for increasing the single-shot precision is the low tracer concentration. To increase the concentration, all elements of the fuel supply system would need to be heated, but with anisole already a modest temperature increase would greatly elevate the saturation vapor pressure. Precision could also be increased by choosing a different way of dealing with the temperature difference between motored calibration (flatfield) and fired measurements. For example, only the image-wide mean difference could be corrected for, since the spatially resolved temperature field is noisy. When there are no severe spatial temperature gradients, this trade-off of decreased accuracy for increased precision might be acceptable. Finally, although the absolute accuracy of the CFD simulation is not known, the systematic deviation of the LIF-based temperature from the CFD results may imply inaccuracies. A more accurate temperature would also make the LIF-deduced λ more accurate. The temperature dependence of the signal detected in the red channel utilizing a BS310 plus BP340 ± 20 nm is weak up to 650 K. In that range the LIF signal would not necessarily demand temperature correction. Thus, at intermediate temperatures, e.g. in the early compression stroke, a simple single-camera setup might yield reasonable accuracy in λ .

Chapter 6 - Overall conclusions and future work

6.1 Overall conclusions

This thesis reports on quantitative imaging of mixing processes in two spark-ignited internal combustion engines, one motored with DI of a liquid multi-component surrogate and the other fired with PFI of methane. Measurements were performed by fluorescence imaging of aromatic “tracers” seeded in small amounts into the non-fluorescing surrogate fuel.

The first part of this work is on the effect of preferential evaporation after gasoline DI. For this purpose, two aromatic tracers, 1,4-difluorobenzene and 1-methylnaphthalene, were added to the surrogate fuel consisting of light-to-medium (*n*-pentane and *iso*-octane) and heavy components (*n*-undecane). LIF imaging provided spatially resolved two-dimensional data on the component segregation once per cycle. The measurement error induced by variations in temperature was assessed by means of two-color anisole LIF thermometry as well as calculations under the assumption of adiabatic fuel/bulk-gas mixing. Besides LIF imaging, the liquid spray penetration was visualized by RGB-illuminated diffuse back-illumination and Mie scatter imaging. Additionally, the influence of flow velocity measured via particle image velocimetry on fuel segregation was discussed.

The second experimental part of this work presents two-color LIF imaging as a technique for simultaneously quantifying the temperature T and the air/fuel ratio λ in an optically accessible PFI engine operated on methane. Snapshot images of λ were determined from LIF imaging of fluorescence from anisole vaporized into the methane fuel. As in the first part of the work, errors due to deviation between the local temperature in the calibration and in the fired PFI measurement were accounted for to improve the accuracy in λ . Collaborating researchers performed simultaneous infrared absorption measurements of methane concentration over a short path near the spark plug electrode, and a RANS-type CFD simulation. A comparison of LIF imaging with infrared absorption and the simulation showed deviations in the spatio-temporal evolution of λ and T in each of the methods. The errors in the quantification of λ , in particular those due to the deviation from the linearity implicit in the “FARLIF” approximation, were discussed.

The optical setups of each of the two LIF experiments were similar, both consisting of a two-camera setup with spectral separation of the fluorescence via a beam-splitter and tracer-specific filters. However, the photophysics exploited to derive the tracer-concentration ratio on one hand and λ on the other were different. In the gasoline DI experiment, the (calibrated) LIF signal was associated with *concentration*-ratio of the light and heavy components of the fuel since the experiment was carried out in the absence of fluorescence-quenching oxygen. Contrary to this, in determining λ in the oxygen-containing environment of the fired methane-fueled engine, it was assumed that the LIF signal from anisole is proportional to the *fuel/air ratio* (or the inverse of λ). A quantification of the fuel concentration is not possible here since the residual-gas concentration is not known. For both of the two studies the quantification of the desired quantity is influenced by deviations in temperature between calibration and measurement. Thus, the local temperature was determined, in both cases via two-color LIF of

anisolet. Additionally, in the gasoline DI experiment, the local temperature was also calculated by assuming adiabatic fuel-nitrogen mixing in the two-tracer experiment and compared to the local temperature from two-color anisolet thermometry. The final single-shot precisions and accuracies in the tracer-concentration ratio S_{DFB}/S_{IMN} , the temperature, determined via two-color thermometry T_{2CT} and via adiabatic mixing T_{AM} , as well as the air/fuel ratio λ and the temperature by two-color thermometry in air T are summarized in Table 6-1.

A pair of aromatic tracers was added to the multi-component surrogate representing the light-to-medium and heavy components of the fuel. The error induced by fluctuations in temperature was assessed via adiabatic mixing and compared to the local temperature by means of two-color anisolet LIF thermometry from another engine run. To increase accuracy in the predicted fuel-component fractions, the temperature deviation between temperature in flatfield images and the actual DI experiment was corrected. Injection at -47.75°CA was compared to injection at -67.75°CA both with 4 mm and 9 mm intake-valve lift. Taking the measurement uncertainty into account, tracer segregation and therefore preferential evaporation of the multi-component fuel are significant for all investigated conditions. A significantly heterogeneous fuel mixture was found until at least 4.6 ms aSOI. The high-volatility components of the fuel-vapor mixture were concentrated downstream at the tip of the vapor cloud, while a mixture with high proportion of low-volatility components were found upstream near the tip of the injector. This was consistent with previous results in a high-pressure vessel [97, 98]. Compared to the quasi-quietescent high-pressure vessel, the in the engine in-cylinder flow influences the location of the different components, and the change in temperature with crank angle influences the obtainable LIF signal. Turbulent mixing decreases the effect of preferential evaporation towards TDC, the bulk-flow velocity primarily affects the distribution of the fuel components, and injection later in the compression stroke decreases the overall segregation of fuel-components.

The temperature from two-color anisolet thermometry for the early injection case showed that the ensemble-mean temperatures at -55°CA in the fuel-vapor region are less than 25 K lower than the adiabatic-core temperature. This corresponds to a relative error induced by temperature inhomogeneities of less than 11% throughout the measured crank-angle range. Adiabatic mixing, however, underpredicted the temperature near the piston surface by about 10 K and indicated that the temperature in the fuel-vapor region is less than 35 K lower than the core temperature translating into a maximum error of 18% in the tracer-concentration ratio. Towards TDC, the error becomes less due to the then reduced temperature sensitivity of the tracer-concentration ratio. Overall, adiabatic mixing neglects the heat transfer between surfaces and gas phase, which negatively influences the accuracy in the vicinity of these surfaces. The precision in temperature from two-color LIF thermometry is significantly worse than that from adiabatic mixing.

One of the last steps in the two-tracer-LIF data processing was to relate the tracer-concentration ratio to local fuel-component concentration. To do so, results of model calculations by Bardi et al. [104] are used. It was seen that the strongest segregation occurs close to the injector tip and spark plug where the overall fuel mass-fraction is low. In regions of high fuel mass-fractions, e.g. near the piston surface, the segregation is less pronounced but still significant. In these regions spatial segregation of *n*-pentane from *iso*-octane and *n*-

undecane is significant. In a fired engine, the separation of the fuel components with late gasoline injection may affect the subsequent processes of ignition, combustion, and pollutant formation. Additionally, fuel-component segregation could increase the tendency for autoignition if local surface hot-spot coincide with adjacent regions of high concentrations of more reactive gasoline fractions.

Table 6-1: Summary of single-shot precision and accuracy in the quantification of the tracer-concentration ratio in N_2 , air/fuel ratio λ in air, temperature via adiabatic mixing T_{AM} in N_2 , two-color LIF thermometry in air T and in absence of oxygen T_{2CT} .

Quantity	Resolution / mm	Single-shot precision	Accuracy
----------	-----------------	-----------------------	----------

Chapter 4 - Preferential evaporation of a multi-comp. gasoline surrogate in a DI engine

S_{DFB}/S_{IMN} (no O_2)	0.24	~9%	-55°C at $S_{DFB}/S_{IMN} = 1$	After correction: < 18% at 510 K, < 1% at 730 K
T_{2CT} (anisole, no O_2)	0.96	~2% (6 K)	-55°C at $S_{DFB}/S_{IMN} = 1$	Better than T_{AM}
T_{AM} (DFB and IMN, no O_2)	0.24	< 1% (1 K)	-55°C at $S_{DFB}/S_{IMN} = 1$	Good in adiabatic core, poor near surfaces

Chapter 5 - Mixture formation in a PFI natural gas engine

λ (anisole, air)	0.70	~6.7%	-360 to -100°C at $\lambda = 1$	< 9% at $\lambda = 2$ and $T < 608$ K < 12% at $\lambda = 1$ and $T < 608$ K ~37% at $\lambda = 0.2$ and 325 K < 12% for relevant λ and T
		< 16.3%	-90 to -20°C at $\lambda = 1$	
T (anisole, air)	0.70	~8.9% (32 K)	-360 to -100°C at $\lambda = 1$	Deviation from CFD may be due to inaccurate calibration or boundary conditions in CFD
		< 10.4% (66 K)	-90 to -20°C at $\lambda = 1$	

PFI of natural gas was investigated in the second part of this work. The applicability of a two-color LIF imaging technique to simultaneously quantify temperature and air/fuel ratio in an optically accessible natural gas fueled engine was tested. Snapshot images of λ were derived from the LIF signal of anisole added to the methane fuel. Again, the influence of temperature on the LIF signal was corrected for, which was necessary to increase the accuracy in λ . The simultaneous acquisition of temperature and air/fuel ratio added additional experimental complexity but in return improved the accuracy. As a result, the λ -evolution from LIF coincided reasonably well with that from IR absorption and in CFD simulation. Qualitatively, there was good agreement in the spatio-temporal evolution of λ from LIF imaging and the simulation, both clearly showing that in-cylinder mixture formation consisted of clockwise tumble convection with gradual mixing. There was an offset in the time at which the fuel-rich portion of the fresh gas enters the cylinder. Sampled from around the spark-plug sensor in LIF images

and CFD simulation, the temporal evolution of λ also agreed well with the IR absorption measurement. From LIF and CFD it was seen that heat transfer from the hot IR-sensor cage into the bulk gas causes significantly higher temperatures in the probe volume of the IR measurement, making the simultaneous measurement of temperature also necessary in that experimental technique.

LIF imaging at 1200, 1500, and 2500 min^{-1} engine speed with overall fuel-lean and fuel-rich mixtures was presented. The SNR is quite low late in the compression stroke when in-cylinder temperatures are high. This negatively influences the measurement precision. The closed-valve PFI significantly causes gradual mixing of the cold fresh charge with the hotter residual gas early in the cycle. With increasing engine speed and intake pressure, the penetration depth of the cold rich fresh charge into the combustion chamber also increases but decreases the overall temperature during gas exchange. Close to TDC, the temperature images are noisy, but no large-scale gradients in temperature can be seen.

The linearity between the LIF signal and λ^{-1} was addressed by an additional experiment in which the homogeneous air-fuel mixture was successively diluted with nitrogen, while keeping the fuel-mass flow and overall mass flow constant. Here it was seen that the accuracy in λ is lowest at low λ (low oxygen concentration) and high temperatures, i.e., for $\lambda = 4$ the error is on the order of 2%. At $\lambda = 1$ the deviation from linearity is below 11% up to 608 K, but at $\lambda = 0.2$ and 325 K the deviation is about 37%, increasing to 70% at 608 K. Since in PFI λ may only be low early in the cycle where temperatures are also low, the deviation there is on the order of 11%. It was also found that SLIPI LIF is capable of improving the detection limit in λ from about 3.3 with conventional LIF imaging to 5.5, but in return reduces the spatial resolution. From this data the temperature-pressure dependence of the Stern-Volmer coefficient was evaluated. It was found that the Stern-Volmer coefficient in this work coincides well with literature data.

Comparing the single-shot *precisions* in temperature as listed in Table 6-1, two-color LIF thermometry in the absence of oxygen with anisole is about five times better than the measurements in air mixtures. The precision in the temperature images from the adiabatic-mixing model is even better. *Accuracy* in temperature is harder to address. Here, adiabatic mixing may have the lowest accuracy, especially near surfaces, where the situation is not adiabatic, and thus two-color thermometry may be more accurate here. But in two-color thermometry the accuracy is mainly affected by inaccuracies in the calibration of the temperature as function of the channel ratio. Since the red-shift of the spectrum that is exploited is also influenced by oxygen, the accuracy in the temperature in oxygen-containing environments is lower than without oxygen.

6.2 Future work

The restrictive assumptions made in the model translating the tracer-concentration ratio into fuel-mass composition may not apply for the complex situation of droplet evaporation in an engine spray. Alternatively, if the LIF-based imaging data are to be compared with CFD

simulations, it may be preferable to include the tracers in the simulation's evaporation model, allowing for a direct comparison with the experimental data to evaluate the accuracy of that particular evaporation model. The downside of this approach is that a model may differ in the accuracy with which it predicts major fuel components vs. sub-percent trace species.

In LIF imaging with a gaseous fuel the main obstacle to better single-shot precision is the low tracer concentration. To increase the concentration, all elements of the fuel supply system would need to be heated, but with anisole already a modest temperature increase would greatly elevate the saturation vapor pressure. Precision could also be increased by choosing a different way of dealing with the temperature difference between motored flatfield images and images from fired measurements. For example, only the image-wide mean difference could be corrected for, since the spatially resolved temperature field is noisy. When there are no severe spatial temperature gradients, this trade-off of decreased accuracy for increased precision might be acceptable. A more accurate temperature would also make the LIF-deduced λ more accurate. Also, it was shown that with anisole as a tracer, the temperature dependence in the "red" channel (BS310 plus BP340 \pm 20 nm) is weak up to 650 K, so it may be reasonable to utilize this or a similar filter arrangement for single-color measurements without any temperature correction.

Chapter 7 - Bibliography

1. Gniffke, P. "Umweltbundesamt - Treibhausgas-Emissionen in Deutschland - Emissionsentwicklung 1990 bis 2017". 2019, Available from: umweltbundesamt.de/daten/klima/treibhausgas-emissionen-in-deutschland.
 2. Health Effects Institute. "State of Global Air 2019". 2019, Available from: stateofglobalair.org/sites/default/files/soga_2019_report.pdf.
 3. Schulz, C., and Sick, V., "Tracer-LIF diagnostics: quantitative measurement of fuel concentration, temperature and fuel/air ratio in practical combustion systems", *Prog. Energy Combust. Sci.* 31(1):75-121, 2005.
 4. Kranz, P., and Kaiser, S.A. "Laser-induced-fluorescence based visualization of a multi-component fuel in a direct-injection engine". *Research Association for Combustion Engines eV, Frankfurt/Main Germany, Final Report, Project 1203*. 2018, Doc. No.: 1203.
 5. Bruneaux, G., Grisch, F., Kaiser, S., and Schulz, C. "Development of quantitative mixture measurement techniques for multi-component fuels including bio-fuel mixtures for automotive applications". *Research Association for Combustion Engines eV, Frankfurt/Main Germany, Final Report, Project 1110*. 2016, Doc. No.: 1101.
 6. Heywood, J., "Engine types and their operation", in *Internal Combustion Engine Fundamentals*, McGraw-Hill Education. 1988, p. 10.
 7. Merker, G.P., Haußmann, G., Eckert, P., Rakowski, S., Eichlseder, H., and Tschöke, H., "Thermodynamische und chemische Grundlagen", in *Grundlagen Verbrennungsmotoren*, Springer Fachmedien Wiesbaden: Springerlink. 2014, p. 16.
 8. Eifler, W., Schlücker, E., Spicher, U., and Will, G., "Gemeinsame Grundlagen der Kolbenmaschinen", in *Küttner Kolbenmaschinen*, Vieweg+Teubner Verlag. 2009, p. 16.
 9. Kleiber, M., and Joh, R., "D3 Stoffwerte von sonstigen reinen Fluiden", in *VDI-Wärmeatlas*, Springer Berlin Heidelberg: Berlin, Heidelberg. 2013, p. 357-488.
 10. Heywood, J., "Combustion stoichiometry", in *Internal Combustion Engine Fundamentals*, McGraw-Hill Education. 1988, p. 68 - 72.
 11. Heywood, J.B., "Mixture Preparation in SI Engines", in *Internal Combustion Engine Fundamentals 2E*, McGraw-Hill Education. 2018, p. 295-344.
 12. Ando, H., and Arcoumanis, C., "Flow, Mixture Preparation and Combustion in Four-Stroke Direct-Injection Gasoline Engines", in *Flow and Combustion in Reciprocating Engines*. 2008, p. 137-171.
 13. Heywood, J.B., "Exhaust Gas Treatment", in *Internal Combustion Engine Fundamentals 2E*, McGraw-Hill Education. 2018, p. 678-710.
 14. Baumgarten, C., "Mixture Formation in Internal Combustion Engines", in *Heat, Mass Transfer*. 2006, p. 5-23.
 15. Ohnesorge, W.V., "Die Bildung von Tropfen an Düsen und die Auflösung flüssiger Strahlen", *J. Appl. Math. Mech.* 16(6):355-358, 1936.
 16. Baumgarten, C., "Mixture Formation in Internal Combustion Engines", in *Heat, Mass Transfer*. 2006, p. 139-157.
 17. Pagel, S., *Verdampfungs- und Selbstzündungsmodelle für Mehrkomponenten-Gemische*, PhD thesis, University of Hannover, VDI-Verlag, Germany, 2004.
 18. Eichler, J., and Eichler, H.J., "Festkörperlaser", in *Laser*. 2010, p. 143-178.
-

19. Eichler, J., and Eichler, H.J., "Pulsbetrieb", in *Laser*. 2010, p. 319-337.
 20. Eichler, J., and Eichler, H.J., "Frequenzumsetzung", in *Laser*. 2010, p. 351-366.
 21. Khare, R., and Shukla, P.K., "Temporal Stretching of Laser Pulses", in *Coherence and Ultrashort Pulse Laser Emission*. 2010, p. 206-207.
 22. Kojima, J., and Nguyen, Q.V., "Laser pulse-stretching with multiple optical ring cavities", *Appl. Opt.* 41(30):6360-6370, 2002.
 23. Elprocus. "Light Emitting Diodes Circuit Working Principle and Application". 2019, Available from: elprocus.com/light-emitting-diode-led-working-application/.
 24. Menser, J., Schneider, F., Dreier, T., and Kaiser, S.A., "Multi-pulse shadowgraphic RGB illumination and detection for flow tracking", *Exp. Fluids* 59(6):90, 2018.
 25. Willert, C., Stasicki, B., Klinner, J., and Moessner, S., "Pulsed operation of high-power light emitting diodes for imaging flow velocimetry", *Meas. Sci. Technol.* 21(7), 2010.
 26. Willert, C.E., Mitchell, D.M., and Soria, J., "An assessment of high-power light-emitting diodes for high frame rate schlieren imaging", *Exp. Fluids* 53(2):413-421, 2012.
 27. Raffel, M., Willert, C.E., Wereley, S.T., and Kompenhans, J., "Physical and Technical Background", in *Particle Image Velocimetry*. 2007, p. 69-72.
 28. Dehn, A., Kersting, M., and Weinmann, K. "Knowledge base - CCD sensor types". 2019, Available from: stemmer-imaging.com/en/knowledge-base/ccd/.
 29. "The Bayer Sensor Strategy". 2020, Available from: red.com/red-101/bayer-sensor-strategy.
 30. Jiang, J., Liu, D., Gu, J., and Süsstrunk, S. "What is the space of spectral sensitivity functions for digital color cameras?". in *IEEE Workshop on Applications of Computer Vision (WACV)*. January 15th - 17th, 2013. Tampa, FL, USA.
 31. *Product-Manual Intensified Relay Optics - IRO*, ed.: 1004689, LaVison GmbH, LaVision GmbH, Anna-Vandenhoeck-Ring 19, D-37081 Göttingen, 2016. p. 10-12, Available from: lavision.de/de/downloads/manuals/.
 32. Sauer, M., Hofkens, J., and Enderlein, J., "Basic Principles of Fluorescence Spectroscopy", in *Handbook of Fluorescence Spectroscopy and Imaging*. 2011, p. 1-30.
 33. Koban, W., Koch, J.D., Hanson, R.K., and Schulz, C., "Oxygen quenching of toluene fluorescence at elevated temperatures", *Appl. Phys. B* 80(6):777-784, 2005.
 34. Tran, K.H., Morin, C., Kühni, M., and Guibert, P., "Fluorescence spectroscopy of anisole at elevated temperatures and pressures", *Appl. Phys. B* 115(4):461-470, 2014.
 35. Wang, Q., Tran, K.H., Morin, C., Bonnetty, J., Legros, G., and Guibert, P., "Predicting fluorescence quantum yield for anisole at elevated temperatures and pressures", *Appl. Phys. B* 123(7):199, 2017.
 36. Reboux, J., Puechberty, D., and Dionnet, F., "A New Approach of Planar Laser Induced Fluorescence Applied to Fuel/Air Ratio Measurement in the Compression Stroke of an Optical S.I. Engine", SAE Tech. Pap. 941988, 1994, doi:[10.4271/941988](https://doi.org/10.4271/941988).
 37. Scholz, J., Röhl, M., Wiersbinski, T., and Beushausen, V. "Verification and Application of Fuel-Air-Ratio-LIF". in *13th Int. Symp. on Applications of Laser Techniques to Fluid Mechanics*. June 26th - 29th, 2006. Lisbon, Portugal.
 38. Wellander, R., Berrocal, E., Kristensson, E., Richter, M., and Aldén, M., "Three-dimensional measurement of the local extinction coefficient in a dense spray", *Meas. Sci. Technol.* 22(12), 2011.
-

39. Berrocal, E., Kristensson, E., Richter, M., Linne, M., and Alden, M., "Multiple Scattering Suppression in Planar Laser Imaging of Dense Sprays by Means of Structured Illumination", *At. Sprays* 20(2):133-139, 2010.
 40. Mishra, Y.N., Kristensson, E., and Berrocal, E., "Reliable LIF/Mie droplet sizing in sprays using structured laser illumination planar imaging", *Opt. Express* 22(4):4480-4492, 2014.
 41. Berrocal, E., Kristensson, E., Richter, M., Linne, M., and Alden, M., "Application of structured illumination for multiple scattering suppression in planar laser imaging of dense sprays", *Opt. Express* 16(22):17870-17881, 2008.
 42. Mishra, Y.N., Abou Nada, F., Polster, S., Kristensson, E., and Berrocal, E., "Thermometry in aqueous solutions and sprays using two-color LIF and structured illumination", *Opt. Express* 24(5):4949-4963, 2016.
 43. Neil, M.A., Juskaitis, R., and Wilson, T., "Method of obtaining optical sectioning by using structured light in a conventional microscope", *Opt. Lett.* 22(24):1905-1907, 1997.
 44. Mishra, Y.N., Kristensson, E., Koegl, M., Jönsson, J., Zigan, L., and Berrocal, E., "Comparison between two-phase and one-phase SLIPI for instantaneous imaging of transient sprays", *Exp. Fluids* 58(9):110, 2017.
 45. Wygnanski, I., and Fiedler, H., "Some measurements in the self-preserving jet", *J. Fluid Mech.* 38(03):577-612, 1969.
 46. Schiffmann, P., Abraham, P.S., Reuss, D., and Sick, V. "High-speed Three-component Flow Imaging in an Optical Engine". in *Combustion Institute Central States 2012 Spring Meeting*. April 22nd - 24th, 2012. Dayton, OH, USA.
 47. Raffel, M., Willert, C.E., Wereley, S.T., and Kompenhans, J., "Mathematical Background of Statistical PIV Evaluation", in *Particle Image Velocimetry*, Springer-Verlag Berlin Heidelberg: Berlin, Heidelberg. 2007, p. 79-95.
 48. *FlowMaster DaVis 8.2 Product Manual*, LaVision GmbH, Göttingen Germany, 2013. p. 182, Available from: lavisoin.de/de/downloads/manuals/.
 49. Melling, A., "Tracer particles and seeding for particle image velocimetry", *Meas. Sci. Technol.* 8(12):1406-1416, 1997.
 50. Raffel, M., Willert, C.E., Wereley, S.T., and Kompenhans, J., "Particle Generation and Supply", in *Particle Image Velocimetry*, Springer-Verlag Berlin Heidelberg: Berlin, Heidelberg. 2007, p. 21-28.
 51. Keane, R.D., and Adrian, R.J., "Optimization of particle image velocimeters. I. Double pulsed systems", *Meas. Sci. Technol.* 1(11):1202-1215, 1990.
 52. Kranz, P., Schulz, C., and Kaiser, S.A. "LIF-based visualization of preferential evaporation of a multi-component fuel in an SIDI engine". in *8th European Combustion Meeting*. April 18th - 21st, 2017. Dubrovnik, Croatia.
 53. Kranz, P., and Kaiser, S.A., "LIF-based imaging of preferential evaporation of a multi-component gasoline surrogate in a direct-injection engine", *Proc. Combust. Inst.* 37(2):1365-1372, 2019.
 54. Geschwindner, C., Kranz, P., Welch, C., Schmidt, M., Böhm, B., Kaiser, S.A., and De la Morena, J., "Analysis of the interaction of Spray G and in-cylinder flow in two optical engines for late gasoline direct injection", *Int. J. Engine Res.* 21(1):169-184, 2019.
 55. Kohse-Hoinghaus, K., and Jeffries, J.B., "Applied combustion diagnostics", Taylor & Francis: New York. 2002, p. 1-672.
-

56. Eckbreth, A.C., "Laser Diagnostics for Temperature and Species in Unsteady Combustion", in *Unsteady Combustion*, Gordon and Breach Publishers: Amsterdam, The Netherlands. 1996, p. 393-410.
 57. Nauwerck, A., Gindele, J., Spicher, U., Roskamp, H., and Landwehr, G., "Investigation of the Transient In-Cylinder Flow Inside a Two Stroke Engine with Particle-Image-Velocimetry", SAE Tech. Pap. 2000-01-0902, 2000, doi:[10.4271/2000-01-0902](https://doi.org/10.4271/2000-01-0902).
 58. Gessenhardt, C., Schulz, C., and Kaiser, S.A., "Endoscopic temperature imaging in a four-cylinder IC engine via two-color toluene fluorescence", *Proc. Combust. Inst.* 35(3):3697-3705, 2015.
 59. Sasaki, T., Yoshida, K., Urata, Y., and Ishii, K., "Introduction to the optically accessible engine for investigation of in-cylinder phenomena", *JSAE Review* 21(4):573-575, 2000.
 60. Miles, P. "The History and Evolution of Optically Accessible Research Engines and Their Impact on Our Understanding of Engine Combustion". in *ASME 2014 Internal Combustion Engine Division Fall Technical Conference, ICEF 2014*. Oct. 19th – 22nd, 2014. Columbus, Indiana, USA.
 61. Kashdan, J.T., and Thirouard, B., "A Comparison of Combustion and Emissions Behaviour in Optical and Metal Single-Cylinder Diesel Engines", *SAE Int. J. Engines* 2(1):1857-1872, 2009.
 62. Bowditch, F.W., and Withrow, L.L. "Cylinder and piston assembly". United States Patent Office, Patent No.:US739920A, 1960.
 63. Pickett, L. "Sandia National Laboratories - Engine Combustion Network". 2017, Available from: ecn.sandia.gov/.
 64. Costa, M., Marchitto, L., Merola, S.S., and Sorge, U., "Study of mixture formation and early flame development in a research GDI (gasoline direct injection) engine through numerical simulation and UV-digital imaging", *Energy* 77:88-96, 2014.
 65. Zhao, F., Lai, M.C., and Harrington, D.L., "Automotive spark-ignited direct-injection gasoline engines", *Prog. Energy Combust. Sci.* 25(5):437-562, 1999.
 66. Moreira, A.L.N., Moita, A.S., and Panão, M.R., "Advances and challenges in explaining fuel spray impingement: How much of single droplet impact research is useful?", *Prog. Energy Combust. Sci.* 36(5):554-580, 2010.
 67. Oh, H., and Bae, C., "Effects of the injection timing on spray and combustion characteristics in a spray-guided DISI engine under lean-stratified operation", *Fuel* 107:225-235, 2013.
 68. Park, C., Kim, S., Kim, H., and Moriyoshi, Y., "Stratified lean combustion characteristics of a spray-guided combustion system in a gasoline direct injection engine", *Energy* 41(1):401-407, 2012.
 69. Stiehl, R., Schorr, J., Krüger, C., Dreizler, A., and Böhm, B., "In-Cylinder Flow and Fuel Spray Interactions in a Stratified Spray-Guided Gasoline Engine Investigated by High-Speed Laser Imaging Techniques", *Flow Turbul. Combust.* 91(3):431-450, 2013.
 70. Piock, W.F., Befrui, B., Berndorfer, A., and Hoffmann, G., "Fuel Pressure and Charge Motion Effects on GDI Engine Particulate Emissions", *SAE Int. J. Engines* 8(2):464-473, 2015.
 71. Fansler, T.D., Reuss, D.L., Sick, V., and Dahms, R.N., "Invited Review: Combustion instability in spray-guided stratified-charge engines: A review", *Int. J. Engine Res.* 16(3):260-305, 2015.
-

-
72. Drake, M.C., and Haworth, D.C., "Advanced gasoline engine development using optical diagnostics and numerical modeling", *Proc. Combust. Inst.* 31(1):99-124, 2007.
 73. Fansler, T.D., Stojkovic, B., Drake, M.C., and Rosalik, M.E., "Local fuel concentration measurements in internal combustion engines using spark-emission spectroscopy", *Appl. Phys. B* 75(4-5):577-590, 2002.
 74. Peterson, B., Reuss, D.L., and Sick, V., "On the ignition and flame development in a spray-guided direct-injection spark-ignition engine", *Combust. Flame* 161(1):240-255, 2014.
 75. Sementa, P., Maria Vaglieco, B., and Catapano, F., "Thermodynamic and optical characterizations of a high performance GDI engine operating in homogeneous and stratified charge mixture conditions fueled with gasoline and bio-ethanol", *Fuel* 96:204-219, 2012.
 76. Song, J., and Park, S., "Effect of Injection Strategy on the Spray Development Process in a Single-Cylinder Optical Gdi Engine", *At. Sprays* 25(9):819-836, 2015.
 77. Gutierrez, L., Mansfield, A.B., Fatouraie, M., et al., "Effects of Engine Speed on Spray Behaviors of the Engine Combustion Network "Spray G" Gasoline Injector", SAE Tech. Pap. 2018-01-0305, 2018, doi:[10.4271/2018-01-0305](https://doi.org/10.4271/2018-01-0305).
 78. Parrish, S.E., Zhang, G., and Zink, R.J., "Liquid and Vapor Envelopes of Sprays from a Multi-Hole Fuel Injector Operating under Closely-Spaced Double-Injection Conditions", *SAE Int. J. Engines* 5(2):400-414, 2012.
 79. Blessinger, M., Manin, J., Skeen, S.A., Meijer, M., Parrish, S., and Pickett, L.M., "Quantitative mixing measurements and stochastic variability of a vaporizing gasoline direct-injection spray", *Int. J. Engine Res.* 16(2):238-252, 2014.
 80. Sphicas, P., Pickett, L.M., Skeen, S.A., and Frank, J.H., "Inter-plume aerodynamics for gasoline spray collapse", *Int. J. Engine Res.* 19(10):1048-1067, 2017.
 81. Hamzah, A., Poursadegh, F., Lacey, J., Petersen, P., Brear, M.J., and Gordon, R. "A comparison of diffuse back-illumination (DBI) and Mie-scattering technique for measuring the liquid length of severely flashing spray". in *20th Australasian Fluid Mechanics Conference*. Dec. 5th - 8th, 2016. Perth, Australia.
 82. Itani, L.M., Bruneaux, G., Hermant, L., and Schulz, C., "Investigation of the Mixing Process and the Fuel Mass Concentration Fields for a Gasoline Direct-Injection Spray at ECN Spray G Conditions and Variants", SAE Tech. Pap. 2015-01-1902, 2015, doi:[10.4271/2015-01-1902](https://doi.org/10.4271/2015-01-1902).
 83. Lacey, J., Poursadegh, F., Brear, M.J., et al., "Generalizing the behavior of flash-boiling, plume interaction and spray collapse for multi-hole, direct injection", *Fuel* 200:345-356, 2017.
 84. Manin, J., Jung, Y., Skeen, S.A., Pickett, L.M., Parrish, S.E., and Markle, L., "Experimental Characterization of DI Gasoline Injection Processes", SAE Tech. Pap. 2015-01-1894, 2015, doi:[10.4271/2015-01-1894](https://doi.org/10.4271/2015-01-1894).
 85. Montanaro, A., and Allocca, L., "Flash Boiling Evidences of a Multi-Hole GDI Spray under Engine Conditions by Mie-Scattering Measurements", SAE Tech. Pap. 2015-01-1945, 2015, doi:[10.4271/2015-01-1945](https://doi.org/10.4271/2015-01-1945).
 86. Montanaro, A., Allocca, L., and Lazzaro, M., "Iso-Octane Spray from a GDI Multi-Hole Injector under Non- and Flash Boiling Conditions", SAE Tech. Pap. 2017-01-2319, 2017, doi:[10.4271/2017-01-2319](https://doi.org/10.4271/2017-01-2319).
-

87. Westlye, F.R., Penney, K., Ivarsson, A., Pickett, L.M., Manin, J., and Skeen, S.A., "Diffuse back-illumination setup for high temporally resolved extinction imaging", *Appl. Opt.* 56(17):5028-5038, 2017.
 88. Payri, R., Salvador, F.J., Martí-Aldaraví, P., and Vaquerizo, D., "ECN Spray G external spray visualization and spray collapse description through penetration and morphology analysis", *Appl. Therm. Eng.* 112:304-316, 2017.
 89. Zhang, R., Bohac, S.V., and Sick, V., "Stability of isooctane mixtures with 3-pentanone or biacetyl as fluorescence tracers in combustion experiments", *Exp. Fluids* 40(1):161-163, 2006.
 90. Davy, M., Williams, P., Han, D., and Steeper, R., "Evaporation characteristics of the 3-pentanone–isooctane binary system", *Exp. Fluids* 35(1):92-99, 2003.
 91. Jung, J., Park, S., and Bae, C., "Combustion characteristics of gasoline and n -butane under lean stratified mixture conditions in a spray-guided direct injection spark ignition engine", *Fuel* 187:146-158, 2017.
 92. Ma, X., He, X., Wang, J.-x., and Shuai, S., "Co-evaporative multi-component fuel design for in-cylinder PLIF measurement and application in gasoline direct injection research", *Appl. Energy* 88(8):2617-2627, 2011.
 93. Han, D., and Steeper, R.R., "An LIF equivalence ratio imaging technique for multicomponent fuels in an IC engine", *Proc. Combust. Inst.* 29(1):727-734, 2002.
 94. Steeper, R., De Zilwa, S., and Fayoux, A., "Co-Evaporative Tracer-PRF Mixtures For LIF Measurements In Optical HCCI Engines", SAE Tech. Pap. 2005-01-0111, 2005, doi:[10.4271/2005-01-0111](https://doi.org/10.4271/2005-01-0111).
 95. Krämer, H., Einecke, S., Schulz, C., Sick, V., Natrass, S.R., and Kitching, J.S., "Simultaneous Mapping of the Distribution of Different Fuel Volatility Classes Using Tracer-LIF Tomography in an IC Engine", SAE Tech. Pap. 982467, 1998, doi:[10.4271/982467](https://doi.org/10.4271/982467).
 96. Koban, W., Schorr, J., and Schulz, C., "Oxygen-distribution imaging with a novel two-tracer laser-induced fluorescence technique", *Appl. Phys. B* 74(1):111-114, 2002.
 97. Itani, L.M., *Development and application of optical diagnostic techniques for assessing the effects of preferential evaporation of multi-component fuels under engine-relevant conditions*, PhD thesis, University of Paris-Saclay, Paris-Saclay, France, 2015.
 98. Itani, L.M., Bruneaux, G., Di Lella, A., and Schulz, C., "Two-tracer LIF imaging of preferential evaporation of multi-component gasoline fuel sprays under engine conditions", *Proc. Combust. Inst.* 35(3):2915-2922, 2015.
 99. Cordier, M., Itani, L., and Bruneaux, G., "Quantitative measurements of preferential evaporation effects of multicomponent gasoline fuel sprays at ECN Spray G conditions", *Int. J. Engine Res.* 21(1):185-198, 2019.
 100. Benzler, T., Dreier, T., and Schulz, C., "UV absorption and fluorescence properties of gas-phase p-difluorobenzene", *Appl. Phys. B* 123(1):39, 2017.
 101. Lind, S., Retzer, U., Will, S., and Zigan, L., "Investigation of mixture formation in a diesel spray by tracer-based laser-induced fluorescence using 1-methylnaphthalene", *Proc. Combust. Inst.* 36(3):4497-4504, 2017.
 102. Kaiser, S.A., and Long, M.B., "Quantitative planar laser-induced fluorescence of naphthalenes as fuel tracers", *Proc. Combust. Inst.* 30(1):1555-1563, 2005.
-

103. Benzler, T., Faust, S., Dreier, T., and Schulz, C., "Low-pressure effective fluorescence lifetimes and photo-physical rate constants of one- and two-ring aromatics", *Appl. Phys. B* 121(4):549-558, 2015.
 104. Bardi, M., Di Lella, A., and Bruneaux, G., "A novel approach for quantitative measurements of preferential evaporation of fuel by means of two-tracer laser induced fluorescence", *Fuel* 239:521-533, 2019.
 105. Holderbaum, T., and Gmehling, J., "PSRK: A Group Contribution Equation of State Based on UNIFAC", *Fluid Phase Equilib.* 70(2-3):251-265, 1991.
 106. Faust, S., Goschütz, M., Kaiser, S., Dreier, T., and Schulz, C., "A comparison of selected organic tracers for quantitative scalar imaging in the gas phase via laser-induced fluorescence", *Appl. Phys. B* 117(1):183-194, 2014.
 107. Medaerts, F., and Puechberty, D., "In-Cylinder Fuel/Air Mixture and Flame Front Visualization in a Transparent Engine Using PLIF: A Comparison Between Natural Gas and Gasoline Used as a Fuel", SAE Tech. Pap. 982524, 1998, doi:[10.4271/982524](https://doi.org/10.4271/982524).
 108. Rubas, P.J., Paul, M.A., Martin, G.C., Coverdill, R.E., Lucht, R.P., Peters, J.E., and DelVecchio, K.A., "Methane Jet Penetration in a Direct-Injection Natural Gas Engine", SAE Tech. Pap. 980143, 1998, doi:[10.4271/980143](https://doi.org/10.4271/980143).
 109. Salazar, V.M., Kaiser, S.A., and Halter, F., "Optimizing Precision and Accuracy of Quantitative PLIF of Acetone as a Tracer for Hydrogen Fuel", *SAE Int. J. Fuels Lubr.* 2(1):737-761, 2009.
 110. Salazar, V.M., and Kaiser, S.A., "Influence of the In-Cylinder Flow Field (Tumble) on the Fuel Distribution in a DI Hydrogen Engine Using a Single-Hole Injector", *SAE Int. J. Engines* 3(1):309-325, 2010.
 111. Scarcelli, R., Wallner, T., Matthias, N., Salazar, V., and Kaiser, S., "Mixture Formation in Direct Injection Hydrogen Engines: CFD and Optical Analysis of Single- and Multi-Hole Nozzles", *SAE Int. J. Engines* 4(2):2361-2375, 2011.
 112. Kirchweger, W., Haslacher, R., Hallmannsegger, M., and Gerke, U., "Applications of the LIF method for the diagnostics of the combustion process of gas-IC-engines", *Exp. Fluids* 43(2-3):329-340, 2007.
 113. Friedrich, W., Grzeszik, R., and Wensing, M., "Mixture Formation in a CNG-DI Engine in Stratified Operation", SAE Tech. Pap. 2015-24-2474, 2015, doi:[10.4271/2015-24-2474](https://doi.org/10.4271/2015-24-2474).
 114. Friedrich, W., Grzeszik, R., Helmich, M., Bossmeyer, T., and Wensing, M. "Characterization of High Pressure Natural Gas Injections for Stratified Operation of a Spark Ignited Engine by Simultaneous Fuel Concentration and Air Entrainment Measurements". in *18th International Symposium on the Application of Laser and Imaging Techniques to Fluid Mechanics*. July 4th - 7th, 2016. Lisbon, Portugal.
 115. Tomita, E., Kawahara, N., Nishiyama, A., and Shigenaga, M., "In situ measurement of hydrocarbon fuel concentration near a spark plug in an engine cylinder using the 3.392 nm infrared laser absorption method: application to an actual engine", *Meas. Sci. Technol.* 14(8):1357-1363, 2003.
 116. Grosch, A., Beushausen, V., Thiele, O., and Grzeszik, R., "Crank Angle Resolved Determination of Fuel Concentration and Air/Fuel Ratio in a SI-Internal Combustion Engine Using a Modified Optical Spark Plug", SAE Tech. Pap. 2007-01-0644, 2007, doi:[10.4271/2007-01-0644](https://doi.org/10.4271/2007-01-0644).
-

117. Witzel, O., Klein, A., Meffert, C., Wagner, S., Kaiser, S., Schulz, C., and Ebert, V., "VCSEL-based, high-speed, in situ TDLAS for in-cylinder water vapor measurements in IC engines", *Opt. Express* 21(17):19951-19965, 2013.
 118. Witzel, O., Klein, A., Meffert, C., Schulz, C., Kaiser, S.A., and Ebert, V., "Calibration-free, high-speed, in-cylinder laser absorption sensor for cycle-resolved, absolute H₂O measurements in a production IC engine", *Proc. Combust. Inst.* 35(3):3653-3661, 2015.
 119. Grosch, A., Wackerbarth, H., Thiele, O., Berg, T., and Beckmann, L., "Infrared spectroscopic concentration measurements of carbon dioxide and gaseous water in harsh environments with a fiber optical sensor by using the HITEMP database", *J. Quant. Spectrosc. Radiat. Transfer* 133:106-116, 2014.
 120. Bauke, S., Golibrzuch, K., Rotter, F., Wackerbarth, H., Thiele, O., and Berg, T., "Quantitative, time-resolved detection of CH₄ concentrations in flows for injection analysis in CNG engines using IR absorption", *JSSS* 6(1):185-198, 2017.
 121. Golibrzuch, K., Digulla, F.-E., Bauke, S., Wackerbarth, H., Thiele, O., and Berg, T., "Optical sensor system for time-resolved quantification of methane densities in CH₄-fueled spark ignition engines", *Appl. Opt.* 56(22):6049-6058, 2017.
 122. Müller, F., Schmitt, M., Wright, Y.M., and Boulouchos, K., "Determination of Supersonic Inlet Boundaries for Gaseous Engines Based on Detailed RANS and LES Simulations", *SAE Int. J. Engines* 6(3):1532-1543, 2013.
 123. Seboldt, D., Lejsek, D., Wentsch, M., Chiodi, M., and Bargende, M., "Numerical and Experimental Studies on Mixture Formation with an Outward-Opening Nozzle in a SI Engine with CNG-DI", SAE Tech. Pap. 2016-01-0801, 2016, doi:[10.4271/2016-01-0801](https://doi.org/10.4271/2016-01-0801).
 124. Bartolucci, L., Scarcelli, R., Wallner, T., Swantek, A., Powell, C.F., Kastengren, A., and Duke, D., "CFD and X-Ray Analysis of Gaseous Direct Injection from an Outward Opening Injector", SAE Tech. Pap. 2016-01-0850, 2016, doi:[10.4271/2016-01-0850](https://doi.org/10.4271/2016-01-0850).
 125. Deshmukh, A., Mayer, D., Bode, M., et al. "LES of Direct Gas Injection in Internal Combustion Engines". in *In LES for Internal Combustion Engine Flows*. Nov. 30th - Dec. 1st, 2016. Rueil-Malmaison, France.
 126. Twellmeyer, A., Kopple, F., and Weigand, B., "Evaluating Different Measures to Improve the Numerical Simulation of the Mixture Formation in a Spark-Ignition CNG-DI-Engine", SAE Tech. Pap. 2017-01-0567, 2017, doi:[10.4271/2017-01-0567](https://doi.org/10.4271/2017-01-0567).
 127. Rothamer, D.A., Snyder, J.A., Hanson, R.K., and Steeper, R.R., "Two-Wavelength PLIF Diagnostic for Temperature and Composition", *SAE Int. J. Fuels Lubr.* 1(1):520-533, 2008.
 128. Lind, S., Zigan, L., Trost, J., Leipertz, A., and Will, S., "Simultaneous two-dimensional measurement of fuel-air ratio and temperature in a direct-injection spark-ignition engine using a new tracer-pair laser-induced fluorescence technique", *Int. J. Engine Res.* 17(1):120-128, 2016.
 129. Zigan, L., Trost, J., and Leipertz, A., "Simultaneous imaging of fuel vapor mass fraction and gas-phase temperature inside gasoline sprays using two-line excitation tracer planar laser-induced fluorescence", *Appl. Opt.* 55(6):1453-1460, 2016.
 130. Lind, S., Trost, J., Zigan, L., Leipertz, A., and Will, S., "Application of the tracer combination TEA/acetone for multi-parameter laser-induced fluorescence measurements in IC engines with exhaust gas recirculation", *Proc. Combust. Inst.* 35(3):3783-3791, 2015.
-

131. Faust, S., *Characterisation of organic fuel tracers for laser-based quantitative diagnostics of fuel concentration, temperature, and equivalence ratio in practical combustion processes*, PhD thesis, University of Duisburg-Essen, Duisburg, Germany, 2013.
 132. Goschütz, M., *Endoskopische Brennraumdiagnostik im seriennahen Ottomotor durch Chemilumineszenz und laserinduzierte Fluoreszenz*, PhD thesis, University of Duisburg-Essen, Duisburg, Germany, 2018.
 133. Retzer, U., Fink, W., Will, T., Will, S., and Zigan, L., "Fluorescence characteristics of the fuel tracer 1-methylnaphthalene for the investigation of equivalence ratio and temperature in an oxygen-containing environment", *Appl. Phys. B* 125(7):124, 2019.
 134. Faust, S., Dreier, T., and Schulz, C., "Photo-physical properties of anisole: temperature, pressure, and bath gas composition dependence of fluorescence spectra and lifetimes", *Appl. Phys. B* 112(2):203-213, 2013.
 135. Zabeti, S., Aghsaee, M., Fikri, M., Welz, O., and Schulz, C., "Optical properties and pyrolysis of shock-heated gas-phase anisole", *Proc. Combust. Inst.* 36(3):4525-4532, 2017.
 136. Kranz, P., Fuhrmann, D., Kaiser, S., et al., "In-cylinder LIF imaging, IR-absorption point measurements, and CFD simulations to evaluate mixture formation in a CNG-fueled engine", *SAE Int. J. Engines* 11(6):1221-1238, 2018.
 137. Shahbaz, M.A., Goschütz, M., and Kaiser, S.A. "Endoscopic Anisole-LIF Imaging of Flame Propagation and Temperature Fluctuations in a Production SI Engine". in *8th European Combustion Meeting*. April 18th - 21st, 2017. Dubrovnik, Croatia.
 138. Tran, K.H., Guibert, P., Morin, C., Bonnet, J., Pounkin, S., and Legros, G., "Temperature measurements in a rapid compression machine using anisole planar laser-induced fluorescence", *Combust. Flame* 162(10):3960-3970, 2015.
 139. Gessenhardt, C., *Endoskopische Bestimmung des Temperaturfeldes im Brennraum von Ottomotoren mittels laserinduzierter Fluoreszenz*, PhD thesis, University of Duisburg-Essen, Munich, Germany, Hut, 2014.
 140. Peterson, B., Baum, E., Böhm, B., Sick, V., and Dreizler, A., "Evaluation of toluene LIF thermometry detection strategies applied in an internal combustion engine", *Appl. Phys. B* 117(1):151-175, 2014.
 141. Zegers, R.P.C., Yu, M., Bekdemir, C., Dam, N.J., Luijten, C.C.M., and de Goey, L.P.H., "Temperature measurements of the gas-phase during surrogate diesel injection using two-color toluene LIF", *Appl. Phys. B* 112(1):7-23, 2013.
 142. Tea, G., Bruneaux, G., Kashdan, J.T., and Schulz, C., "Unburned gas temperature measurements in a surrogate Diesel jet via two-color toluene-LIF imaging", *Proc. Combust. Inst.* 33(1):783-790, 2011.
 143. Kokjohn, S., Reitz, R.D., Splitter, D., and Musculus, M., "Investigation of Fuel Reactivity Stratification for Controlling PCI Heat-Release Rates Using High-Speed Chemiluminescence Imaging and Fuel Tracer Fluorescence", *SAE Int. J. Engines* 5(2):248-269, 2012.
 144. Espey, C., Dec, J.E., Litzinger, T.A., and Santavicca, D.A., "Planar laser rayleigh scattering for quantitative vapor-fuel imaging in a diesel jet", *Combust. Flame* 109(1):65-86, 1997.
 145. Kokjohn, S.L., Musculus, M.P.B., and Reitz, R.D., "Evaluating temperature and fuel stratification for heat-release rate control in a reactivity-controlled compression-ignition
-

- engine using optical diagnostics and chemical kinetics modeling", *Combust. Flame* 162(6):2729-2742, 2015.
146. Hwang, W., Dec, J.E., and Sjöberg, M., "Fuel Stratification for Low-Load HCCI Combustion: Performance & Fuel-PLIF Measurements", SAE Tech. Pap. 2007-01-4130, 2007, doi:[10.4271/2007-01-4130](https://doi.org/10.4271/2007-01-4130).
147. Dec, J.E., and Hwang, W., "Characterizing the Development of Thermal Stratification in an HCCI Engine Using Planar-Imaging Thermometry", *SAE Int. J. Engines* 2(1):421-438, 2009.
148. Kim, T., and Ghandhi, J.B., "Quantitative 2-D Fuel Vapor Concentration Measurements in an Evaporating Diesel Spray using the Exciplex Fluorescence Method", SAE Tech. Pap. 2001-01-3495, 2001, doi:[10.4271/2001-01-3495](https://doi.org/10.4271/2001-01-3495).
149. Kojima, H., Takahashi, E., Tsujimura, T., Furutani, H., and Kashiwazaki, T., "Acetone PLIF Measurements of Temperature and Concentration Distributions in a High-Temperature and High-Pressure Spray", SAE Tech. Pap. 2015-01-1840, 2015, doi:[10.4271/2015-01-1840](https://doi.org/10.4271/2015-01-1840).
150. Manin, J., *Analysis of Mixing Processes in Liquid and Vaporized Diesel Sprays through LIF and Rayleigh Scattering Measurements*, PhD thesis, Universidad Politécnica de Valencia, Valencia, Spain, 2011.
151. Sahoo, D., Petersen, B., and Miles, P.C., "Measurement of Equivalence Ratio in a Light-Duty Low Temperature Combustion Diesel Engine by Planar Laser Induced Fluorescence of a Fuel Tracer", *SAE Int. J. Engines* 4(2):2312-2325, 2011.
152. Bensing, D., *Aufbau eines optisch zugänglichen Einzylinder-Viertaktmotors und charakterisierende Messungen*, PhD thesis, University of Duisburg-Essen, Duisburg, Germany, 2013.
153. Schild, M., *Quantitative Untersuchungen zur Zylinderinnenströmung, Gasphasentemperatur und frühen Flammenausbreitung mittels bildgebender Messtechniken*, PhD thesis, University of Duisburg-Essen, Duisburg, Germany, 2016.
154. Jung, Y., Manin, J., Skeen, S., and Pickett, L.M., "Measurement of Liquid and Vapor Penetration of Diesel Sprays with a Variation in Spreading Angle", SAE Tech. Pap. 2015-01-0946, 2015, doi:[10.4271/2015-01-0946](https://doi.org/10.4271/2015-01-0946).
155. Laven, P. "MiePlot v4.6". 2. October 2018, Available from: philiplaven.com/mieplot.htm.
156. Siebers, D.L., "Liquid-Phase Fuel Penetration in Diesel Sprays", SAE Tech. Pap. 980809, 1998, doi:[10.4271/980809](https://doi.org/10.4271/980809).
157. Janas, P., Wlokas, I., Böhm, B., and Kempf, A., "On the Evolution of the Flow Field in a Spark Ignition Engine", *Flow Turbul. Combust.* 98(1):237-264, 2016.
158. Jacques, B., and Miles, P., "In-Cylinder Flow", in *Encyclopedia of Automotive Engineering*, John Wiley & Sons, Ltd. 2014.
159. Nijegorodov, N., Vasilenko, V., Monowe, P., and Masale, M., "Systematic investigation of the influence of methyl groups upon fluorescence parameters and the intersystem crossing rate constant of aromatic molecules", *Spectrochim. Acta A* 74(1):188-194, 2009.
160. Engineering-ToolBox. "Autoignition temperature and flash point hydrocarbons". 2017, Available from: engineeringtoolbox.com/.
161. Makino, A., and Law, C.K., "On the controlling parameter in the gasification behavior of multicomponent droplets", *Combust. Flame* 73(3):331-336, 1988.
-

-
162. Zhang, R., and Sick, V., "Multi-Component Fuel Imaging in a Spray-Guided Spark-Ignition Direct-Injection Engine", SAE Tech. Pap. 2007-01-1826, 2007, doi:[10.4271/2007-01-1826](https://doi.org/10.4271/2007-01-1826).
163. Zigan, L., Schmitz, I., Flügel, A., Wensing, M., and Leipertz, A., "Structure of evaporating single- and multicomponent fuel sprays for 2nd generation gasoline direct injection", *Fuel* 90(1):348-363, 2011.
164. Bauke, S., Golibrzuch, K., Wackerbarth, H., et al., "Optical sensor system for time-resolved quantification of methane concentrations: Validation measurements in a rapid compression machine", *J. Quant. Spectrosc. Radiat. Transfer* 210:101-110, 2018.

7.1 Author's contributions to publications

7.1.1 Journal articles

[136]: In-cylinder LIF imaging, IR-absorption point measurements, and CFD simulations to evaluate mixture formation in a CNG-fueled engine

Published

Patrick Kranz, Daniel Fuhrmann, Sebastian A. Kaiser, Stephan Bauke, Kai Golibrzuch, Hainer Wackerbarth, Peter Kawelke, Julian Luciani, Jasper Zachow, Manuel Schütte, Olaf Thiele and Thomas Berg

SAE International Journal of Engines 11(6):1221-1238, 2018

This paper reports on the methodology of LIF imaging and IR-absorption that were applied in the same engine to derive the air/fuel ratio. Results from the two experiments are compared to a CFD simulation.

I and Dr. D. Fuhrmann carried out the LIF experiment. We were responsible for the LIF imaging as well as the modifications, which needed to be done to the test bench. I post-processed and visualized the results of the LIF data and was main responsible for managing and writing the paper. Sections about IR absorption and CFD simulation were written by Laser-Laboratorium Göttingen e.V. and Volkswagen AG, respectively.

[53]: LIF-based imaging of preferential evaporation of a multi-component gasoline surrogate in a direct-injection engine

Published

Patrick Kranz and Sebastian A. Kaiser

Proceedings of the Combustion Institute 37(2):1365-1372, 2019

This paper reports on a two-tracer two-color LIF imaging technique that can quantify the fuel-component segregation in an optically accessible DI engine.

I was responsible for developing, planning and the execution of the LIF experiments as well as the data evaluation. I was responsible for writing the paper, which was pre-reviewed by Prof. Kaiser.

[54]: Analysis of the interaction of Spray G direct injection and in-cylinder flow in optical engines for late injection

Published

Christopher Geschwindner, Patrick Kranz, Cooper Welch, Marius Schmidt, Benjamin Böhm, Sebastian A. Kaiser and Joaquín de la Morena

International Journal of Engine Research, 21(1):169-184, 2019.

This paper reports on the interaction of the liquid spray and the flow of the surrounding gas after GDI by the Spray G injector (ECN) in two optically accessible engines. The paper was published in a special issue of IJER on ECN-related topics.

I planned and carried out the experiments at UDE. I processed the PIV, DBI, and Mie scattering data. C. Geschwindner and I were the main authors responsible for writing the paper.

Steam reforming of CH₄ at a combined heat-power plant to improve engine efficiency and emissions

In preparation

Patrick Kranz, Kai Banke, Carsten Spieker, Christian Spitta, Sebastian A. Kaiser

The manuscript reports on syngas produced by steam reforming of CH₄ that is then used to fuel a combined heat-power unit. The goal of this strategy is to improve the trade-off between electric efficiency and pollutant emissions.

I planned and carried out the experiments at the combined heat-power plant with couple steam reformer at UDE. I processed the data. K. Banke and I are the main authors responsible for writing the manuscript. The steam reformer was developed by the project partner ZBT GmbH.

7.1.2 Conference papers

- [52] Kranz, P., Schulz, C., and Kaiser, S.A., "LIF-based visualization of preferential evaporation of a multi-component fuel in an SIDI engine", in *8th European Combustion Meeting*. April 18th - 21st 2017: Dubrovnik, Croatia.
- [4] Kranz, P., Kaiser, S.A., "Laser-induced-fluorescence based visualization of a multi-component fuel in a direct-injection engine", in *Heft R 584 – Tagungsband Motoren – FVV fall meeting*. Sept. 27th 2018: Würzburg, Germany.

7.1.3 Conferences poster

Kranz, P., Schiffmann, P., Kaiser, S.A., Sick, V., "Independent component analysis to link combustion variability in a spark-ignited engine with flow-field variation", *36th International Symposium on Combustion*. Aug. 1st - 5th 2016: Seoul, South Korea.

7.2 Supervised student projects and theses

Charfi, B., "Stereo particle image velocimetry (PIV) of the steady-state intake flow in the cylinder head of a spark-ignition engine". *Master thesis*, University of Duisburg-Essen, (2016).

Gori, G., *LIF-thermometry in an optical engine operated on natural gas*. Visiting scholar from von Karman Institute for Fluid Dynamics – Belgium, University of Duisburg-Essen, (2016).

Chen, T., "A LabVIEW-based control system for the intake-air flow of a single-cylinder internal combustion engine". *Bachelor thesis*, University of Duisburg-Essen, (2017).

Lennackers, P., "Visualization of the spray distribution in a direct-injection gasoline type engine using RGB-diffuse backlight illumination and Mie scattering". *Master thesis*, University of Duisburg-Essen, (2017).

Tuncer, A., "Design and testing of a counter-flow heat exchanger for fuel pre-heating in a gasoline direct-injection engine". *Bachelor thesis*, University of Duisburg-Essen, (2018).

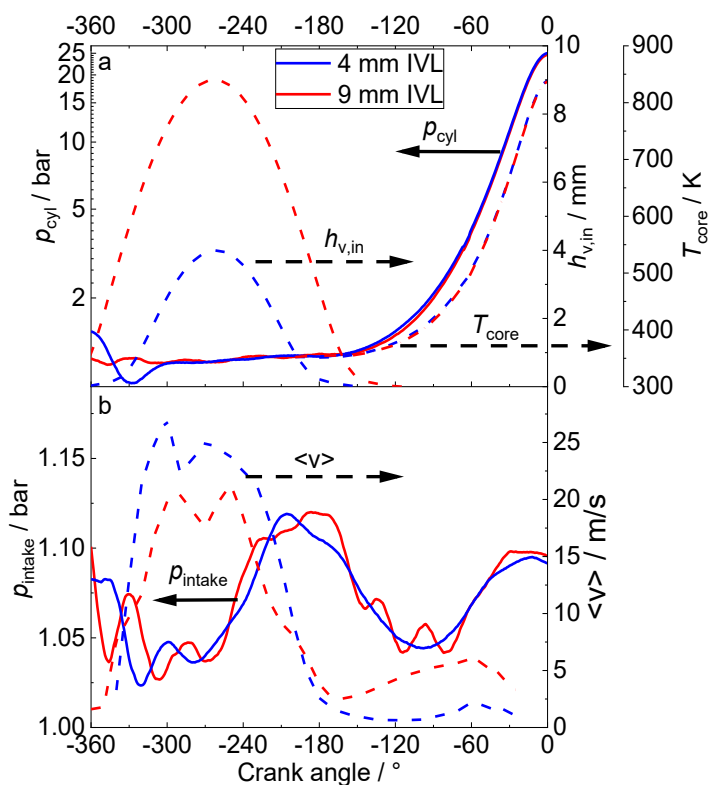
Zimmer, M., "Spectroscopic investigation of the influence of temperature and oxygen on the fluorescence of "tracers" in liquids". *Master thesis*, University of Duisburg-Essen, (2018).

Grau, T., "Structured Laser Illumination Planar Imaging (SLIPI) in LIF. Testing, Methods, Processing". *Lab-course in combustion and thermodynamics*. (Praktikum Verbrennung und Thermodynamik), University of Duisburg-Essen, (2018).

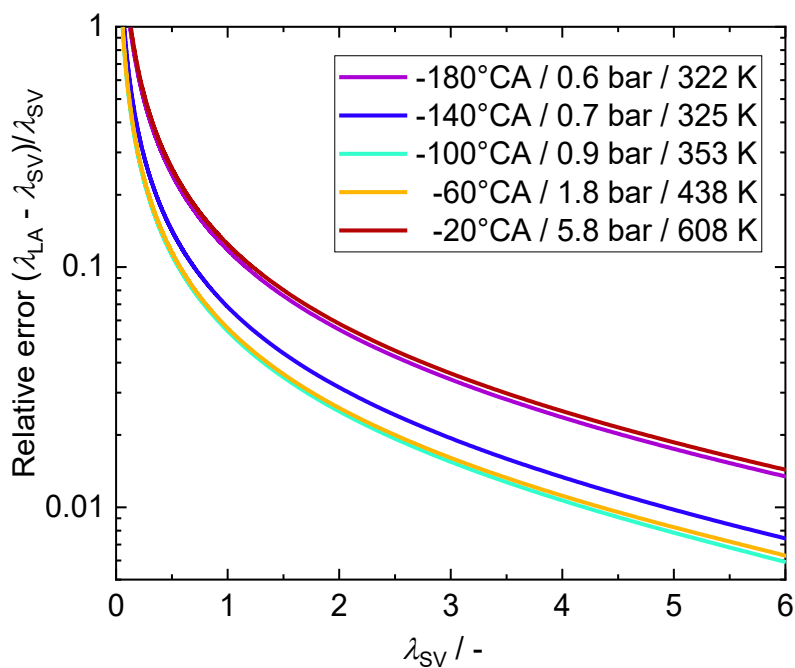
Radoi, M., *Particle Image Velocimetry in a gasoline-type optical engine*. Visiting scholar from IFP school – France, University of Duisburg-Essen, (2018).

Cakoglu, E., "Experimental investigation of thermo-chemical recuperation in a combined heat-power generator unit". *Master thesis*, University of Duisburg-Essen, (2019).

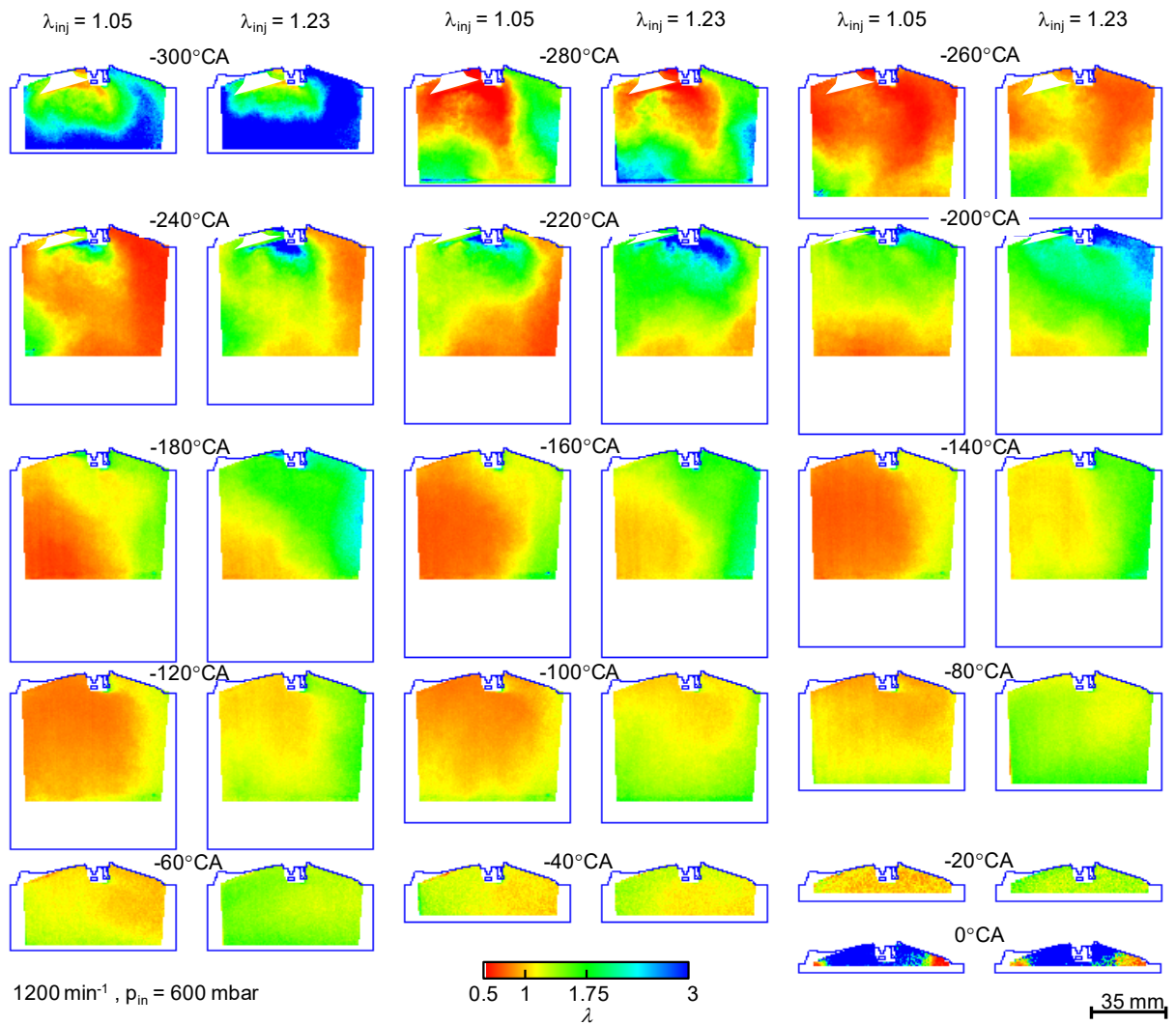
Chapter 8 - Appendices



Appx. 8-1: (a) in-cylinder pressure, intake-valve lift, and adiabatic core temperature; (b) intake pressure and mean velocity averaged throughout the FOV. Traces for 1200 min^{-1} at 4 mm and 9 mm IVL of the optical engine at UDE are shown.



Appx. 8-2: Relative error in λ for the summation of both channel's LIF signal $S_{FF} = S_{FF}^{(b)} + S_{FF}^{(r)}$.



Appx. 8-3: Field-wide comparison of λ as crank-angle evolution from LIF imaging of operation at $\lambda_{PFI} = 1.05$ and 1.23 from conventional LIF imaging. Engine speed is 1200 min^{-1} , intake pressure 600 mbar. LIF images at each crank angle are ensemble averages of 20 non-consecutive cycles (every second cycle).

DuEPublico

Duisburg-Essen Publications online

UNIVERSITÄT
DUISBURG
ESSEN

Offen im Denken

ub | universitäts
bibliothek

Diese Dissertation wird über DuEPublico, dem Dokumenten- und Publikationsserver der Universität Duisburg-Essen, zur Verfügung gestellt und liegt auch als Print-Version vor.

DOI: 10.17185/duepublico/72672

URN: urn:nbn:de:hbz:464-20200902-151157-0

Alle Rechte vorbehalten.